FUSED DEPOSITION OF PLA MATRIX COMPOSITE FOR 4D APPLICATIONS

THESIS

SUBMITTED IN FULFILLMENT OF THE REQUIREMENTS FOR THE REGISTRATION OF THE DEGREE OF

DOCTOR OF PHILOSOPHY

In

(Mechanical Engineering)

Submitted By

Sudhir Kumar

Registration No. 901808007

Under the Guidance of

Dr. TP Singh
Professor, Deptt. of Mech. Engg.
Thapar Institute of Engineering and Technology, Patiala, Punjab, India

Dr. Ajay Batish
Professor, Deptt. of Mech. Engg.
Thapar Institute of Engineering and Technology, Patiala, Punjab, India

Dr. Rupinder Singh
Professor, Deptt. of Mech. Engg.
National Institute of Technical Teachers Training and Research, Chandigarh, India

THAPAR INSTITUTE
OF ENGINEERING & TECHNOLOGY
(Deemed to be University)

DEPARTMENT OF MECHANICAL ENGINEERING

THAPAR INSTITUTE OF ENGINEERING & TECHNOLOGY

PATIALA–147004, PUNJAB, INDIA.

June 2021

THAPAR INSTITUTE OF ENGINEERING AND TECHNOLOGY, PATIALA

CANDIDATE'S DECLARATION

I hereby acknowledge that the work which is being presented in this thesis entitled "FUSED DEPOSITION OF PLA MATRIX COMPOSITE FOR 4D APPLICATIONS" (**University Roll Number: 901808007**) in fulfillment of the requirement for the award of Ph.D. (Mechanical Engineering) submitted in the Department of Mechanical Engineering at Thapar Institute of Engineering and Technology, Patiala, India is an authentic record of my hard work carried out during a period from July 2018 to Dec 2020 under the supervision of Dr. T.P Singh (Professor and Head of Mechanical Engineering Department, Thapar Institute of Engineering and Technology, Patiala, India), Dr. Ajay Batish (Professor Mechanical Engineering Department, Thapar Institute of Engineering and Technology, Patiala, India) and Dr. Rupinder Singh (Professor, Mechanical Engineering Department, National Institute of Technical Teachers Training & Research, Chandigarh, India). The work presented in this thesis report has been not presented in any other University/Institute for the award of a Ph.D. degree.

Sudhir Kumar.
(Sudhir Kumar)

This is to certify that the above statement made by the candidate is correct to the best of my knowledge.

Dr. T.P Singh
Professor and Head
Deptt. Of Mechanical Engg.
T.I.E.T, Patiala
Thesis Supervisor

Dr. Ajay Batish
Professor
Deptt. Of Mechanical Engg.
T.I.E.T, Patiala
Thesis Supervisor

RSingh
Dr. Rupinder Singh
Professor
Deptt. Of Mechanical Engg.
NITTTR, Chandigarh
Thesis Supervisor

(Signature of Head of Mechanical Engineering Department, T.I.E.T, Patiala)

Abstract

In the past two decades, fused deposition modeling (FDM) has been explored widely as one of the low-cost additive manufacturing (AM) techniques for a different range of thermoplastics and thermoplastic composites. In the current scenario, various industries (such as medicine, construction, mechanical, electrical, etc.) are using FDM for printing critically designed products. Various range of polymeric materials such as polylactic acid (PLA), acrylonitrile butadiene styrene (ABS), polyamide (PA6), polyvinyl chloride is available for FDM applications. PLA is one of the widely used materials for FDM applications. Especially bio compatibility issues have been explored widely by various research groups. But little has been reported on the in-house feedstock filament development and printing capability for multi-material (product comprising of different composite materials at each successive layer of 3D printed design) and hybrid composites (all reinforcements in a single composite).

In this work, PLA was reinforced with PVC, wood powder, and magnetite powder (Fe_3O_4) for preparing multi/hybrid composites to support 4D applications. The reinforcement of PVC in PLA has been chosen to make the PLA material flexible and use the waste PVC in the PLA matrix. The wood powder has been reinforced in the PLA matrix to reduce the thermal conductivity to control the heat flow from the material matrix. Fe_3O_4 powder has been used to provide the 4D capability to the newly designed composite matrix to acquire the property of self-assembly when triggered with the external magnetic field (as stimulus). Two different types of prototypes (a) hybrid blend (PLA/PVC/wood powder/Fe_3O_4 powder in single composite) and (b) multi-material with four different feedstock filaments ((a) PLA, (b) PLA/PVC, (c) PLA/wood powder and (d) PLA/Fe_3O_4 powder) have been used in a single prototype. To explore the properties of two different types of prototypes, the selected material matrix has been initially prepared as feedstock filament using twin-screw extrusion (TSE) followed by 3D printing on an FDM setup. At each step of processing, Taguchi orthogonal array (OA) approach has been used to prepare the components so that optimization of processing conditions may be achieved for maximizing the results. After developing functional prototypes of different combinations, properties such as mechanical, morphological, rheological, thermal and magnetic, were tested. Finally, the prepared composites were tested for addressing the recycling issues.

Acknowledgment

The author is highly obliged to Dr. Prakash Gopalan (Director, Thapar Institute of Engineering and Technology, Patiala, India) for his help in carrying out the present research work.

I express my profound thanks to my research supervisors Dr. T.P Singh (Professor and Head, Mechanical Engineering Department, Thapar Institute of Engineering and Technology, Patiala, India), Dr. Ajay Batish (Professor Mechanical Engineering Department, Thapar Institute of Engineering and Technology, Patiala, India) and Dr. Rupinder Singh (Professor, Mechanical Engineering Department, National Institute of Technical Teachers Training & Research, Chandigarh, India) for their keen interest, expert guidance, valuable suggestions and persistent encouragement which inspired me to submit this thesis in the present form. They have been responsible for smoothing all the rough edges in this investigation by their constructive criticism and deep insight.

I am very thankful to my family who has been always supportive of me and has inspired me to follow my passion for research.

My unyielding faith in God has made me capable to face all the hardships with courage and helped me to cross all hurdles, which came my way in this journey which later converted into fruitful success. I also want to express my gratitude towards Manufacturing Research Lab at Guru Nanak Dev Engineering College, Ludhiana, India for providing me the required technological support.

Sudhir Kumar.

(Sudhir Kumar)

List of Publications

The current work of **“FUSED DEPOSITION OF PLA MATRIX COMPOSITE FOR 4D APPLICATIONS”** got widely accepted and we were able to publish 15 SCI, 3 Scopus, and 13 Elsevier based Book chapters.

List of SCI publications

Serial number	Title of Paper	Journal Name	Impact factor
1	Investigations of polylactic acid reinforced composite feedstock filaments for multimaterial three-dimensional printing applications	Proceedings of the Institution of Mechanical Engineers, Part C (2019 Sep; 233(17):5953-65.)	Published/1.386
2	Multi material printing and characterization for mechanical and surface properties of functionally graded prototype	Proceedings of the Institution of Mechanical Engineers, Part C (2019 Oct; 233(19-20):6741-53.)	Published/1.529
3	On investigation of rheological, mechanical and morphological characteristics of waste polymer-based feedstock filament for 3D printing applications	JTCM (Journal of thermoplastic composites) June 2019 DOI: https://doi.org/10.1177/0892705719856063	Published/1.529
4	Investigations for magnetic properties of PLA-PVC-Fe3O4-wood dust blend for self-assembly applications	JTCM (Journal of thermoplastic composites) DOI: https://doi.org/10.1177/0892705719857778	Published/1.529
5	On mechanical characterization of 3-D printed PLA-PVC-wood dust-Fe3O4 composite	JTCM (Journal of thermoplastic composites) DOI: https://doi.org/10.1177/0892705719879195	Published/1.529
6	On flexural, pullout and fractured surface characterization for multi material 3D printed functionally graded prototype	Journal of Composite Materials JCM 2020 Jul; 54(16):2087-99.	Published/1.972
7	Additive Manufacturing of Smart Materials Exhibiting 4d Properties: A State of Art Review	JTCM (Journal of thermoplastic composites) DOI: https://doi.org/10.1177/0892705719895052	Published/1.529

8	On flexural and pull-out properties of 3D printed PLA based hybrid composite matrix	Materials Research Express 2020 Jan 20; 7(1):015330.	Published/1.929
9	Investigations for mechanical, thermal and magnetic properties of polymeric composite matrix for four-dimensional printing applications	Journal of the Brazilian Society of Mechanical Sciences and Engineering (BMSE) 2020 Apr; 42(4):1-5.	Published/1.755
10	On investigations of thermal conductivity, circumferential compressive strength and surface characterization of 3D printed hybrid blended magnetostrictive PLA composite	JTCM (Journal of thermoplastic composites) DOI: https://doi.org/10.1177/0892705720907651	Published/1.529
11	Comparison of mechanical and morphological properties of 3D printed functional prototypes: multi and hybrid blended thermoplastic matrix.	JTCM (Journal of thermoplastic composites) DOI: https://doi.org/10.1177/0892705720925136	Published/1.529
12	Three-dimensional printing of dual thermoplastic materials with different layer combinations: Tensile, flexural, and fractured surface investigations	JTCM (Journal of thermoplastic composites) DOI: https://doi.org/10.1177/0892705720925123	Published/1.529
13	Multi material 3D printing of PLA-PA6/TiO2 polymeric matrix: Flexural, wear and morphological properties	JTCM (Journal of thermoplastic composites)	Published/1.529
14	Fused filament fabrication: A comprehensive review	JTCM (Journal of thermoplastic composites)	Accepted/1.529
15	Multi stage primary and secondary recycled PLA composite matrix for 3D printing applications	Proceedings of the National Academy of Sciences, India Section A: Physical Sciences	Communicated/0.921

List of Scopus Publications

Serial number	Title of paper	Journal	Remarks
1	On process capability comparison of hybrid and multi blend PLA matrix composite: Magnetic and surface properties view point	Materials Today Proceedings/ Conference Bits Dubai (IMMT 2019)	Published /1.09

2	Metal Matrix Composite: A-Methodological Review	Advances in Materials and Processing Technologies (TMPT)	Published/NA
3	3D printed tensile and flexural prototypes of thermoplastic matrix reinforced with multi-materials: A statistical analysis	Materials Today Proceedings/ Conference IIT Indore (IMMT 2020)	Published /1.09

List of Book Chapters

Serial number	Title of paper	Book name	Publisher	Remarks
1	Polymer waste as fused deposition modelling feed stock filament for industrial applications	Reference module in material science and material engineering	Elsevier	Published
2	In-house fabrication of PLA matrix based FDM filament for four dimensional applications	Reference module in material science and material engineering	Elsevier	Published
3	On investigation of dimensional deviation for hybrid composite matrix of PLA	Advances in Metrology and Measurement of Engineering Surfaces, 99-107	Springer, Singapore	Published
4	Primary and secondary recycling of thermosetting polymers: A review	Encyclopedia of Materials: Plastics and Polymers, edited by Professor Saleem Hashmi, Dublin, Ireleand	Elsevier	Published
5	Primary and secondary recycling of thermoplastics: A review	Encyclopedia of Materials: Plastics and Polymers, edited by Professor Saleem Hashmi, Dublin, Ireleand	Elsevier	Published
6	Thermoplastic polymer composites	Encyclopedia of Materials: Plastics and Polymers, edited by Professor Saleem Hashmi, Dublin, Ireleand	Elsevier	Published
7	Thermosetting polymers for 4D printing	Encyclopedia of Materials: Plastics and Polymers, edited by Professor Saleem Hashmi, Dublin, Ireleand	Elsevier	Published

8	Dual/ multi printing of thermosetting polymers	Encyclopedia of Materials: Plastics and Polymers, edited by Professor Saleem Hashmi, Dublin, Ireleand	Elsevier	Published
9	Dual/ multi printing of thermoplastic polymers	Encyclopedia of Materials: Plastics and Polymers, edited by Professor Saleem Hashmi, Dublin, Ireleand	Elsevier	Published
10	Multi material printing of recycled thermoplastics and thermosetting polymers	Encyclopedia of Materials: Plastics and Polymers, edited by Professor Saleem Hashmi, Dublin, Ireleand	Elsevier	Published
11	On process capability of multi stage primary and secondary recycled PLA composite matrix for 3D printing applications	Encyclopedia of Materials: Plastics and Polymers, edited by Professor Saleem Hashmi, Dublin, Ireleand	Elsevier	Published
12	On wear properties of 3D printed hybrid blended PLA composite	Encyclopedia of Materials: Plastics and Polymers, edited by Professor Saleem Hashmi, Dublin, Ireleand	Elsevier	Published
13	On wear of Multi material 3D printed PLA composite	Encyclopedia of Materials: Plastics and Polymers, edited by Professor Saleem Hashmi, Dublin, Ireleand	Elsevier	Published

List of Table

List of Figures

Index

CHAPTER 1

INTRODUCTION

1.1 Three-dimensional (3D) printing

3D printing is an additive manufacturing (AM) technique that was commercially introduced in the late 1980s. The technique is used to print 3D models of intricate designs. AM is one of the most recent fields for low-cost product development. It offers a wide range of variability in the design matrix of a product which makes it suitable for critical designs which were previously not possible with any other manufacturing techniques. These parameters of AM affect the quality of the product significantly. The regression analysis has shown the inverse relation between raster width and surface roughness. Although a significant number of studies have been reported on the development of various 3D printing techniques yet a lot of research is still required for making 3D printed products cost-effective [1]. Different techniques of AM are used to 3D print the ready-to-use products under different AM processes based on the physical condition of processing material as categorized below [2].

(1) Liquid-based AM
  (a) Fused deposition modeling (FDM)
  (b) Stereolithography (SLA)
  (c) Polyjet printing

(2) Solid based AM
  (a) Laminated object manufacturing (LOM)

(3) Powder-based AM
  (a) Selective laser sintering (SLS)
  (b) Electron beam melting (EBM)
  (c) Laser engineered net shaping (LENS)

1.1.1 FDM

Fused deposition modeling (FDM) is an additive manufacturing (AM) technique capable of printing complex designs with commercial and non-commercial feedstock filaments using different processing parameters. The low-cost effectiveness and compatibility of the FDM setup for feedstock filaments developed on a laboratory scale make it different from other AM techniques. FDM is a 3D printing technique of polymeric material in which raw material is first fed as feedstock filament through a tractor-trolley system. The processed feedstock is then heated in a nozzle and gets melted and flows out through it on a 3D printing bed. The 3D printing machine may be operated with different printing parameters such as nozzle angle, raster width, thickness, shape, and geometry of an object. These parameters play a vital role in the final product properties. The object which is to be 3D printed is the first 3D modeled and the model design in .STL file format is made to run on FDM integrated computer [3]. The material from the nozzle is extruded in the form of a thin ribbon which facilitates the joining of one layer over the other [4]. The deposited material in the layer form is known as road [5-6]. The support structure also gets generated automatically and after solidification, the final product is removed from the printing bed [7]. Figure 1.1 shows the schematics of the FDM printing setup.

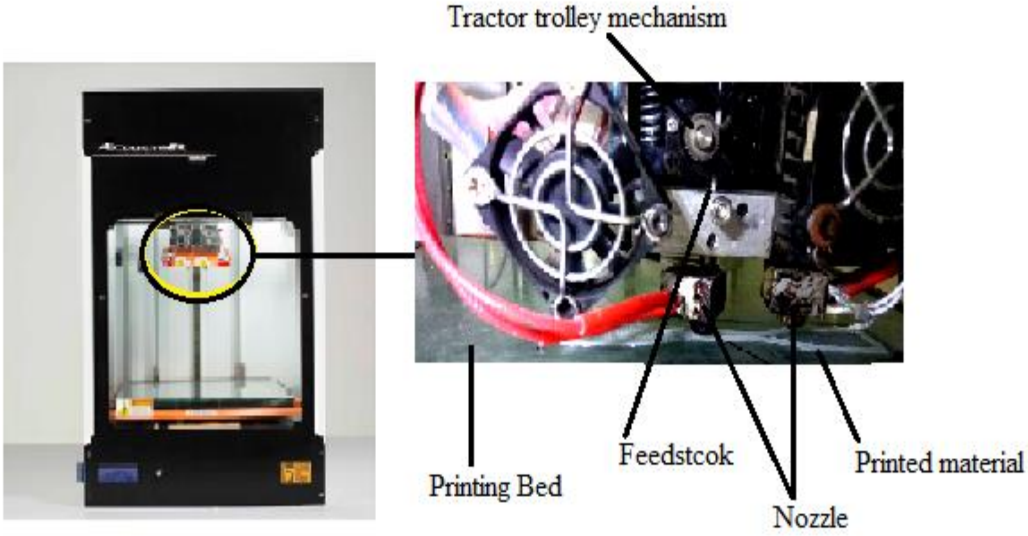

Figure 1.1 Schematics of 3D printing setup

Different feedstock materials and composites are available commercially and prepared on a laboratory scale that may be categorized by Figure 1.2. It has been observed that the nanocomposites prepared on a lab-scale have a great edge over the micro-composites as the properties obtained for nano-composite material are far better than micro-composites [5]. Various researchers have used commercially available feedstock filaments, but the virgin polymeric feedstock filaments have their limitations such as low thermal conductivity, poor electrical conductivity, diamagnetic character, inadequate mechanical properties, and surface properties, etc. To overcome these issues, researchers have tried reinforcements of various foreign particles into the polymeric matrix of virgin polymer. The polymeric blend of a composite may be prepared by two routes (a) mechanical route and (b) chemical route. The reinforcement particles may be categorized into two classes (depending on their size) (i) microparticles (ii) nanoparticles. Based on these, the composites may also be categorized into two classes (1) micro composites and (2) nanocomposites.

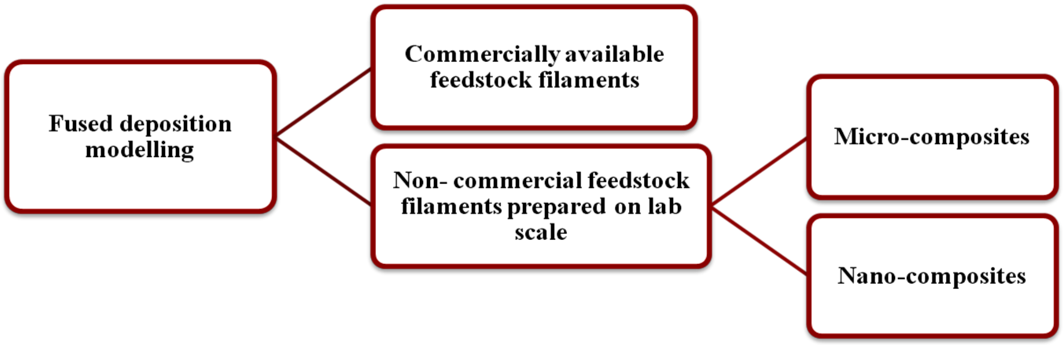

Figure 1.2 Classification of FDM on availability of feedstock filament

1.1.2 SLA

Stereo-lithography is a type of three-dimensional printing in which the material is added layer by layer using photopolymerization in which light enhances the chain reaction in polymer molecules so that they can cross-link each other. This technique is intensively used in printing smart materials such as soybean oil epoxidized acrylate with some curing chemical, methacrylate hyaluronic acid, hydrogels such as Agarose, Alginate, etc [8-12]. Figure 1.3 shows the schematics of SLA.

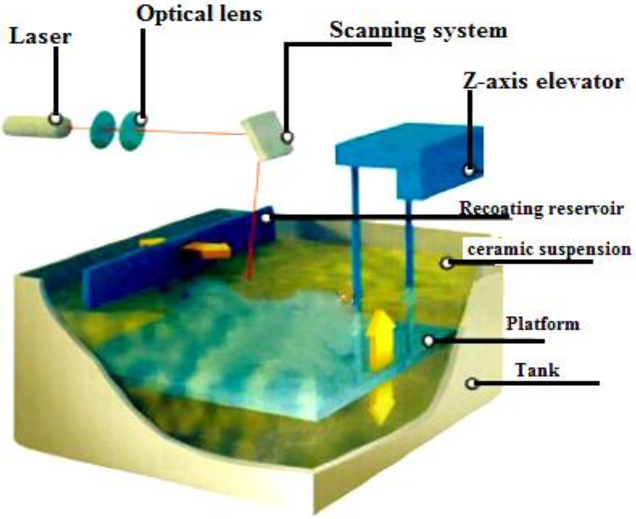

Figure 1.3 Schematics of SLA system [13]

1.1.3 Polyjet printing

Direct write printing is also known as maskless lithography. There are several approaches to DWP such as inkjet printing, spray jet printing, and laser writing, etc. In this type of printing, modified ink cartridges can be filled with the material that needs to be printed. These types of printing take the help of a robotic arm therefore sometimes known as robotic printing. Materials such as VeroWhite1 and Tangoblack1, Glassy shape memory polymer, etc. have also been printed through this technology [14- 16]. One chemical acting as the curing agent is generally used so that when it evaporates the resin or the printed material gets solidified fast e.g., PLA, benzophenone, is printed via this technique, and dichloromethane is used as a curing agent [17-18]. Figure 1.4 shows the schematics of polyjet printing.

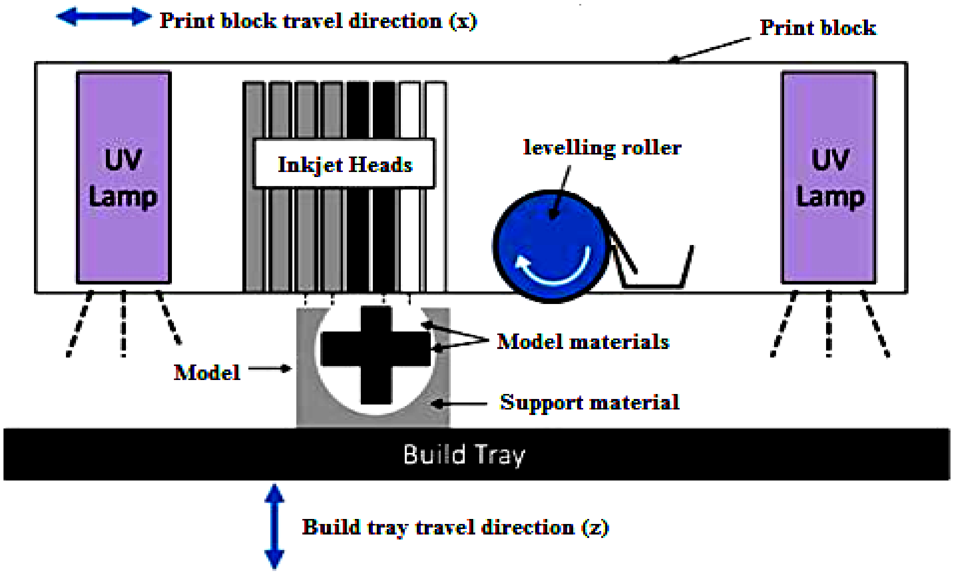

Figure 1.4 Schematics of polyjet printing [19]

1.1.4 SLS

SLS route of additive manufacturing represents a way in which laser is used as a source to melt the powder which is generally known as powder sintering where a laser works with the guidance of a 3D model and melts at a certain defined space as per built 3D model. Figure 1.5 shows the schematic of the SLS system [20]. Various researchers have worked with the SLS system and observed that the 3D printed parts of the SLS system have an edge over the other 3D printed parts in terms of mechanical and morphological properties.

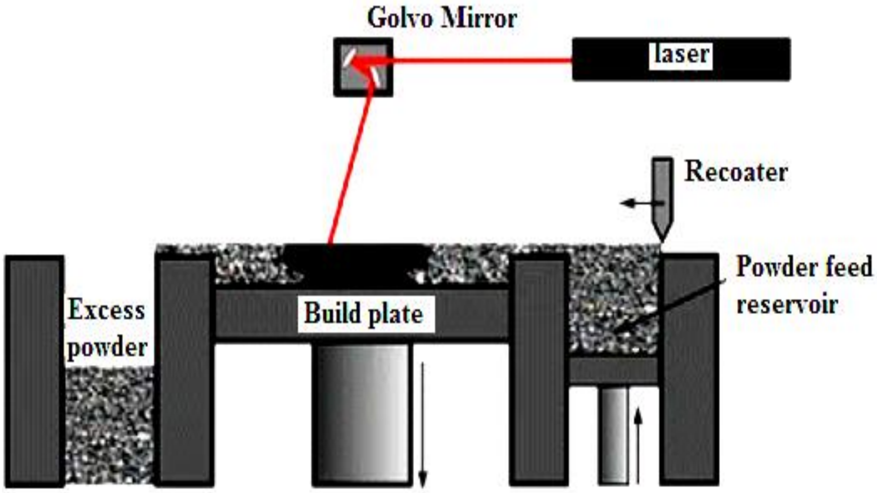

Figure 1.5 Schematics of SLS setup of 3D printing [20]

1.1.5 LOM

In this rapid prototyping technique, the layers of material to adhere to the substrate plate are glued with the base using a roller heater. The mechanism of LOM [20] is very simple in which a different range of materials such as plastics and non-plastics may be combined to one object for the required application. Figure 1.6 shows the schematic of the LOM technique. Multi-material objects can easily be printed using this technique of manufacturing. The LOM-based product may have superior properties than only a single material-based matrix but depends on the adhesion force of different materials with each other.

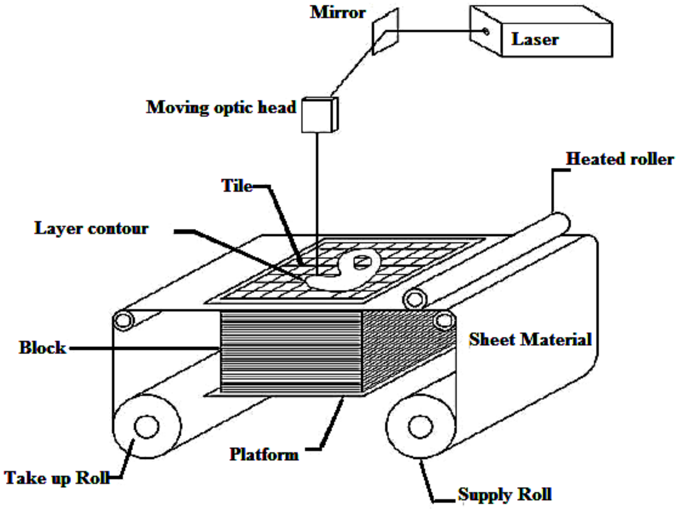

Figure 1.6 Schematics of LOM technique [20]

The above techniques of AM have represented 3D printing techniques where the different range of materials and processing conditions result in a solidified product. It should be noted that the properties obtained for 3D printed products for different production techniques vary from each other, depending on the processing conditions and complexity of the design. Some of the advantages of 3D printing are given below:

- → Low-cost component production
- → Low weight components manufacturing
- → Easy production of intricate designs
- → Easy modifications in dimensions of components

1.2 Definition of 4D printing

The last decade has witnessed the transformation of 3D printing towards 4D printing. 4D printing may be defined as the printing of smart materials and designs, which can transform their shapes and properties at the required time when triggered by external stimulus [21]. Various nanocomposites have been explored to induce smart nature in composites [22]. Shape memory alloys (SMA) represent one such category of the smart matrix which can be actuated with external stimulus and the SMA can memorize their state of change [23-26]. Similarly, design-based smartness has also been explored by researchers and it was observed that structures having specific edge dimensions and joint angles may be triggered with stimulus for the change in shape [27-29]. Figure 1.7 shows the 4D behavior of 3D printed parts on the application of an external stimulus.

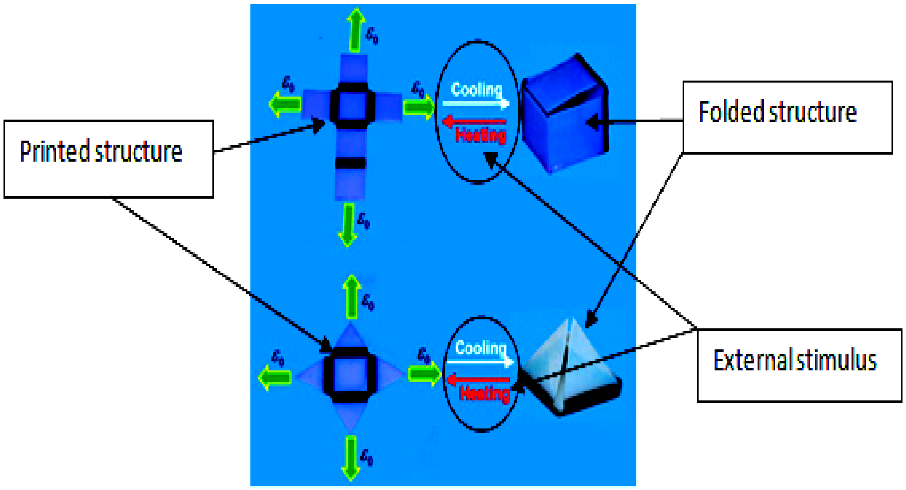

Figure 1.7 4D behavior of 3D printed part on the application of stimulus [29]

1.2.1 Programming for 4D printed components

4D printing refers to the 4D behavior of 3D printed objects based on time and stimulus. The solidified 3D printed objects when triggered with external stimulus at the required time may provide some change in structure and shape which is recognized as 4D property The 4D nature of objects is not a new concept, but recently recognized for a range of applications. The 4D nature in 3D printed objects may be due to external and internal forces. In the case of external forces, the objects are triggered with different external stimuli depending on the nature of the material matrix and dimension whereas, for internal forces, the material matrix itself has some capabilities to respond to external conditions such as heat and pH value of the environment. Meta-materials are those materials that possess special characteristics due to their shape, geometry, orientation angle, or joint angles. Various 3D printed objects show time property producing 4D behavior. FDM technique may be used for printing parts that can be engineered to behave like meta-materials which can be trained for shape memory effect [30]. Various shape memory polymers and shape memory alloys have been used extensively for different applications. These materials are used for different external stimuli depending on whom they respond to accurately.

1.2.2 Shape memory polymer V/s Shape changing polymer V/s Meta-materials

Table 1.1 gives the basic differences between shape memory polymers, Shape changing polymers and meta-materials

Table 1.1: Shape memory polymer V/s shape-changing polymer V/s Meta-materials

Factors	Shape Memory Polymers (SMP)	Shape-Changing Polymers (SCP)	Meta-materials
Definition	Those materials respond to the applied external stimuli [31].	These materials also respond to external stimuli, but as external stimuli or factor is removed, they acquire their original shape [31].	That material has shape-changing behavior due to its geometry or joint angles [33].
Category	(a). One way programmed (b). Two ways programmed [32].	Single category only depends on local external stimulus [31].	Single category only depends on local external stimulus [33].

1.2.3 One way programmed SMP

Shape memory polymers are programmed only for a single step and when further contraction or expansion is needed another stimulus is provided so that material can take the required shape at the required instant [32]. In figure 1.8 one-way programming is illustrated where “A” refers to the original shape at the time (t) equal to zero (0), “B” refers to the step where shape A get changed and acquire the required shape with the application of external stimulus which may be mechanical, electrical, thermal, pH based, etc. One-way programming is not cyclic as a further application of the same stimulus may not lead to shape A. Many SMP such as PEEK, polyurethane, polyvinyl chloride, polyamide, etc has been 3D printed for various applications using different additive manufacturing platform.

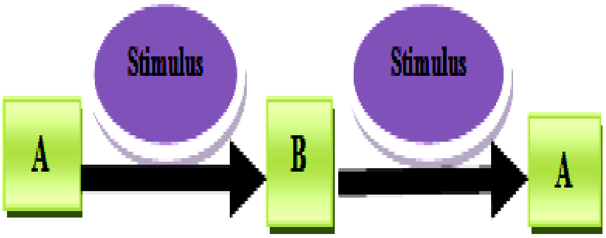

Figure 1.8 One way programmed SMP

1.2.4 Two-way programmed SMP

Shape memory polymers are programmed for single-step but give reversible change phenomenon and when further contraction or expansion is needed no extra stimulus is applied only stimulus is turned off on requirement [32]. Figure 1.9 illustrates the two-way programming of smart materials where “A” refers to the original shape of the material and “B” refers to the changed shape of material on application of stimulus which may be of any type. When the stimulus is applied, the shape of the object changes from A to B, and whenever the original shape is required, the stimulus is turned off.

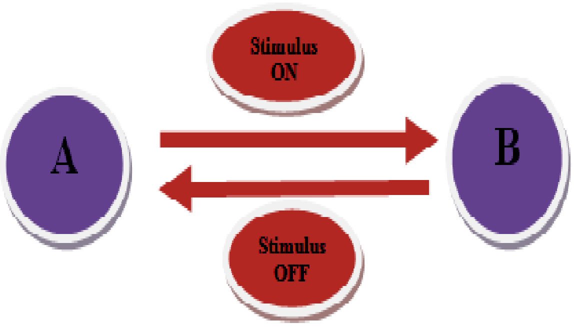

Figure 1.9 Two-way programming of SMP

1.2.5 Multiple shape memory polymers

The above described SMP was one-way or two-way programmed materials but having a single temporary shape. One more class of SMP exists which possesses two or more temporary shapes and is called multiple SMP. This property of three-stage change depends mostly on its broad glass transition temperature [33]. Figure 1.10 shows the shape transformation in multiple SMP.

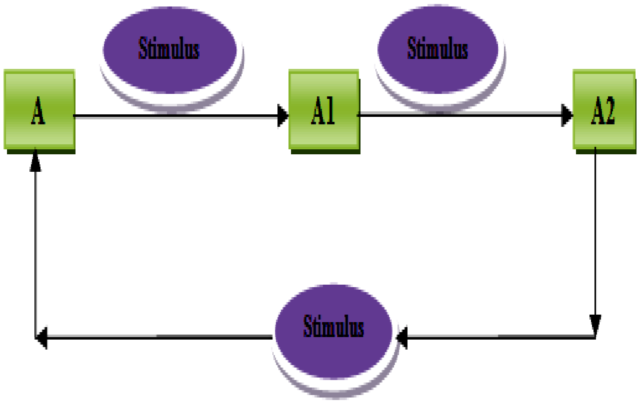

Figure 1.10 Multiple-way programming of SMP

1.2.6 Actuating mechanisms

There are various ways through which smart materials can be actuated such as mechanical-based thermal-based, electrical-based, pH-based, magnetic field-based, light-based, electrochemical-based, ionic strength-based, and biological actuation-based [34]. Figure 1.11 shows the various actuating mechanism which may be applied to get a 4D response depending on the type of material matrix used for 3D printed design.

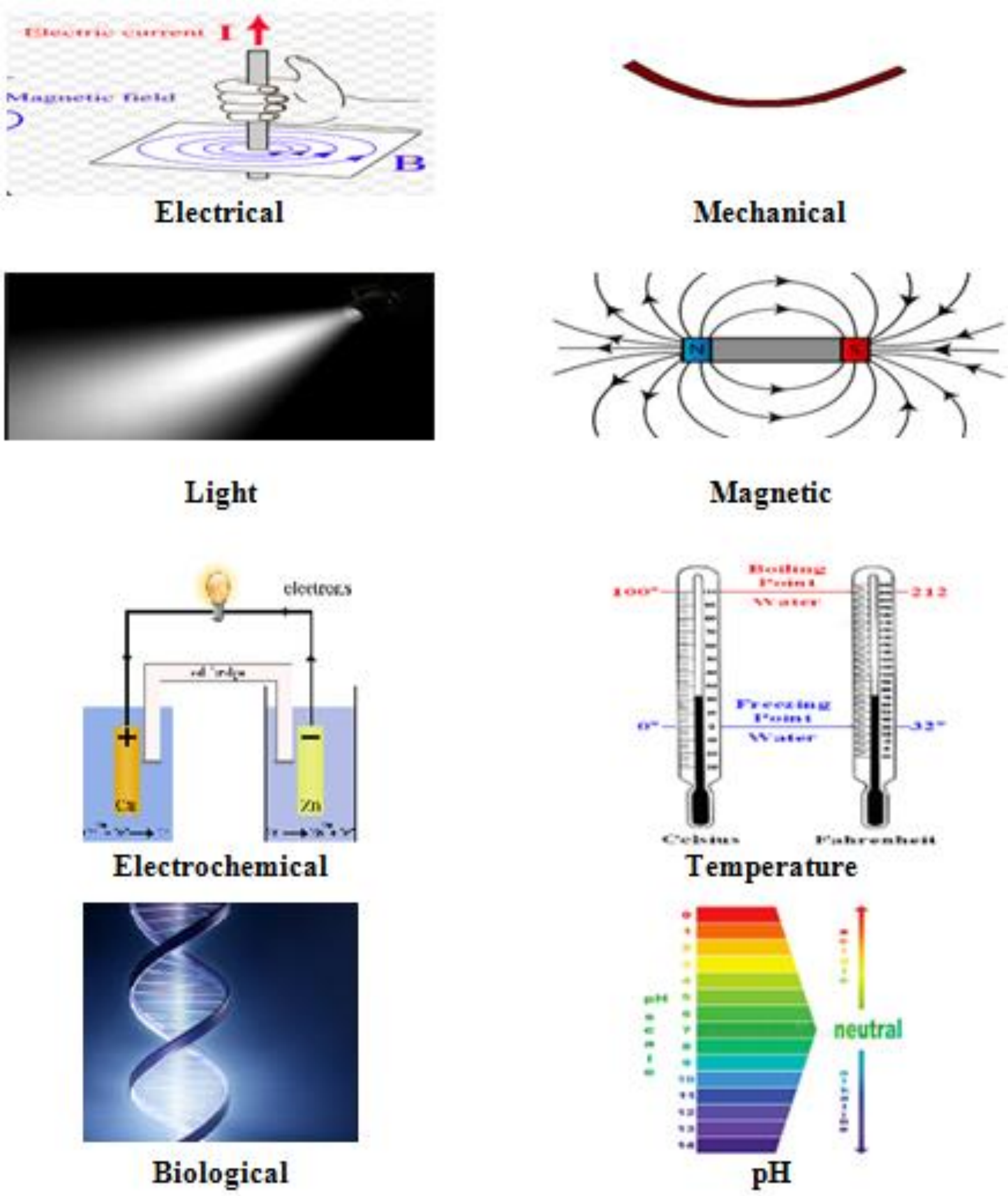

Figure 1.11 Various stimulus for 4D nature [34]

1.2.6.1 pH response based 4D nature

Various pH-responsive materials are available which can change their shape and can be trained to change their shape on basic application of different pH condition in external environmental conditions. Two types of pH-responsive materials are available; which are poly-bases and poly-acids depending on the present functional group in them. Figure 1.12 shows the schematics for a pH-responsive mechanism for 4D nature [35].

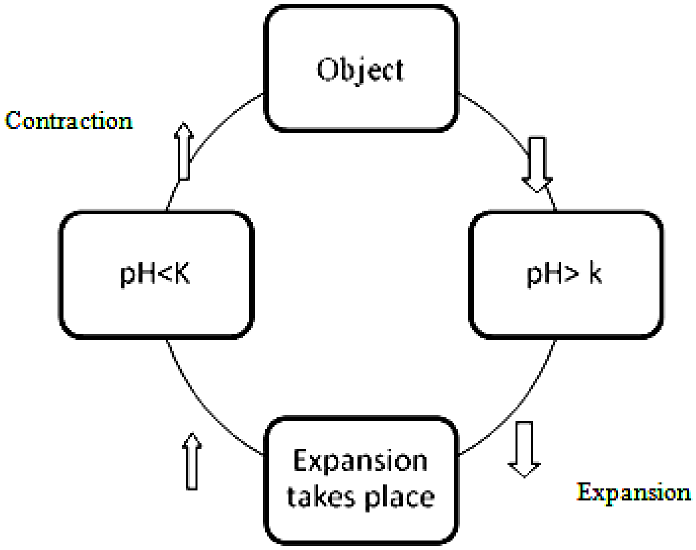

Figure 1.12 Schematics of pH-responsive mechanisms [35]

1.2.6.2 Electrical responsive stimuli

The molecules which are photosensitive show photo-chromic changes in structure (like the change of structure from trans–to-cis photoisomerization) on providing a low amount of external electrical energy [36]. Some materials, when exposed to the electromagnetic field get ionized and thus show the change in structure as the phenomenon of photochromic change. Figure 1.13 shows the schematics of electrical response in the case of 4D materials. Lecuo [37-38] and Spiropyran [39-41] are such materials that respond to electromagnetic fields and get ionized and behave like a smart material. Some materials possess a liquid crystalline structure that has a permanent dipole moment and has optical and geometrical anisotropies due to which they can respond to an external electrical stimulus due to the alignment of the optic axis parallel to the external field [42-44]. Electromagnetic characteristic is essential to various applications such seismic vibration dampers, absorbers, viscosity reduction of crude oil, human muscle stimulators, clutches, actuators, optical finishing systems, medical therapies and micro-fluidic control [45–51]. Figure 1.14 shows liquid crystalline structures in selected thermoplastics.

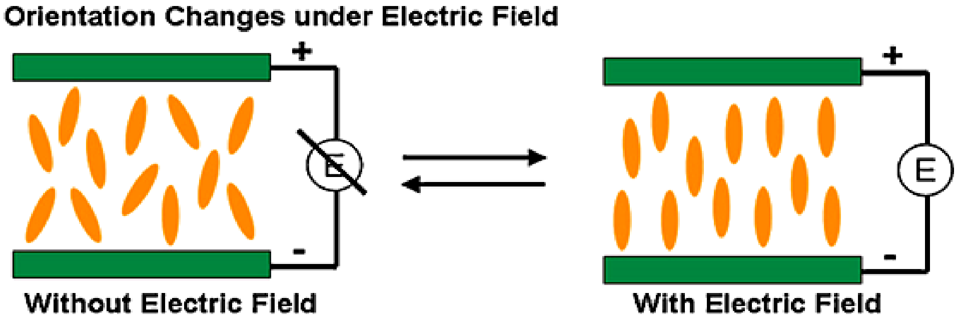

Figure 1.13 Schematics of electrical-based responsive mechanisms [36]

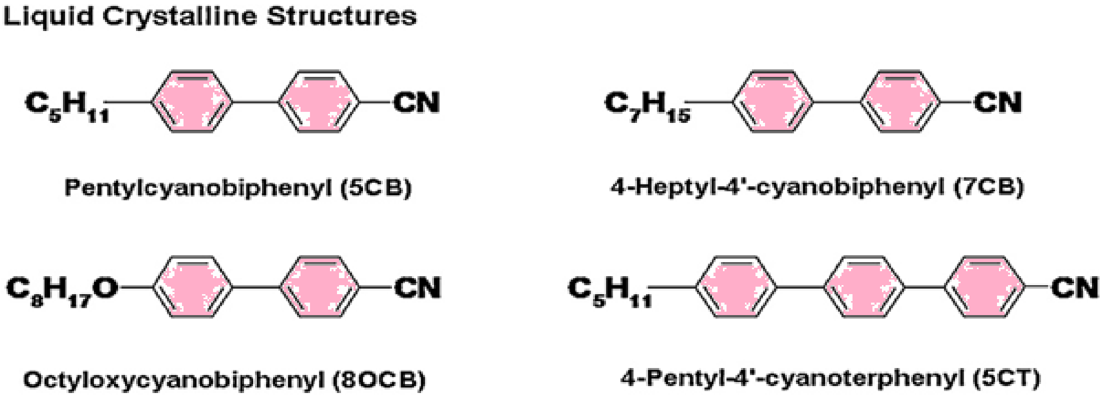

Figure 1.14 Liquid crystalline structures

1.2.6.3 Thermal based actuation

In thermal actuation materials, physical properties play a vital role such as its critical temperature or glass transition temperature, or crystal-melt transition temperature (Tg). The printed structure can be heated to a temperature greater than glass transition temperature up to T_1 at which strain is applied to give a particular required shape to the structure. Then that structure is cooled under external pressure below its glass transition temperature up to T_2. At this stage, stress is removed and thus the material is temporarily fixed in the strained geometry. If the original shape is required from which it started, then the material must be heated up to T_1 [52-53]. The behavior of SMP can be categorized into two types: one is melting-based SMP and the second is glass transition temperature-based SMP. The basic difference between these two is the training of SMP against stimuli. In melting-based SMP (T_m) the strain is given by taking the temperature T_2 near to melting point whereas, in the case of SMP of glass transition temperature-based technique the temperature is varied near T_g [32]. Figure 1.15 shows the mechanism of thermal actuation for SMP.

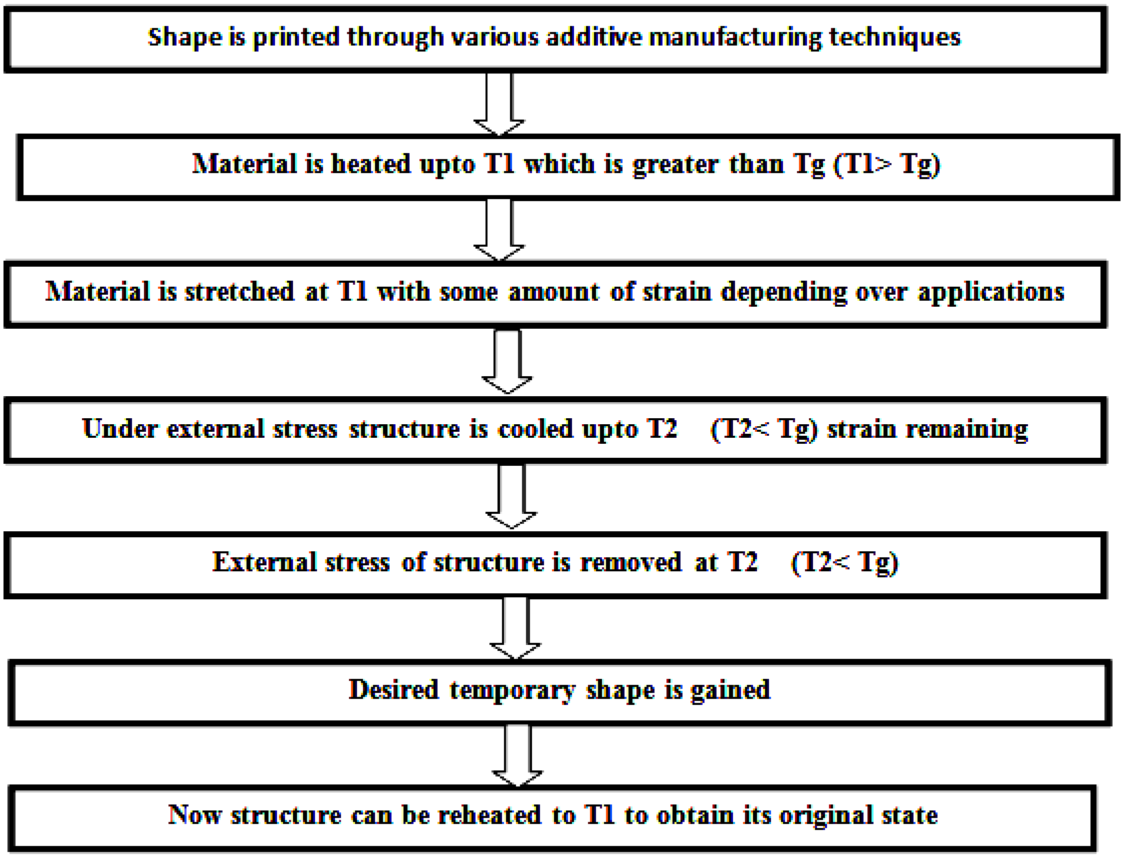

Figure 1.15 Mechanism of thermal actuation for SMP

There are two techniques for thermal actuation of programming (a) constrained and (b) non constrained technique [53]. Table 1.2 shows the basic difference between constrained and unconstrained processes.

Table 1.2 constrained and unconstrained processes

Constrained technique	**Non constrained technique**
Temperature above glass transition temperature is specified up to which the material is heated and external strain is applied	Temperature above glass transition temperature is not specified

Temperature below glass transition temperature is specified up to which material is cooled under external stress	Temperature below glass transition temperature is not specified up to which material is cooled under external stress

1.2.6.4 Hydrothermal based actuation

In this mechanism, material first contracts in cold water and then swell in hot water. This mechanism contains two stimuli, one is hot water and the second is cold water. This cycle of shape-changing can be repeated several times. Again, this mechanism can be used as a constrained mechanism by applying some external load or unconstrained by freely considering it. Polycaprolactone (PLA) was added with Iso-cyanatoethyl methacrylate under nitrogen atmosphere and reacted for 2 h at 85 °C in dioxane the macromonomer was precipitated with cold petroleum ether [54].

1.2.6.5 Osmosis based Stimuli

Most hydrogels are responsive to osmotic pressure due to which they collapse and extend. Water acts as a basic stimulus to these types of smart materials. Those materials having high osmolarity, expand in water, and those having low osmolarity collapse in water. Thus, a composite of hydrogels can be used to produce bending or any other effect [55-62].

1.3 Thermoplastic matrix

The polymeric waste of thermoplastic and thermoset plastic poses a serious threat to all levels of societal balance. Therefore, the reduction of plastic solid waste (PSW) is an important area of research (as thermoplastics have several applications in day-to-day life and their discard rate is also high, which is a leading cause of polymeric waste in the environment). The polymeric granules may be categorized into two types of matrix (a) thermoplastic and (b) thermoset plastic matrix. The difference between the two lies in the polymeric chain present inside the matrix of the polymer. Generally, the thermoplastic matrix is easily recyclable due to straight/linear linkages present among the monomers whereas contrary to it, the thermoset matrix possesses cross-linking of the polymeric chain which is hard to degrade. Therefore, recycling this cross-linked polymer is not possible through all routes of recycling [63-64]. Figure 1.16 shows the categories of polymeric matrixes with applications. The thermoplastic matrix provides an edge over the thermoset matrix as it is recyclable, which is a great concern for society. The researchers have highlighted the importance of polymeric composites for different types of industries and it was found that automobiles, aeronautics, civil, sport, railways, etc. are the major industries being benefited from composite materials [65]. Figure 1.17 shows the percentage of composite materials being used by different industries.

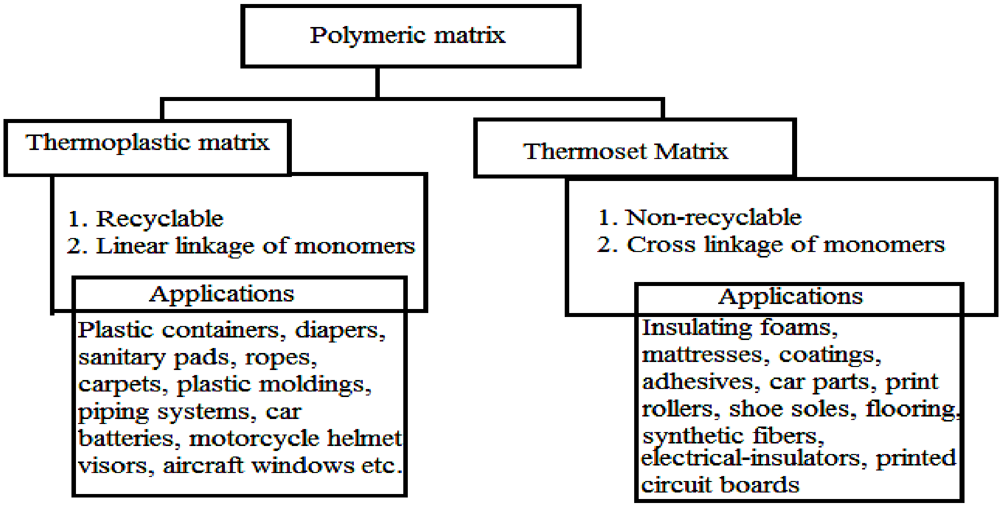

Figure 1.16 Categories of polymeric matrixes

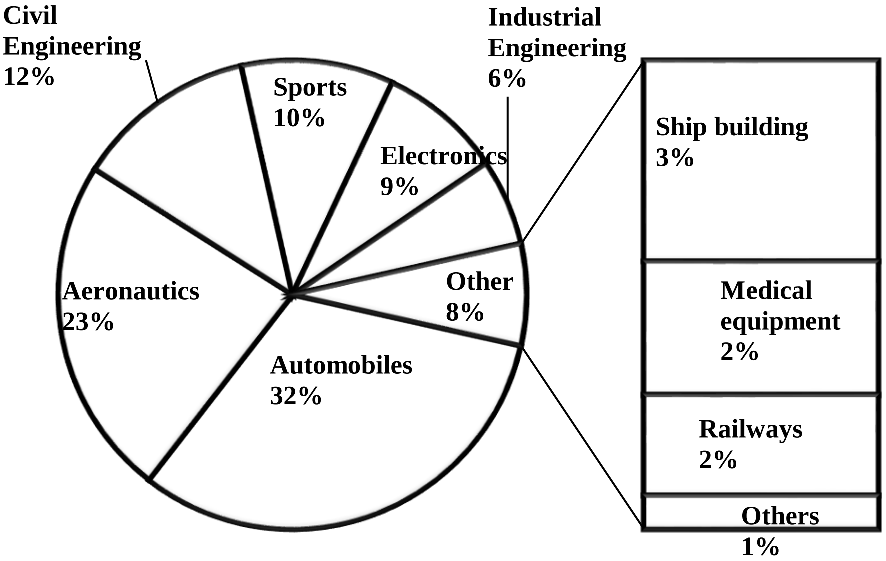

Figure 1.17 Percentage of composite material used by various industries [65]

The thermoplastic solid waste consists of different grades of plastic depending on the functional group present among the chain of monomers. There is a range of thermoplastics available for different applications such as acrylonitrile butadiene styrene (ABS), nylon, low-density polyethylene (LDPE), polyvinyl chloride (PVC), polyethylene terephthalate (PETE), polypropylene (PP), high-density polyethylene (HDPE), polylactic acid, polybenzimidazole, polycarbonate, polyetheretherketone (PEEK), polystyrene (PS), etc. Table 1.3 shows the different thermoplastics with their applications. From Table 1.3 the applications of plastic products are immense and substituting the plastic product is difficult.

Table 1.3 Different thermoplastic available in the market with their applications

Serial number	Symbols	Applications
1		(a) Blister packs (b) Soft-drink bottles (c) Detergents (d) Mineral water bottles etc.
2		(a) Packaging applications (b) Thick wall bottles (c) Flasks (d) Barrels etc.
3		(a) Films for perishables (b) Packs for medications etc.
4		(a) Tubular films (b) Shrink wraps (c) Carrier bags (d) Wrappers etc.

5		(a) Buckets (b) Boxes (c) Bottle caps (d) Adhesive tapes etc.
6		(a) Iceboxes (b) Covers of videotapes (c) Electronic instruments (d) Fast-food packaging etc.

1.4 Different types of recycling processes

There are different routes of recycling plastic solid waste comprising of (1) primary recycling, (2) secondary recycling, (3) tertiary recycling, and (d) quaternary recycling. Table 1.4 shows the differences between these routes of recycling. Fig. 1.18 shows the routes of recycling with a focus on primary and secondary recycling. From Table 2, it is clear that reusability of a plastic product as another product could be made possible through the only primary, secondary and tertiary recycling as quaternary recycling decompose the plastic into liquid form to utilize its energy for different purpose and further usage of that disintegrated polymeric matrix as polymeric granule is not possible [66-67]. The recycling of thermoplastic by primary and secondary routes has been already explored extensively.

Table 1.4 Differences between the various recycling processes

Properties	**Primary recycling**	**Secondary recycling**	**Tertiary recycling**	**Quaternary recycling**
Brief Description	Recycling of the polymeric waste without any change in the base polymeric matrix	Recycling of the polymeric waste with some changes in the base polymeric matrix in terms of foreign infill	Recycling by using chemical alteration in the polymeric chain with the use of heat and chemical reaction	Degradation of the polymeric base with high heat application

Process involved	Reuse	Extrusion and re-melting	Chemical processing and thermolysis	Incineration
Cost involvement	Low cost	Moderate	High	High
Complexity	Less Complex	Less Complex	Complex	Complex

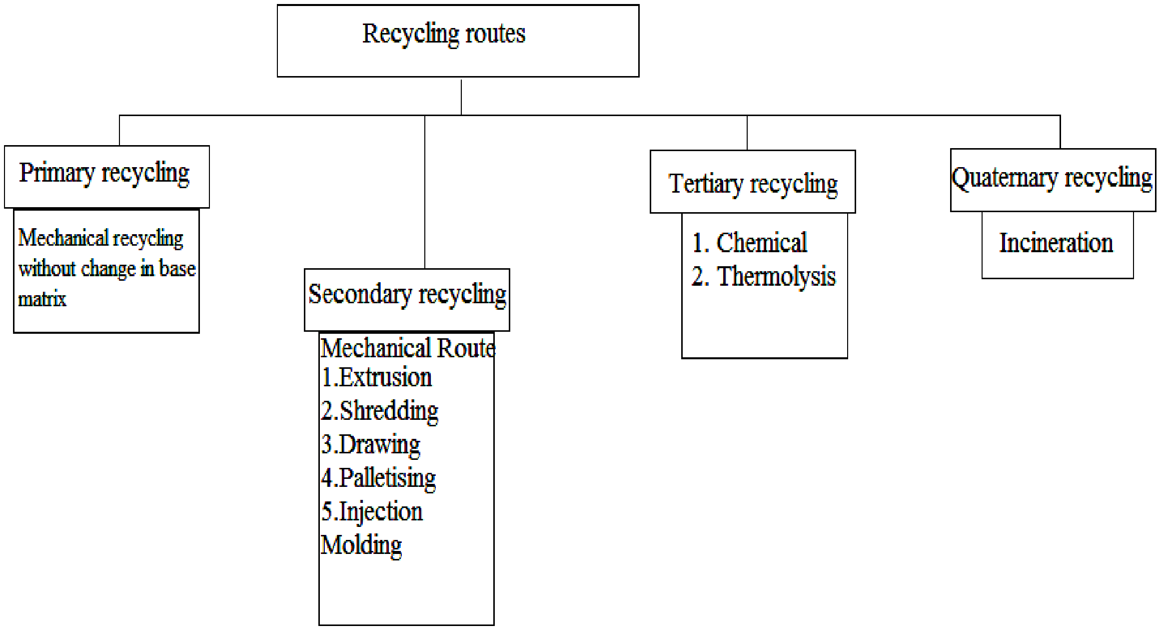

Figure 1.18 Different route of polymer recycling

1.4.1 Primary recycling of thermoplastic matrix

The primary recycling route consists of the reuse of polymer as a different product or change of shape of the polymeric product by using a melting technique without any change in the basic polymeric matrix. This process is also known as closed-loop recycling [68]. The polymeric properties of the recycled polymer are generally inferior to the processed polymer [69-71]. The recycled polymer obtained after recycling may have a different application than the parent polymeric product as the strength of recycled polymer gets decreased and it is further no longer suitable for similar usage [72]. It should be noticed that for primary recycling the solid waste must be least contaminated therefore generally municipal solid waste (MSW) is not a good candidate for the primary recycling process [73].

1.4.2 Secondary recycling of thermoplastic matrix

The secondary recycling of polymer consists of the reshaping of polymeric waste and converting the melted plastic waste again into polymeric granule form and then adding some foreign infill [74-85] to change the basic composition to acquire some improved qualities [85-90] such as high strength, high resistance to heat, etc which was previously not possible in primary recycled polymeric products. Various researchers have worked for secondary recycling of polymeric products for a different range of applications [91-95].

1.5 Present research work

In the present study, functional prototypes of 4D filament have been developed using PLA, PVC, wood powder, and Fe_3O_4 powder. Two different types of prototypes (a) based on hybrid blend (PLA/PVC/wood powder/Fe_3O_4 powder in single composite) and (b) multi-material component in which four different feedstock filaments ((a) PLA, (b) PLA/PVC, (c) PLA/wood powder and (d) PLA/Fe_3O_4 powder) were used in a single component, have been developed. To explore the different properties of two different types of prototypes, the selected material matrix was first developed into feedstock filament using a twin-screw extrusion machine (TSE) and then the FDM platform was used without any hardware and software changes in the machine to 3D print the functional prototypes. At each step of processing Taguchi orthogonal array (OA) approach was used to prepare the component so that optimization of processing condition may be performed later for maximizing the results. After developing functional prototypes of different combinations, various properties were explored for both types of functional prototypes such as mechanical properties, morphological properties, rheological properties, thermal property, and magnetic property, etc. For mechanical properties, a universal tensile testing machine (UTM) (Capacity: 5000N) was used. To explore the morphological properties of porosity testing by metallurgical image analysis software package tool (MIAS) tool, the fractured surface was investigated using Tool maker's microscopic image, scanning electron microscopy (SEM) and Energy dispersive x-ray spectroscopy (EDAX) was performed. Vibration sample magnetometry (VSM) was performed to explore the magnetic properties of prepared 4D feedstock filament. The prepared composite ratios were tested for the recycling issue so that recycling life may be quantified for the newly developed feedstock filament of the material matrix.

1.6 Organization of the thesis

The performed study on the multi-material and hybrid matrix of the polymeric composite of PLA has been divided into 6 chapters as shown by Figure 1.19.

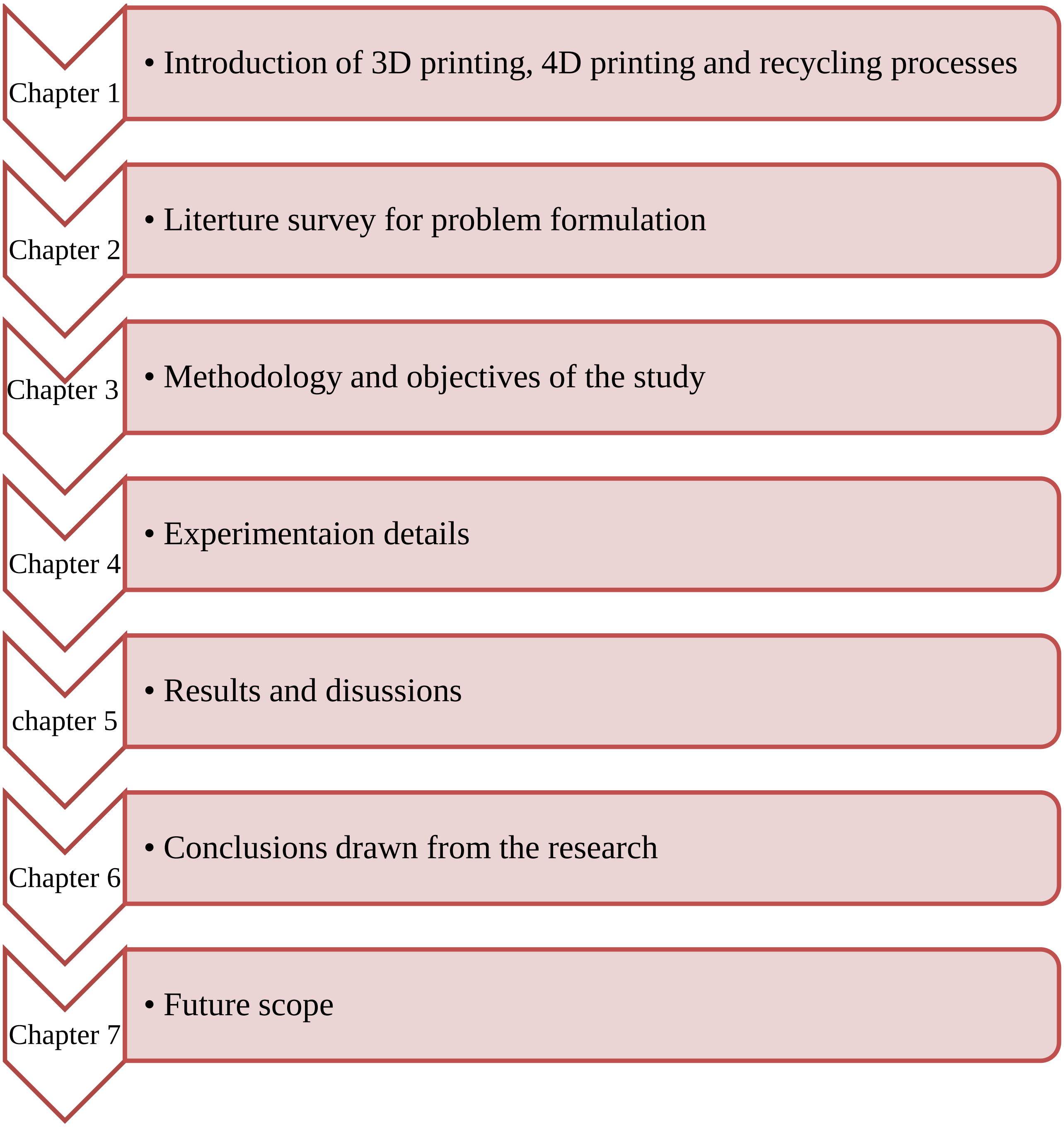

Figure 1.19 Different parts of reported work

CHAPTER 2

REVIEW OF LITERATURE

2.1 Literature review of 4D printing

Meta-materials are those materials that possess special characteristics due to their shape, geometry, orientation angle, or joint angles. Various 3D printed objects show time property producing 4D behavior. FDM, an additive manufacturing technique used for printing parts can be engineered to behave like meta-materials which can be trained for shape memory effect [96]. Magnetorheological (MR) properties of 3D printed objects can be varied using an external magnetic field as a stimulus. These intelligent materials usually are a matrix of host material matrix with MR fluid or MR elastomer and their properties depend on the basic properties of MR whether vulcanized or non-vulcanized [97]. Epoxide functional inorganic/organic composite can be prepared which can be influenced by external magnetic field stimulus. Functional epoxides which are added to these composites make these meta-materials bio-compatible. Being a biocompatible material, it opens a new field of application where a hybrid of inorganic and organic material gives a stable composite, which provides required properties for biomedical application [98]. 3D printed shape memory polymer (SMP) responds to various external stimuli, depending on the complexity of structure and strain rate. Properties of the material, near glass transition temperature, crystallization temperature, melting temperature play a vital role in training the shape memory polymers for giving 4D nature. Heat exposure generates strain rate in samples of SMP, which further shrinks and expands to various strain levels. 3D geometry printed on FDM also has an important role in expansion and contraction overstrain rate. Anisotropy and directionality of the printed geometry affect the properties of SMP. Strain generated due to heat exposure is heterogeneous over structure [99].

3D printing of net-shaped parts using various printing technology employing different metals or powder holds quality to be worked as 4D behavior. Ni-Mn-Ga alloy having magnetic properties can be trained to SMP behavior. The composition of the alloy is vital for the required properties. Post-treatment of composite printed from 3D gives a suitable result to the object. Martensitic transformation gives the SME to the metal composite part printed from additive manufacturing technology and cured by some post-treatment [100]. SMP can be trained to various external stimuli such as heat, pressure, temperature, pH, etc. Biomedical application of such SMP makes these meta-materials of high importance. Hydrogel responding to osmotic pressure also gives a 4D property. These hydrogels mixed with some sort of polymer give the required shape-changing behavior on changing the osmotic pressure conditions. Self-folding devices are also the application of SMP. SMP is of two types, one of which has some inherent properties which respond to external stimuli, and the other is mechanically trained to external conditions for various applications. Scaffolds printed for biomedical applications are a perfect example of time-responsive materials. Two hydrogels having different osmotic properties can be used as a composite to gain shape-changing behavior on applying osmotic pressure. [101-103].

Many smart materials, having piezoelectric properties have been reinforced with a polymer matrix to obtain the desired configuration of a composite. Boron nitride nanotubes and PVDF polymer present one such composition giving piezoelectric properties. L/R ratio of nano-tubes plays important role in composite behavior. Shape memory polymers also provide self-healing properties which are critical to soft actuators to mimic natural tissues [104-105]. 4D printing of smart materials finds suitable application in the medical field such as scaffolds, drug delivery, self-actuators, heat-responsive tissues, etc. various smart materials producing 4D property are printed based on natural phenomena such as activity shown by venus flytrap and shame plant or nocturnal and diurnal plants [106]. Many researchers have used one-way programming of smart materials to external stimuli requiring human interaction at various stages but at the same time, two-way programming can replace human interaction from the system by using other stimuli at the second stage. This process is generally called reversible 4D printing [107].

Meta-materials especially possess their properties of smartness due to their structural features such as joint angles, edge length, and geometry of the shape. One such geometry is famous as the Miura origami structure which can show 4D properties based on its geometry. Generally, a pattern of folds or edges is responsible for their behavior [108-109]. Vulcanized and non-vulcanized rubber which has elastomeric property can be used with some magnetic powder such as Fe_3O_4. Thus, the matrix obtained by composites can be printed using additive manufacturing techniques which will be useful in electronics as well as static applications [110]. Various shape memory polymers and shape memory alloys have been used extensively for different applications. These materials are used for various stimuli depending on whom they respond to accurately or to the required behavior.

Two types of pH-responsive materials are available: (a) poly-bases and (b) poly-acids depending on the present functional group in them as shown by Figure 2.1. These smart materials contain an ionizable functional group that can accept or donate protons upon pH changes in the external environment. Alteration in hydrophobic volume is the basic thing that occurs in these materials upon electrostatic repulsion between the generated charges over them due to which they collapse or expand. Polyacid material swells overtime on a change of external pH due to the release of protons [111-115]. Polybases type of materials contract over pH change due to acceptance of protons [116-122]. Table 2.1 shows the pH-responsive materials that can be blended to obtain multi-responsive smart material.

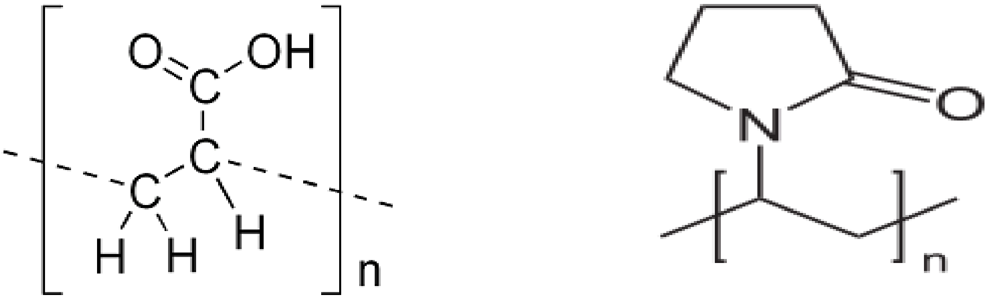

Poly (acrylic acid) (PAAc) (Polyacid structure)

Poly (vinyl pyridine) (PVP) (Polybase structure)

Figure 2.1 Functional representation of polyacid and polybasic groups

Table 2.1 pH-responsive materials and electrical responsive materials

Name of material	Category of material	
Poly (acrylic acid) (PAAc)	Polyacids	pH-responsive
Poly (methacrylic acid) (PMAAc)	Polyacids	
Poly (N, N’-dimethyl aminoethyl methacrylate) (PDMAEMA)	Polybase	
Poly (vinyl pyridine) (PVP)	Polybase	
Pentyl-cyano-bi-phenyl (5CB)	Poly crystalline	Electrical responsive
4 heptyl-4’-cyano-bi-phenyl(7CB)	Poly crystalline	
Octyloxy-cyano-biphenyl(8OCB)	Poly crystalline	
4-pentyl-4’-cyanoterphenyl(5CT)	Poly crystalline	

Various materials have shown thermal responsive behavior over a different range of temperature such as PEEK is trained at a temperature above 180°C [123]. Sulphonated PEEK, polyimide, cyanate SMP have been trained at 200°C, 220°C, and 290°C, respectively [124-126]. Polymethacrylate network have been trained at various temperature such as 52-96°C [127], below recrystallization temperature (RT) [128], 70°C [129], 65°C [130]. A list of materials used with thermal stimuli is provided in Table 2.2. Table 2.3 shows various materials that have been used as multiple SMP.

Table 2.2 Thermal responsive 4D material

Material	**Training temperature**	**Hard phase**	**Soft phase**
PEEK	>180°C	Crystalline	Amorphous structure
Sulphonted PEEK	200°C	Ionic	Amorphous
polyimide	220°C	Crosslink	polyimide
Cyanate SMP	290°C	Crosslink	Amorphous
Polyaspartimide urea	150°C	Crosslink	Polyaspartimide
Polymethacrylate network	56-92°C	Crosslink	PEGDMA
Polymethacrylate network	Below RT	Crosslink	PEGDMA
Polymethacrylate network	70°C	Crosslink	Polyester
Polymethacrylate network	65°C	Crosslink	Low Tg methacrylate
Polyester	45°C	Nano crystal	Polyester
Polyurethane	55°C	Crosslink	PU
Polyurethane	30°C	Crystalline PU	Amorphous PU
Polyurethane	0-60°C	PU	Cross linked polyester
Polyurethane	70°C	PU	Copolyester

Table 2.3 Various materials used as multiple SMP

Material	**Working Temp or switching temperature**	**Hard phase**	**Soft phase**
PFS	25–65°C	Crosslinks	PFS
PCL/PCHMA	70°C -150°C	Crosslinks	PCLTM, PCHMA (Tg)
PCL/PEG	40 °C -70°C	Crosslinks	PCL, PEG
PCL/PPD	40–60 °C, 70–80°C	Crosslinks	PCL, PPD
Two IPN	23°C- 45°C	Crosslinks	Mercaptoacetate-vinyl sulfone; mercaptopropionateacrylate
PCL/PU	40°C -65 °C	Crosslinks	PCL, SM–PU
Epoxy/PCL	40 °C-75 °C	Crosslinks	PEG epoxy or PPG epoxy, PCL
Poly(styrene-grad-n-butyl acrylate)	60-80-100 °C	Hard domains	Soft domains
Bilayer epoxy	56 -90 °C	Crosslinks	Epoxy with high and low Tg
Cross linked PE and PP blends	130-175 °C	Crosslinks	PE PP
EOC, HDPE, LDPE	42-78-122 °C	Crosslinks	LDPE HDPE EOC
Naflon	53 - 140 °C	Physical Crosslinks	Amorphous phase
PMMA/PEG	35 (Tm of PEG) -50-70-110 °C	Physical Crosslinks	Amorphous phase

2.2 Literature survey of thermoplastic composite matrix used on FDM platform

LDPE and HDPE have been reinforced with calcite or calcium carbonate ($CaCO_3$) and their mechanical properties have been explored and it was found that 50% filled polyethylene had better mechanical properties than unfilled polymers. A phase morphology study was also performed to know how the crack propagation occurs in the reinforced composite. It has been found that crack propagation initiated at 50% elongation and was a result of the de-wetting phenomenon and initiated along the transverse direction [143]. Carbon nanotube (CNT) in different proportions varying from 0.5 to 7 weight percentage in LDPE and HDPE matrix have been explored for conductivity and rheological properties of the composite matrix and it has been found that increasing content of CNT increases the interaction of the polymer with reinforced CNT. Reinforcement of CNT (1-2.5 weight percentage) in polymer matrix increased the electrical conductivity of polymer matrix by six orders. A similar increase in percolation has been seen in rheological property with an increase of CNT content [144]. Performance of several coupling agents in wood fiber composite has been explored for mechanical properties such as tensile strength, flexural strength and it has been found that there was a direct relationship between the coupling agent and mechanical properties of composite as coupling agent improves the interfacial bonding between polymer and reinforcement. The maleated polyethylene coupling agent was found to be more effective than oxidized polyethylene and pure polyethylene. Molecular weight with a large number, moderate level of acid number, and low level of concentration of coupling agent was found to be optimized condition for better performance of coupling agent [145].

LDPE, HDPE, and polypropylene (PP) polymer matrix reinforced with liquefied wood has been investigated for its thermal behavior analyzed through DSC and thermogravimetric (TGA) analyses. Increasing the content of liquefied wood (LW) decreases thermal stability while increasing heating rate improves the thermal stability of the composite. LW content (10 weight percentage) decreases the melting temperature of HDPE, LDPE, and PP whereas the HDPE matrix was found to be more thermally stable than the PP matrix for the same content of LW [146]. Wood and clay reinforced LDPE, HDPE, and PP composite polymer matrix has been explored for its properties and it has been found that silicate layer was well dispersed with 3 weight percentage clay in polymer composite and it had better thermal stability than 1 and 5 weight percentage clay in wood polymer composite. Limiting oxygen index (LOI) has been increased and storage and lost modulus were also in direct relation with the presence of clay in wood polymer composite as shown by TGA analyses [147]. HDPE reinforced LDPE polymer matrix has been investigated for single polymer composite preparation and it has been found that the shear strength of the composite was 7.5 MPa whereas it was high for HDPE (17 MPa). It has been found that the high value for mechanical properties was due to epitaxial bonding which resulted in improved adhesion. The tensile modulus of LDPE reinforced with HDPE was found to be increased by a factor of 10. It has been found that 130-132°C temperature was ideal for better bonding. Mechanical properties were found to be in direct relation with the angle of embedding for HDPE fiber film in the LDPE matrix [148]. CB reinforced LDPE, HDPE, and ethylene-vinyl acetate (EVA) polymer matrix has been investigated for electrical conductivity. High structure (CSF-III) and low structured (FEF) carbon black reinforcement was used in the polymer matrix. It has been found that HDPE/CSF-III composite had lower PTC intensity and worse electrical conductivity than HDPE/FEF. HDPE/CSF-III/EVA composite had greater PTC intensity than EVA/CSF-III and HDPE/CSF-III. It was found that absorption of CB on the surface of the polymer was due to free radical reaction which in turn gives rise to PTC intensity behavior [149].

HDPE matrix reinforced with micro size boron nitride (BN) has been explored for its thermal using DSC and TGA analysis. Micro size BN were then balled milled for preparation of nanosized BN and LDPE coated nano BN powder was prepared for composite preparation. It has been found that among pure HDPE, micro size BN composite with HDPE, and nano-size BN composite HDPE the thermal stability was best for nano size BN composite of HDPE [150]. Clay mixed in the HDPE matrix of the polymer has been investigated for microhardness, thermal stability, and flammability using TGA, DSC, LOI, and microhardness test. It has been found that the properties tested were dependent on the type of compatibilizers. Acrylic acid grafted HDPE (HDAA) and maleic anhydride grafted HDPE (HDMA) has shown better thermal stability and low flammability than HDPE compatibilized with ethylene- acrylic acid (EAA) while phase transition of HDPE was independent over the type of compatibilizers [151]. LDPE reinforced with wheat straw coupled with the waterborne agent has been investigated for mechanical properties of composite and size stability. It has been found that LDPE polymer and wheat straw coupled by polyacrylate latex (PAL) improved composite quality while other coupling agents named polymethylene polyphenylene isocyanate (PAPI) resulted in more uniform composite structure quality than others. PAPI/PAL with a 30/70 ratio and 4.5 weight percentage resulted in the best composite for maximum interfacial bonding [152]. Glass fiber (GF) reinforced polymer matrix of LDPE and HDPE have been investigated for the effect of the chain linking on the properties of composite polymer. Long branching in GF/LDPE had increased the elastic modulus in solid form and modulus of storage in the melt state. Crystalline structure formation of HDPE resulted in high tensile properties. GF reinforcement in polymer matrix greatly modified the thermal stability for the various composite of HDPE and LDPE [153].

LDPE and HDPE mixed with ethylene-propylene-dine terpolymer (EPDM) and jute fibers composite matrix has been investigated for mechanical, rheological, and thermal properties of composite using various specified tests. It has been found that increased fiber content and high compatibilizer content lead to an increase in mechanical properties of polymer composite such as flexural strength, impact strength, flexural modulus, etc. HDPE/EPDM/jute fibers have shown large values for storage and loss modulus in comparison to the LDPE composite. Treated composite has shown better properties in contrast to untreated ones [154]. LDPE and HDPE polymer films have been reinforced in polyethylene (PE) using compression molding technique and composite matrix was investigated for mechanical, thermal, and morphological behavior of composite. It has been found that thin films LDPE in PE improves the tensile strength and elastic modulus of PE with a great significance about 60 and 30 times respectively. But the composite of PE/HDPE has shown better elastic modulus than PE/LDPE [155]. Copper (particle size of micro and nano) reinforcement in HDPE and LDPE have been investigated for mechanical properties and it has been found that microparticles had the least significance for the mechanical property of LDPE and HDPE whereas tensile property gets lowered when linear LDPE was used in the matrix. Cu particle reinforcement increases the tensile modulus but decreases the break elongation. While when nano Cu particles were mixed in the matrix have shown better mechanical properties as storage and loss modulus got increased [156].

The use of 3D printed functional prototypes in 4D applications is quite common nowadays and a lot of smart thermoplastic materials having such properties are commercially available. For example, PLA exhibits 4D properties when triggered by external stimuli. Along with this, mechanical properties of PLA printed with a 3D printer have been investigated (for various settings of process parameters such as the number of layers, build orientation, layer thickness, etc.) by some researchers. Also, the effect of the feed rate of the 3D printer on mechanical properties has been evaluated which shows that mechanical properties are directly dependent upon layer thickness and in negative relation with feed rate[157]. The reported studies show that PLA material printed via fused deposition modeling (FDM) has an ultimate tensile strength in the range of 42.28-53.59 MPa, elastic modulus in the range of 2799.43-3497.63 MPa [158]. PLA itself behaves as brittle and a low thermally stable polymer. Its toughness, as well as strength, is increased by reinforcing it with carbon nanotubes (CNT) possessing –COOH functional group which gives it toughness and strength. Mechanical properties such as elongation at break, tensile strength get improved by adding CNT-COOH as reinforcement. Thermal stability, as well as glass transition temperature, also improved and are in positive relation with CNT-COOH addition [159].

Rayon (viscose) when added to PLA fibers by the method of filament winding for hollow structure and by film stacking method improves the mechanical properties specifically elongation at break and strength of fibers in textile industry application [160]. Tensile strength and flexural strength decrease when a seagrass named Posidonia oceanic (PO) is added as filler material in PLA matrix but on the contrary tensile modulus as well as flexural modulus is in positive relation with filler material [161]. Chitin when added with PLA enhances the bio-medical compatibility and application of PLA in implantation such as of bone and joints. Laminated chitin-based PLA polymer composite has a high tensile strength of 25MPa in comparison to pure PLA film that is 18 MPa, and low water absorption 0.265-1.061% when immersed in water for 30 min to 24 hr time interval [162]. PLA shows good characteristics properties when blended with organo-montmorillonites and graphite. This tri-material blended mixture shows good rheological properties in comparison to neat PLA. This mixture was blended using a twin-screw extruder (TSE) at 180°C at 32 rpm for 5 minutes and with 64 rpm for 3 minutes only. Graphene, when added to the PLA matrix, improves the elastic storage modulus but the tri-material blended mixture has more enhanced elasticity and other mechanical properties such as storage modulus and lost modulus [163].

Natural sisal fibers when coated with PLA and reinforced with polyester resin show improvement in flexural strength, breaking strength, and flexural modulus [164]. PLA/PCL (poly-caprolactone) can also be mixed with nano-sized hydroxyapatite which enhances its smart nature and gives a strong response to thermal actuation of a composite at 55°C. Obtained composite of PLA/PCL with n-hydroxyapatite behaves like smart material which response to thermal actuation which is necessary for some biomedical application and packaging application. Furthermore, this composite polymer is biodegradable as they have tested its biodegradability [165]. Ethylene co-vinyl acetate when mixed with PLA makes it thermally stable and increases its damping parameter with a slight increase in storage modulus and viscosity of complex. But ethylene-co-vinyl acetate is less miscible with PLA and is slightly incompatible but dynamic mechanical analysis has shown reinforcement and interaction of particles with each other [166]. The kenaf fiber (KF) which is chemically functionalized and multi-walled carbon nanotubes (MWCNT) addition to the matrix of PLA enhances its physical properties. The particles of KF, MWCNT, and PLA are excellently compatible with each other, which leads to thoroughly chemical bonding of atoms, and around reinforcement transcrystalline structure is generated which improves the physical properties [167].

Multi nano cellulose (MNC) obtained from mechanical treatment of softwood pulp when added to PLA matrix decreases the melt flow index of PLA so, the obtained composite becomes suitable as a filament for FDM. Polyethylene glycol (PEG) is also mixed in this composite such that a certain improvement in melt flow index is obtained which was lost due to the addition of MNC to PLA. PEG decreases the mechanical properties of composite as it weakens the bonding between MNC and PLA. A suitable ratio of 30% MNC, 5% PEG6000, and 65% PLA was obtained which can be used as FDM filament with better mechanical properties in comparison to neat PLA [168]. Polyurethane (PU) elastomer which is a thermoplastic polymer improves the ductility of PLA which inherently is very brittle. Alone reinforcement of 10weight percentage of thermoplastic PU (TPU) to PLA decreases the flexural strength and tensile strength. Glass fiber (GF) reinforcement in PLA improves the elastic modulus and strength of PLA which is very much required in different applications. When 10weight percentage PU, as well as 15weight percentage GF together mixed in the matrix of PLA, significantly improves the mechanical properties of [169].

ZnO and nano-composites also improve the water absorption but on increasing the content of ZnO composite decrement in water absorption is seen while nano-composites increase the water absorption. Mechanical properties of PLA also improve with ZnO and nano-composite addition [170]. Natural fiber such as flax fiber can also be used as reinforcement to the PLA matrix which gives prominent results in comparison to polypropylene (PP)/flax composite. 30 weight percentage addition of flax fiber in composite makes the composite more stiff and also mechanical properties of PLA get improved thus PLA and natural fiber composite may also be used for various industrial applications as compared to other used polymers [171]. PCL/PLA matrix properties can be varied by adding reinforcement of graphene nanoparticles (GNP). Component composition plays an important role in tailoring the properties of the PCL/PLA and GNP blend. GNP when reinforced into PLA/PCL matrix increases the toughening efficiency. GNP has the potential to change the structural as well as mechanical properties of PCL/PLA biocompatible composites [172]. PLA itself behaves as a smart material when worked near its glass transition (T_g) temperature and is used as smart fiber when reinforced with nylon fibers for the textile industry. Nylon, when added to PLA improves the mechanical properties but does not harm the smart behavior of PLA, thus a composite matrix of PLA/Nylon is prepared for textile applications [173].

Carbon fiber (CF) reinforced PLA and virgin PLA have been investigated for the difference of mechanical properties and it has been found that length of fibers in composites played a vital role in enhancing the properties of composite whereas in composite matrix CF was highly intended towards the material supplanting inclination. CF fibers reinforcement with suitable matrix direction enhanced the mechanical properties such as tensile modulus and shear modulus by 795 MPa (for 90° orientation of deposition) and 176 MPa (for 45° orientation), respectively but tensile strength got reduced. From scanning electron microscopy (SEM) it was clear that short fibers of CF in the matrix of PLA were less joined with the PLA due to less surface area of contact which resulted in low strength of composites [174]. Smart textile made up of PLA with nylon matrix can give a dynamic performance or four-dimensional (4D) response in contrast to static applications of 3D printing. It has been found that PLA's response to temperature remained unaffected when mixed with nylon fibers. Composite matrix (PLA and nylon) driven textile represented a new class of composite which has shown dynamic properties or change in shape when exposed to external stimulus [175]. Micro-physiological system (MPS) for cardiac health applications have been investigated with multi-material 3D printing, which opened a new area of vital research as biomedical findings were previously dependent on animal studies but now with MPS system can respond in the same way as animal tissue via in-vitro testing. The embedded sensor in printed parts with piezo-resistive, conductive materials represented a new class of sensors that could give digital reading without being invasive. This approach of multi-material ink printing has given a new class of manufacturing which on demands can print sensors with higher complexity for any tissue structure such as cardiac tissues [176]. Hard and Soft PLA, nylon and ABS filaments have been used for 3D printing of textile and it was found that ABS, nylon, and hard PLA were immensely brittle from the textile application but soft PLA had produced somewhat desirable properties. 3D printing of polymeric material, as a low-cost operation and digitally driven technology has presented a new set of research for the textile industry for the complex design of clothing and multi-material printed textiles for specific needs of textile driven industries such as fashion shows and exhibitions. Textile with 3D printing has been investigated by researchers and it was found that a low mechanical property of printed parts was of the great disadvantages for this additive manufacturing technique. Acrylonitrile butadiene styrene (ABS) as a stiff and brittle material was not suitable for textile applications, therefore a soft PLA composite matrix has been explored with different designs of printing. It has been found that soft PLA represented a good compatible material for textile applications with optimum mechanical strength [177-178].

Dual extrusion has been investigated for printing purposeful anatomical models by some researchers. Flexible part such as a muscle has been printed with flexible element and for bone, PLA filament was used. Vocal cord for the anatomical model purpose has been printed and the combined model of extrusion for hard and soft filaments offered an excellent technique for demonstrating the intrinsic human organ system. Thus, 3D printed parts of the human organ system could be very useful for anatomists for research purposes reducing the need for hard models and invasive surgeries [179]. Carbon nanotube (CNT) and graphene reinforced polybutylene terephthalate (PBT) polymer, an electro-conductive structure, have been printed using 3D printing and it has been found that 3D printed parts of multi composites have superior mechanical and electrical properties whereas composite in which graphene was reinforced with PBT have shown poor performance than composite reinforced with CNT. It has been found that new materials must be optimized for their melt flow rate or index (MFI) and solidification characteristics which ultimately drive their mechanical properties [180]. Multi-layer printing is also correlated to 4D printing as two different materials can be printed in a single object for 4D behavior. One such double-layer printing has been investigated based on the PLA composite matrix and carbon fiber reinforced polyether-ether-ketone (PEEK) polymer matrix. It has been found that double-layer laminates were different in bending behavior as shown by the electro-caloric deformation test. PLA-based laminates have shown less deformation value of 7mm as compared to 10mm for CF/PEEK composite. Also, similar results were obtained for the deformation force which was 100 MN for PLA and 200 MN for CF/PEEK-based composite. Thus, multi-material laminate printing has shown a new way for manufacturing of new class of biomedical sensors and actuators [181]. Carbon black (CB) reinforced polyethylene (PE) matrix has been explored for its crystalline structure and conductivity properties and to find the relationship between morphological and conductivity properties using DSC, small-angle X-ray scattering (SAXS), and wide-angle X-ray diffraction (WAXD) characteristic tests. It has been found that the positive temperature coefficient (PTC) increases with increased content of CB in the matrix of polyethylene while a significant effect of PTC was not seen in the amorphous structure of CB/PE. Annealing of the composite increased the PTC intensity in the composite which, in turn, modified the properties of the composite. Crystallinity, as well as the lamellar size and long spacing, had also a significant effect on the PTC intensity of the composite [182].

Multi-material printed parts have been investigated by researchers and it has been found that weak chemical and physical bondage between the composite polymers lead to weak strength of printed objects. The single-layer temperature adjusting transition method (SLTAT) has been investigated for the improvement of multi-material printed objects in which bond layer temperature has been adjusted to improve the bond strength. PCL/PLA composites have shown 28% enhanced tensile strength when the bond layer temperature was 130°C [183]. Polyurethane (PU) reinforced with hexagonal boron nitride (hBN) has been explored for 3D printing base additive manufacturing of microelectronic components with thermal conductance and electrical insulation property. It has been found that hBN reinforced particles get highly supplanted in the direction of printing and a 2.8 times improvement in thermal conductance has been reported [184].

PLA is a biodegradable thermoplastic polymer that has been widely used with various reinforcements for different applications. In the past, magnetic microspheres of PLA in different ratios have been prepared by the chemical (emulsion solvent extraction) method. The particles were tested for biodegradability and it has been found that these magnetic microspheres were hemocompatible. Further, when a large percentage (up to 60%) of magnetite was mixed chemically with PLA there was an agglomeration of magnetite which was not good for composite mixture and 40% magnetite in the composite mixture was found optimum [185]. PLA coated with magnetite powder (30weight percentage) is biocompatible as researchers have found that magnetic and nonmagnetic microspheres led to equal growth of the cell when tested for cell growth assay through in vitro and in vivo analysis [186]. PLA polymer coated with magnetite powder composite has been prepared for magnetic field responsiveness and an efficient drug delivery system. A comparative analysis of the surface property, structure, and chemical nature has been performed to know the effectiveness of prepared composite and it has been found that prepared composite behaves intermediate of the parent material in terms of chemical nature such as electrophoresis value and surface thermodynamic property (surface free energy) [187]. The study reveals that a maximum 40weight percentage of magnetite can be added to polymer matrix with a chemically established method such as emulsification and mini emulsion polymerization. Weight ratio plays a vital role in administering the magnetite content in magnetic polymer latex [188]. Polyurethane (PU) polymer which holds shape memory property has been reinforced with magnetite powder up to 40weight percentage and has been tested for magnetic, thermal, and electrical properties. Results have shown that electrical resistivity is in negative relation with magnetite concentration whereas thermal conductivity is in positive relation. Shape recovery time also got increased (approximately 4 min) with the reinforcement [189]. The polyethylene co-vinyl acetate (EVA) reinforced with Fe_3O_4 by two-layer compress molding shows improvement in hardness, but the reduction in strength at break and elongation at break. The composite has shown good flame resistance also. Moreover, the composite was thermally stable [190]. Composite of poly (methacrylic acid) (PMAA) reinforced with magnetite powder has been tested for its characteristics such as magnetic properties and chemical bondage etc. using various techniques such as transmission electron microscopy (TEM), X-ray diffraction, and VSM testing and it has been found that the prepared composite holds lattice constant (by XRD) value of 0.838 which means the sample is magnetic as this value is close to the lattice value of magnetite (0.839) and particles occupied nearly spherical shape (TEM results) and magnetic moment (VSM results) of the composite particle was 40 emu/gm [191].

PLA when reinforced with nano clay (cloisite C30B) (1-5% by weight) and nano cellulose (1-5% by weight) exhibits excellent barrier properties which are necessary for food packaging applications. Thus, PLA being a biocompatible polymer can easily be used for the food packaging industry when a suitable nano clay and cellulose nanofibres are mixed in the matrix of PLA. This PLA hybrid material reduces 90% oxygen transmission rate and 70% water vapor transmission rate thus showing excellent barrier properties with bio-compatibility [192]. Different concentration of chitin (1-20%) in addition to PLA base matrix by using solvent casting method and a laminated composite of chitin-based PLA (LCP) using hot press method shows excellent bio-compatibility and opens bio-medical application for such composites such as bone and dental implants. At 500°C thermogravimetric analysis (TGA) shows that chitin gets 100% degradation, PLA sheet gets 95% of degradation, 5% chitin-based PLA part gets 87% of degradation, and laminated chitin based PLA made via hot press method get 97% of degradation. LCP polymer composite shows ductility of 25MPa which is greater than the pure PLA (18 MPa) [193]. PLA reinforced with magnetite powder and polyethylene glycol (PEG) has been tested for drug delivery application and it has been found that drug loading and efficiency of encapsulation was higher with the increase in magnetite and PEG content in composite. The magnetite nanoparticles prepared by the co-precipitation method were tested for crystal structure and magnetic properties. Magnetite was mixed from 5-25% in PLA composite matrix and it has been found that sample containing 25% of magnetite have shown maximum magnetization and sample with 5% of magnetite was poor in magnetization [194]. PLA composite reinforced with poly-lactic co-glycolic acid (PLGA) and interferon alpha-2B has shown potential for efficient drug delivery application. Researchers have reinforced 10 to 30% Fe_3O_4 for this purpose and it has been found that PLGA microspheres have shown better magnetization than PLA and 20% reinforcement of magnetite has shown the best results and almost all required properties have been obtained with this percentage reinforcement [195]. Polyvinyl alcohol (PVA) reinforced with magnetite powder has shown changes in the crystal, magnetic and chemical structure when irradiated. It has been also found that polymeric composite having magnetite in the matrix was super-paramagnetic and no coercivity and retentivity have been shown by resulted in the polymer composite. XRD results of the samples have shown that magnetite particles were spherically distributed all over the surface and agglomeration of particles was absent [196]. Magnetite particles prepared with different methods have a critical impact on magnetic properties. Magnetite particles prepared with co-precipitation and hydrolysis method have shown different magnetic range which indicated that preparing magnetite particles could have an important role to play in the required properties range. Polyvinylidene fluoride (PVDF) reinforced with magnetite particles has shown that with an increase of magnetite content in the matrix, magnetic properties get improved. The hydrolysis method has shown better magnetization of magnetite particles in comparison to the co-precipitation method [197].

PVC/PP/HAp/chitosan composite is a bio-compatible thermoplastic that can be used in medical applications. The mechanical properties of PVC/PP/HAp/chitosan composite depend on the parametric set of conditions of extrusion. It has been found that 200°C screw temperature, 20Kg load, 50 rpm of screw rotations are the best conditions of extrusion [198]. PLA, when reinforced with nano-size HAp particles decreases the MFI (melt flow index) as well as other mechanical properties such as elongation, break strength, and ultimate strength. Further, 3D printed part is treated externally with a vapor smoothing process which improves 80-87% surface finish of the printed part [199]. Polyamide 6 (PA6) can be recycled with good mechanical properties by recycling it with TSE and thus recycled PA6 can be further used with good mechanical strength. Parametric optimization of TSE was reported in this research which gives the best setting of TSE for recycling the PA6 polymer [200].

Researchers have tried to explore FDM with different feedstock filament materials such as carbon-reinforced polymers, metal-reinforced polymers, ceramic reinforced polymers, and CNT reinforced polymers, and various other reinforced or composite feedstock filaments for different range of applications. The flexible nature of FDM has made it possible to print a different range of feedstock filaments without causing any change in machine interface such as hardware or software [201-202]. PLA a biodegradable polymer with almost similar properties to ABS has been recently explored by researchers for medical, structural applications. The effect of build orientation (one of the input parameter of 3D printing) on the printed part of PLA has been investigated for prediction of mechanical (tensile) property of the material and it has been found that supplanting of material with 0° has shown maximum tensile property in comparison to other angles of deposition because of the parallel deposition of material to the product length. Fatigue testing of PLA printed part with different build orientation varying from 0-45° has been investigated and it has been found that under constant loading part with 0° supplanted layers have shown maximum strength whereas in case of dynamic loading part with 45° supplanted layers have shown better fatigue value in comparison to other parts made with different input parameter. It was found that an increase in the temperature of the product leads to a decrease in the fatigue life cycle of the product [203-204].

3D printed scaffolds with high porosity and geometrical porosity have been investigated for fatigue behavior and it was found that with reversal strain load application, strain-softening of samples has been seen. Circular geometry of pores has exhibited stable fatigue life, whereas triangular geometric pores were inefficient for fatigue loading conditions. Low-stress concentration in the case of circular pores was found to be the reason for better fatigue resistance of scaffold. Thus, varying geometry of pores lead to fatigue life improvement of 3D printed PLA scaffold with high significance. Circular pore-based printed samples were found to be deformed due to buckling whereas in triangular pore-based specimens simple shear mechanism has been seen as the deformed geometry has a 45° inclination to the load [205]. PLA reinforced with wood particles from 0-50 weight percentage has been investigated for the 3D printing conditions and mechanical properties were investigated for the printed samples. It has been found that printed parts with a high level of wood content have shown a decrease in tensile strength of specimen while loading up to 10% (tensile strength: 57MPa) has shown better mechanical property than neat PLA (tensile strength: 55MPa). Surface roughness and porosity were found to increase with the increased loading of wood particles. Further, DMA analysis has shown a decrease in storage modulus with high wood reinforcement [206].

Various 3D printers are available in today's world for different fields of applications. An open-source replicating rapid prototype (Rep-Rap) 3D printer has been used for the printing of PLA to investigate the mechanical properties of printed parts with a different set of input conditions. The ultimate tensile strength of samples was reduced with 90°orientation deposition of layers as fracturing force was perpendicular to the layer of deposition. Further, it was noticed that layer thickness up to 0.15 mm maximum strain rate has been obtained and for the 0.2 mm layer thickness minimum strain rate has been obtained [207]. Filaments of wood and polymeric material have been investigated for mechanical, morphological, and chemical properties in which content of wood powder changed from 20-40 weight percentage, it has been found that 20 weight percentage wood in composite improved the tensile properties while increasing further wood contend lead to a reduction in properties whereas high content of wood in polymeric matrix leads to improvement in flexural properties and hardness of printed specimens [208]. Highly dense PLA blocks have been prepared with 3D printing and examined for the tensile, compressive, and fracture properties. The effect of extrusion direction has been investigated with the loading conditions in testing. It has been found that when the material was loaded in the direction of deposition, the results were better for the mechanical properties in comparison to loading in any other direction such as in the transverse direction [209].

2.3 Literature survey for thermal conductivity of the thermoplastic composite matrix

The researchers have investigated the thermal conductivity of polymers and have found that amorphous and virgin polymers have shown low thermal conductivity (ranging between 0.1-0.3 W/mK) [210]. Polyvinyl-alcohol (PVA) reinforced with cellulose nanocrystals (CNC) have been investigated by researchers for the different molecular weight of PVA, different loading of CNC fillers in PVA and for different ordering parameters and it has been observed that with increasing content of CNC in the base matrix the thermal conductivity has improved up to 3.45 W/mK. The

CNC orientation in the composite matrix has a vital role to play in the improved thermal conductivity of the prepared composite [211]. Researchers have also worked for the super thermal conductivity of the polymeric composites for thermal management application and have observed that polyethylene when carefully deposited in the perfect chain without entangling of atoms may result in a better thermally conductive chain with thermal conductivity of 62 W/mK. which was higher than for some of the ceramic and metals [212].

Hybridized fillers reinforcement, one of the techniques to prepare electrically and thermally active polymeric composite have been investigated by some researchers and it has been observed that deposition of different fillers in the matrix for different continuous phases of polymeric crystal has resulted in multi-functional components with high thermally and electrically active component [213]. Polymeric composite with lower weight of reinforcement and high thermal and electrical conductance may have some good application for lightweight components such as for electronic and electrical parts as these composites may be used for replacement of heavyweight components from circuits which are generally made of metal or ceramic composites. These lightweight components may also find application in the manufacturing of fuel cells [214-215]. The effect of filler dimension has also played important role in the conductivity of composites, but some researchers have also used similar thickness, aspect ratio, and size of filler in hybrid composites so that compatibility of composite would be enhanced in comparison to different size fillers. It has been observed that 44% of filler (graphene and boron nitride) enhances the thermal conductivity by 35 times [216].

Some research groups have investigated the effect of graphene reinforcement in epoxy-based thermoset polymers and have observed that when graphene content in epoxy resin is increased more than 40 wt.%, the thermal conductivity of composite reached 12 W/mK. Moreover, graphene presence in the composite has enormously enhanced the electrical conductivity of the component [217-218]. LDPE and PVC reinforced with a varying range of carbon materials and weight percentage in the composite have been investigated for the thermal conductivity and it has been observed that with increasing carbon chain in a composite the conductive chain of the composite increases to the same extent. It was observed that temperature has a negative relation with the thermal conductivity of composite material [219]. Researchers have also investigated some fundamental theoretical models for thermal conductivity approximation and have suggested an equation that may be used to calculate the thermal conductivity of any composite material whose parent component thermal conductivity is known already. The observation has suggested that the theoretical model was accurate [220].

Further, new parameters were added in the standard theoretical equation to enhance the predictability of the model such as length/diameter (L/D) ratio, which was incorporated into the model equation [221]. The comparative study of graphene and CNT have suggested that graphene has shown higher thermal conductivity in comparison to CNT tubes. Therefore, graphene may also be used in electronic applications where the superconductive composite is required with the reduced weight of components [222]. The microstructure of a polymer composite may also be designed as per the requirement so that it may behave as superconductive material from a thermal viewpoint. Researchers have explored this and have observed that filler orientation and filler agglomerates have a positive effect on the thermal and electrical properties of composites [223]. It has been observed that phonons are the responsible factors for polymeric heat conduction. The length of the phonon in the case of polymer is very low due to which most of the polymeric matrix exhibit a small thermal conductivity range varying from 0.1-0.5 W/mK. But the flexibility of polymer for processing conditions, preparation of composites, lightweight components, etc. attract the scientists to explore the polymeric matrix for higher thermal conductivity with some reinforcement of metal/ceramic powder.

Various filters such as Al_2O_3, silica powder, Fe powder, graphene powder, etc. have been used by previous researchers to make the polymeric matrix more thermally conductive [224-225]. Polyimide matrix with boron nitride (BN) up to 30 weight percentage has shown thermal conductivity of 0.71 W/mK which was higher than the polyimide alone. Moreover, the presence of BN particles in polyimide has also increased the thermal stability by increasing the glass transition temperature as well as heat resistance index [226]. Polyethylene glycol (PEG) polymeric base in addition to Al_2O_3 have shown better thermal conductivity (0.42 W/mK) than virgin PEG (0.29 W/mK). Only 4 weight percentage of Al_2O_3 has resulted in nearly 41% improvement in thermal conductance of composite [227]. It has been observed by previous studies that the amorphous structure of polymeric material results in low thermal conductivity ($k<0.2$ W/mK) whereas crystalline and dense structure such as high-density polymer ethylene (HDPE) results in better thermal conductivity ($k>0.5$ W/mK) [228]. Also, it has been observed that the amorphous structure of polymers shows strange phenomena as up to glass transition (T_g) temperature the thermal conductivity shows improvement whereas after T_g the thermal conductivity decreases [229-230]. Researchers have investigated the effect of carbon black as reinforcement in the polymeric matrix and have found that the carbon black has less contribution towards thermal conductivity whereas its effect on electrical conductivity was significant [231]. Researchers have observed that covalent bond formation between filler and the polymeric base has resulted in a better transfer of phonon which is responsible for heat carrying capacity thus ultimately leading to better thermal conductivity [232].

2.4 Literature survey for commercially available feedstock filaments of FDM

Different ranges of polymeric materials are present in the market for FDM. Some of the common materials used on FGDM working are ABS, PLA, PA, PP, polycarbonate (PC), polyethylene (PE), etc. The commercially available feedstock filaments of different polymeric materials for various applications have been explained as follows

ABS is a common thermoplastic that is available in the form of feedstock filament for FDM applications. It has been observed that ABS when 3D printed on an FDM platform has anisotropic properties and shown 65-72% tensile strength and 80-90% compressive strength in comparison to injection molded parts [233]. The strength of the ABS-based fabricated part was less but the design intricacy of FDM was one of the important reasons to fabricate part through FDM technique rather than injection molding. ABS-based translucent parts were fabricated for the packing of mechanical and electrical components. Post-processing techniques were used for increasing the translucency of part such as (i) elevated temperature technique which resulted in improved transmissivity but shrinkage was observed in fabricated part, (ii) resin in-filtration, and (iii) surface sanding which resulted in a 16% increase in transmissivity without dimensional shrinkage [234]. It has been observed from dynamic mechanical analysis (DMA) that the ABS printed part with normal built style possessed more strength than double dense and sparse structures whereas the loss modulus was found to be enhanced with increasing temperature but the reduction in viscosity was observed for the fabricated part of ABS [235]. The process optimization study of FDM for ABS based feedstock filament has proved that the selection of input process parameters was the critical step where the behavior of printed prototype might get changed such as with raster angle of -45°/45°

has shown maximum tensile strength as compared to other raster angles, whereas for flexural properties 0/90° raster angle has shown optimized results [236].

It has been observed for the wear resistance of the FDM build a prototype that layer thickness of 0.127mm, raster angle of 0°, raster width of 0.5064mm, an air gap of 0.008mm, and build orientation of 0° has provided an optimized FDM processing condition for minimum wear of part. Extensive studies of FDM process parameters have been performed to predict the behavior of build prototypes for wear property [237]. The electrical conductivity of the printed prototype was enhanced by chemical deposition of Copper (Cu) particles on a 3D printed prototype of ABS using the chemical etching method and it was observed that the electrical insulator ABS has been successfully converted into the conductor and highest electrical conductivity was observed for parts which were chemically etched with chromic acid in comparison to etching done with any other acids [238]. Various other researchers have also explored the FDM processing parameters to highlight the mechanical performance of functional prototypes based on ABS [239-245].

These days' researchers have been focusing on a biodegradable polymeric matrix such as PLA. For mechanical performance, it has been observed that 225°C of nozzle temperature has given the best tensile modulus for virgin PLA. Whereas part geometry has also played a significant role in mechanical performance and processing temperature controlled the morphological behavior of PLA [246]. Various 3D printers based on FDM technology are available in the market today such as Divide by zero model, Cube-2 3D printer, Stratasys FDM, and many others. Researchers have explored the tensile properties of PLA for a different set of input parameters. Build orientation with 0° has shown maximum tensile strength among various build orientation angles [247]. Further fatigue property of PLA-based 3D printed part has shown maximum fatigue life for 45° build orientation for the cyclical loading on the universal tensile testing machine (UTM) [248]. PLA represents a biodegradable polymer with high strength properties and thus is beneficial for biomedical applications. Researchers have explored the fusion of silver particles on the 3D printed surface of PLA for antimicrobial applications. The study suggested that the printed structure had voids in inter and intra-layer which was found beneficial for the synthesis of foreign particles on its surface [249].

PA, one of the thermoplastic polymers, which exist in semi-crystalline form with great flexibility and low density (1 g/cm^3), high fatigue and flexural strength is one of the important thermoplastics which could have a great role in FDM based applications such as the aerospace industry, consumer goods, etc. Researchers have observed that built-up angle plays a vital role in the mechanical strength of PA specimens. Moreover, anisotropy of tensile strength was present for different directions whereas for compressive strength low anisotropy has been observed [250]. The high shrinkage stress of nylon-6 was one of the problems of the FDM fabricated prototype which hinders the applicability of the material for a wide range of fields. Researchers have explored the infusion of maleic anhydride grafted poly (ethylene 1-octene) (POE-g-MAH) into the polymeric matrix of nylon-6 to address the shrinkage issue of polyamide and have successfully prepared polyamide which had low shrinkage after solidification of 3D printed part [251]. Various researchers have explored the FDM process parameters for optimizing the printing condition as well as the output properties for polyamide-based feedstock filaments [252-254].

PC is a thermoplastic that possesses high toughness and optical transparency (in some cases). Researchers have explored the feedstock filaments of PC for FDM applications. Dynamic mechanical analysis of 3D printed parts has shown that the number of build parameters has affected positively the tensile modulus of parts whereas testing conditions have a significant impact on the mechanical performance of fabricated prototypes [255]. Fabrication of prototypes and simulation of failure analysis was performed by researchers to explore the validity of the failure model with that of practically obtained results. Predictability of practical results with failure model has shown close relationship thus isotropic material has shown high predictability for failure modes [256]. Input process parameters such as build angle, orientation angle, raster width, infill speed, etc. have been explored by researchers to optimize the printing condition for PC-based feedstock filaments [257-258, 259-261]. It has been observed that with the decrease in contour and increase in raster to the raster air gap, the creep strain increases (up to 10) [262].

PP thermoplastic polymer also represents a class of polymer that can also be used for FDM application. Researchers have explored the mechanical, flexural properties of PP-based 3D printed prototypes for their possible applications [263]. Different input process parameters have been optimized for the printing of PP and it has been observed that orientation angle of 0°, the layer thickness of 0.35mm, and infill of 100% represented the optimized conditions for 3D printing of PP based thermoplastic feedstock filament [264]. The feedstock filament of the PP matrix has been explored for the in-house fabrication of a nanoreactor with an integrated magnetic stirrer on an

FDM setup [265]. Table 2.4 shows the various commercially obtainable feedstock filaments with their application on the FDM platform.

Table 2.4 Various polymeric materials (commercially available) used on the FDM platform

Materials		Studies performed
ABS	(a)	FDM process optimization
	(b)	Dynamic behavior analysis of FDM fabricated part
	(c)	Prototype printing for packaging of mechanical and electrical components
	(d)	Wear analysis and process optimization of functional prototypes
	(e)	Enhancement of electrical conductivity of functional prototypes for electrical and electronics applications
PLA	(a)	Testing of PLA properties for FDM 3D printed part for future biomedical application
	(b)	FDM process optimization for 3D printed part of PLA
	(c)	Fusion of silver particles on PLA prototype for antimicrobial function in the biomedical field
	(d)	Comparison of different FDM machine setups to characterize reproducibility of 3D printed parts
	(e)	Textile based design printing on FDM setup for soft PLA matrix
	(f)	Characterization of Adhesiveness of FDM fabricated prototype
	(g)	Comparative study of ABS and PLA prototypes fabricated on a 3D printer
PA	(a)	Anisotropic characterization of nylon-based 3D printed specimen for compressive as well as tensile testing
	(b)	Reduction of shrinkage of the polyamide-based 3D printed part

	(c)	FDM process optimization for 3D printed part
PC	(a)	DMA analysis of 3D printed prototype for characterizing the PC feedstock filament
	(b)	Finite element analysis (FEA) of isotropic PC based prototype
	(c)	FDM process optimization for mechanical performance
	(d)	Creep analysis for 3D printed prototype
PP	(a)	FDM process optimization and mechanical properties evaluation for PP polymeric feedstock filament
	(b)	In-house fabrication of miniature nanoreactor

2.5 Literature survey for non-commercial feedstock filaments of FDM developed in-house

Various researchers have used commercially available feedstock filaments as explained above, but the virgin polymeric feedstock filaments have their limitations such as low thermal conductivity, poor electrical conductivity, diamagnetic character, inadequate mechanical properties, and surface properties, etc. To overcome these issues, researchers have tried reinforcements of various foreign particles into the polymeric matrix of virgin polymer. A polymeric blend of composites may be prepared by two routes (a) mechanical route and (b) chemical route. The reinforcement particles may be categorized into two classes (depending on their size) (i) microparticles (ii) nanoparticles. Based on these, the composites may also be categorized into two classes (1) micro composites and (2) nanocomposites.

2.5.1 Micro composites

Various types of reinforcement have been tried in the polymeric matrix for different applications and alteration of properties of the base polymer. In this part, we will only discuss the reinforcements which are done in the polymeric base matrix for the preparation of lab-scale feedstock filaments for FDM platform applications. Low-density polymer ethylene (LDPE) has been reinforced with SiC/Al_2O_3 particles and the prepared composite has been used for feedstock filament development for FDM. It has been observed that LDPE with 50weight percentage, SiC with 25 weight percentage, and Al_2O_3 with 25 weight percentage could be used to prepare feedstock and has shown best mechanical performance on selected input processing parameter of FDM [266-267]. Nylon polymeric base has been extruded with Al-Al_2O_3 reinforcement and successfully feedstock filament has been developed for FDM and it has been observed that three compositions (Nylon 60 weight percentage, Al- varying from 26-30 weight percentage and Al_2O_3 varying of 10-14 weight percentage) for composite may be selected as per the melt flow index (MFI) requirement. It has been also observed that with the reinforcement of foreign particles (Al/ Al_2O_3) in the nylon matrix the tensile properties have been affected and got reduced in comparison to virgin nylon matrix [268-269]. DMA analysis of ABS-Cu blend has suggested that with increased Cu filler (22-26% by volume) in polymer matrix the storage modulus and loss modulus have improved significantly [270].

Various fibers such as carbon fiber (CF), glass fiber (GF), and Kevlar fiber (KF) have been tested as reinforcement in nylon matrix and it has been observed that the reinforcement of CF in nylon matrix improved the tensile strength of the composite by 6 times that of non-reinforced matrix [271]. By the reinforcement of thermotropic liquid crystalline polymer (TLCP) in PP, it has been proved that with an increased fiber content of TLCP (up to 40 wt.%) in the polymeric matrix the mechanical properties were found to improve by a significant difference. 1.5 times enhancement in tensile modulus has been observed for 40 weight percentage reinforcement of TLCP in comparison to pure PP and 100% improvement in comparison to ABS filament [272]. PP has been blended with tricalcium phosphate (TCP) for bone graft application and it has been observed that the prepared composite possessed 12 MPa of ultimate compressive strength and 263 MPa of compressive modulus. The printed porous structure on FDM held 150–200-micron pore size which was beneficial for cell growth application as per free area requirement [273]. Friction welding of two dissimilar plastics has been performed using reinforcement of Al powder which makes the polymeric matrix compatible for feedstock preparation. FDM platform was used to print objects which were joined at a later stage [274].

Nylon polymeric base has been reinforced with iron powder (Fe) to improve the thermal conductivity of the composite and prepared feedstock filament has been printed on FDM. It was observed that the prepared prototype had thermal conductivity greater than the virgin nylon matrix and some other composites [275]. Some researchers have also added polymer as reinforcement in another polymeric base to improve the polymer behavior for some specific applications such as for biocompatibility, wear resistance, etc. Ultra-high molecular weight polyethylene (UHMWPE) has been added in high-density polyethylene (HDPE) to improve the mechanical and wear characteristics of the composite for biomedical implant application [276]. Researchers have explored the PP matrix with reinforcement of GF and maleic anhydride polyolefin (POE-g-MA) by varying content from 0-30 weight percent. It has been observed that the addition of GF has improved the tensile modulus whereas the flexibility of feedstock filament was reduced. On the other hand, the POE-g-MA has reduced the tensile strength and improved the flexibility of the fabricated part [277]. The fiber orientation in the case of FDM processing has been explored and it was observed that FDM was capable of orienting short fibers inadequate direction ultimately resulting in better mechanical properties in comparison to simple compression molding technique [278-279]. Table 2.5 shows the list of composite polymeric materials prepared for feedstock filament on a lab scale for various applications.

Table 2.5 Polymeric micro-composite used for the preparation of feedstock filament for FDM application

Polymer	Reinforcement	Studies performed
LDPE	SiC/Al_2O_3	Preparation of feedstock filament with better mechanical properties for LDPE
Nylon	(a) Al-Al_2O_3	Development of alternative feedstock comparable to ABS filament in mechanical performance
	(b) CF, GF, and KF fiber	Comparative study for the mechanical performance of different fiber reinforced nylon matrix
	(c) Al powder	Prepare compatible composites of ABS and nylon for frictio9n welding application
	(d) Fe powder	Enhancement of thermal conductivity of the polymeric matrix
	(a) Cu	Dynamic behavior analysis of polymeric blend

ABS	(b) TLCP	Feedstock filament preparation with modified mechanical properties for FDM printed prototype
	(c) Al powder	Prepare compatible composites of ABS and nylon for joining of dissimilar plastic
	(d) Al/Al_2O_3	Wear characterization for the 3D printed part
	(e) CF	To enhance the mechanical property for fabricated part
PP	(a) TLCP fiber	Feedstock filament preparation with modified mechanical properties for FDM printed prototype
	(b) TCP	Biocompatible scaffold printing with porous structure
	(c) GF and POE-g-MA	To alter the mechanical properties of PP based fabricated part on FDM setup
HDPE	UHMWPE	Biomedical implant application with excellent mechanical property

2.5.2 Nano-composites

Nano-composites are those composites in which foreign particles which are added to the polymeric matrix are of nano-size (10^{-9}mm). It has been observed that in nano-composites ceramic and metallic reinforcements have been performed whereas in micro-composites the foreign particles are of micro-size (10^{-6}mm). Non-metallic (polymeric, wood, clay), ceramic and metallic, every type of reinforcement has been done by researchers.

PEEK has been tested with nano-sized CNT varying from 1-5 weight percentage in the polymeric matrix to evaluate the tensile strength of the prepared part fabricated through FDM. It has been observed that nanoparticles of CNT when reinforced in polymeric base reduced the porosity of part in comparison to virgin PEEK. No significant improvement has been observed for mechanical properties [280]. PU/PLA reinforced with graphene oxide (GO) has been examined for its biocompatibility and anisotropic behavior of nanocomposite. Mechanical and thermal properties were observed to be enhanced significantly with the addition of nanosized GO [281]. PLA in reinforcement with multi-walled CNT (MWCNT) has been explored for high electrical conductivity and a prototype of a liquid sensor has been printed for sensor application. Various input process parameters affecting the topography of the printed prototype have been evaluated for the optimized condition for best results [282]. PU reinforced with MWCNT has been tested for strain sensor applications and various properties such as mechanical, electrical; piezo-resistivity, etc. have been evaluated for the printed part. MWCNT has improved the stiffness of composite which ultimately made it compatible for printing on FDM setup whereas some insignificant reduction in elastic modulus was observed. The piezo-resistivity was observed to be 176 on gauge factor and was repeatable for various cyclic loading [283]. PLA has been reinforced with silica nano clay (4 weight percentage) to evaluate the composite mechanical, dynamic and morphological behavior. It has been observed that a 115% improvement in elastic modulus was obtained when silica nano clay was added to the polymeric matrix. Mechanical, dynamic, and morphological properties were observed to improve than virgin PLA product [284-285].

ABS has been reinforced with graphene nanoparticles (4 weight percentage) by researchers and has been explored for the build orientation of FDM and it has been observed that prototypes printed with composite feedstock have shown improved elastic modulus and storage modulus with better thermal stability [286]. Researchers have tried polybutylene terephthalate (PBT) with the reinforcement of CNT and graphene separately and tried to compare the printability and mechanical response of printed prototypes. It has been observed that all the observed properties (mechanical, morphological, printability, and thermal stability) for PBT/CNT were better than PBT/graphene composite [287]. Researchers have investigated the combination of Polyvinylidene fluoride (PVDF) matrix with Barium titanate ($BaTiO_3$) to club functional properties such as piezoelectric behavior, pyroelectric and dielectric behavior. It has been observed that the value for piezoelectric constant was three times higher for the FDM printed object of the composite in comparison to solvent cast nano-composite [288]. It has been also observed for the MWCNTs/BaTiO3/PVDF multi-composite that CNT has improved the dielectric property of the composite and a suitable composite ratio for required dielectric and loss properties were obtained for 1.7 weight percentage CNT, 45 weight percentage BaTiO3, and 53.3 weight percentage of polymeric matrix [289-290]. Table 2.6 shows different nanocomposites prepared on a lab-scale to prepare feedstock filaments of FDM.

Table 2.6 Polymeric nano-composite used for the preparation of feedstock filament for FDM application

Polymer	**Reinforcement**	**Studies performed**
PEEK	CNT	Mechanical property evaluation for PEEK and CNT composite
PU/PLA	GO	Effect of composite formation on the mechanical and thermal property along with biocompatibility
PLA	(a) MWCNT	Functional prototype printing of highly conductive liquid sensors
	(b) Silicate nano clay	Evaluation of nano clay composite on mechanical, thermal, and dynamic properties of fabricated part on FDM
	(c) Graphene	Evaluation for the mechanical, magnetic, and electrical properties of composite
PU	MWCNT	FDM printing of thermoplastic-based strain sensors
ABS	MWCNT	Mechanical and thermal property evaluation for FDM printed electrically and thermally conductive composite feedstock filament
	Graphene	Evaluation of printed prototype with composite feedstock filament for mechanical, dynamic, and thermal properties
PBT	CNT and Graphene	Comparative analysis of two different nanocomposites for FDM application
PVDF	$BaTiO_3$	Introduce homogeneity in dispersion with FDM printing and club the properties of $BaTiO_3$ in PVDF matrix
	MWCNT/BaTiO3	Enhance dielectric property of the multi-composite for electronic sensor applications

2.6 Research gaps and problem formulation

Based on the literature review, the following gaps have been identified

(a) It has been observed that many researchers have worked in the field of 3D printing of commercially available materials, but very few have reported the 3D printing of thermo-sensitive and magneto-sensitive filament for 4D applications. Further, it has been observed that very little work has been reported on thermal and magnetic actuation together.

(b) PLA in a combination of PVC reinforcement is very less studied which may be used as waste management of polymers as waste PVC can be reinforced into the matrix of PLA.

(c) Few studies have been reported on polymeric composite applications for the 3D printing of tiles. These tiles may have three important characteristics (a) Self-assembly, (b) thermal insulation, and (c) plastic solid waste management. For self-assembly, Fe_3O_4 powder was used in this study. Whereas, for thermal insulation, the wood powder was used as the replacement of wood/timber.

(d) Smart materials are used in actuators, sensor applications and can be fabricated by conventional manufacturing processes as well as by 3D printing.

(e) Thus, the shape memory polymeric composites (SMPC) developed at a lab-scale have certain advantages over the shape memory polymer (SMP). In SMPC it is possible to customize the matrix properties to support printability, tailormade mechanical, physical, thermal, morphological properties and can be developed at a low cost.

CHAPTER 3

METHODOLOGY

This chapter highlights the objectives of the study and the step-by-step methodology of research work carried out to accomplish the objectives

3.1 Objectives of the study

1. To prepare FDM feedstock filament (for commercial open-source 3D printer) comprising of PLA, PVC, Fe_3O_4, and wood powder by mechanical blending with TSE

2. To perform rheological (based on melt flow index (MFI)) and thermal analysis (based upon DSC) of feedstock prepared by the TSE process

3. To perform parametric optimization of feedstock filament wire for mechanical, morphological, magnetic properties for final selection of feedstock filament for 3D printing

4. To print functional prototypes on FDM with prepared feedstock filaments and perform parametric optimization from mechanical, morphological, thermal, and magnetic properties viewpoint.

3.2 Methodology used to achieve the objectives

Figure 3.1 shows the methodology used to attain all the objectives of the present study.

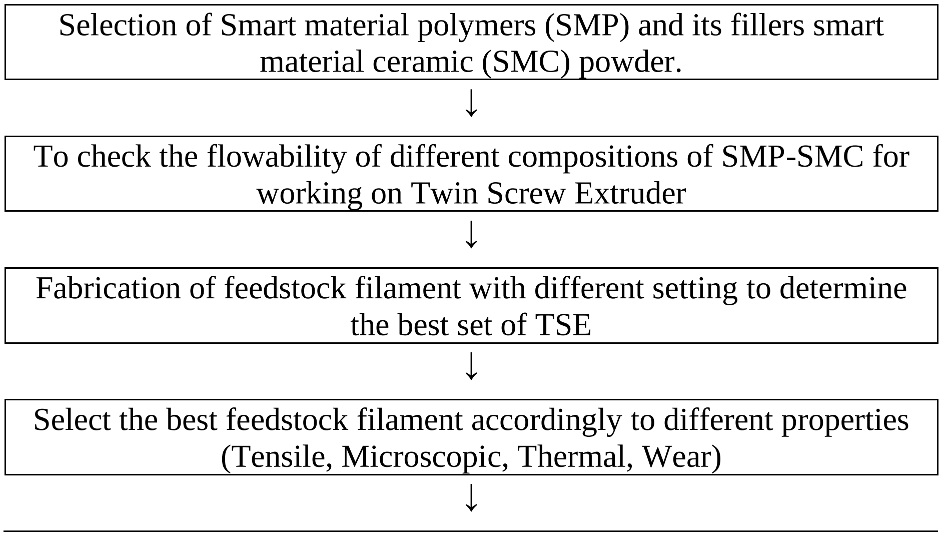

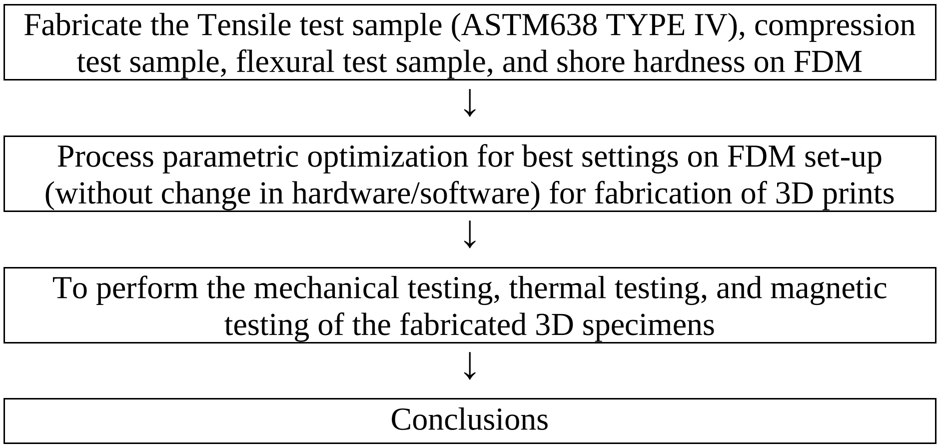

Fabricate the Tensile test sample (ASTM638 TYPE IV), compression test sample, flexural test sample, and shore hardness on FDM

↓

Process parametric optimization for best settings on FDM set-up (without change in hardware/software) for fabrication of 3D prints

↓

To perform the mechanical testing, thermal testing, and magnetic testing of the fabricated 3D specimens

↓

Conclusions

Figure 3.1 Methodology used to attain the objectives

3.3 Different stages of work

The study deals with the development of functional prototypes of 4D feedstock filaments using PLA, PVC, wood powder, and Fe_3O_4 powder. Fe_3O_4 particle reinforcement in the PLA matrix has been considered smart ceramic powder (as it induces magnetic properties in the hybrid material matrix). This study is divided into five stages: -

3.3.1 Stage 1

Parametric optimization of TSE process for mechanical, morphological, rheological, thermal, and magnetic properties for **feedstock filament based on hybrid blend** (PLA/PVC/wood powder/Fe_3O_4 powder in a single composite).

3.3.2 Stage 2

Parametric optimization of TSE process for mechanical, morphological, rheological, and thermal **feedstock filament based on a multi-material matrix** in which four different feedstock filaments (a) PLA, (b) PLA/PVC, (c) PLA/wood powder, and (d) PLA/Fe_3O_4 powder were explored separately.

3.3.3 Stage 3

Development of 3D printed tensile and flexural functional prototypes based on ASTM D638 Type IV and ATM D790, respectively, and optimize the 3D printing process parameters for mechanical, thermal, and morphological properties **for a hybrid functional prototype made of a hybrid blend-based feedstock filament of stage 1.**

3.3.4 Stage 4

Development of 3D printed tensile and flexural functional prototypes based on ASTM D638 Type IV and ATM D790, respectively, and optimize the 3D printing process parameter for mechanical, thermal, and morphological properties for a multi-material **functional prototype made of the multi-material feedstock of stage 2.**

3.3.5 Stage 5

The material matrix selected on stages 1 and 2 were again processed for the recycling issue so that adequate assessment of material matrix life up to 50% reduction in mechanical properties may be performed.

CHAPTER 4

EXPERIMENTATION

This chapter presents the details of experimentation carried out in this research work, results thereof, and a detailed analysis of the results.

4.1 Experimentation for stage 1

4.1.1 Sieve shaking of wood powder

Waste wood dust was collected from a local industry that was composed of a mixture of wood particles of different sizes. Therefore, there was a need to segregate wood dust of 44–60-micron size so that there would be fewer compatibility issues while extrusion and 3D printing through FDM. The compatible sizes of reinforcement in the material matrix reduce the chances of nozzle choking when extrusion is performed on the TSE machine and while printing the prepared filament through FDM. Figure 4.1 shows the different sizes of wood particles (a) Waste wood dust collected from the local market (b) Sieve shaker (c) Fine wood dust collected after sieve shaker (50 microns).

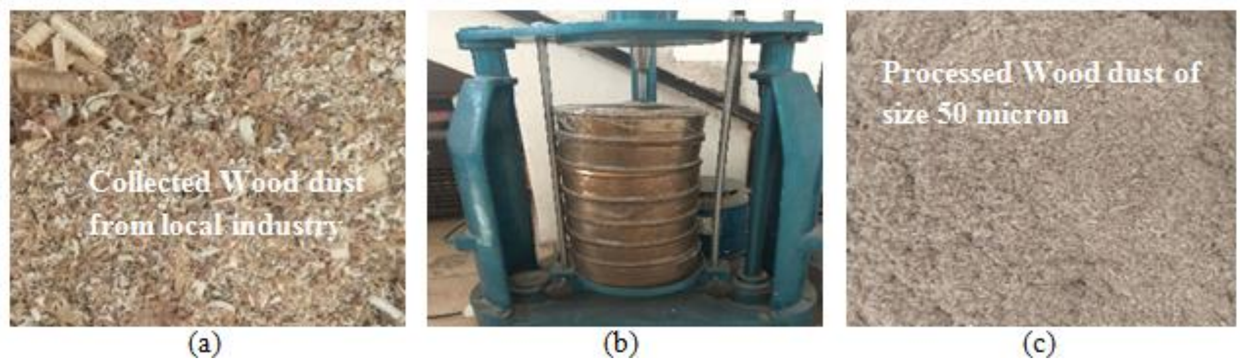

Figure 4.1 processing of wood dust (a) collection, (b) sieve shaker machine, and (c) fine wood particle (50 microns)

4.1.2 Mechanical blending of PLA-PVC-wood dust-Fe_3O_4 powder

Initially, three compositions/ proportions were selected based on pilot experimentation (see Table 4.1) and coconut oil was used as a binder for preparing the blend so that wood dust and Fe_3O_4 powder get attached to the surface of PLA-PVC while blending the composite. Coconut oil has been used as a binding agent based on commercial field practices.

Table 4.1 Different proportion of reinforcement in PLA composite matrix

Composition/ proportion	Matrix and reinforcements	Weight (g)	Proportion in composite Percentage
1	PLA	20	50
	PVC	10	25
	Magnetite powder (Fe_3O_4) (44 micron)	8	20
	Wood dust (50 microns)	2	5
2	PLA	21	52.5
	PVC	6	15
	Magnetite powder (Fe_3O_4) (44 micron)	10	25
	Wood dust (50 microns)	3	7.5
3	PLA	20	50
	PVC	9	22.5
	Magnetite powder (Fe_3O_4) (44 microns)	7	17.5
	Wood dust (50 microns)	4	10

4.1.3 Taguchi L9 orthogonal array (OA) used for parametric optimization of TSE process

After mechanical blending of PLA/PVC with wood dust and Fe_3O_4, extrusion of the composite mixture was performed on TSE (Make: Thermo Fisher; Model: Haake Mini CTW) by using Taguchi L18 O.A and feedstock filament of 1.75 ± 0.015mm diameter was obtained. Table 4.2 shows the input parameters for TSE which was used to prepare feedstock filaments.

Table 4.2 Process variables and their level for TSE process

Input process variable	Operating condition
Torque (3 level)	(a) 0.10Nm (b) 0.12Nm (c) 0.15Nm

Screw Temperature (3 levels)	(a) 160°C (b) 165°C (c) 170°C
Applied load (2 levels)	(a) 5Kg (b) 10Kg

The above conditions were used with three compositions as given in Table 1 for the feedstock filaments. Table 4.3 shows the control log of experimentation for feedstock filament preparation.

Table 4.3 Control log of experimentation for TSE process

Serial number	Load (Kg)	Composition	Torque (Nm)	Screw temperature (°C)
1	5	1	0.1	160
2	5	1	0.12	165
3	5	1	0.15	170
4	5	2	0.1	160
5	5	2	0.12	165
6	5	2	0.15	170
7	5	3	0.1	165
8	5	3	0.12	170
9	5	3	0.15	160
10	10	1	0.1	170
11	10	1	0.12	160
12	10	1	0.15	165
13	10	2	0.1	165
14	10	2	0.12	170
15	10	2	0.15	160

16	10	3	0.1	170
17	10	3	0.12	160
18	10	3	0.15	165

4.1.4 Vibration sample magnetometer testing (VSM)

All the hybrid samples of feedstock filaments of wire prepared by the TSE machine were tested for their magnetic properties with VSM setup (Make: Lakeshore 7404 VSM) by providing it an external magnetic field of 1 Tesla. The different magnetic properties such as magnetization, coercivity, and retentivity were observed so that optimized extrusion conditions can be obtained to maximize the magnetic properties of feedstocks.

4.1.5 DSC analysis

Thermal analysis for best and worst samples as per mechanical properties was performed using DSC setup (Model: Mettler, Toledo) for 3 heating and 3 cooling cycles varying from 30°C to 250°C of a heating cycle, 250 °C to 30 °C of the cooling cycle.

4.1.6 Morphological properties testing

The samples of feedstock were observed under Tool maker’s microscope and metallurgical image analysis software (MIAS) was used to analyze the fractured surface and porosity of the sample. Scanning electron microscopy and energy-dispersive X-ray spectroscopy (EDS) have been performed to know the morphological features and element composition present in the composite so that some relation between mechanical, magnetic, and morphological characteristics may be established.

4.1.7 Process capability analysis for magnetic, surface hardness, and porosity of feedstock

Ten samples of enough length were prepared of the optimum diameter of feedstock filament. Similarly, feedstock filament of the hybrid blend (PLA-50 weight percentage, polyvinyl chloride (PVC)-25 weight percentage, wood powder-5%, and Fe3O4-20 weight percentage) was prepared using optimized TSE standard conditions. All the filaments were subjected to VSM testing, surface characteristic testing such as surface hardness and surface porosity, and process capability analysis was performed.

4.2 Experimentation for stage 2

4.2.1 Mechanical blending of different compositions

Mechanical mixing of polymers and reinforcement was the first step for this investigation. PLA has been taken as the base polymer as the problem is related to multi-material printing of different layers of different filaments that would be added over each other to have a good strength of adhesion between two different filaments deposited layer the base of every filament would be common. For investigation of change of behavior of PLA with different reinforcements. PVC, wood powder, and Fe_3O_4 powder were added, separately in PLA. PVC ratio in PLA has been varied from 10 to 25 weight percent. The wood powder has been added to the PLA matrix in 2.5-10 weight percentage as adding more wood powder enhances the chances of choking the extrusion nozzle. The Fe_3O_4 has been added to the PLA matrix from 10 weight percent to 20wt.%. In the end, a multi blend (PLA 50 wt.%, PVC 25 wt.%, magnetite 20%, and wood powder 5 weight percentage) has also been prepared.

4.2.2 Melt Flow rate testing, twin-screw extrusion (TSE), and universal tensile testing (UTM)

Different polymers and polymer composites were tested for their melt flow rate as it was one of the important rheological properties of the thermoplastic polymer. The melt flow index of the polymer has been tested with ASTM D1238 in which 2.16 kg weight and 190°C temperature of testing conditions were used. The same composites ratios which were tested for melt flow rate were then twin-screw extruded so that filaments can be prepared with 1.60 to 1.75 mm diameter wire. Prepared samples of filaments were then tested with universal UTM for different mechanical properties and to obtain a stress-strain curve to know the behavior of composites.

4.2.3 Morphological, thermal analysis and VSM (Vibration sample magnetometer)

Filaments were then tested with MIAS, a software package that has been used for porosity testing of composites so that the behavior of composites could be well explained with reasoning for the same. For the thermal behavior of the composite, DSC has been performed for the 3 cooling and 3 heating cycles. This test has been performed to know the thermal behavior of composites. The VSM of PLA with 20% Fe_3O_4 and a multi blend of PLA (single composite of different reinforcement) has been performed (by using Lakeshore VSM model machine) to know the difference between the magnetic properties.

4.3 Experimentation for stage 3

4.3.1 FDM printing of tensile, flexural, and circular disc

The selected feedstock filament of stage 1 was used to 3D print the tensile and flexural specimens to explore the mechanical, morphological, pull out and other properties. The tensile specimen was 3D printed as per ASTM D638 Type IV and flexural samples were 3D printed using ASTM D790 standard conditions. Three input variables of FDM (a) infill density; (b) infill angle and (c) infill speed were selected and Taguchi l9 methodology was used to optimize the results as given by Table 4.4. Table 4.5 shows the design of experimentation (DOE) for Taguchi l9 used for 3D printing. While other printing parameters, remained constant as given by Table 4.6. Figure 4.2 shows the dimensions of the 3D printed sample (a) tensile specimen and (b) flexural specimen. Figure 4.3 shows the different input parameters which may be changed for better functional properties. Figure 4.4 shows the actual 3D printing setup with detailing of the printer setup.

Table 4.4 Levels of input parameter for 3D printing of hybrid blend-based composite

Conditions	Selected values
Infill density (percentage) (3 levels)	(d) 60 (e) 80 (f) 100
Infill angle (degree) (3 levels)	(d) 45 (e) 60 (f) 90
Infill speed (mm/s) (3 level)	(c) 50 (d) 70 (e) 90

Table 4.5 DOE based on Taguchi L9 for 3D printing of hybrid blend-based composite

Serial number	ID	IA	IS

1	60	45	50
2	60	60	70
3	60	90	90
4	80	45	70
5	80	60	90
6	80	90	50
7	100	45	90
8	100	60	50
9	100	90	70

ID: Infill Density; IA: Infill angle; IS: Infill speed

Table 4.6 Constant printing parameters

Parameters	**Value**
Bed temperature	65°C
Fill pattern	Rectilinear
Nozzle temperature	235°C
Filament Diameter	1.70mm
Nozzle diameter	0.5mm
Solid layers	Top 3, Bottom 3
Travel speed	130mm/s

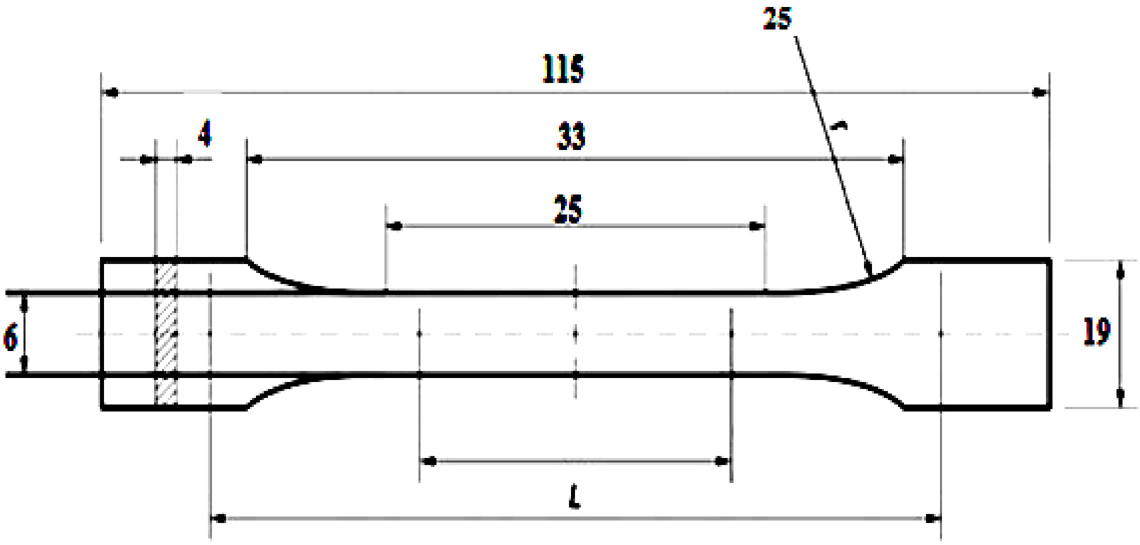

(a) (All dimensions in mm)

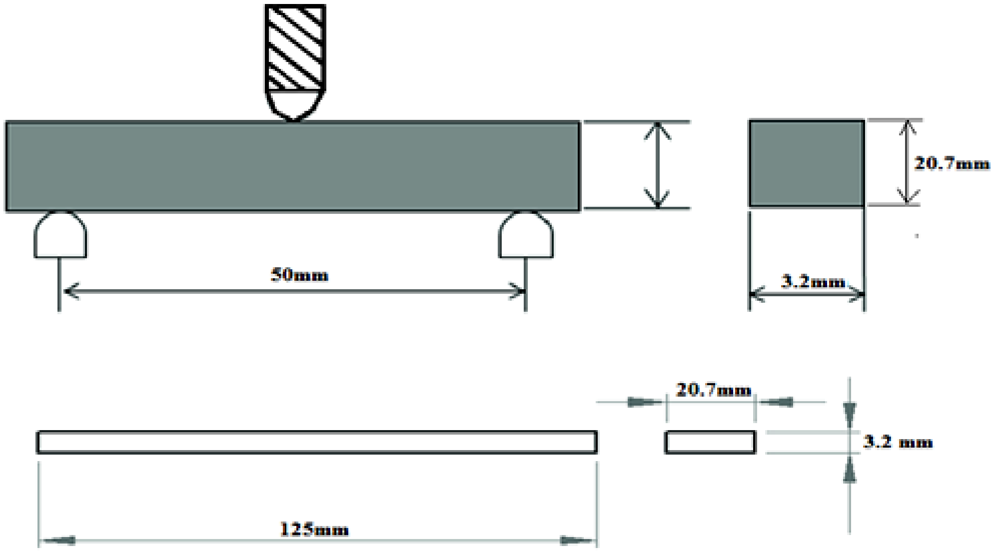

(b)

Figure 4.2 Standard 3D printed functional prototype for (a) tensile and (b) flexural specimen according to ASTM D638 Type IV and ASTM D790 standard

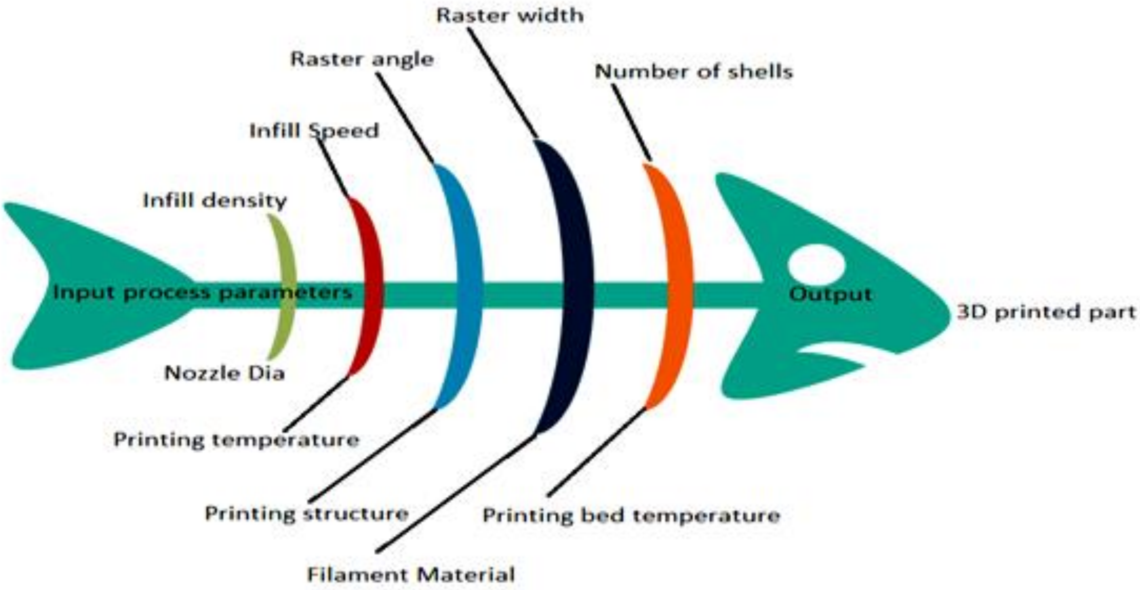

Figure 4.3 Various input parameters of 3D printing

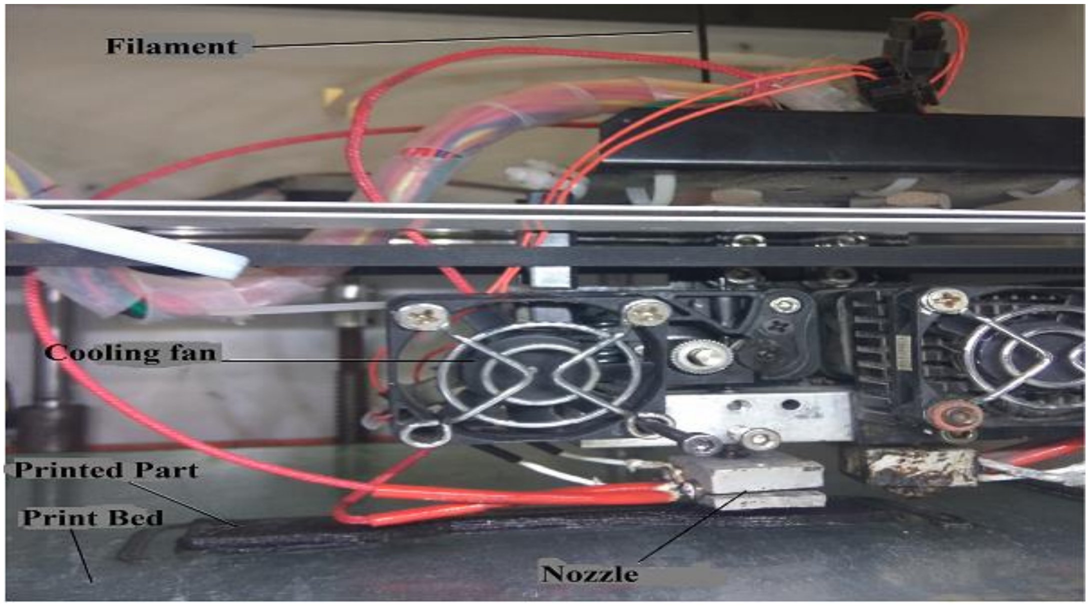

Figure 4.4 3D printing setup with details

4.3.2 Mechanical testing on UTM

All 3D printed functional prototypes were subjected to tensile testing using universal tensile testing (UTM) (Make: Shanta Engineering's, India) whose capacity was 5000N. Shore D hardness of samples was investigated using a shore D tester.

4.3.3 Thermal conductivity test

The printed specimens/discs were subjected to thermal conductivity testing using Lee disc methodology. Lee disc apparatus consisted of steam chamber, lee disc, heating equipment, pot for steam production, pipe to join pot with stem chamber and two temperature sensors, one for steam chamber and the other for lee disc as shown in Figure 4.5.

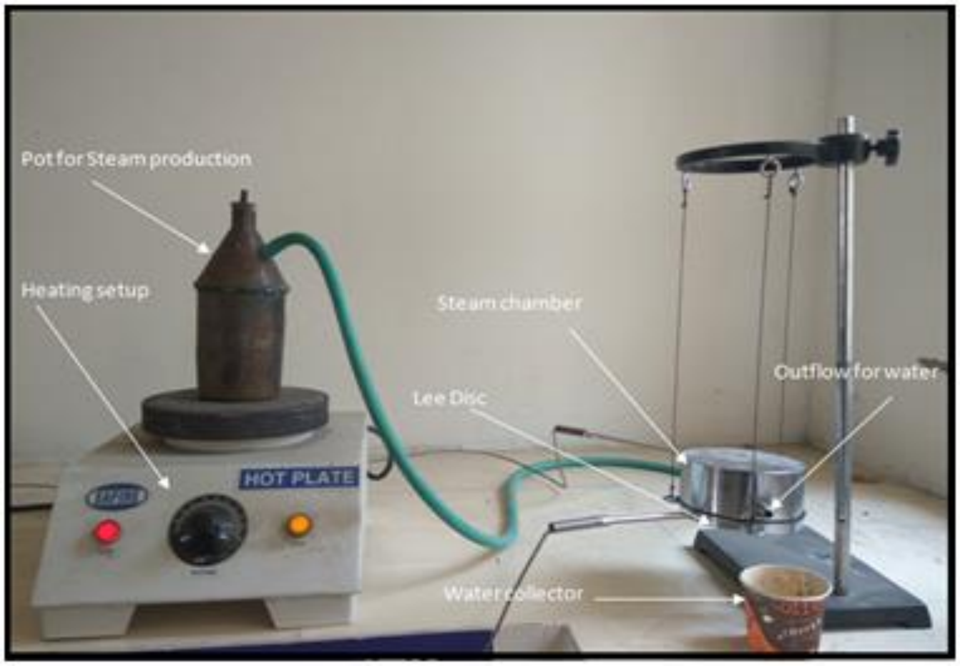

Figure 4.5 Lee disc apparatus used for thermal conductivity measurement

4.3.4 Circular compression testing on UTM setup

The UTM setup (make Shanta engineering, India) with 5000N capacity was used for compressive testing of the circular disc. To avoid slippage of the disc while in compression testing, a specially designed circular fixture was 3D printed (see Figure 4.6) and peak load, break load, peak strength, break strength, and stress vs. strain plot was taken from testing for further optimization of processing conditions. The stress vs. strain plot was used to calculate the modulus of the toughness of the printed discs. Figure 4.7 shows the 3D printed circular disc and Figure 4.8 shows the UTM setup in actual testing. While compression testing on UTM in testing module/software circular object has been taken with grip separation of 110mm.

4.3.5 Morphological testing

Samples were subjected to microstructural analysis using porosity testing using standard ASTM B276 and microstructural graphs using a toolmaker microscope to analyze the behavior of results for 3D printed samples.

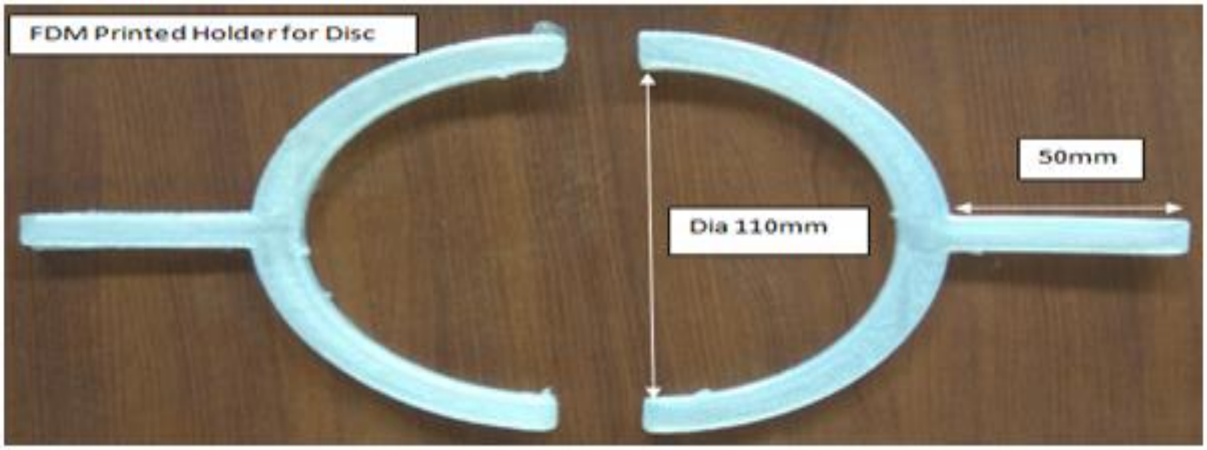

Figure 4.6 3D printed fixture for holding of the disc while circular compression testing on UTM

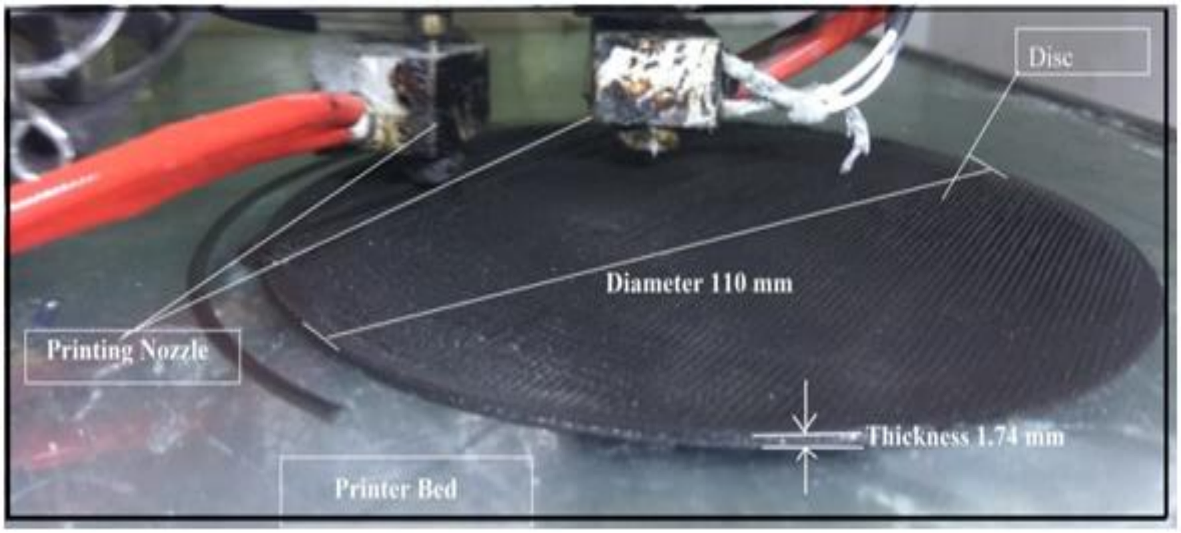

Figure 4.7 3D printing of disc

Figure 4.8 Circular compressive testing on UTM setup

4.4 Experimentation for stage 4

4.4.1 Multi-material printing using FDM

The prepared feedstock filaments of stage 2 for four different materials of required diameter were then used for 3D printing of tensile specimens as per ASTM D638 type IV using DOE (see Table 4.7 for a different level of input parameters of FDM and Table 4.8 for DOE) based on Taguchi L9 orthogonal array (OA) to optimize the printing conditions for mechanical properties of functionally graded printed part. The printed standard tensile specimen has 6 layers (each layer of 0.53mm) in which 1 layer of virgin PLA, 1 layer of PVC reinforced PLA, 2 layers of wood powder reinforced PLA and 2 layers of Fe_3O_4 reinforced PLA exists (see Figure 4.9)

Table 4.7 Variable and fixed input parameters of FDM

Input parameters of FDM used as variable		
Infill density (%) (3 level)	Infill angle (degree) (3 level)	Infill speed (mm/s) (3 level)
(a) 60 (b) 80 (c) 100	(g) 45 (h) 60 (i) 90	(f) 50 (g) 70 (h) 90
Fixed parameters	(a) Bed temperature: 65°C (b) Nozzle diameter: 0.5mm (c) Fan output: 50% (d) Fill pattern: rectilinear (e) Number of parameters: 4	

Table 4.8 DOE based on Taguchi L9 OA for 3D printing of multi-material composite

Experiment 1		Experiment 2		Experiment 3	
ID	60	ID	60	ID	60
IA	45	IA	60	IA	90
IS	50	IS	70	IS	90
Experiment 4		Experiment 5		Experiment 6	
ID	80	ID	80	ID	80
IA	45	IA	60	IA	90
IS	70	IS	90	IS	50
Experiment 7		Experiment 8		Experiment 9	
ID	100	ID	100	ID	100
IA	45	IA	60	IA	90
IS	90	IS	50	IS	70

Note: ID: Infill density (%); IA: Infill Angle (°); IS: Infill speed

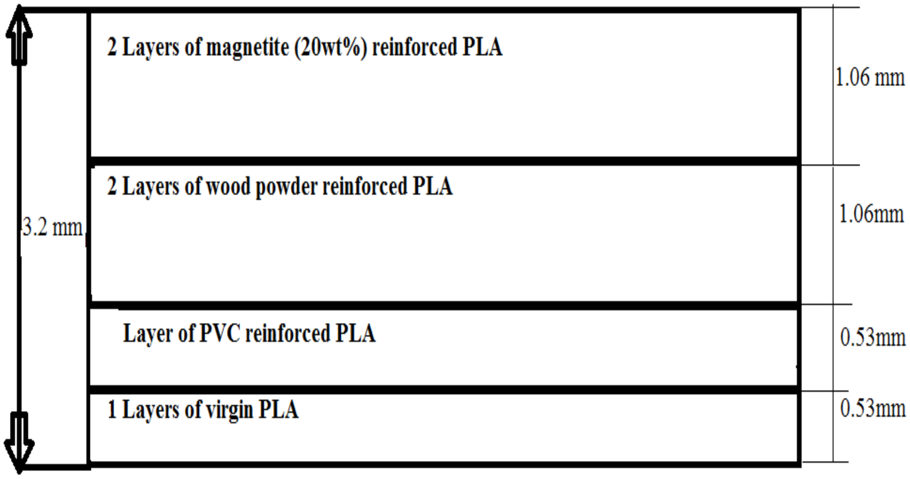

Figure 4.9 Multi-material printed part of different layer

4.4.2 Mechanical testing and Morphological testing

The prepared flexural and tensile specimens were then tested for their flexural, tensile, and pull-out properties using a UTM machine (Make: Shanta Engg., India) of 5000N capacity. For tensile, flexural, and pull-out properties peak load (PL), break load (BL), peak strength (PS), and break strength (BS) were measured. Stress vs. strain diagrams were plotted, so that the mechanics of the material of composite may also be explained based. Figures 4.10, 4.11, and 4.12 show the testing setup for tensile, flexural, and pull-out conditions. Further, for optimization of mechanical properties, analysis of variance (ANOVA) method has been used using MiniTab 17 statistical software package. The Shore D tester and tool maker’s microscope has been used for hardness and fractured surface characterization.

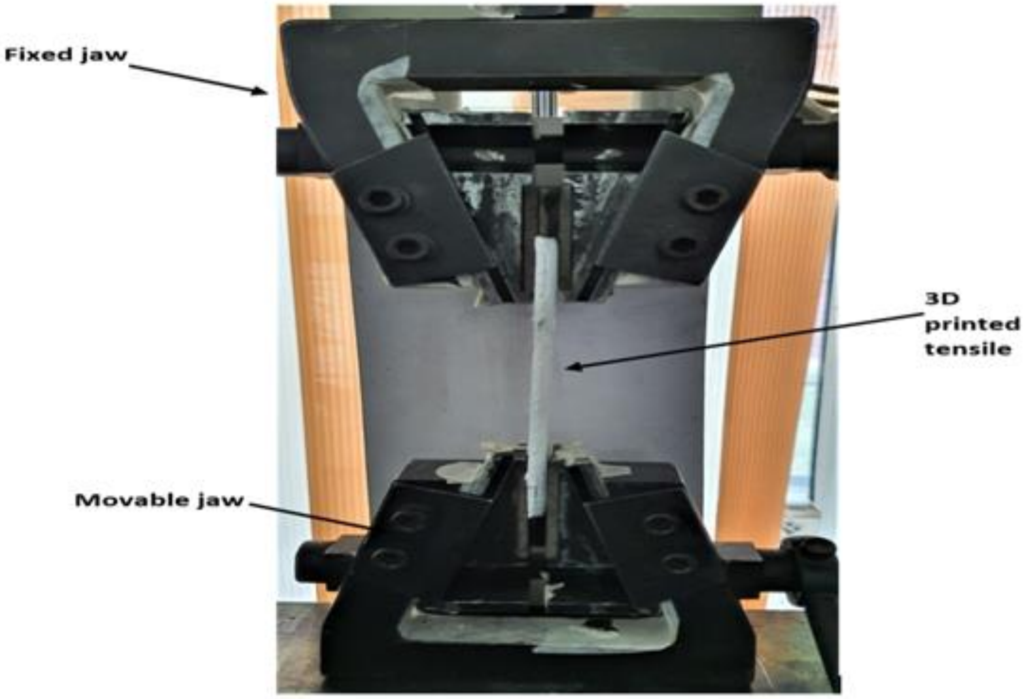

Figure 4.10 Tensile testing of the specimen on UTM

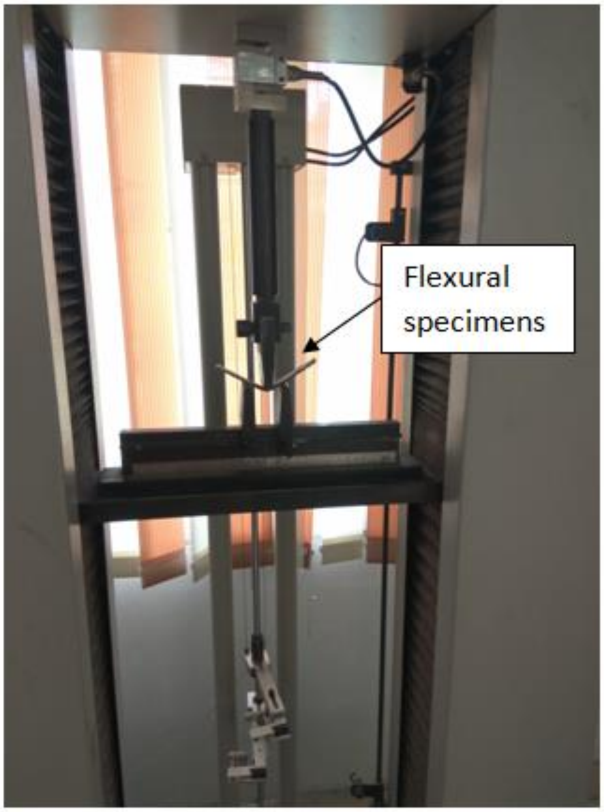

Figure 4.11 Flexural testing of the specimen on UTM

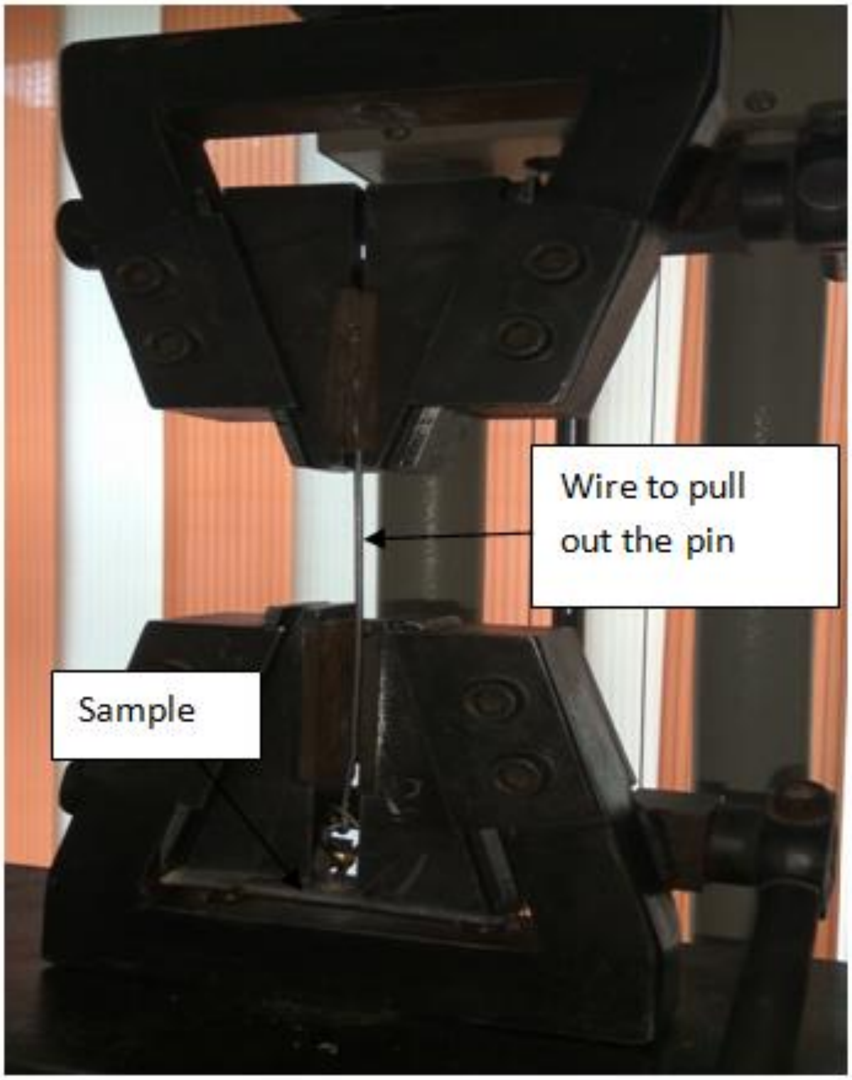

Figure 4.12 Pull out testing of the specimen on UTM

4.5 Experimentation for Stage 5

Figure 4.13 shows the methodology of recycling of selected composite ratio.

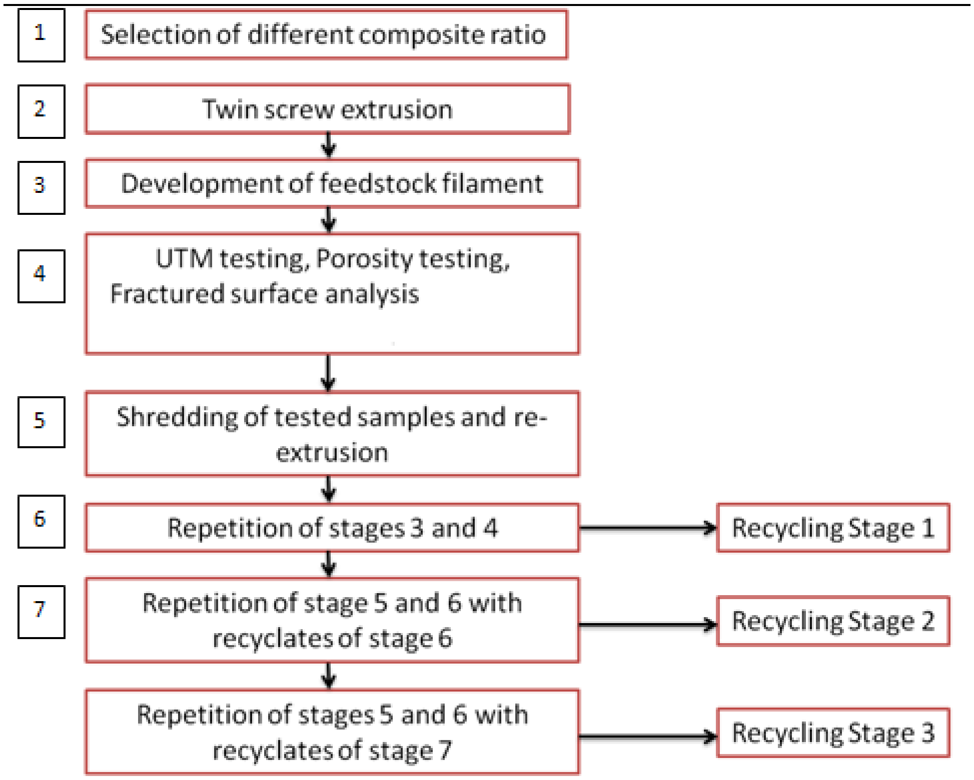

Figure 4.13 methodology for recycling of selected composite ratio at stage 1 and 2

4.5.1 Composite preparation

The selected composites of PLA (hybrid and multi-material matrix selected at stage 1 and 2) were prepared using the method of mechanical mixing in which polymeric grains of PLA were bonded to wood, Fe_3O_4 powder, and PVC grains using coconut oil as a binder and constant stirring the mixture in a preparing bowl for 5-10 min. The prepared composite was then placed in a preheated oven at 45°C for half an hour and then it was used for further experimentation. All the reinforcements (PVC, wood powder (50µm size), and Fe_3O_4 powder (44µm) size) used in the composite matrix of PLA were mixed using the method of weight percentage. The trial experimentation performed previously made it clear that approximately 50g of sample was enough to develop feedstock of required length and recyclates for another re-extrusion cycle. Figure 4.14 (a-e) shows the polymeric matrix of PLA, composite matrix of PLA/wood, composite matrix of PLA/PVC, composite matrix of PLA/Fe_3O_4, and composite matrix of a hybrid blend of PLA/PVC/wood/Fe_3O_4 powder.

Figure 4.14 Polymeric matrix of (a) PLA, (b) PLA/wood, (c) PLA/PVC, (d) PLA/Fe_3O_4, (e) hybrid blend of PLA/PVC/wood/Fe_3O_4 powder

4.5.2 Multi (Three) stage recycling and mechanical testing of feedstock filaments and differential scanning calorimetry (DSC)

In this study multi (three) stages of recycling were performed to know the strength of recycled material at each stage for possible 3D printing applications. The feedstock filaments were fabricated by using the prepared material matrix and the material matrix was re-extruded to get the recyclates which were further shredded and reprocessed as raw material for the second time recycling to prepare feedstock filaments of that recycled material. The process was repeated three times and feedstock filaments of diameter Φ1.75±0.05mm were prepared successfully (for each stage). The prepared samples were tested for their mechanical properties using a universal tensile testing setup (UTM) (Make: Shanta Engineering, Pune, India, Capacity: 5000N). Relative strength change was calculated using equation 1 for each stage of recycling. Figures 4.15 and 4.16 show the twin-screw extrusion of recycled pellets and the UTM testing setup in use, respectively. The prepared composite of feedstock filament of PLA, PLA R1, PLA R2, and PLA R3 was analyzed for the thermal properties using a DSC machine for two stages of heating and cooling.

Relative strength change

$$= \frac{\sigma 1(virgin) - \sigma 2(stress\ of\ feedstock\ of\ that\ satge)}{\sigma 1} \ldots\ldots.(1)$$

4.5.3 Porosity testing and fractured surface analysis

The fractured samples were investigated for porosity holes under the metallurgical image analysis software (MIAS) package tool at ×100 magnification using testing standards ASTM B276. The porosity holes were tested as the internal structures of composites have a vital role to play towards their mechanical strength. The destructed samples were also investigated under Toolmaker's microscope so that the fractured surface may be analyzed for the type of failure in UTM testing.

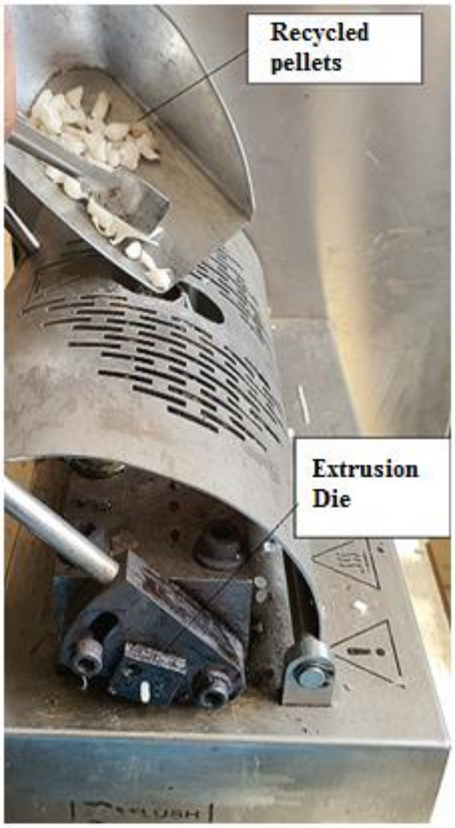

Figure 4.15 Twin-screw extrusion setup

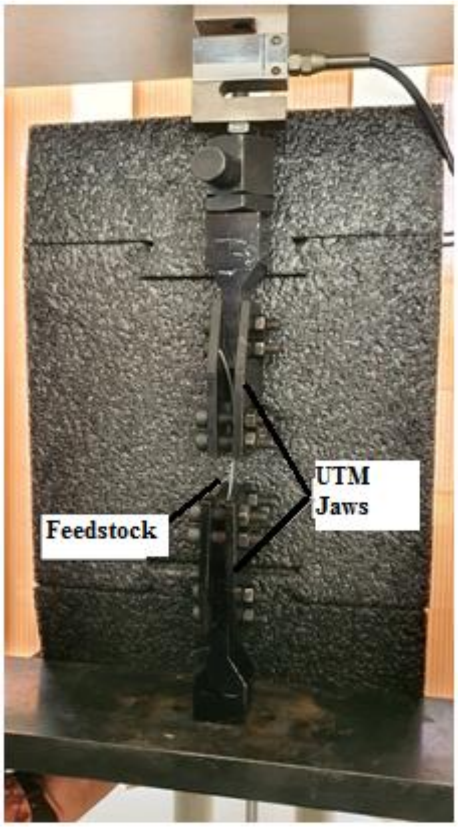

Figure 4.16 UTM testing setup for feedstock filaments

CHAPTER 5

RESULTS AND DISCUSSION

5.1 Results and discussion for stage 1

5.1.1 UTM results

Based upon the experimental details given in Table 4.3, samples were prepared on TSE and tested using UTM setup and mechanical properties were recorded (Table 5.1). It has been observed that sample 6 with of 5 kg, torque 0.15 Nm, screw temperature 170°C for composition 2 has provided the best results whereas a slight difference has been observed in mechanical properties for sample 10th. Therefore, an analysis of variance (ANOVA) statistical tool has been applied to the results to optimize the condition for best TSE conditions. Based on Table 5.1, signal to noise (SN) ratios for all properties were calculated (see Table 5.2) by using equation 2.

$$\eta = -10 \log\left[\frac{1}{n}\sum_{k=1}^{n}\frac{1}{y^2}\right] \ldots\ldots\ldots\ldots\ldots\ldots\ldots\ldots\ldots\ldots\ldots\ldots \quad (2)$$

Where η is the SN ratio, n is the number of the experiment, and y is the material properties at experiment number k. Based upon Table 5.2, for peak load, the main effect plot is shown in Figure 5.1. Table 5.3 shows the ANOVA for SN ratio of peak load based on Table 5.2. As observed from Table 5.3, temperature contributes is 83.94% towards the best condition for load at peak. The p-value for the temperature and load was less than 0.05 which means that these are significant parameters at a 95% confidence level. Further, Table 5.4 shows the ranking of input parameters for output as peak load. As observed from Figure 5.1, a load of 5kg, composition at level 2, the torque of 0.12 Nm, and 170°C screw temperature are the optimized conditions for TSE. This may be because when a load of 5kg was applied to push/feed the composite material into the screws of TSE, it resulted in better dispersion of reinforcements in the PLA matrix. On increasing the load, the slippage of feedstock material was observed. The composition at level 2 has shown better results which were observed due to the high percentage of PLA which ensures better flowability of the material. It was observed that the torque of 0.12 Nm resulted in screw rotations around 50-55rpm whereas torque at 0.10 Nm resulted in in25-30rpm and torque at 0.15Nm resulted in 70-75rpm. It has been observed that better dispersion was achieved with screw rpm at 50-55. Finally, the processing temperature of 170°C was found to be the best condition as PLA has melting point around 150°C but for the bulk being processed continuously, high temperature may have resulted in better thermal diffusion thus resulting in better mechanical properties. The optimized conditions for peak load were found to be inside the selected design of experimentation. Further, the modulus of toughness which is an important property was calculated by using equation 3 as given below

$$\text{Modulus of toughness} = \frac{1}{2} \times \text{stress} \times \text{strain} \ldots\ldots (3)$$

It has been observed that maximum modulus of toughness was obtained for samples 3 and 16 whereas sample 6 also possesses comparable modulus of toughness and thus a suitable candidate for applications in crash testing whereas sample 17 held a low modulus of toughness.

Table 5.1 Observations for mechanical properties of hybrid blend

Serial number	PL (N)	PE (mm)	BL (N)	BE (mm)	PS (MPa)	BS (MPa)	%PE	%BE	Shore D hardness	Modulus of toughness (MPa)
1	23.5	2.1	21.5	4.2	11.69	9.76	3.12	5.92	61.5	0.41
2	35.3	3.01	33.5	2.92	15.56	13.52	4.15	3.95	62.5	0.39
3	38	4.4	36	4.7	18.23	16.42	4.99	6.85	64	0.77
4	26.4	2.15	24.5	4.23	10.98	8.24	3.2	5.8	60	0.35
5	35.3	3.21	33.2	2.76	15.56	13.56	4.25	3.82	61.9	0.37
6	39.4	4.21	37.6	4.65	17.82	15.82	5.24	7.01	65.2	0.74
7	32.8	2.9	29.9	2.8	14.62	12.56	4.18	3.62	62	0.35
8	38.4	4.3	36.2	4.74	15.84	13.81	5.4	7.23	66.4	0.65
9	27.9	2.04	25.5	4.12	11.23	9.23	3.4	5.85	59	0.38
10	39.2	4.37	36.8	4.68	17.68	15.7	5.6	7.26	65.8	0.73
11	23.5	2.12	20.9	4.06	12.1	10.32	3.48	5.92	59.5	0.42
12	26.9	3.23	24.5	2.95	14.8	12.8	4.72	3.78	61.5	0.38
13	27.4	2.95	25.4	2.84	14.35	12.41	4.81	3.69	62.5	0.35
14	37.6	4.05	35.6	4.92	17.48	15.56	5.98	7.4	64.5	0.77
15	24.2	2.1	22.1	4.13	11.56	9.11	3.62	5.91	58.5	0.38
16	38.5	3.95	36.2	4.86	17.52	15.62	5.76	7.58	65.5	0.76
17	3.4	1.92	20.98	4.12	11.12	8.91	3.21	5.43	58.5	0.37
18	27.9	2.98	25.9	2.78	14.58	12.58	4.48	3.85	61.5	0.35

PL: peak load; PE: peak elongation; BL: break load; BE: break elongation; %PE: percentage peak elongation; %BE: Percentages break elongation

Table 5.2 SN ratios for mechanical properties for hybrid blend

Serial number	PL (N)	PE (mm)	BL (N)	BE (mm)	PS (MPa)	BS (MPa)	%PE	%BE	Shore D Hardness
1	27.42	6.44	26.65	12.46	21.36	19.79	9.88	15.45	35.78
2	30.96	9.57	30.50	9.31	23.84	22.62	12.36	11.93	35.92
3	31.60	12.87	31.13	13.44	25.22	24.31	13.96	16.71	36.12
4	28.43	6.65	27.78	12.53	20.81	18.32	10.10	15.27	35.56
5	30.96	10.13	30.42	8.82	23.84	22.65	12.57	11.64	35.83
6	31.91	12.49	31.50	13.35	25.02	23.98	14.39	16.91	36.28
7	30.32	9.25	29.51	8.94	23.30	21.98	12.42	11.17	35.85
8	31.69	12.67	31.17	13.52	24.00	22.80	14.65	17.18	36.44
9	28.91	6.19	28.13	12.30	21.01	19.30	10.63	15.34	35.42
10	31.87	12.81	31.32	13.40	24.95	23.92	14.96	17.22	36.36
11	27.42	6.53	26.40	12.17	21.66	20.27	10.83	15.45	35.49
12	28.60	10.18	27.78	9.40	23.41	22.14	13.48	11.55	35.78
13	28.76	9.40	28.10	9.07	23.14	21.88	13.64	11.34	35.92
14	31.50	12.15	31.03	13.84	24.85	23.84	15.53	17.38	36.19
15	27.68	6.44	26.89	12.32	21.26	19.19	11.17	15.43	35.34
16	31.71	11.93	31.17	13.73	24.87	23.87	15.21	17.59	36.32
17	27.38	5.67	26.44	12.30	20.92	19.00	10.13	14.70	35.34
18	28.91	9.48	28.27	8.88	23.28	21.99	13.03	11.71	35.78

PL: peak load; PE: peak elongation; BL: break load; BE: break elongation; %PE: percentage peak elongation; %BE: Percentages break elongation

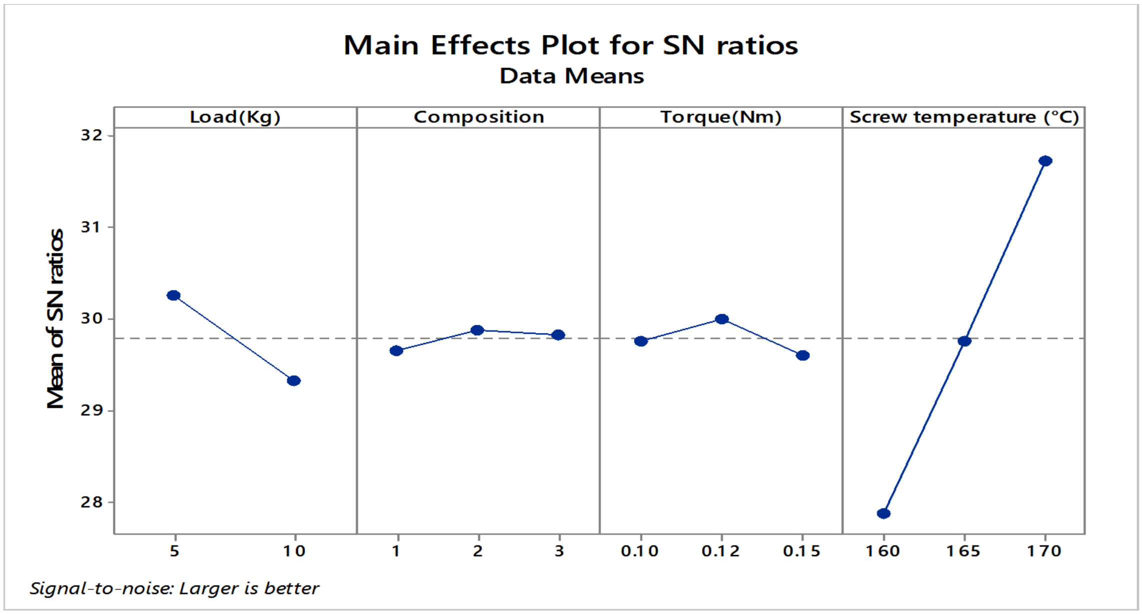

Figure 5.1 SN ratio graph for peak load with Larger is better condition for hybrid blend based matrix

Table 5.3 ANOVA table for SN ratio of Peak Load for the hybrid blend

Source	DF	Seq SS	Adj SS	Adj MS	F	P	% contribution
Load	1	3.8859	3.8859	3.8859	9.86	0.011	7.3829
composition	2	0.1741	0.1741	0.0871	0.22	0.806	0.3307
Torque	2	0.4502	0.4502	0.2251	0.57	0.582	0.8553
Temperature	2	44.1811	44.1811	22.0906	56.03	0.000	83.9407
Residual Error	10	3.9423	3.9423	0.3942			
Total	17	52.6337					

Note: Deg. of freedom is denoted by DF; Sum of the square is given by Seq SS; the adjacent sum of the square is shown by Adj SS; Fishers value as F; Probability is denoted by P.

Table 5.4 Ranking of input parameters for hybrid blend

Level	Load	composition	Torque	Temperature
1	30.24	29.64	29.75	27.87
2	29.31	29.87	29.98	29.75
3		29.82	29.60	31.71
Delta	0.93	0.23	0.38	3.84

Rank	2	4	3	1

5.1.2 Optimization of Peak load for TSE

Further, based on Table 5.4 and 5.5, the peak load property was optimized for the prediction of theoretical value based on ANOVA analysis. Optimized value was calculated using equation 4 and predicted value for peak load was calculated using equation 5.

$$\boldsymbol{m} = \text{ mean of SN values for peak load analysis } = \ 29.78 \text{ (from Table 5.2)}$$

$$\mathrm{m_A} = \text{ maximum value of peak load } 30.24\text{(from Table 5.4)}$$

$$\mathrm{m_B} = \text{maximum value for composition } 29.87\text{(from Table 5.4)}$$

$$\mathrm{m_C} = \text{ maximum value for torque } 29.98\text{(from Table 5.4)}$$

$$\mathrm{m_D} = \text{ maximum value for temperature } 31.71 \text{ (from Table 5.4)}$$

$$\text{Ŋ opt} = \ \mathrm{m} \ + \ (\mathrm{m_A} - \mathrm{m}) + \ (\mathrm{m_B} - \mathrm{m}) + \ (\mathrm{m_C} - \mathrm{m}) + \ (\mathrm{m_D} - \mathrm{m}) \dots \dots (4)$$

$$\text{Ŋ opt} = 29.78 \ + \ (30.24 - 29.78) \ + \ (29.87 - 29.78) \ + \ (29.98 - 29.78) \ + \ (31.71 - 29.78)$$

$$\text{Ŋ opt} = 32.46 \text{ dB}$$

$$\mathrm{Y_{opt}^2} = 10^{\frac{\text{Ŋ (opt)}}{10}} \quad \dots \dots \dots . (5)$$

$$\mathrm{Y_{opt}^2} = 10^{\frac{(32.46)}{10}}$$

$$\mathrm{Y_{opt}} = 41.97\mathrm{N}$$

The predicted value for the peak load is 41.97 N. The actual observed value was near the predicted value thus making the selected model significant. Similar observations were made for other mechanical properties (Table 5.5).

Table 5.5 Optimized and predicted results for mechanical properties for the hybrid blend

Properties	Ŋ$_{(opt)}$ (dB)	Predicted (Y$_{(opt)}$)	Observed values
Peak Load(N)	32.46	41.97	39.68

Peak Elongation (mm)	12.93	4.43	4.82
Break load(N)	32.12	40.36	38.95
Break Elongation (mm)	13.649	4.8133	4.34
Strength at peak (MPa)	25.12	18.03	17.25
Strength at break (MPa)	24.31	16.43	16.53
Percentage elongation at peak	15.41	5.895	6.20
Percentage elongation at break	17.3	7.32	8.65
Shore D hardness	36.47	66.60	65.80

5.1.3 Combined optimization of mechanical properties

Further, based on Table 5.2, all output properties were analyzed collectively and overall parametric results were obtained for the best and worst conditions of TSE. Combined optimization was performed by maximizing SN values for different mechanical properties by using MiniTab 18 software package tool. Figure 5.2 shows the SN graph for combined optimization which suggested that 10Kg of load, the composition of 1st level, the torque of 0.15Nm, and screw temperature of 3rd level were the optimized conditions. It has been observed that experiment number 10 is the best condition and experiment number 17 gives the poor conditions (Table 4.3) regarding the mechanical properties. Tables 5.6 and 5.7 show the ANOVA table and the rank table based on the combined SN ratios (for maximum the better type case). Further, it was noticed that load and torque had insignificant contributions toward output properties whereas maximum (>98%) contribution was observed from screw temperature (table 5.6). It may be concluded that screw temperature was the only significant parameter among the selected input variables for TSE.

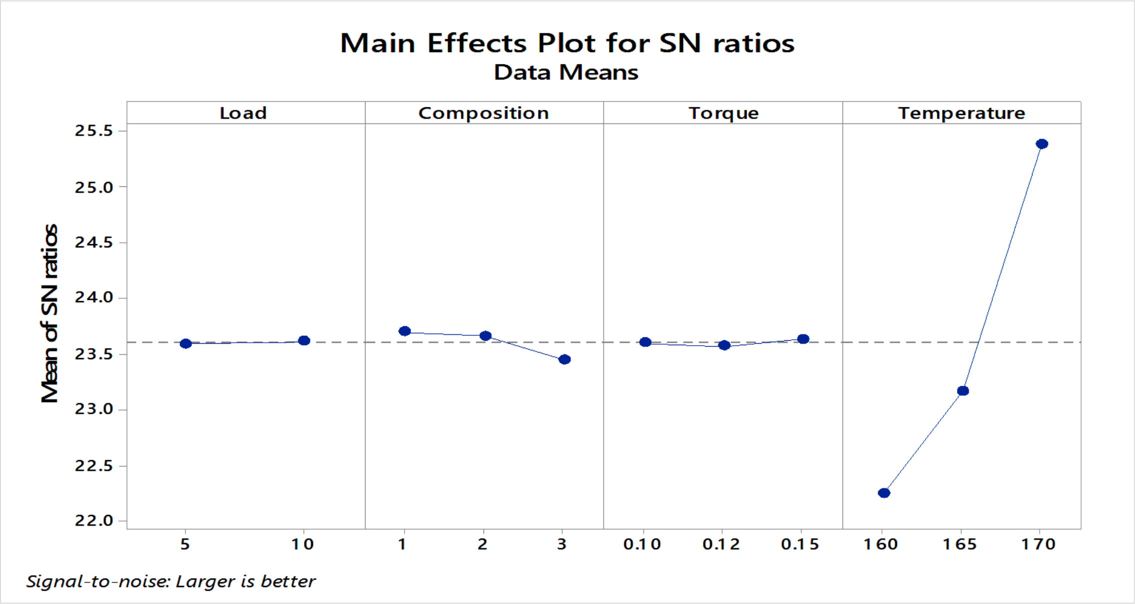

Figure 5.2 SN graph for combined values of mechanical properties for hybrid blend-based matrix

Table 5.6 ANOVA for SN ratios for combined optimization for the hybrid blend

Source	DF	Seq SS	Adj SS	Adj MS	F	P	Percentage contribution
Load	1	0.0923	0.0923	0.0923	1.93	0.195	0.245
Composition	2	0.1006	0.1006	0.0503	1.05	0.384	0.267
Torque	2	0.0284	0.0284	0.0142	0.30	0.749	0.075
Temperature	2	36.8998	36.8998	18.4499	386.27	0.000	98.14
Residual Error	10	0.4776	0.4776	0.0478			
Total	17	37.5989					

Table 5.7 Ranking of input parameters for combined optimization for hybrid blend

Level	Load	Composition	Torque	Temperature
1	23.59	23.70	23.60	22.25
2	23.61	23.66	23.57	23.17
3		23.45	23.64	25.39
Delta	0.02	0.24	0.06	3.13

Rank	4	2	3	1

5.1.4 Surface properties characterization

From mechanical properties optimization viewpoint, it was observed that sample 10 was found the best whereas sample 17 was the worst among all. To further give conclusive evidence for such behavior, a surface characterization study has been performed by using a Shore D hardness tester, metallurgical image analyzer, and tool maker’s microscope.

5.1.5 Shore D hardness

The prepared samples with experimental conditions of 10th and 17th samples were subjected to shore D hardness testing and it has been observed that sample 10 had a hardness of 65.8 shore D, whereas sample 17 had 58.5 shore D surface hardness. Figure 5.3 shows a comparison of Shore D hardness for two samples which justifies that better processing conditions have resulted in better surface hardness of prepared feedstock filaments whereas sample 6 had comparable surface hardness as observed from Table 5.1. This may be since the screw temperature which was observed as the most significant parameter for the current investigation was higher for experimental run 10 than that of 17. This resulted in better diffusion of particles and well-diffused particles were joined better thus resulting in better mechanical properties.

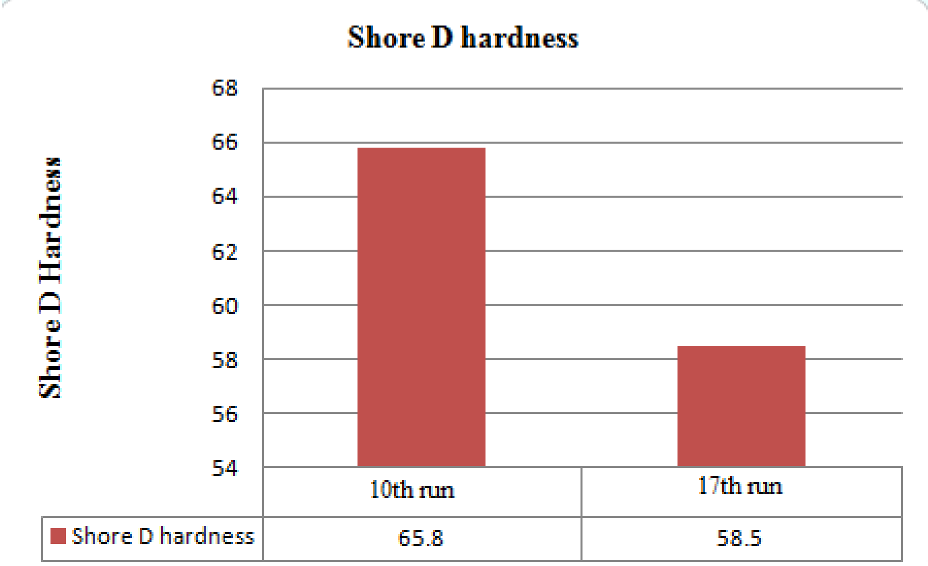

Figure 5.3 Shore D hardness results for 10th and 17 samples as per Table 4.3

5.1.6 Porosity analysis and surface roughness evaluation

The 18 different feedstock filaments were subjected to porosity analysis using metallurgical image analyzer software (MIAS). Figure 5.4 shows the photomicrographs taken at ×100 for all samples which shows that higher porosity in a sample leads to low hardness and poor mechanical properties. As indicated by the porosity results of sample 10 and sample 17, it clearly shows that the high porosity of sample 17 resulted in poor mechanical properties as indicated by Table 5.1. The percentage porosity of sample 10 is 7.18 whereas s the percentage porosity of sample 17 is 20.41. Figure 5.5 provides the comparative porosity data at the surface of all 18 samples which indicates the porosity for each sample. It has been observed that porosity was different for each sample due to different input processing conditions. For a better understanding of the relation between mechanical and morphological properties, the cross-sections of fractured samples on UTM were tested under the tool maker's microscope on ×30 magnification (Figure 5.6). It has been observed that more voids were present for the sample with high porosity which resulted in the poor mechanical performance of prepared samples. Samples 10 and 6 have fewer voids in comparison to sample 17 which justifies their better suitability from the mechanical and morphological viewpoint. Further, the porosity images for samples 10 and 17 were subjected to an image processing software tool for measurement of R_a value and it has been observed that the R_a value for sample 10 was low in comparison to sample 17. This may be due to better dispersion of reinforcement (as observed from 3D rendered image) in PLA matrix resulting in low R_a value and better mechanical properties (Figure 5.7).

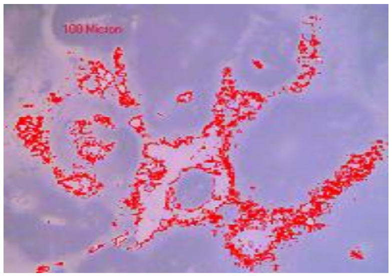

Sample 1
Percentage porosity 9.73

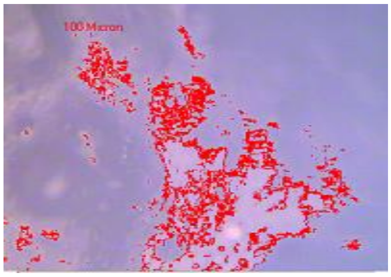

Sample 2
Percentage porosity 10.03

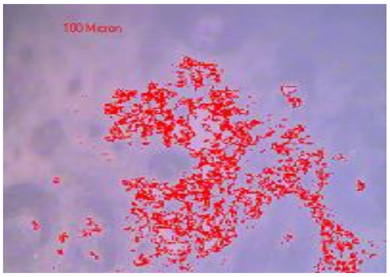

Sample 3
Percentage porosity 11.29

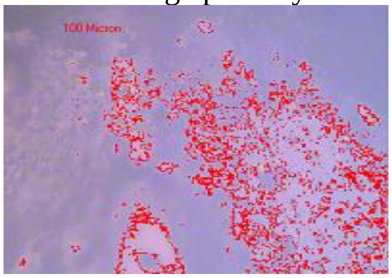

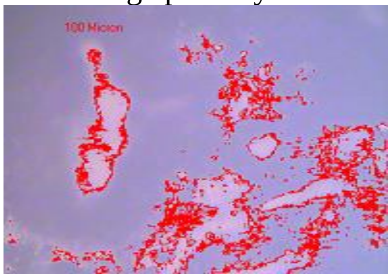

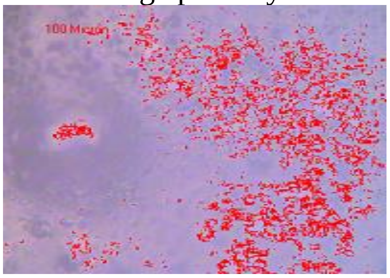

Sample 4
Percentage porosity 9.25

Sample 5
Percentage porosity 11.22

Sample 6
Percentage porosity 10.33

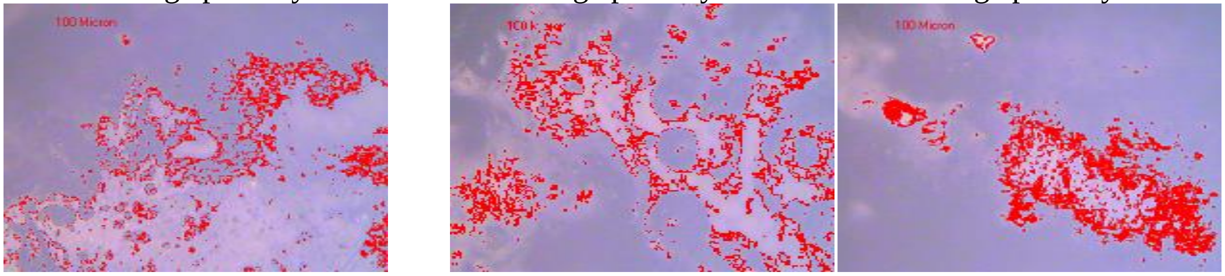

Sample 7
Percentage porosity 8.79

Sample 8
Percentage porosity 12.6

Sample 9
Percentage porosity 11.04

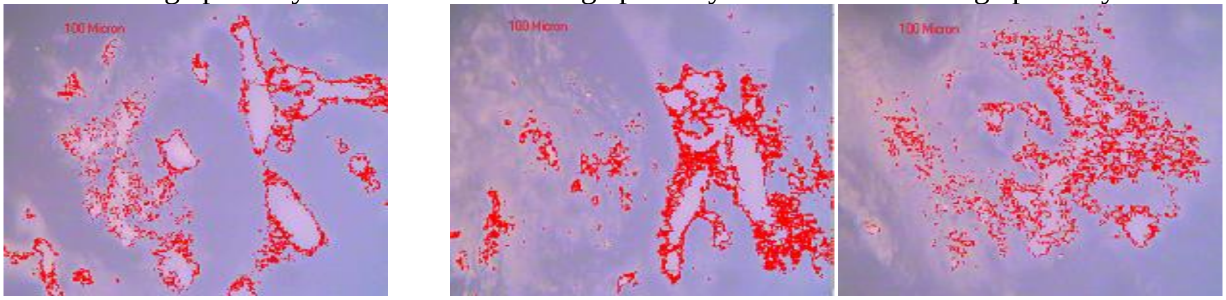

Sample 10
Percentage porosity 7.18

Sample 11
Percentage porosity 10.79

Sample 12
Percentage porosity 8.21

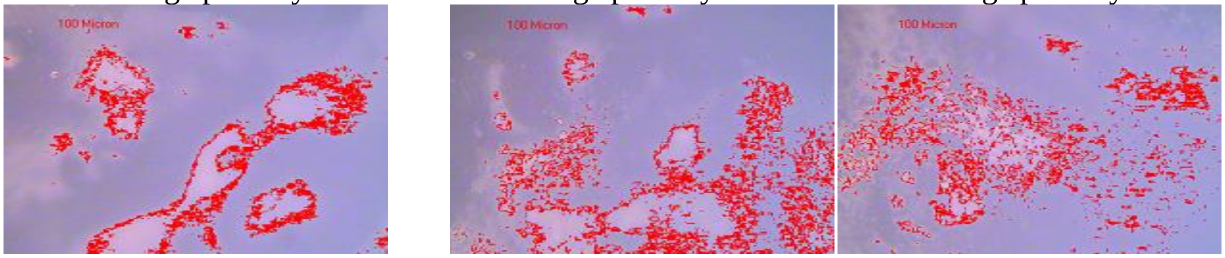

Sample 13
Percentage porosity 9.2

Sample 14
Percentage porosity 14.55

Sample 15
Percentage porosity 10.38

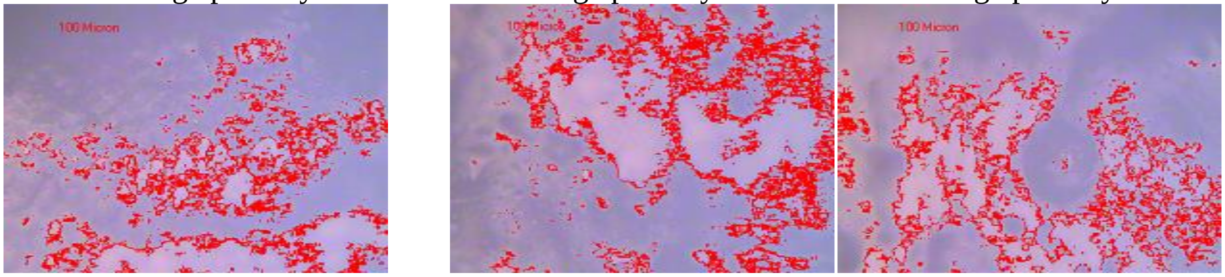

Sample 16
Percentage porosity 14.22

Sample 17
Percentage porosity 20.41

Sample 18
Percentage porosity 14.43

Figure 5.4 Porosity results of 18 samples extruded via TSE using MIAS as per Table 4.3

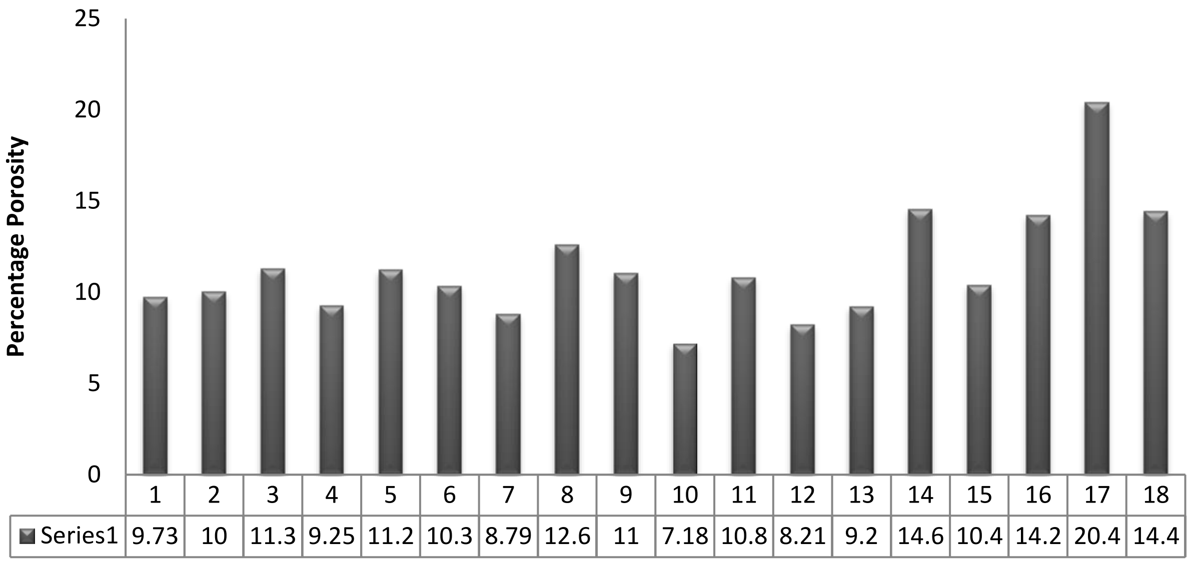

Figure 5.5 Percentage porosity results by MIAS as per Table 4.3

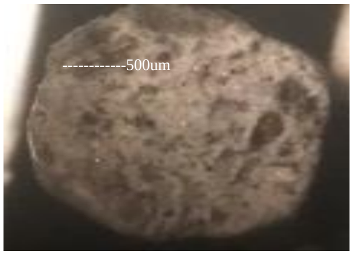

Sample 1

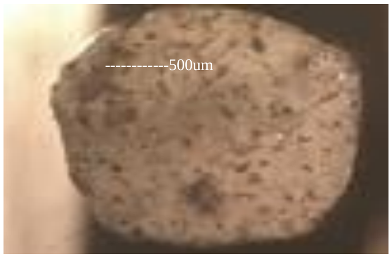

Sample 2

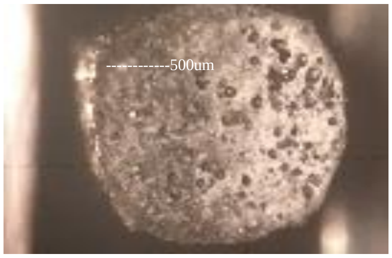

Sample 3

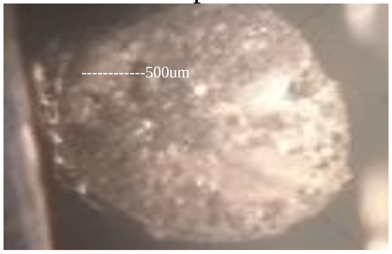

Sample 4

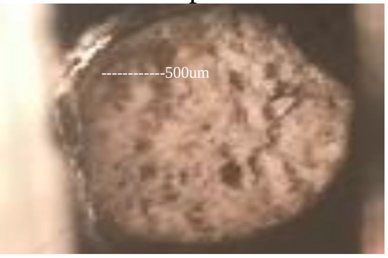

Sample 5

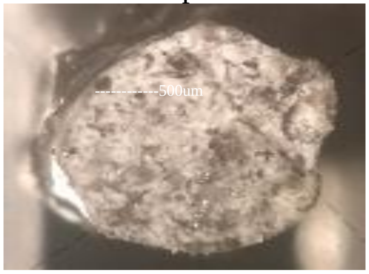

Sample 6

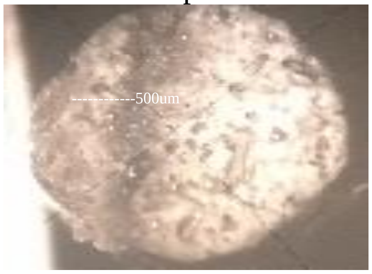

Sample 7

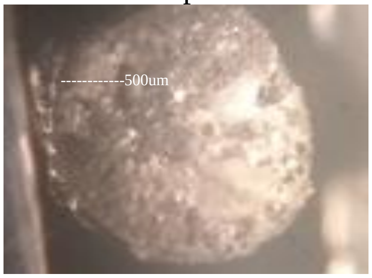

Sample 8

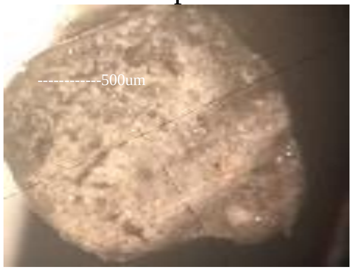

Sample 9

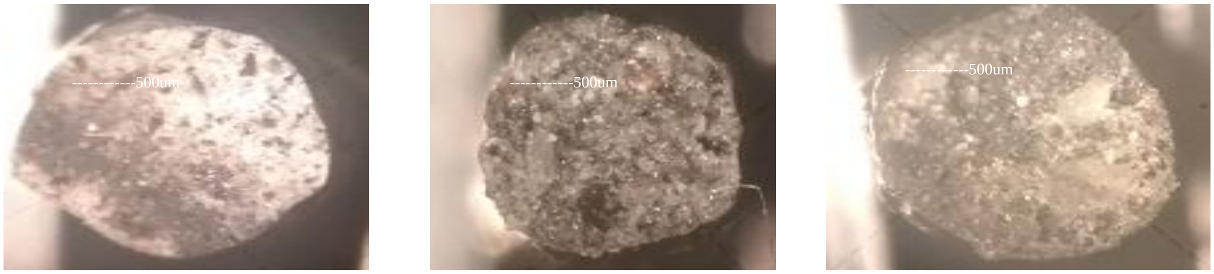

Sample 10 Sample 11 Sample 12

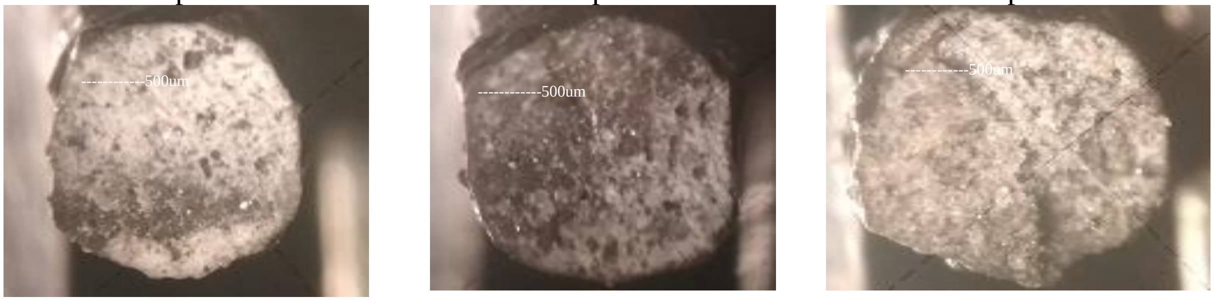

Sample 13 Sample 14 Sample 15

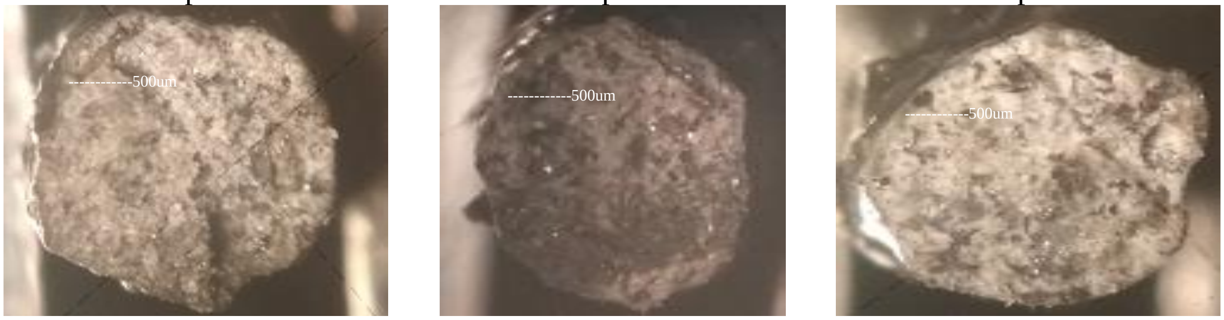

Sample 16 Sample 17 Sample 18

Figure 5.6 Microscopic view of wire surface as per Table 4.3

Sample No.	3D rendered image	Surface roughness profile
10	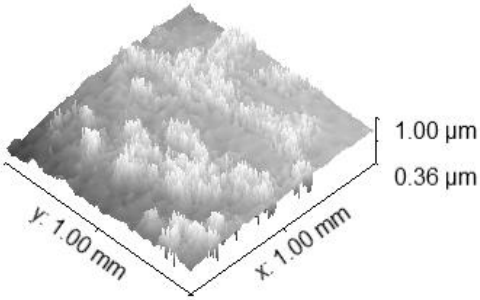	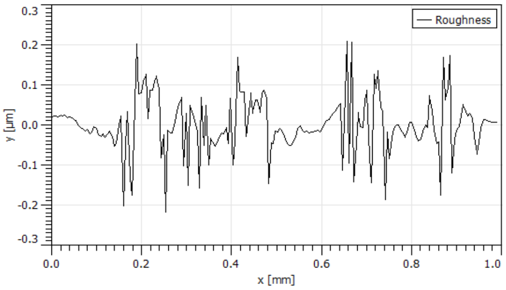 Ra: 49.25nm at cut off length 0.04mm

17

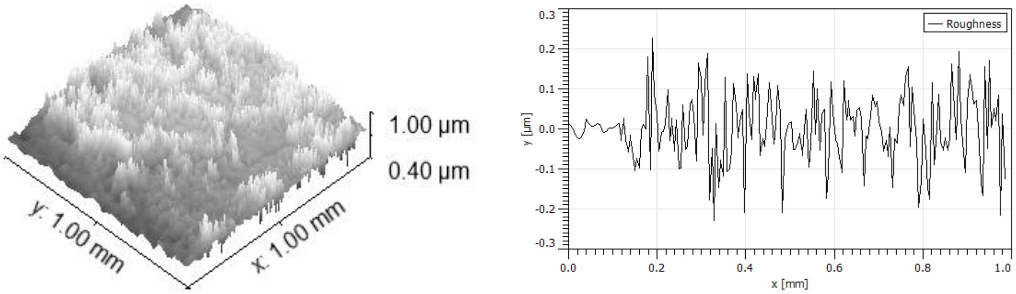

Ra: 64.10nm at cut off length 0.04mm

Figure 5.7 Surface roughness for 10th and 17th experiment as per Table 4.3

5.1.7 DSC analysis

Thermal analysis for best and worst samples as per mechanical properties was performed using DSC setup (Model: Mettler, Toledo) for 3 heating and 3 cooling cycles varying from room temperature(25ºC) to 200°C of a heating cycle, 200 °C to room temperature of the cooling cycle. The evaluation was performed under controlled experimental conditions of continuous heating (endothermic changes, 5ºC/min) in the 25-200ºC range through three consecutive cycles at 50ml/min of N_2 gas supply.

The DSC trend has shown that experiment noumber10 has better thermal stability because from 2nd heating cycle the intake energy gets stabilized as it takes 4.34J/g (2nd heating cycle) to 4.28J/g (3rd heating cycle) but sample 17 shows that the intake heat capacity reduces drastically from 12.85J/g (2nd heating cycle) to 1.08J/g (3rd heating cycle). Thus, it may be concluded that the thermal stability of sample 17 in comparison to sample 10 is poor and that validates the poor mechanical performance for sample 17.

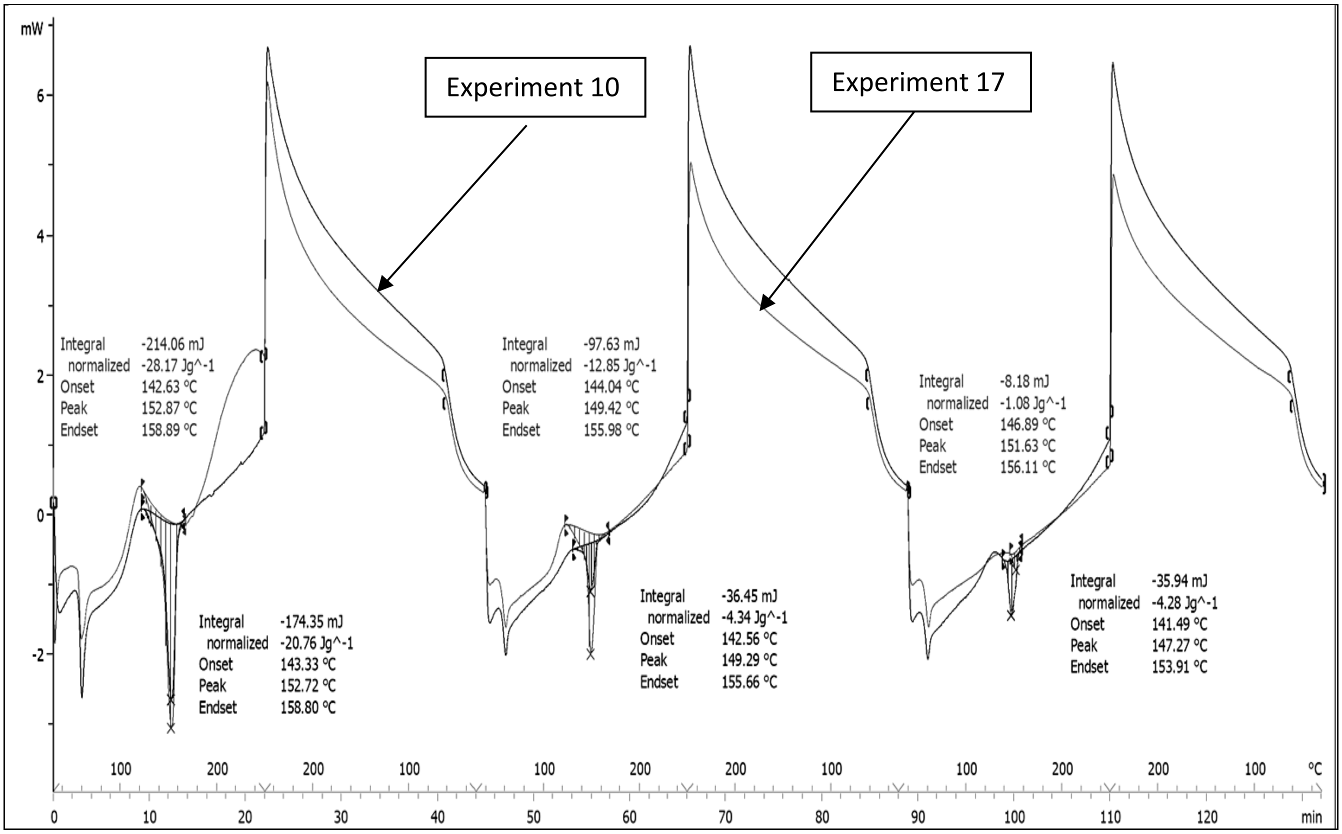

Figure 5.8 DSC analysis of experiment 10 (best) and experiment 17 (worst) as per Table 4.3

5.1.8 Vibration sample magnetometer (VSM) testing

Three compositions of PLA reinforced with PVC, wood dust, and Fe_3O_4 were used for the extrusion process (Table 4.1). To confirm that whether the sample holds any magnetic property so that it can behave as 4D filament, VSM testing was performed (Make: Lakeshore 7404 VSM machine). Table 5.8 shows the result of VSM which was analyzed for a further selection of the best sample. Based upon Table 5.8 and Figure 5.9, it has been observed that magnetization was highest for composition 1 (24.26 emu/gm) which was, therefore, the best candidate for selection of the composite from a magnetic property viewpoint. In the present investigation, the mechanical properties were also found better for composition 1. This may be because less quantity of wood dust in the composite may have poor hindrance for magnetic properties in comparison to compositions 2 and 3.

Table 5.8 VSM results for different magnetic properties for a hybrid blend

S. No.	Composition	Magnetic properties		
		Magnetization ‘m’ emu/g	Coercivity ‘H’ oersted (emu/g)	Retentivity/ Remanence ‘M_r’ Gauss
1	Composition1	24.26	72.36	8.88×10^{-03}
2	Composition2	19.52	74.97	1.12×10^{-02}
3	Composition3	14.48	76.88	7.93×10^{-03}

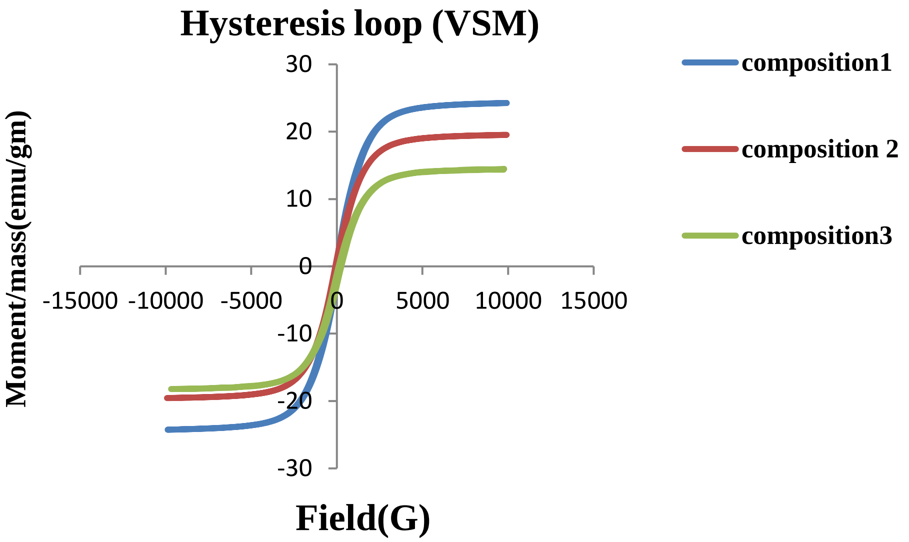

Figure 5.9 Hysteresis loop for VSM tested samples as per Table 4.1

5.1.9 Parametric optimization for magnetic properties of hybrid feedstock filament

Table 5.9 provides results of magnetic properties which were obtained from VSM testing (as per DOE given in Table 4.3). Magnetization, coercivity, and retentivity were important properties for any magnetic sample. Therefore, only these properties were used for the optimization of twin-screw extrusion conditions. Figure 5.10 shows the hysteresis loop for the best and the worst sample, which is sample 2 and 8, respectively (Table 5.9). This clearly shows that the samples obtained by extrusion behave as magnetic material but low retentivity values were obtained which clearly showed that the samples were super-paramagnetic. As observed from Figure 5.10, sample 2 possesses the maximum value of magnetization (0.2283emu) and sample 8 the least (0.1524emu). All the samples which were tested for VSM had 0.00785gm of weight so for standard units for the moment (emu/g); magnetization can be divided with a unit weight of the sample. On performing calculation of moment (emu/g), it was observed that the maximum value of moment was obtained for sample 2 which is 28.66emu/g and the lowest magnetization was for sample 8 which was 19.40emu/gm. It has been observed that there was a 31.35% decrease in magnetization for the 8th extrusion condition.

From Table 5.9, it may be interpreted that 20-weight percent loading of magnetite powder has given maximum magnetization and 17.5 weight percentage magnetite powder reinforcement has given least magnetic property. It has been seen that loading of 25 weight percentage was ineffective in comparison to loading of 20 weight percent. This may be attributed to the reason that the composition 1 (PLA 50%, PVC 25 weight percentage, $Fe_3O_4$20 weight percentage, and wood powder 5 weight percentage) was reinforced with the least amount of wood powder which affects the distribution of composite matrix whereas in composition 2 in which Fe_3O_4 (25 weight percentage) was greater than composition 1 but the reinforcement of wood powder in composition 2 was 7.5 weight percentage than composition 1 (5 weight percentage). Therefore, it has shown a low magnetization value. Table 10 shows the SN table for all the magnetic properties.

Table 5.9 Magnetic properties value table for hybrid blend

Serial number	**Magnetization (emu)**	**Coercivity (Oersted (emu/g))**	**Retentivity (M_r)(Gauss)**
1	0.1837	72.3690	8.88E-03
2	0.2283	75.2536	1.72E-02
3	0.1712	73.1253	8.52E-03
4	0.1925	72.2451	8.46E-03
5	0.2156	76.1253	1.12E-02
6	0.1763	74.3168	8.60E-03
7	0.1847	75.7864	1.23E-02
8	0.1524	73.6953	7.93E-03
9	0.1678	71.9986	9.15E-03
10	0.1625	73.5641	8.20E-03
11	0.1856	72.1542	9.23E-03
12	0.2008	76.1049	2.11E-02
13	0.1925	75.6894	1.67E-02

14	0.1754	73.5641	6.99E-03
15	0.1824	71.9653	7.95E-03
16	0.1584	73.9865	6.85E-03
17	0.1697	71.9748	7.56E-03
18	0.1756	75.2563	1.45E-02

Table 5.10 SN ratio table for magnetic properties for hybrid blend

Serial number	Magnetization (emu)	Coercivity (Oersted (emu/g))	Retentivity (M_r)(Gauss)
1	-14.718	37.19	-41.032
2	-12.83	37.53	-35.289
3	-15.33	37.28	-41.391
4	-14.311	37.18	-41.453
5	-13.327	37.63	-39.016
6	-15.075	37.42	-41.31
7	-14.671	37.59	-38.202
8	-16.34	37.35	-42.015
9	-15.504	37.15	-40.772
10	-15.783	37.33	-41.724
11	-14.628	37.17	-40.696
12	-13.945	37.63	-33.514
13	-14.311	37.58	-35.546
14	-15.119	37.33	-43.11
15	-14.78	37.14	-41.993
16	-16.005	37.38	-43.286

17	-15.406	37.14	-42.43
18	-15.11	37.53	-36.773

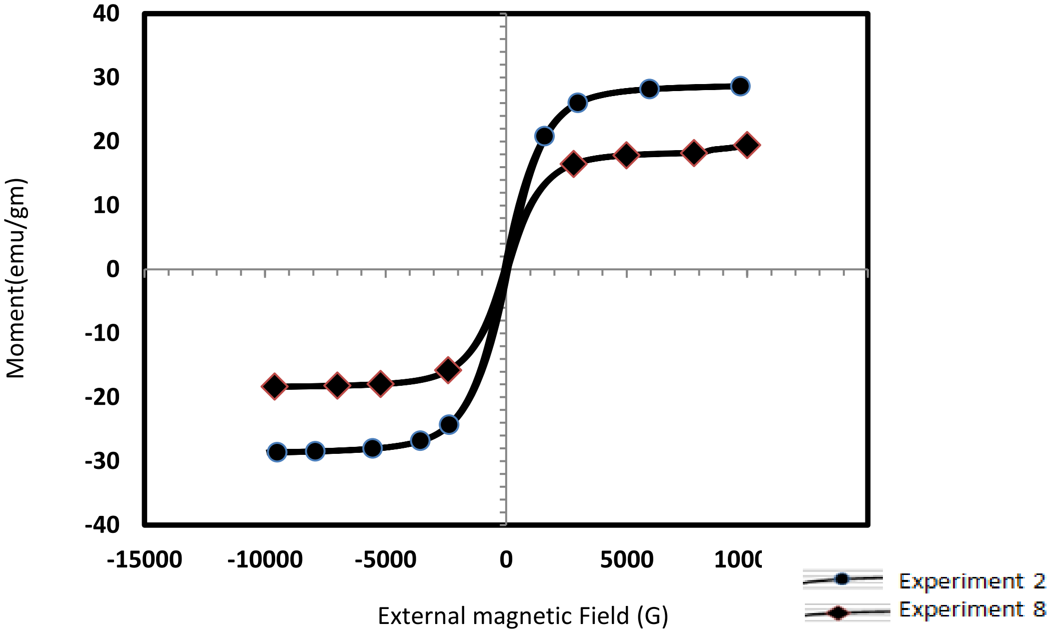

Figure 5.10 Hysteresis loop for experiment 2 and 8 as per Table 4.3

Based on Tables 5.9 and 5.10, all the properties were optimized using Minitab 18.1 software package. Basic ANOVA was used for optimization. Table 5.11 provides the analysis of variance for SN ratios for magnetization property and it clearly shows that the p-value for composition and screw temperature is less than 0.05 which means these parameters are significant for extrusion from a magnetic property viewpoint. It has been also found that screw temperature contributes maximum towards the magnetization property which is 55.39% and composition also contributes significantly with 29.35%. Table 5.12 shows the response table which is useful in finding the rank of the input parameters for the output. From this rank Table 5.12, it was observed that screw temperature which gives maximum contribution towards extrusion is given the first rank. Figure 5.11 shows the main effect plot for magnetization which indicates that for magnetization screw temperature of 165°C, the torque of 0.12Nm, 2nd composition, and the load of 5Kg play an important role for larger is the better case. Figure 5.12 shows the matrix plot of all the input parameters with the output results. It can be seen from Figure 5.12 when the load is 5Kg, magnetization was higher. Composition 1 has provided maximum magnetization of 0.2283 as can be seen from Table 5.9 that screw temperature of 165°C gives maximum magnetization value. Figure 5.13 shows the residual plots for the SN ratio which show that our output results are independent as they do not follow any trend in the residual vs. order graph. Similarly, in the normal probability plot, the values are very near the line thus our data follows normal properties. Similarly, the residual vs. fit graph clearly shows that most of the values are near the centerline. Only some values distract from the center which shows that our data is homogeneous and very less scattered.

Table 5.11 ANOVA for SN ratios for magnetization for hybrid blend

Source	DF	Seq SS	Adj SS	Adj MS	F	P	percentage contribution
Load	1	0.4943	0.4943	0.4943	4.63	0.057	3.67
Composition	2	3.9604	3.9604	1.9802	18.54	0.000	29.35
Torque	2	0.4970	0.4970	0.2485	2.33	0.148	3.68
Screw Temperature	2	7.4752	7.4752	3.7376	35.00	0.000	55.39
Residual Error	10	1.0680	1.0680	0.1068			
Total	17	13.4949					

DF: degree of freedom, Seq SS: sum of squares, Adj SS: adjusted sum of square, F: fisher value, P: probability

Table 5.12 Response Table for Signal to Noise Ratio for magnetization

Level	Load	Composition	Torque	Screw Temperature
1	-14.68	-14.54	-14.97	-14.89
2	-15.01	-14.49	-14.61	-14.03
3		-15.51	-14.96	-15.61
Delta	0.33	1.02	0.36	1.58
Rank	4	2	3	1

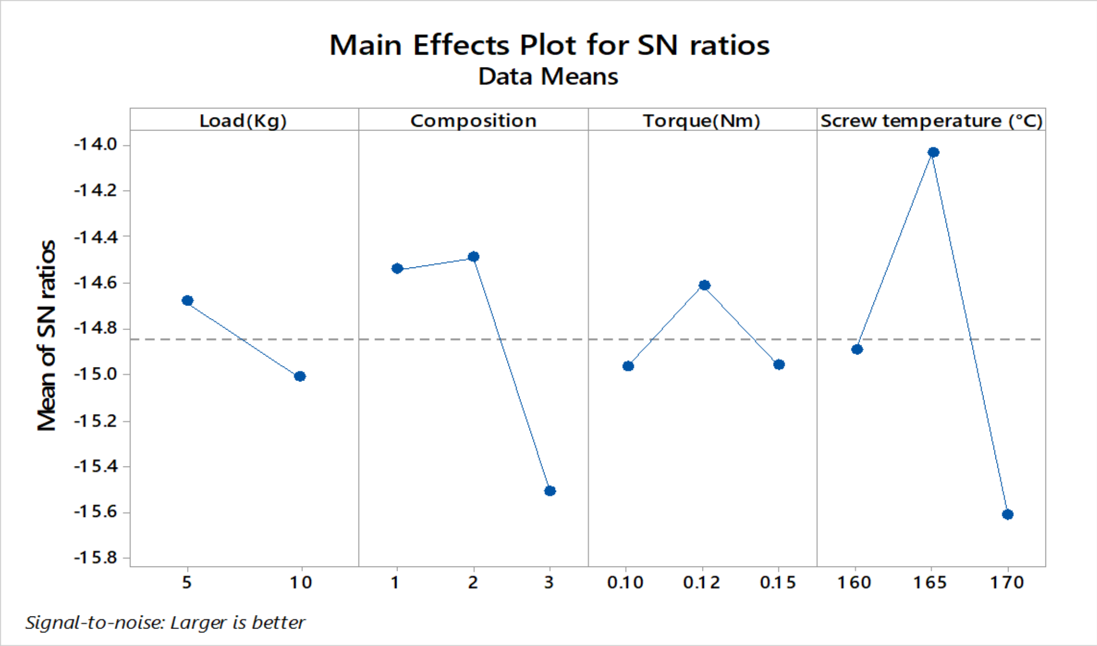

Figure 5.11 Main effect plot of magnetization for SN ratio

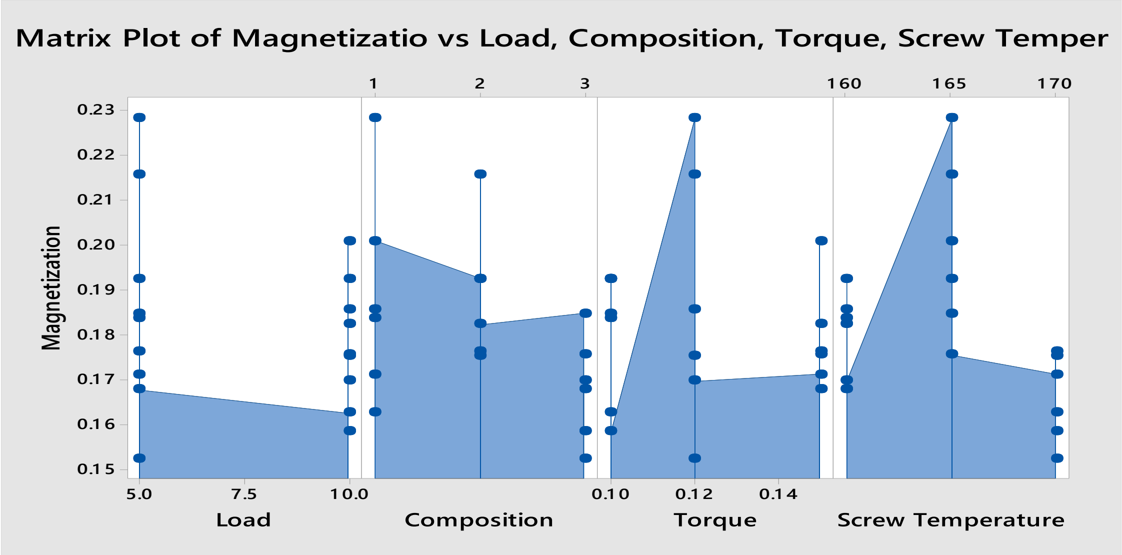

Figure 5.12 Matrix plots of all the input parameters with magnetization

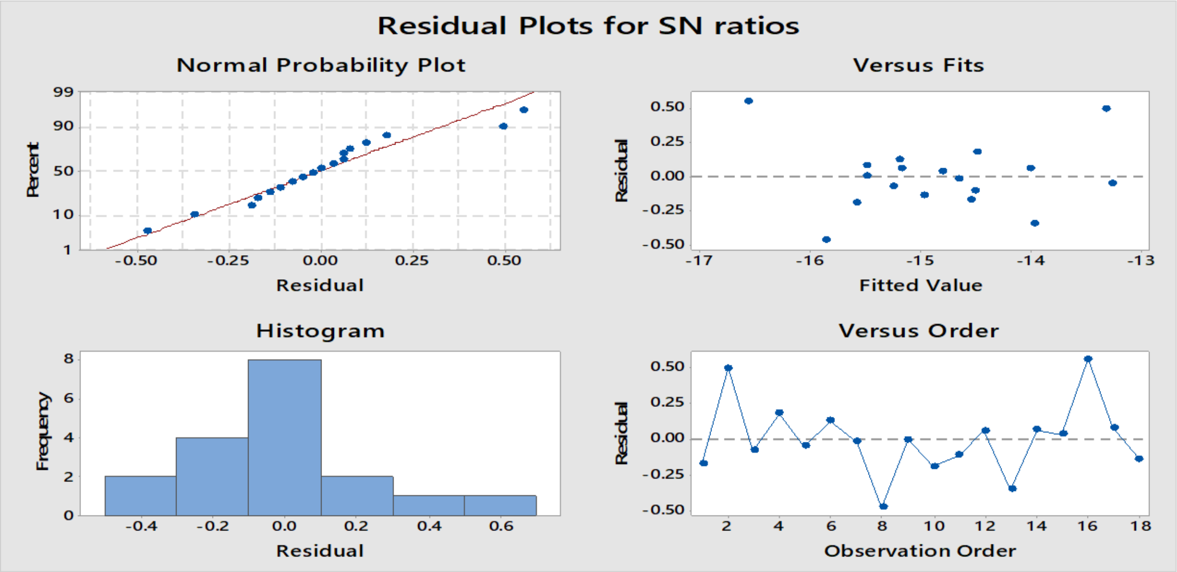

Figure 5.13 Residual plot for magnetization

Optimized and predicted values of the best twin-screw extrusion setting were calculated using equations4 and 5, respectively.

$$\boldsymbol{m} = \text{ mean of SN values for peak load analysis } = -14.84 \text{ (from Table 5.10)}$$

$$\mathrm{m_A} = \text{ max value of peak load } -14.68 \text{(from Table 5.12)}$$

$$\mathrm{m_B} = \text{max value for composition } -14.49 \text{(from Table 5.12)}$$

$$\mathrm{m_C} = \text{ max value for torque } -14.61 \text{(from Table 5.12)}$$

$$\mathrm{m_D} = \text{ max value for temperature } -14.03 \text{ (from Table 5.12)}$$

$$\text{Ŋ opt} = \mathrm{m} + (\mathrm{m_A} - \mathrm{m}) + (\mathrm{m_B} - \mathrm{m}) + (\mathrm{m_C} - \mathrm{m}) + (\mathrm{m_D} - \mathrm{m})$$

$$\text{Ŋ opt} = -14.84 + \big(-14.68 - (-14.84)\big) + \big(-14.49 - (-14.84)\big) + \big(-14.61 - (-14.84)\big) + \ (-14.03 - (-14.84))$$

$$\text{Ŋ opt} = -13.29$$

$$\mathrm{Y_{opt}^2} = 10^{\frac{\text{Ŋ (opt)}}{10}}$$

$$Y_{opt}^{2} = 10^{\frac{(-13.29)}{10}}$$

$$Y_{opt} = 0.2165 \text{ emu}$$

The optimized result for the magnetization property was observed to be 0.2165emu. On running the optimized condition for the load: 5Kg, torque: 0.12Nm, temperature:165°C and composition 2, which was the 5th running condition in Taguchi orthogonal assay (see Table 4.3), the magnetization value was observed to be 0.2156 which was equal to the predicted result. In the same manner, the other two properties were optimized, the optimized and actual results are shown in Table 5.13. Figure 5.14 shows the optimized condition for the coercivity from which we get to know that load of 5Kg, composition 2, torque: 0.10Nm and screw temperature of 165°C provides the optimized results but this condition was outside the L18 array so we again extruded a sample for this optimized condition and actual value also came very near the predicted value. Figure 5.15 shows the main effect plot for the retentivity of samples which shows that load of 10Kg, 1st composition, 0.15Nm of torque, and 165°C of screw temperature gives optimized result.

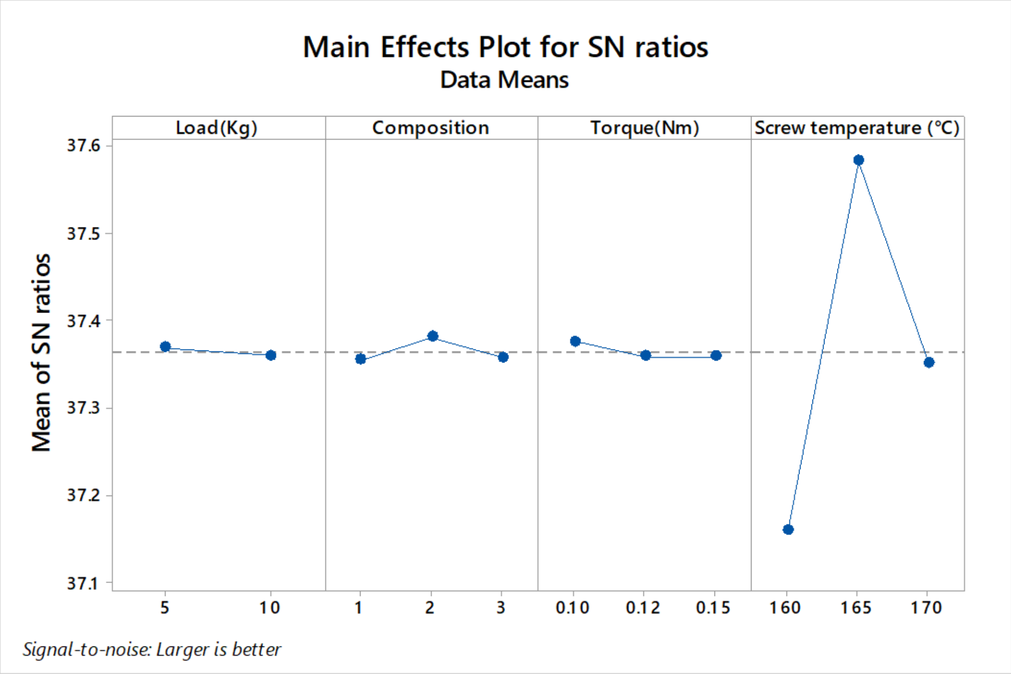

Figure 5.14 Main effect plot for coercivity

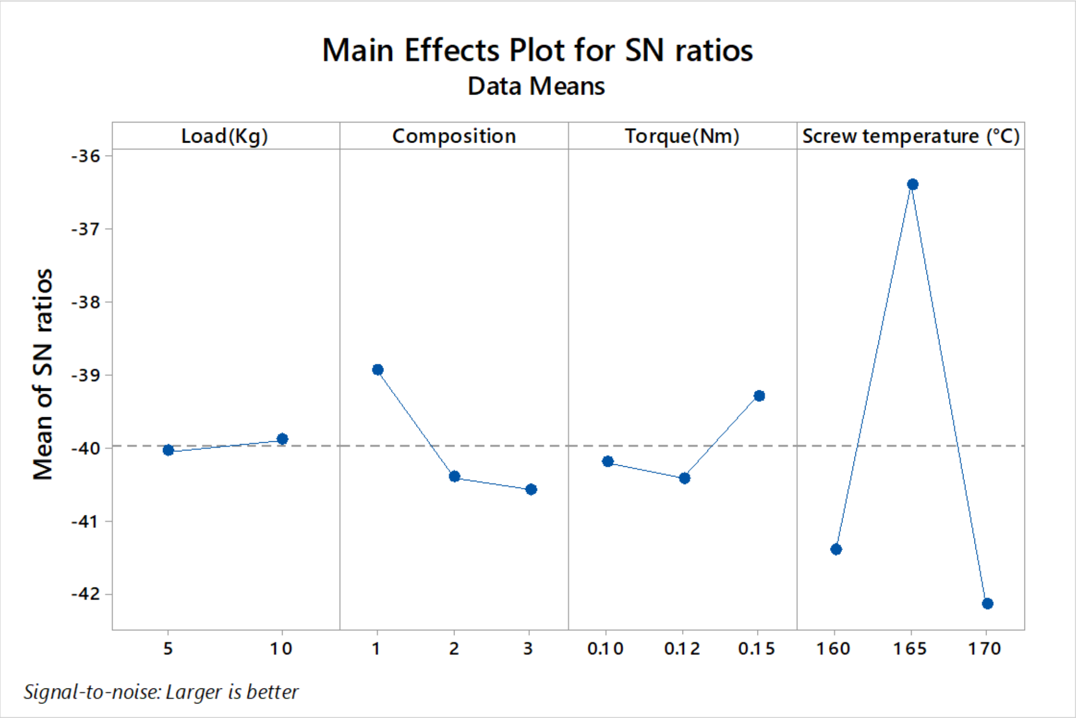

Figure 5.15 Main effect plot for Retentivity

Table 5.13 optimized and actual results for the optimized condition for magnetic properties of hybrid blend

Attributes	Ŋ$_{(opt)}$ (dB)	Y$_{(opt)}$	Actual values at predicted set up Y$_{(opt)}$
Magnetization (emu)	-13.29	0.2165	0.2156
Coercivity (Oersted (OE))	37.62	76.0043	75.7895
Retentivity (Gauss(G))	-34.59	1.86E-02	1.14E-02

5.1.10 Interaction of input parameters with output for magnetic properties

To know the effect of input parameters on the output properties, regression analysis has been done and contour plots have been plotted to explain the actual interactions of the different input parameters with the output. As screw temperature and composition are giving maximum contribution and have been ranked as 1st and 2nd for each property, therefore, for contour plotting, the composition has been taken on the y-axis and screw temperature has been taken on the x-axis, and output properties have been shown with different color coding in the plot as can be seen from Figure 5.16, 5.17 and 5.18 for magnetization, coercivity, and retentivity, respectively. Torque and load play the least role in extrusion conditions; therefore, these were fixed with 0.123Nm and 7.5Kg of load which is average values of the torque and load for every set of conditions for extrusion. Equation 6, 7 and 8 give the regression interaction equation for magnetization, coercivity, and retentivity, respectively which were used for making contour plots in MiniTab 18.1 software package in which 4 levels of interaction is selected as we have 4 input parameters. Equation 6, 7, and 8 show the regression equations for magnetization, coercivity, and retentivity

(L = Load, T = Torque, C = Composition and ST = Screw temperature)

$$
\begin{aligned}
\text{Magnetization}& \\
&= -27.59 + 2.965\,L + 11.18\,C - 83.8\,T + 0.2029\,ST - 1.120\,L \times C \\
&\quad + 6.97\,L \times T - 0.02147\,L \times ST + 15.33\,C \times T - 0.0792\,C \times ST \\
&\quad + 0.227\,T \times ST - 1.552\,L \times C \times T + 0.00794\,L \times C \times ST \\
&\quad - 0.0138\,L \times T \times S \ldots\ldots..(6)
\end{aligned}
$$

$$
\begin{aligned}
\mathrm{Coercivity} &= -1572 + 182\,\mathrm{L} + 537\,\mathrm{C} - 1733\,\mathrm{T} + 11.64\,\mathrm{ST} - 53.6\,\mathrm{L} \times \mathrm{C} - 8\,\mathrm{L} \times \mathrm{T} \\
&\quad - 1.276\,\mathrm{L} \times \mathrm{ST} + 719\,\mathrm{C} \times \mathrm{T} - 3.78\,\mathrm{C} \times \mathrm{ST} - 3.1\,\mathrm{T} \times \mathrm{ST} - 73.2\,\mathrm{L} \times \mathrm{C} \times \mathrm{T} \\
&\quad + 0.379\,\mathrm{L} \times \mathrm{C} \times \mathrm{ST} + 1.44\,\mathrm{L} \times \mathrm{T} \times \mathrm{ST} \ldots\ldots..(7)
\end{aligned}
$$

$$
\begin{aligned}
\mathrm{Retentivity} &= -3.88 + 0.457\,\mathrm{L} + 0.98\,\mathrm{C} + 4.1\,\mathrm{T} + 0.0268\,\mathrm{ST} - 0.096\,\mathrm{L} \times \mathrm{C} \\
&\quad - 1.04\,\mathrm{L} \times \mathrm{T} - 0.00311\,\mathrm{L} \times \mathrm{ST} + 1.38\,\mathrm{C} \times \mathrm{T} - 0.0070\,\mathrm{C} \times ST \\
&\quad - 0.051\,\mathrm{T} \times ST - 0.144\,\mathrm{L} \times \mathrm{C} \times \mathrm{T} + 0.00069\,\mathrm{L} \times \mathrm{C} \times ST \\
&\quad + 0.0091\,\mathrm{L} \times \mathrm{T} \times \mathrm{ST} \ldots\ldots..(8)
\end{aligned}
$$

As observed from Figure 5.16, the contour loop for magnetization shows that when torque at 0.123Nm and load at 7.5Kg is fixed then magnetization decreases with an increase in temperature, and also low magnetization value is obtained for composition 3 in which 17.5% of magnetite powder is mixed with PLA composite matrix. When the temperature is low, about 160°C, maximum magnetization value is obtained for composition 1 in which 20 weight percentage of magnetite powder is mixed whereas composition 2 in which maximum amount of magnetite powder 25 weight percentage is mixed gives intermediate results for magnetization. This may be because, in composition 2, PLA is 52.5 weight percentage and wood dust are 7.5 weight percentage which is higher than composition 1 in which PLA 50 weight percentage and wood dust 5 weight percentage are mixed. Therefore, it may be due to the reason that while preparing the mixture of different compositions, with a large amount of wood dust present inside the matrix, reduced the magnetization as one can see from trends. In sample 1 only 5 weight percentage wood dust is mixed thus having the highest magnetization and as the composition of wood dust increases from 5 to 7.5 weight percentage in sample 2, magnetization decreases. Similarly, when wood dust is 10 weight percentage in the composite matrix, the magnetization value was the least. But with increased screw temperature, magnetization decreased. Similarly, from Figure 5.17, the contour graph for coercivity (when torque at 0.123Nm and load at 7.5Kg is fixed) gives that the coercivity is low (<65emu/g) when the temperature is low and as the temperature increases coercivity also increases (>80emu/g). For the 3rd composition in which magnetite powder (17.5 wt.%) is mixed in the composite matrix, the value of coercivity was found to be low whereas for composition 1 in which 20 weight percentage magnetite powder is mixed holds maximum coercivity and follows the same trend as followed by magnetization. It has been clear from Figure 5.18 (contour graph for retentivity (when torque at 0.123Nm and load at 7.5Kg is fixed) that the retentivity is low (<0.00) when the temperature is low and as the temperature increases retentivity also increases (>0.03). Similarly, for the 3rd composition in which magnetite powder (17.5 wt.%) is mixed in the composite matrix, the value of retentivity was found to be low whereas for composition 1 in which 20 weight percentage magnetite powder is mixed, holds maximum retentivity and follows the same trend as followed by magnetization and coercivity as seen in Figure 5.16 and 5.17.

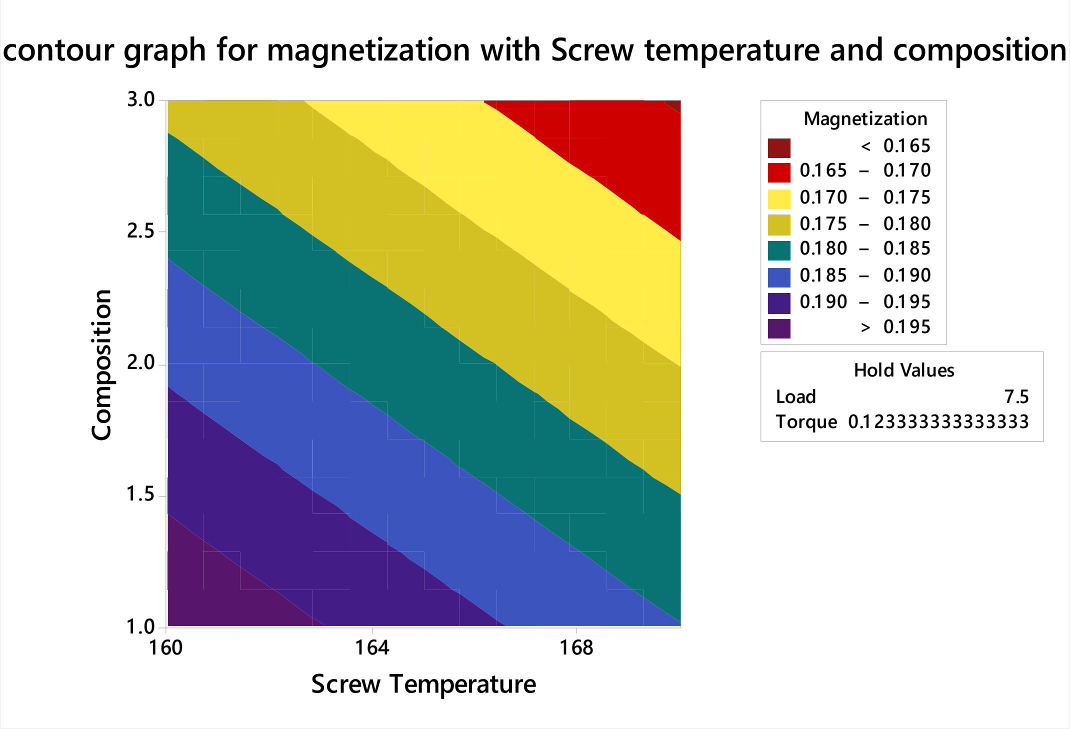

Figure 5.16 Contour plot for magnetization

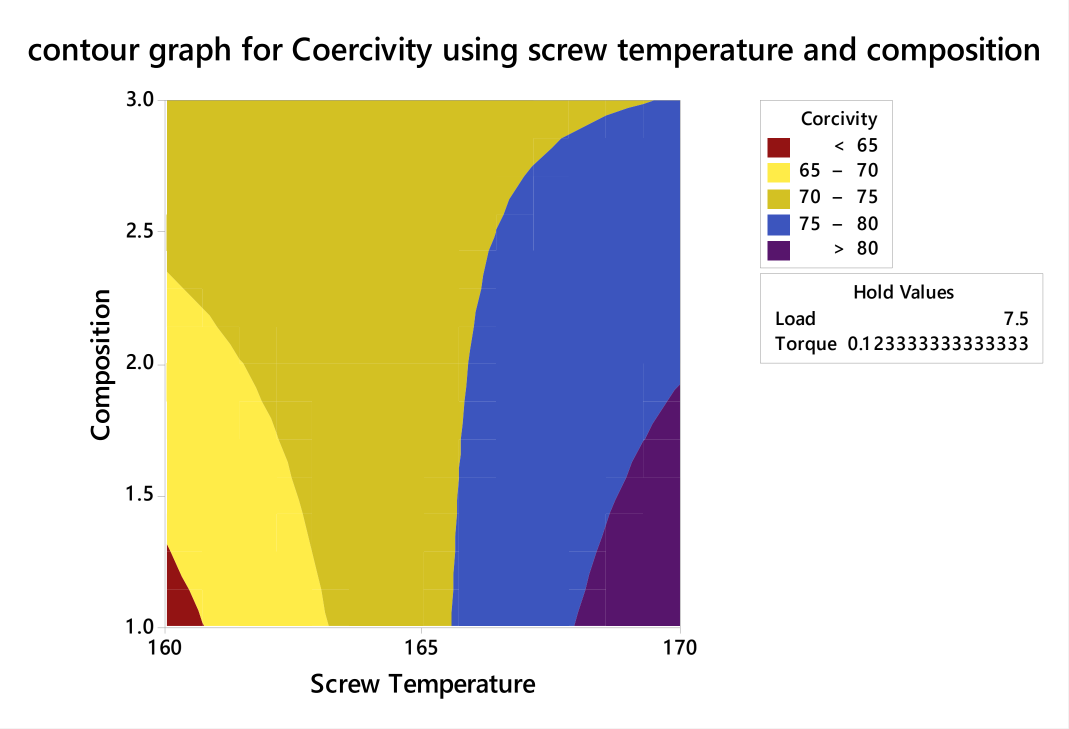

Figure 5.17 Contour plot for coercivity

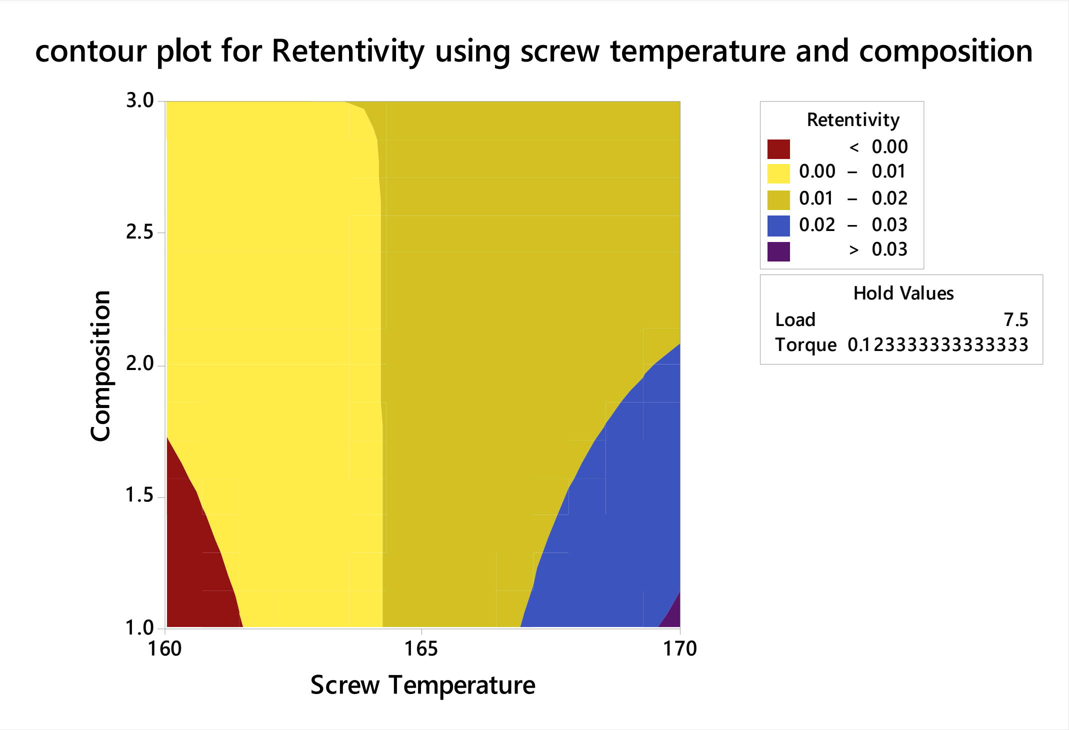

Figure 5.18 Contour plot for retentivity

5.1.11 Correlation of morphological properties and hardness with magnetic properties

From Table 5.9 one can see that magnetization for sample 2 is maximum (0.2283 emu) and sample 8 has the minimum magnetization value (0.1524 emu). For these samples, porosity results are as shown in Figure 5.19 which were obtained through MIAS using ×100 magnification. Sample 2 had low porosity of 10.03% in comparison to sample 8 which is having a porosity value equal to 12.6%. Figure 5.20 shows the histogram for magnetization and Figure 5.21 shows the graph for shore D hardness. Figure 5.22 shows the porosity graph for all the samples in which it is clear that porosity values are independent of the magnetic properties as there is no co-relation observed between magnetic properties and porosity. Similar is the case with shore D hardness. Thus, it is ascertained that porosity values and shore D hardness contributes towards the mechanical properties but not significantly for magnetic properties. This may be attributed to the fact that magnetite powder in the composite may not be present in large amounts on the surface but deep into the matrix of the composite thus leading to a contradiction in results of surface properties with that of magnetic properties. In general, wherever magnetite powder is more there should be more hardness but in the present case sample 8 had maximum hardness (>66 Shore D) but magnetization (>0.15 emu) was not the maximum that meant this behavior was due to intermixing of magnetite particles in the inner matrix of the composite. Magnetite particles were present in less percentage on the surface and have moved into the inner matrix thus leading to contradictory results. Thus, to correlate magnetic and mechanical properties, multi-material printing may be one of the solutions in which different layers of different materials can be printed in a single object thus leading to required results.

(a) Porosity 10.03%

(b) Porosity 12.6%

Figure 5.19 Porosity results for (a): Sample 2 and (b) Sample 8 as per Table 4.3

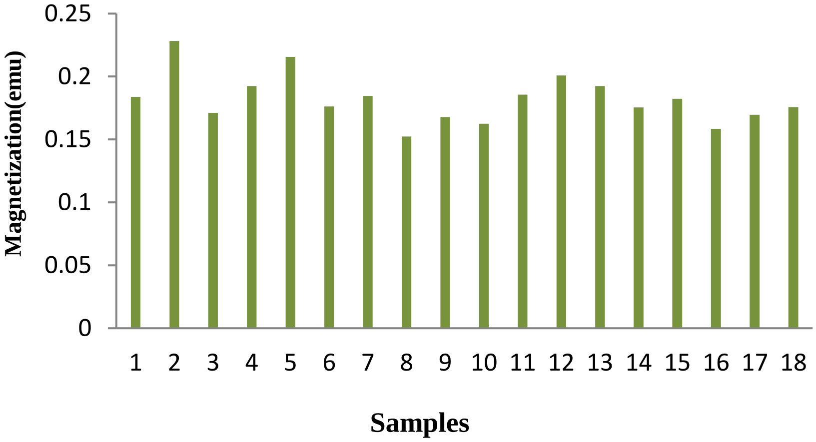

Figure 5.20 Graph for magnetization as per Table 4.3

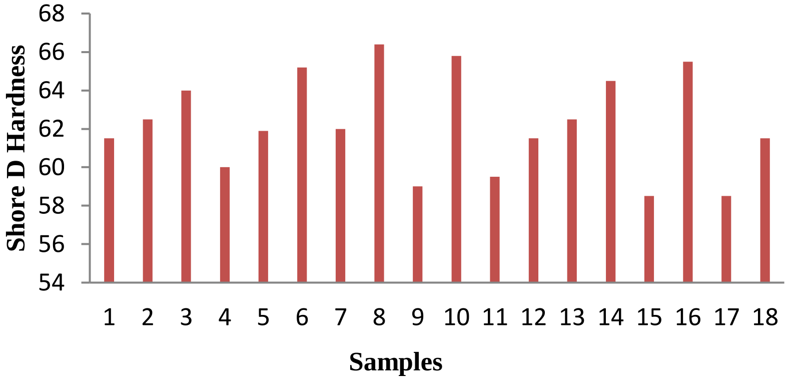

Figure 5.21 Graph for Shore D hardness as per Table 4.3

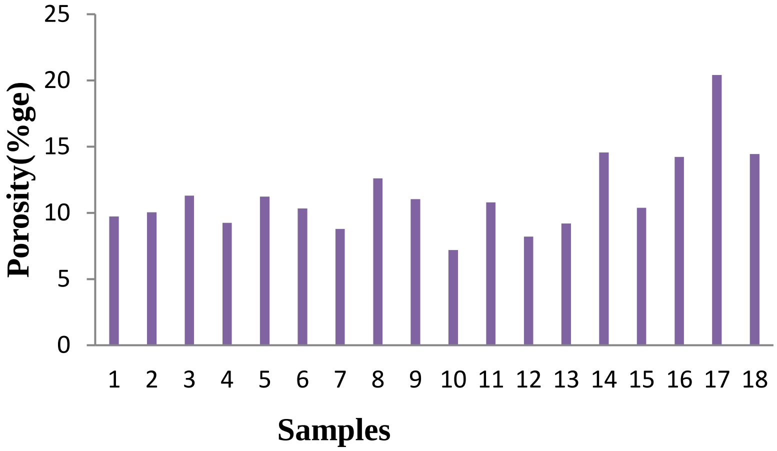

Figure 5.22 Graph for Porosity as per Table 4.3

5.1.12 SEM results

As observed from Table 5.9, sample 2 has shown maximum magnetization of 28.66 emu/gm or 0.2281emu and sample 8 has shown minimum magnetization of 19.40emu/gm or 0.1524emu. Therefore, these two samples have been taken as the best and the worst samples, respectively, and were tested for SEM which clarifies the contradictory behavior of magnetic properties with that of mechanical property such as Shore D hardness and porosity. Figure 5.23 shows the SEM images of (a) sample number 2 and (b) 8 of feedstock filament samples. It was observed that the magnetite particles were not present on the surface of samples and rather they get mixed into the inner matrix of the composite due to which on the surface, magnetite particles do not contribute towards hardness. Further, from the comparative analysis, it is clear that the surface texture of sample 8 is non-uniform, therefore, has high porosity as compared to sample 2.

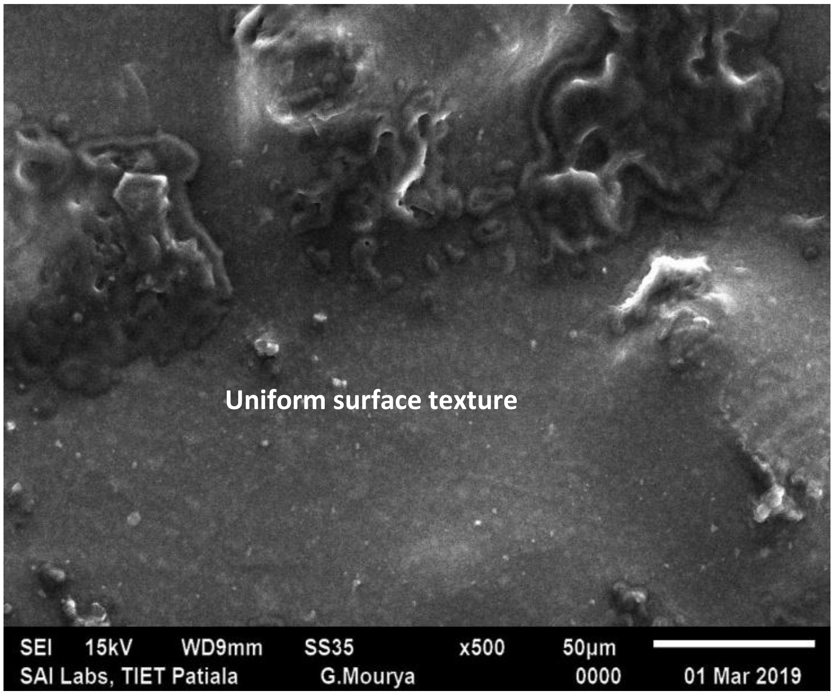

(a)

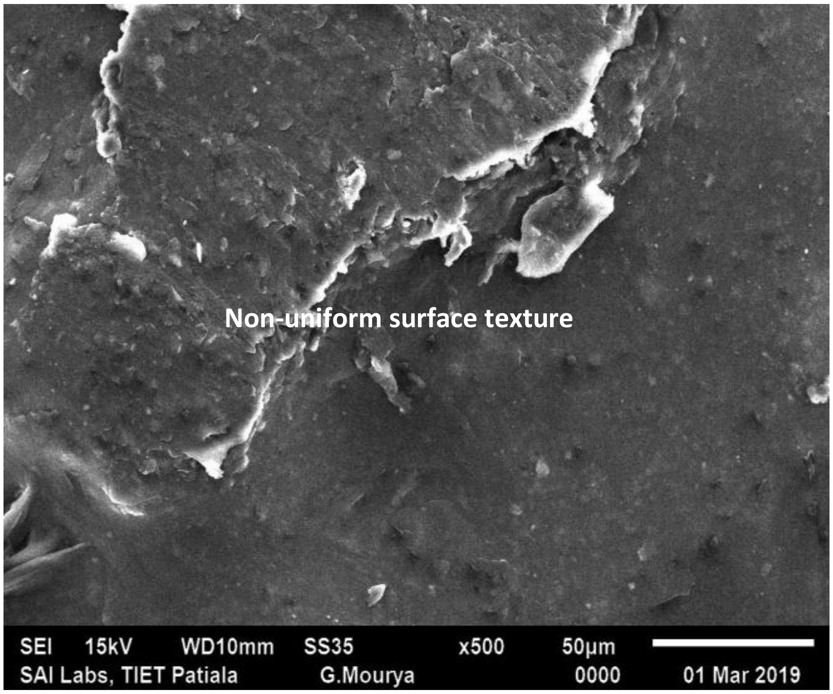

(b)

Figure 5.23 SEM image of (a) 2nd filament and (b) 8th filament as per Table 4.3

5.1.13 EDS Analysis

EDS of samples 2 and 8 has been performed to know the elements present on the surface of the filaments. Figure 5.24 shows the EDS images of (a) 2nd sample and (b) 8th sample, with their spectrum graph which shows the elements present on the composite surface. As one can observe from spectrum 4 of EDS (for full selection of image) for 2nd sample (see Figure 5.25), the Fe element was just 1.15% (maximum of the four spectrums selected) of the composition of the total elements on the surface of selection. It clearly shows that magnetite particles are mixed thoroughly and have moved deep inside of the matrix due to which magnetic properties are not in correlation with mechanical properties. Thus, to have the impact of magnetite particles on the surface, multi-material printing may be a better option. Moreover, carbon element is present in a huge percentage on the surface (>55%) which contributes towards the mechanical properties of the composite. Similarly, from the spectrum EDS image of the 8th sample (see Figure 5.26), it has been observed that Fe content on the surface is 1.59% (maximum of the four spectrums selected) of the total elements present on the surface which is higher than the Fe content in case of filament 2. It, therefore, has a more heterogeneous surface texture as can be seen in Figure 5.23. It, therefore, has surface hardness. The presence of more Fe content and oxygen element on the surface leads to more porosity (12.60%) as shown in Fig.10 (d) in the porosity graph.

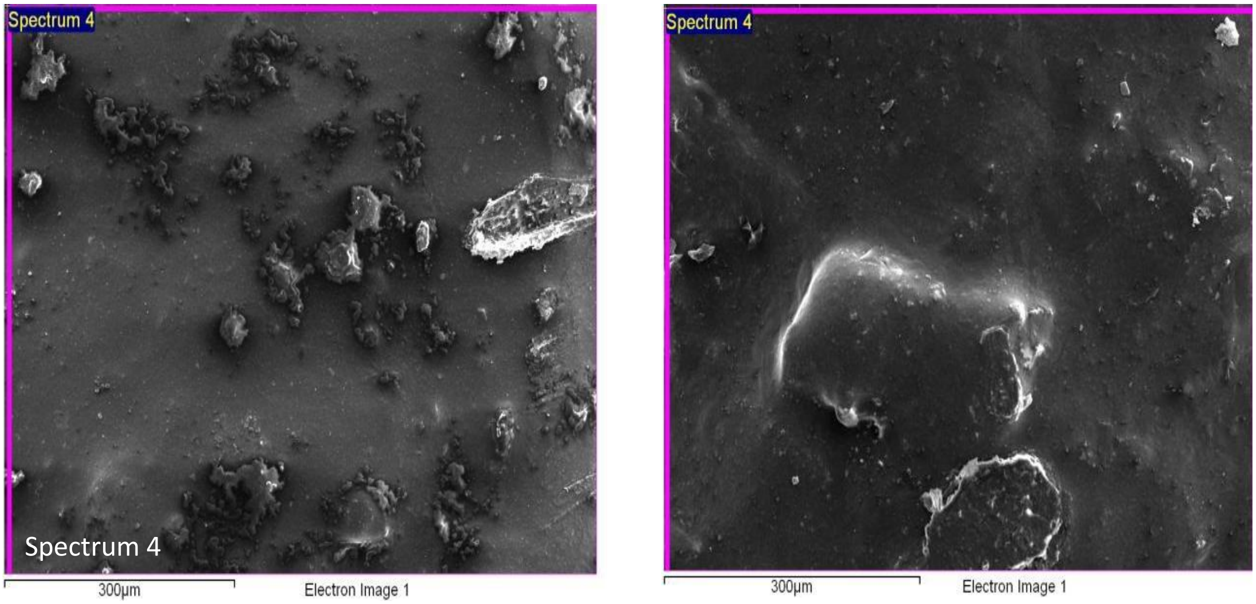

(a) (b)

Figure 5.24 EDS spectrum image for (a) 2nd filament and (b) 8th filament sample as per Table 4.3

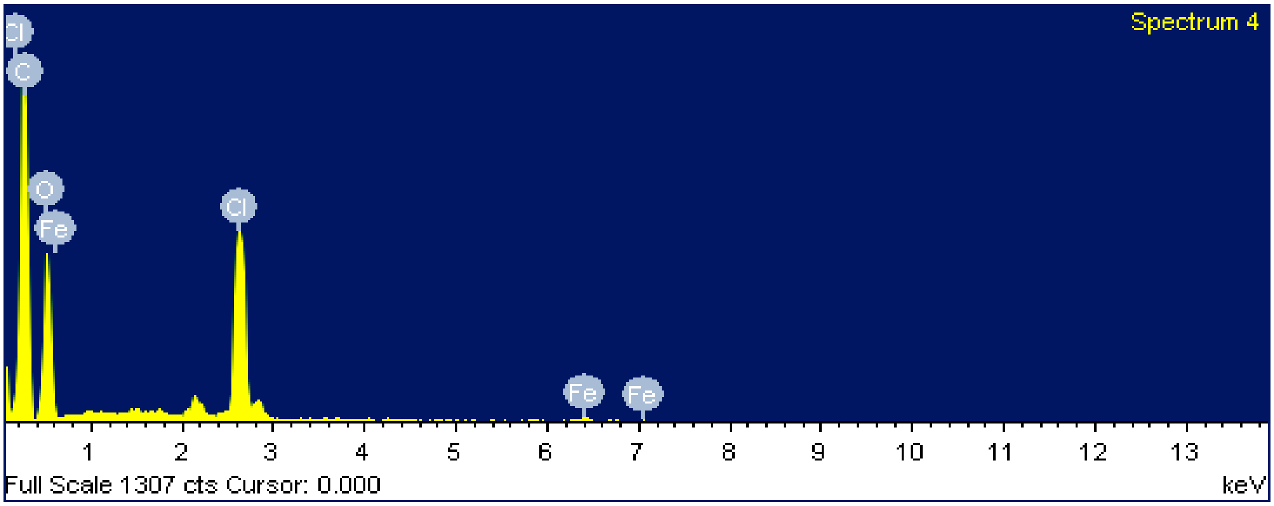

Spectrum	C	O	Cl	Fe	Total
Spectrum 1	55.68	31.10	12.07	1.15	100.00
Spectrum 2	68.86	24.50	6.44	0.19	100.00
Spectrum 3	56.85	32.80	9.47	0.88	100.00
Spectrum 4	58.92	30.12	9.97	0.99	100.00

Figure 5.25 EDS spectrum and element composition present on surface for 2nd filament

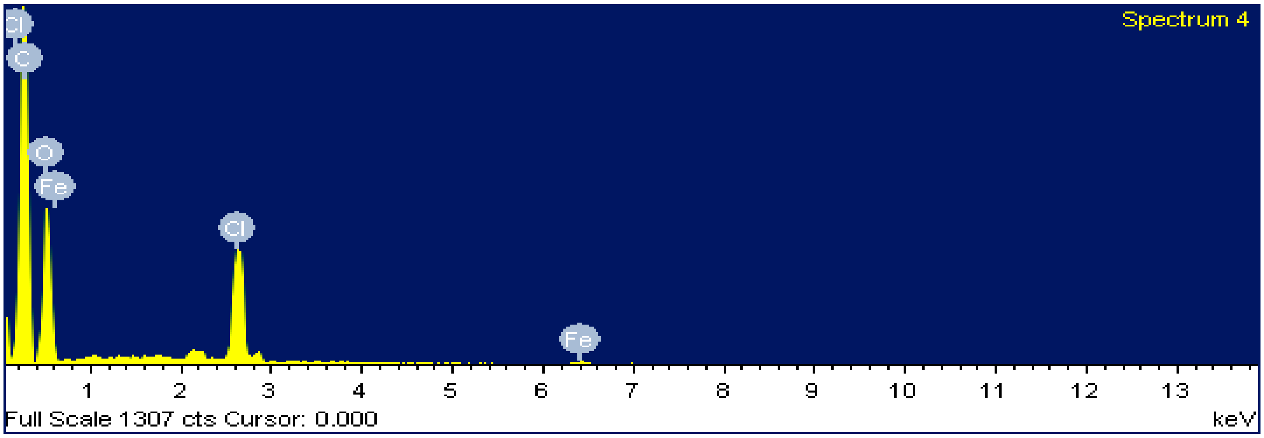

Spectrum	In stats.	C	O	Cl	Fe	Total
Spectrum 1	Yes	57.13	32.60	8.68	1.59	100.00
Spectrum 2	Yes	57.02	37.78	3.99	1.21	100.00
Spectrum 3	Yes	62.57	30.48	6.08	0.87	100.00
Spectrum 4	Yes	59.95	31.88	7.16	1.01	100.00

Figure 5.26 EDS spectrum and element composition present on surface for 8th filament as per Table 4.3

5.1.14 Process capability analysis for feedstock filament of hybrid composition for magnetization, surface hardness, and percent porosity

Ten samples of sufficient length were prepared of the optimum diameter of feedstock filament. Similarly, feedstock filament of the hybrid blend (PLA-50 weight percentage, polyvinyl chloride (PVC)-25 weight percentage, wood powder-5 weight percentage, and Fe_3O_4-20 weight percentage) was prepared using optimized TSE standard conditions. All the filaments were subjected to VSM testing, surface characteristic testing such as for surface hardness and surface porosity, and process capability analysis was performed. Table 5.14 shows the values of magnetization, coercivity, and retentivity for the 10 samples of each blend. The surface characteristics for the single-particle reinforced matrix and hybrid matrix-based feedstock filament of PLA are given in Table 5.15. The results for magnetization, coercivity, surface hardness, and surface porosity were further subjected to statistical tools for the calculation of process capability for the TSE machine. To check whether the process is in statistical control or not statistical tool was used to evaluate the C_p and C_{pk} values and to calculate those values equations (7) and (8) were used. The C_p signifies that the process is capable of producing products with required specifications whereas Cpk signifies that the process is well capable as the process can adhere to the target specifications.

$$C_p = \frac{(\mathrm{USL} - \mathrm{LSL})}{6\sigma} \ldots\ldots\ldots\ldots\ldots\ldots\ldots.(7)$$

$$C_{pk} = \min\left[\frac{\mu - \mathrm{LSL}}{3\sigma}, \frac{\mathrm{USL} - \mu}{3\sigma}\right] \ldots\ldots\ldots(8)$$

*Where USL is the Upper specification limit and LSL: lower specification limit.

Table 5.14 Magnetic properties of hybrid and single-particle reinforced blend

Serial number	Single-particle reinforced matrix of PLA		Hybrid matrix of PLA	
	Magnetization (emu/g)	Coercivity (Oersted (emu/g))	Magnetization (emu/g)	Coercivity (Oersted (emu/g))
1	28.91	84.61	28.62	74.54
2	28.60	84.52	28.52	75.01

3	28.41	84.74	28.36	74.62
4	28.95	83.95	28.91	75.12
5	27.89	83.86	27.94	74.98
6	27.97	84.35	27.99	75.21
7	28.23	84.51	28.46	74.65
8	27.89	83.98	27.98	74.80
9	28.74	84.94	28.67	75.16
10	27.96	83.97	27.93	74.92

Table 5.15 Surface characteristics for hybrid and single-particle reinforced matrix of PLA.

Serial number	Single-particle reinforced matrix of PLA		Hybrid matrix of PLA	
	Surface hardness (Shore D)	Percentage porosity (%age)	Surface hardness (Shore D)	Percentage porosity (%)
1	61.5	5.14	66	7.18
2	59.5	5.41	65	7.14
3	60	5.12	66.5	6.95
4	59.5	5.45	66.5	6.88
5	60.5	5.62	65.5	6.93
6	60	5.11	66	7.14
7	59	5.65	65.5	7.20
8	60.5	4.99	66	7.24
9	59.5	5.54	66.5	6.98
10	60.5	5.32	66	7.04

Table 5.16 shows the USL and LSL values for various properties taken for the capability analysis. From the capability analysis for the feedstock filament made from a hybrid blend of PLA matrix, it was observed that the values were falling in limits between the USL and LSL. From the normality test, it was observed that the data followed the normal distribution and thus may be a suitable candidate for statistical control evaluation as observed from Figure 5.27 (a). Figure 5.27 (b) (Histogram) showed that all the values observed for the different samples for magnetization were in specified limits thus making the process standard and reliable. The value for C_p (1.21) and C_{pk} (1.08) was greater than 1. Similar studies have been performed on the other observed properties and it was observed that C_p and C_{pk} for each property were greater than 1 which suggested that the optimized conditions of TSE were statistically significant and reliable for the mass/batch production. Table 5.17 shows the observed values of C_p and C_{pk} for the different properties.

Table 5.16 USL and LSL values for magnetic and Surface properties.

Serial number	Single-particle reinforced matrix of PLA			Hybrid matrix of PLA		
	Magnetization (emu/g)	Surface hardness (Shore D)	Percentage porosity (%age)	Magnetization (emu/g)	Surface hardness (Shore D)	Percentage porosity (%age)
USL	30	64	7	30	70	8
LSL	27	56	4	27	64	5

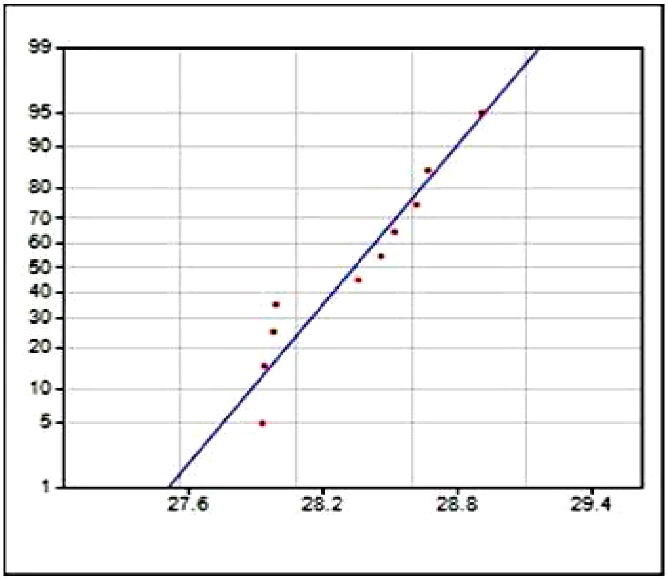

(a)

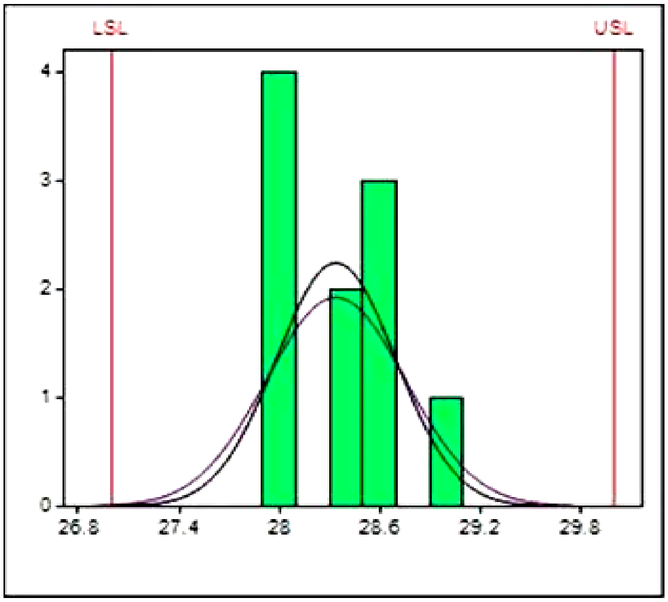

(b)

Figure 5.27 (a) Normality test graph and (b) histogram for a control chart.

Table 5.17 Values of σ, C_p and C_{pk} for magnetic and surface properties for the hybrid composite matrix of PLA

Serial number	Single-particle reinforced matrix of PLA	Hybrid matrix of PLA

	Magnetization	Surface hardness	Percentage porosity	Magnetization	Surface hardness	Percentage porosity
σ	0.4344	0.8865	0.3487	0.4147	0.5910	0.0965
C_p	1.15	1.5	1.43	1.21	1.69	3.45
C_{pk}	1.04	1.49	1.28	1.08	1.1	3.22

5.2 Results and discussion for stage 2

5.2.1 Rheological properties testing

Melt flow index (MFI) or MFR has been tested for different compositions of reinforcement or virgin polymers. Maintaining standard conditions of testing (190°C temperature, 2.16Kg of Load), five trials were performed for each composite ratio. Table 5.18 shows the MFI results of PVC reinforced PLA and virgin polymers of PLA and PVC. It has been observed (Table 5.18) that as the reinforcement level of PVC increases, the MFI of the composite also increases. This means that the MFI of the composite has a direct relationship with the level of loading of PVC in the PLA matrix. This may be attributed to the fact that in the virgin polymer of PLA, there are strong intramolecular bonds but when PVC molecules are loaded into the matrix of PLA, the inter-molecular bonds are not that much strong and thus the MFR is increased as it became easy to melt the composite than the virgin polymer PLA. The second reason for the enhancement of MFR may be due to an increase in the length of the fiber as it is a fact that higher length leads to low strength and ultimately leading to high MFR. For 25% reinforcement of PVC in PLA, 51.82% improvement of melt flow rate has been observed. Reduction in bond strength of the composite could also be validated from UTM testing and microstructural analysis of the composite which has been done after preparation of polymer filament. Similar trends have been seen for Fe_3O_4 reinforced polymer matrix of PLA as shown in Table 5.19. The increased MFI of Fe_3O_4 based composite may be attributed to the heat-absorbing capacity of the reinforced material. As Fe_3O_4 absorbed heat from the system of the MFI chamber, the polymer matrix got melted easily and thus MFI got enhanced. Table 5.19 also shows the MFI for the multi blend (PLA 50 wt.%, PVC 25 wt.%, Magnetite 20 weight percentage, and wood powder 5 weight percentage). The MFI range of multi blend was found near to 25% PVC reinforced PLA and 20% magnetite reinforced PLA which indicated that though the presence of wood powder reduces the MFI Fe_3O_4 content dominated in the composite which improved the heat-absorbing capacity thus higher MFI was obtained for the multi blend.

Table 5.18 MFI (g/10min) results for different compositions/proportions of PLA and PLA/PVC matrix

Serial number	PLA	PVC	PLA with 10% PVC	PLA with 15% PVC	PLA with 20% PVC	PLA with 25% PVC
1	28.79	25.76	33.51	36.78	38.18	41.43
2	27.26	24.92	34.62	35.55	39.54	42.96
3	28.83	24.76	33.43	36.13	39.43	42.58
4	26.94	25.41	32.96	34.93	38.98	43.24
5	28.23	24.72	34.08	35.62	40.03	42.42
Avg.	28.01	25.114	33.72	35.81	39.23	42.53

Table 5.19 MFI results of PLA with Fe_3O_4 powder reinforcement

Serial number	PLA with 10% Fe_3O_4	PLA with 15% Fe_3O_4	PLA with 20% Fe_3O_4	Multi-Blend
1	34.08	38.53	40.72	41.42
2	33.52	37.76	41.56	42.55
3	34.56	38.72	40.98	42.16
4	33.96	37.93	41.21	43.25
5	34.21	39.21	41.33	42.46
Avg.	34.07	38.43	41.16	42.37

When the wood powder has been reinforced into the PLA matrix, a decreasing trend has been obtained for the MFI as shown in Table 5.20. It may be due to the entrapment of wood particles in the PLA matrix. Wood powder being an insulator, when reinforced in polymer resists the heat flow in the MFI machine chamber and thus lowers the MFI of PLA. Moreover, the large presence of wood powder in the PLA matrix hinders the proper mixing of wood powder with PLA as they get self-aggregated when present in large amounts/volume. Therefore, only up to 10% loading of wood powder in PLA matrix has been done. A maximum reduction of 26.54% of MFI has been obtained for 10% wood powder reinforced PLA.

Table 5.20 MFI results of PLA with wood powder reinforcement

Serial number	PLA with 2.5% wood	PLA with 5% wood	PLA with 10% wood
1	26.13	22.14	18.87

2	25.42	23.54	17.98
3	25.68	22.67	18.53
4	24.97	23.01	19.56
5	25.31	22.68	18.72
Avg.	25.50	22.81	18.73

5.2.2 Universal Tensile Testing (UTM)

The composites were then extruded using 170°C screw temperature, 45rpm of screw rotation, and 5kg of loading condition. The filaments obtained were of 1.65mm-1.75mm diameter which was compatible with the requirement of the 3D printing machine. These filaments were then tested on the UTM machine (UTM, Make: Shanta Engineering, Pune, INDIA) for investigation of mechanical properties such as peak load, peak elongation, break load, break elongation, strength at peak, strength at break, %age elongation at peak, %age elongation at break, etc.

From the tensile testing, it has been noticed that when PLA was reinforced with PVC from 10 weight percent to 25 weight percentage mechanical properties of PLA were disturbed as peak elongation and break elongation and have reduced by 47.61% and 50%, respectively. This means the addition of PVC into the PLA matrix has decreased the strength of the molecular bonding which resulted in reduced peak and break strength and other mechanical properties as shown in Table 5.21. But this reduced strength of the composite may not be significant depending on the application in multi-material printing for different multi-layer components produced by 3D printing based on the position of the layer deposited (any intermediate layer).

Similar results have been obtained for wood powder reinforcement in the PLA base matrix. MFI in the case of wood powder reinforced polymer has been reduced due to the heat resistive nature of the wood powder. Mechanical properties were also reduced. This may be attributed to the fact that wood powder being heated resistive, absorbs only a little heat from the system due to which its bonding with the polymer was very weak resulting in low mechanical strength.

In the case of Fe_3O_4 reinforcement, the mechanical properties of PLA have reduced for peak load, break load, strength at peak and break but break elongation, percentage elongation improved while peak elongation remained the same. This may be attributed to the reason that the magnetite particles were throughout and evenly present in the composite structure resulting in strong intermolecular bondage. But the heat content of magnetite was capable of melting the polymer with much ease which resulted in high MFI as explained in the MFI result section. The Fe_3O_4 particles have provided crack resistance because of having high heat capacity at the time of extrusion. They provide good heat to the polymers in their vicinity thus forming a better bond. At the time of the break, crack propagation was less due to which break elongation and percentage break elongation of the specimen were found improved.

Table 5.21 UTM results of PLA based polymer composite

C	**PL (N)**	**PE (mm)**	**BL (N)**	**BE (mm)**	**SP (MPa)**	**SB (MPa)**	**% EP**	**% EB**	**E (MPa)**	**Stress (MPa)**	**Strain**
Pure PVC	61.7	260.3	55.53	271.89	25.66	23.1	289	302	6.61	25.66	3.88
Pure PLA	141.7	3.99	127.53	4.18	45.13	40.61	7	7	755.77	45.13	0.06
10% PVC	103.9	2.47	93.51	2.47	33.09	29.78	4	4	937.77	33.09	0.04
15% PVC	53.9	3.61	48.51	3.61	17.17	15.45	5	5	332.94	17.17	0.05
20% PVC	41.6	2.47	37.44	4.18	13.25	11.92	4	7	221.89	13.25	0.06
25% PVC	36.2	2.09	32.58	2.09	11.53	10.38	3	3	386.17	11.53	0.03
10% Fe_3O_4	91.6	3.8	82.44	5.32	29.17	26.25	5	7	383.82	29.17	0.08
15% Fe_3O_4	106.4	3.61	95.76	6.84	33.89	30.5	5	9	346.83	33.89	0.10
20 % Fe_3O_4	107.8	3.99	97.02	12.16	34.33	30.9	5	15	197.62	34.33	0.17
2.5% Wood	130.9	2.66	117.81	2.85	41.69	37.52	3	4	1,023.96	41.69	0.04
5% Wood	115.7	3.23	104.13	3.42	36.85	33.16	4	4	754.24	36.85	0.05
10% Wood	73.5	3.42	66.15	3.61	23.41	21.07	4	5	453.93	23.41	0.05
Multi blend Composite	38	4.4	36	4.7	18.23	16.42	5	7	271.51	18.23	0.07

C: Composite; PL: peak Elongation; BL: Break Elongation; EP: Elongation at peak; EB Elongation at the break; SP: Strength at peak; SB: strength at break, % EP: percentage elongation at peak; %EB: percentage elongation at break; E: Young's Modulus

Figure 5.28 provides the stress vs. strain diagram which has given a clear idea of fracture for the polymer composite. From this diagram, it has been found that when the polymer of PLA was reinforced with any of the external reinforcement, the mechanical properties were harmed. However, Fe_3O_4 reinforcement in PLA has improved its strain capacity due to which its break elongation approached 12.16 mm in case of 20 weight percent loading of Fe_3O_4 and strain was found to be 0.152 whereas strain capacity for virgin PLA was 0.05225. Similarly, for the 15% reinforcement of magnetite, the strain was found greater than the virgin PLA strain level. But for all the other reinforcements, the strain was less than that of the virgin PLA polymer. The stress was maximum for the PLA (45.13MPa) and was found lowest for the 25% PVC reinforced composite (11.53 MPa). Similarly, the lowest strain was found for 25 weight percentage reinforcement of PVC in PLA polymer which was 0.0261, and highest for 20% magnetite reinforced PLA polymer composite.

From the stress-strain curve, it has been observed that virgin PLA had maximum strength of 45.13 MPa but the strain range for the same material was low (<0.07). It has been seen that as the reinforcement of PVC or magnetite is done the brittle nature gets converted to ductile nature as suggested by the curves. This may be due to the reason that PLA being a flexible material when get reinforced into brittle material, improves the ductility of the composite and as the PVC content in composite increased the ductility was improved. Similar trends have been observed for the reinforcement of Fe_3O_4. This may be attributed to the fact that as the Fe_3O_4 loading in PLA increases the MFI also increases which means the flowability of material got better which improves the ductility of the material. Moreover, the heat-absorbing capacity of Fe_3O_4 powder may also be a reason for better mechanical properties. It would have absorbed heat from the system while extrusion and got properly mixed in the matrix of PLA which resulted in better properties. But with wood powder loading, the brittleness of PLA composite increased due to which the stress-strain graph shows the brittle failure of the composite matrix lower than the stress-strain graph for virgin PLA matrix. Table 5.22 gives the details of energy absorbed during the UTM testing. From Table 5.22, it has been observed that Fe_3O_4 powder reinforcement made the composite ductile and the composite energy absorbing capacity got increased nearly up to 116% as compared to the virgin PLA matrix. The least energy absorbance has been observed for 20% PVC reinforcement.

Table 5.22 Energy absorbed under deformation by various tested composite filaments

Materials / Composite	Modulus of toughness or energy absorbed (0.5× Stress× Strain)
Virgin PLA	1.3539
10% PVC	0.6618
15% PVC	0.42925
20% PVC	0.3975
10% Fe_3O_4	1.1668
15% Fe_3O_4	1.6945
20 % Fe_3O_4	2.91805
2.5% Wood	0.8338
5% Wood	0.92125
10% Wood	0.58525
Multi blend composite	0.63805

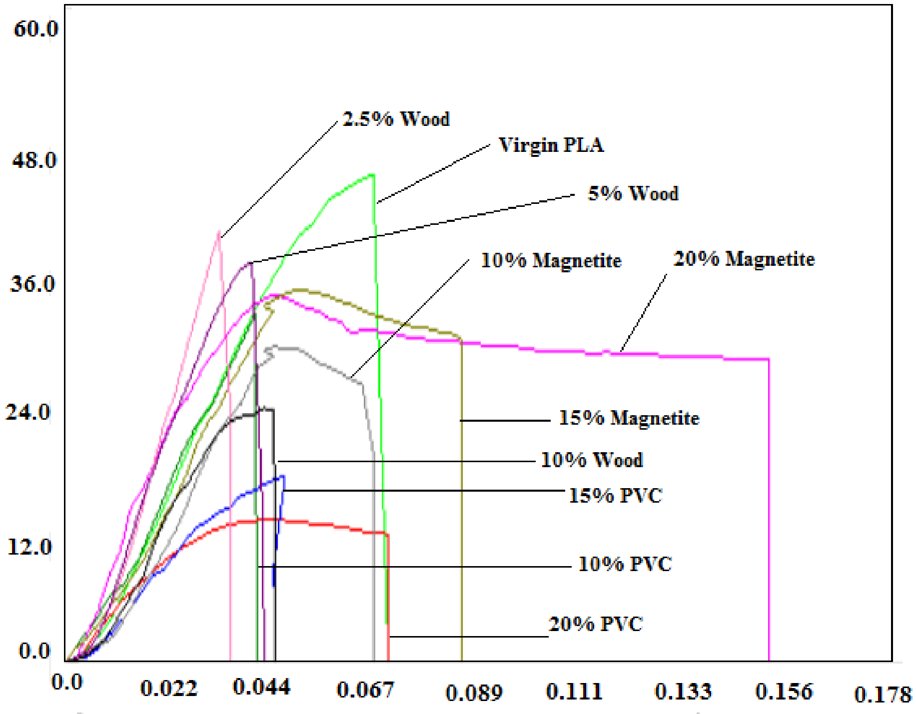

Figure 5.28 Stress vs. Strain for virgin polymer and different polymer composites of PLA

5.2.3 Morphological properties testing

From mechanical and rheological testing, it has been ascertained that reinforcement of foreign matter into PLA matrix has reduced its functional ability, except 20% Fe_3O_4 reinforcement, as it has shown improvement in break elongation and percentage elongation at the break while the peak elongation remains constant. Thus, it was important to test for the morphological properties such as Shore D hardness and microstructural analysis of filaments to have a better understanding of the mechanical behavior of filament obtained through TSE.

5.2.4 Shore D hardness

The hardness of the filaments has been tested using a Shore D hardness tester through which it has been found that for the increased loading of reinforcement of PVC in the PLA matrix, hardness was reduced (see Figure 5.29). This means that PVC polymers were easily blended into the matrix of the polymer and were also present on the surface of PLA matrix composite which reduced surface hardness. Similar trends have been found for the wood powder reinforced polymer composite. Possibly large porosity resulted in low hardness on increased loading of wood powder into the composite.

A dissimilar trend of shore D hardness has been seen for the Fe_3O_4 powder-based composite, which means that Fe_3O_4 powder improves the hardness of filament. But it was not more than the virgin PLA (69.5 Shore D), which indicates that the surface obtained may have some porosity due to which hardness was lower than that of the virgin PLA. An increase in the hardness with the Fe_3O_4 content proved that with reinforcement, polymer composite is not well structured and bonded but contained some holes in the form of porosity which may be seen in the microstructural analysis.

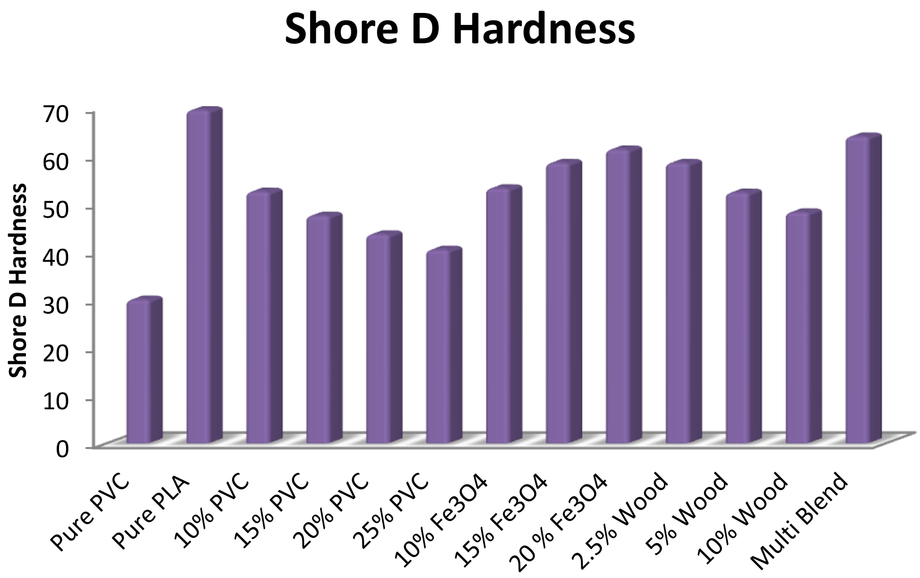

Figure 5.29 Shore D hardness for different composition of PLA and pure polymers

5.2.5 MIAS porosity results

Microstructural analysis of filaments has been obtained using a MIAS software package with a 100-micron scale. It has been noticed that the polymer composites with low hardness have shown larger porosity. This meant that high porosity leads to larger spaces between inter-molecules of reinforced particles and polymer base matrix results in poor mechanical properties as seen in the case of PVC and wood powder reinforced PLA polymer composite matrix. But for the Fe_3O_4, it has been observed that mechanical properties improved for the higher loading of Fe_3O_4 in PLA. This was also clear from the porosity results as low porosity values have been obtained for the higher concentration of Fe_3O_4 in the composite mixture as shown in Figure 5.30. It has been observed that 20 weight percentage of Fe_3O_4 loading in PLA polymer (which has shown best mechanical properties and hardness results among the polymer composites) possesses the lowest porosity of 5.20% whereas the PVC with 25 weight percentage in PLA matrix has shown poorest mechanical properties has also shown highest porosity of 11.74%. The porosity results of PLA-based composites have indicated the relationship of hardness and porosity with mechanical properties. Thus, from the microstructural analysis, it may be ascertained that poor morphological properties lead to poor mechanical properties for the composite. Porosity values for different composites of PLA have been obtained for the surface texture but not on the cross-section of deformed filament. For that purpose, the cross-sectional surface has been seen using ×30 scale which has been shown by Figure 5.31.

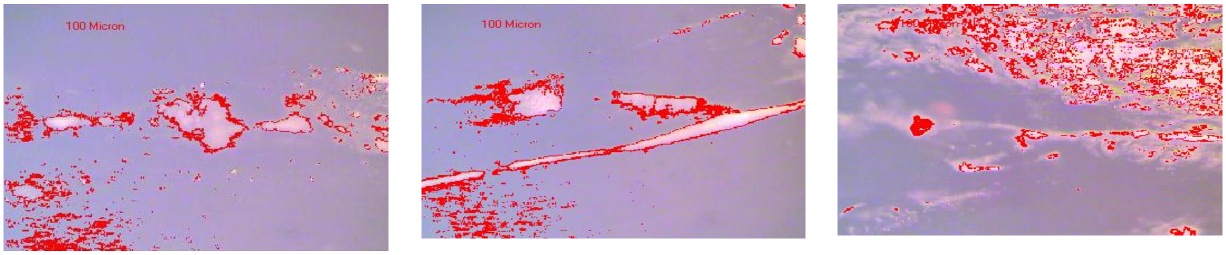

2.5% wood
Porosity 6.18%

5% wood
Porosity 7.59%

10% Wood
Porosity 9.75%

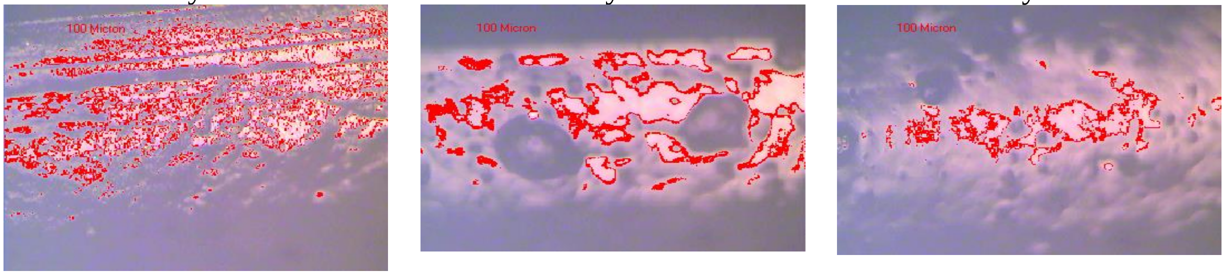

10% Fe3O4
Porosity 10.56%

15% Fe3O4
Porosity 8.94%

20% Fe3O4
Porosity 5.2%

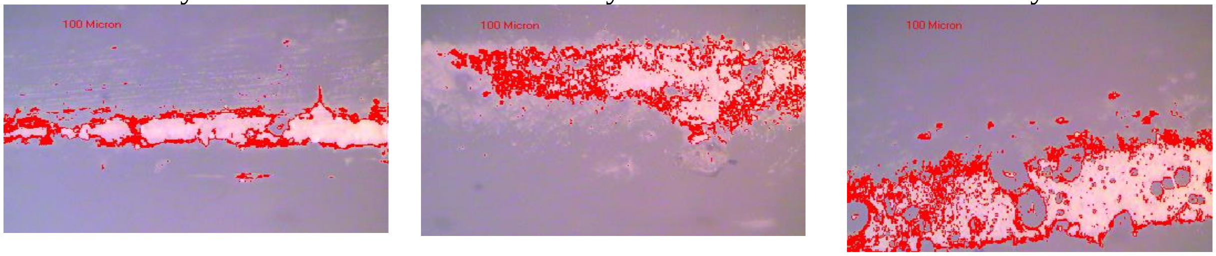

10% PVC
Porosity 5.25%

15% PVC
Porosity 7.91%

20% PVC
Porosity 9.59%

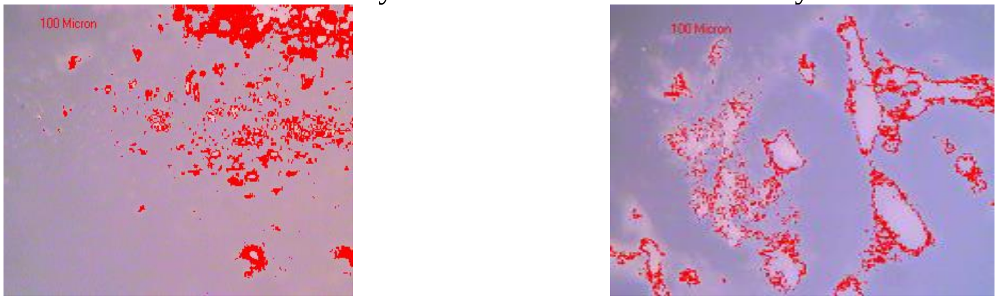

25% PVC
Porosity 11.74%

Multi Blend
Porosity 7.18%

Figure 5.30 MIAS porosity results of different PLA composites (at ×100)

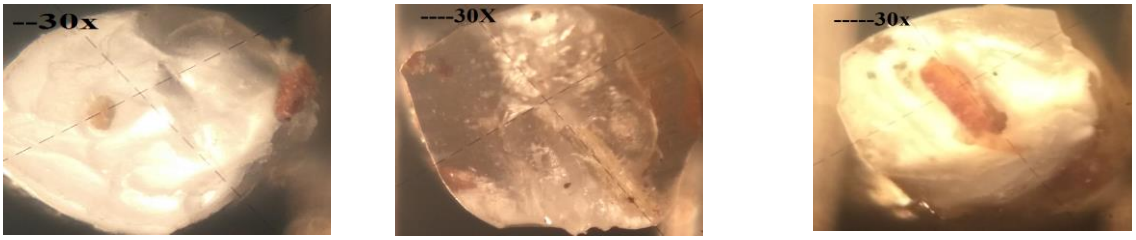

2.5% wood 5% wood 10% Wood

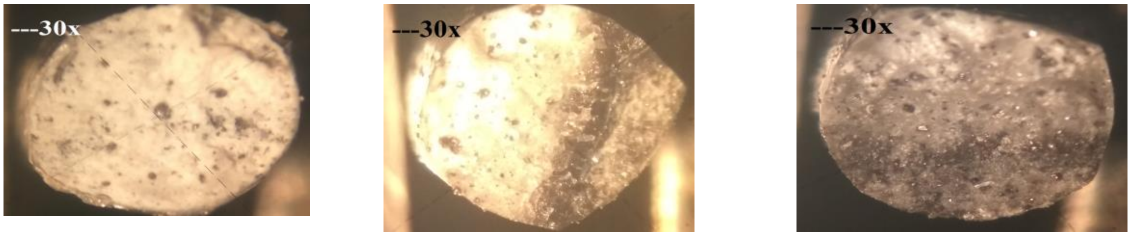

10% Fe_3O_4 15% Fe_3O_4 20% Fe_3O_4

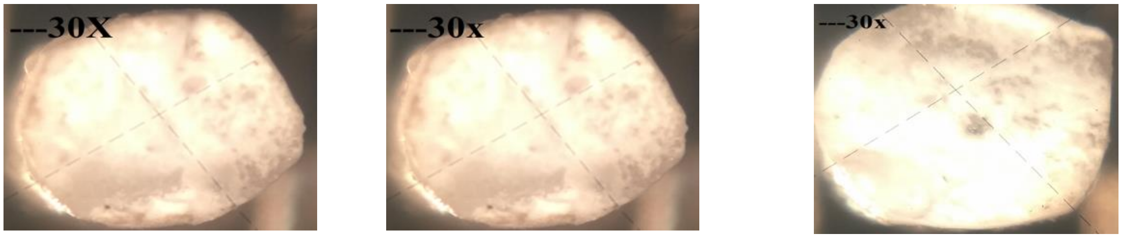

10% PVC 15% PVC 20% PVC

25% PVC Composite (microstructure cross-section)

Figure 5.31 Cross-sectional micro-structural view for different composites of PLA (at ×30)

5.2.6 DSC analysis

DSC of virgin PLA, PLA with 25 weight percentage PVC, PLA with 20% Fe_3O_4, PLA with 5% wood powder, and multi blend have been performed for thermal behavior prediction of PLA-based composites using 3 cycles of cooling and heating. Thermal analysis results suggested that all the samples were thermally stable as there was a marginal change in peak set and peak endpoints as shown in Figure 5.32. It was also observed that virgin PLA was the most stable as integral energy was less divergent for all the three cycles of DSC while for other reinforced samples onset and peak temperature was stable but integral energy was found to decrease significantly for the successive cycles of DSC testing.

5.2.7 VSM Analysis

The VSM has been performed for PLA with 20% magnetite content and multi blend for comparison for the magnetic property. From the VSM results, it has been found that magnetic properties were dependent on the Fe_3O_4 content present in the composite matrix while the presence of other foreign particles in the composite did not harm magnetic properties as shown in Figure 5.33. There were negligible changes in magnetic properties observed for the two samples.

5.2.8 Feasibility of 3D printing with prepared filaments

Feedstock filaments with TSE were tested for their feasibility in 3D printing using fused deposition modeling (FDM), one of the low-cost additive manufacturing techniques. FDM (Model: divide by zero) has been used for printing tensile specimen (ASTM D638 type IV) made of multi blend and flexural sample (ASTM D790) with infill density 100% infill speed 70 mm/s and infill angle of 45° as shown in Figure 5.34.

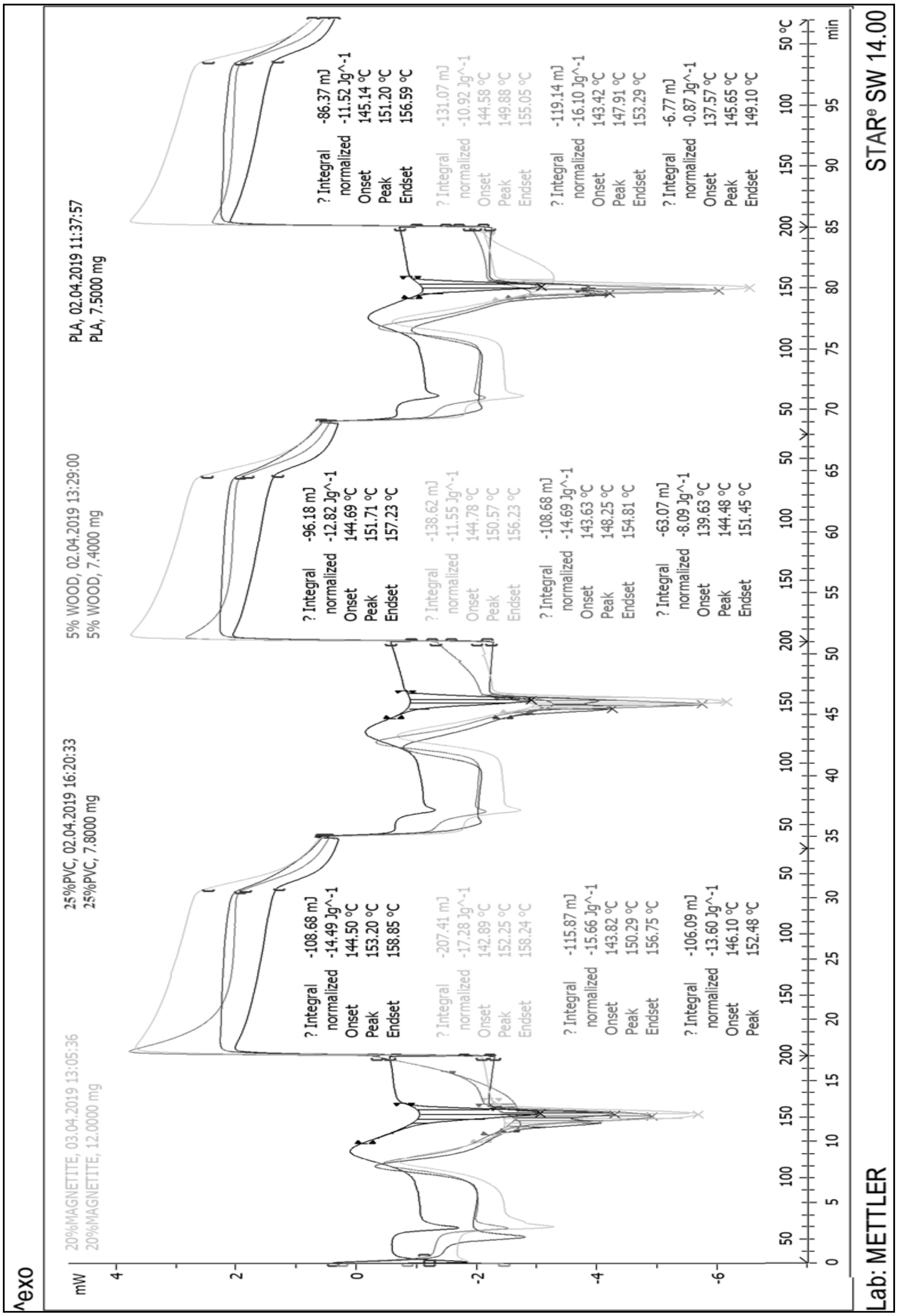

Figure 5.32 DSC for Virgin PLA and PLA composites

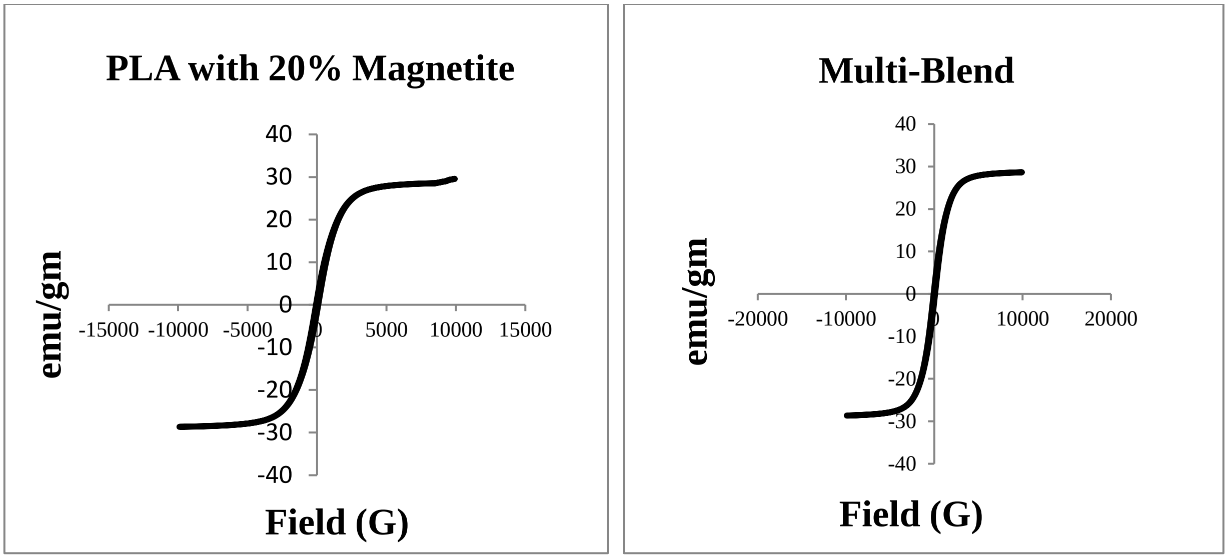

Magnetization	29.55 emu/g
Coercivity	84.61 Oersted (emu/g)
Retentivity	1.42E-02 Gauss

Magnetization	28.65 emu/g
Coercivity	74.54 Oersted (emu/g)
Retentivity	1.27E-02 Gauss

Figure 5.33 Hysteresis loop for (a) PLA with 20% Fe_3O_4 and (b) Multi-blend of PLA

.

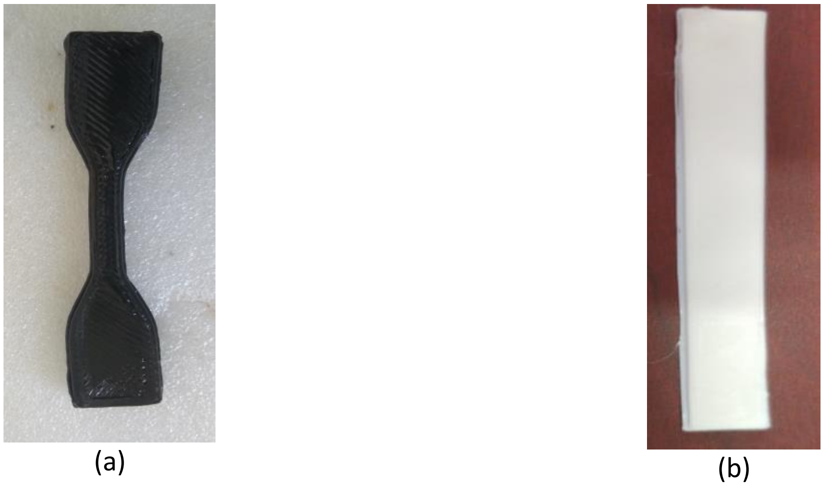
(a) (b)

Figure 5.34: 3D printed sample for (a) tensile specimen made from multi blend as per ASTM D638 Type IV and (b) flexural specimen made from PLA with 20% PVC as per ASTM D790

5.3 Results and discussion for stage 3

5.3.1 TSE results and FDM printing results for tensile samples

The TSE using standard conditions as selected at stage 1 were used for TSE of feedstock filament to develop sufficient length. Figure 5.35 (a) shows the working principle of twin-screw extrusion which consists of three phases. In stage 1, the solid phase, where material enters the barrel and was grounded by the mechanical action of the screw. In the second stage melting phase starts where due to temperature the ground material started melting. At the final stage, the melted material was forced out of the die with screw action. The standard wire of the required diameter for 3D printing as feedstock filament was obtained as shown in Figure 5.35 (b). Using the printing conditions as provided in Table 4.5, samples for tensile testing were printed using FDM with some constant parameters such as bed temperature 65°C, number of perimeters 3, rectangular perimeter, and triangular infill. Figure 5.36 shows the printed samples using FDM.

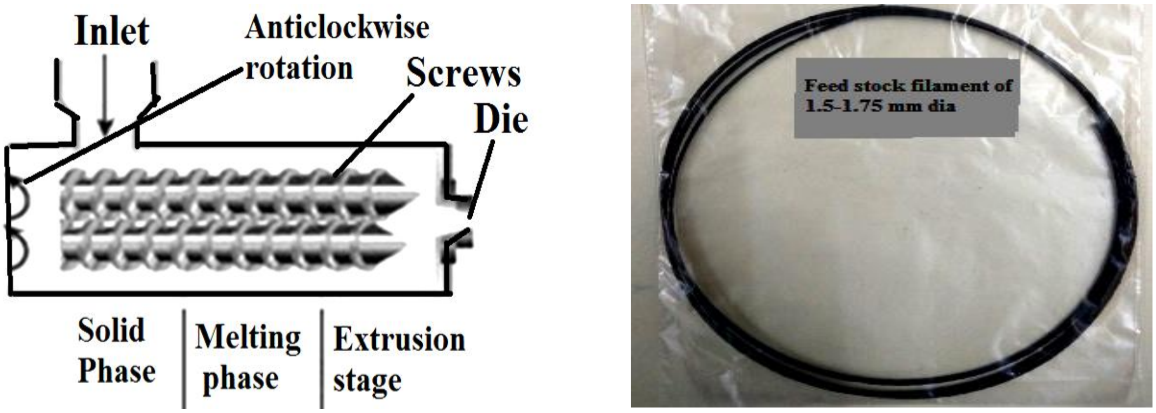

Figure 5.35 (a) Twin Screw Extrusion working principle and (b) extruded feedstock

Figure 5.36 3D Printed tensile specimens as per Table 4.5

5.3.2 UTM testing results of tensile samples

The samples tested with the UTM machine have given results for various mechanical properties but peak strength and break strength have been considered for analysis (Table 5.23). From Table 5.23 it has been figured out that the sample prepared at Serial number 7 has provided the best results for peak strength and break strength. Similarly, sample 5 has shown the least values for peak strength and break strength. The trend for these results may be because, in sample 7, the maximum density of 100 percent, 45° of infill angle, and moderate infill speed of 70 mm/s have been used which resulted in the better deposition of the material with minimum pores as the density was the maximum and orientation angle was the minimum. From the stress-strain curve (Figure 5.37), it has been found that the maximum value of stress exists for sample 7 whereas the minimum for sample 5. Based on Table 5.23, analysis of variance (ANOVA) has been used for predicting the optimized 3D printing parameter for maximum output. From the ANOVA analysis (Table 5.24), it has been observed that the model possesses an error, greater than 10% for each property which was not acceptable for the used confidence interval of 95%. Moreover, no input parameter was significant as the observed probability (p)values were greater than 0.05. But from the main effect plots (Figure 5.38), it was observed that infill density of the third level (100%), infill angle of the first level (45°), and infill speed of second level (70 mm/s) were found to be optimum. This was outside the DOE therefore confirmatory experiments were carried out and the properties were recorded. It has been already explored that Fe_3O_4, when blended in PLA matrix resulted in stiffer matrix and reduction in tensile properties such as 23% in peak strength and 24% in break strength of PLA. But the strain-absorbing capacity of Fe_3O_4 blended PLA was observed to increase by 183%.

The response table shows that infill density has contributed maximum towards peak strength and was ranked first followed by infill angle at 2nd and infill speed at 3rd rank as shown in Table 5.25. It has been observed that the input parameters were not significant, and the model possessed an error of more than 10% as given in Table 5.26. This indicated that either some missing parameters were not considered during the printing or there is an interaction between the two input parameters which has not been considered during ANOVA optimization. Figure 5.38 and Table 5.27 show the confirmatory experiment conducted at infill density of third level (100%), infill angle of the first level (45°), and infill speed of second level (70 mm/s).

Table 5.23 Peak strength, break strength, and young's modulus of tensile samples for 3D printed hybrid blend-based samples

Serial number	Peak Strength (MPa)	Break strength (MPa)
1	20.06 ± 1.13	18.05 ± 1.14
2	18.82 ± 1.23	16.94 ± 1.25
3	14.01 ± 1.03	12.61 ± 1.10
4	24.21 ± 1.20	21.79 ± 1.19
5	11.68 ± 1.02	10.02 ± 1.04
6	17.35 ± 1.23	15.61 ± 1.21
7	29.56 ± 1.25	26.60 ± 1.21
8	23.87 ± 1.22	23.03 ± 1.20
9	21.90 ± 1.21	19.71 ± 1.18

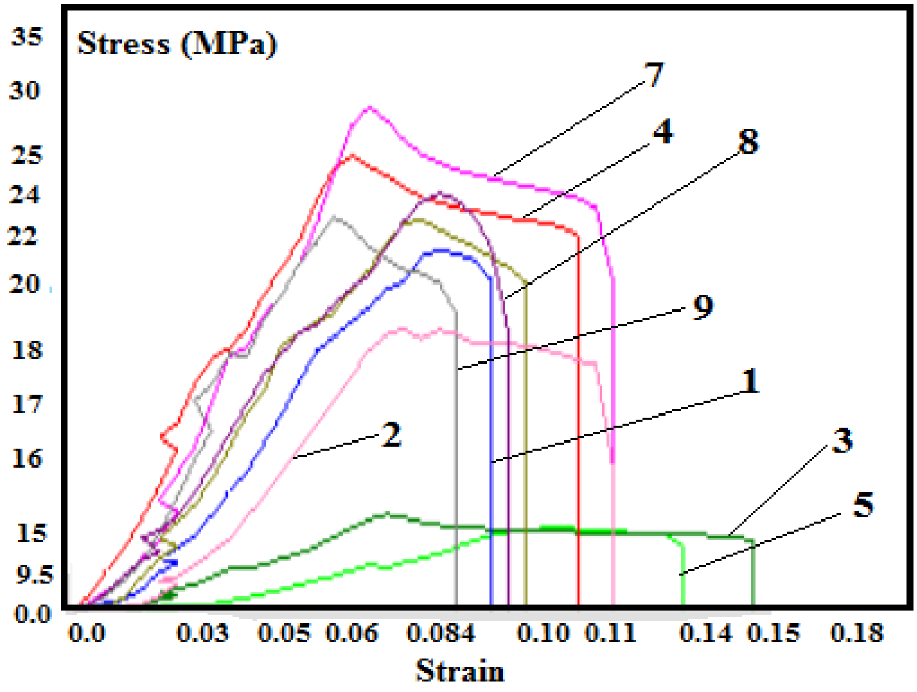

Figure 5.37 Stress vs. strain curve for tested samples as per Table 4.5

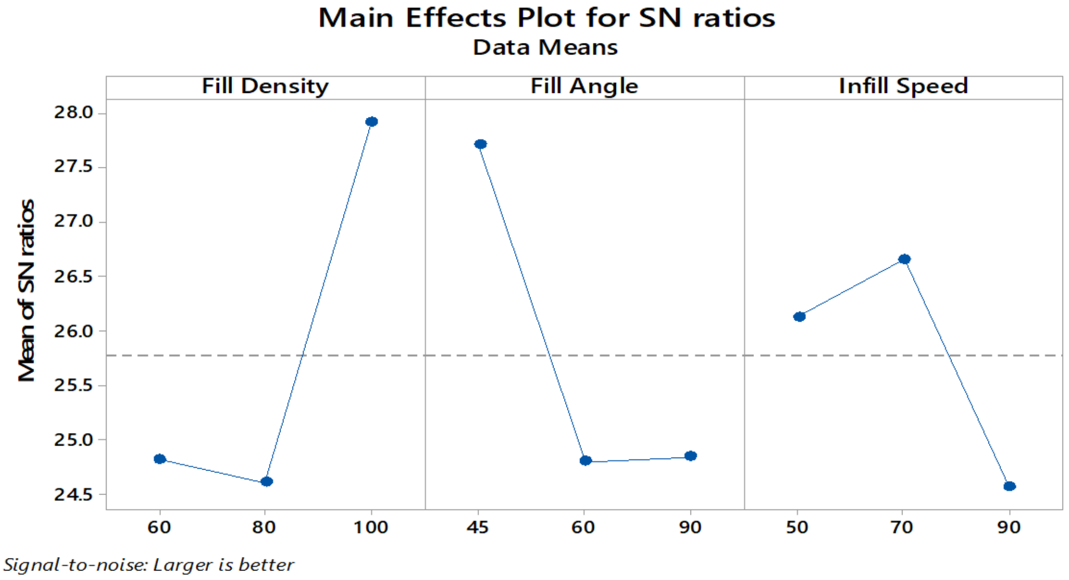

Figure 5.38 Main effect plot for SN ratio for peak strength of hybrid blend-based 3D printed sample

Table 5.24 ANOVA for peak strength for 3D printed hybrid blend-based samples

Source	DF	Seq SS	Adj SS	Adj MS	F	P
Fill Density	2	20.713	20.713	10.357	3.87	0.205
Fill Angle	2	16.740	16.740	8.370	3.13	0.242
Infill Speed	2	7.126	7.126	3.563	1.33	0.429
Residual Error	2	5.346	5.346	2.673		
Total	8	49.925				

Further, the data given in Table 5.23 has been used again for optimizing the 27 trails. Each setting was repeated three times and the historical data approach was used in optimizing the obtained output for the quadratic model. From the historical data approach (Table 5.28) analysis, it has been observed that interaction between parameters played an important role in the output (as those interactions were significant), as F values for some of the variables were greater than 50 or p-value less than 0.0001 and the model was also significant. The model Fisher's (F)-value of 59.73 implies that the model is significant. There is only a 0.01% chance that this F-value could occur due to noise. P-values less than 0.0500 indicate that the model terms are significant. In this case, B, AB, AC, BC, A^2, B^2 are the significant model terms. Values greater than 0.1000 indicate that the model terms are not significant. The Predicted R^2 of 0.9183 is in a reasonable agreement with the Adjusted R^2 of 0.9476; i.e., the difference is less than 0.2 (Table 5.29). Adequate precision measures the signal-to-noise ratio and the ratio greater than 4 is desirable. A ratio of 25.178 indicates an adequate signal.

This model can be used to navigate the design space. The predictability of historical optimization has been given by Figure 5.39, which shows that the predicted and actual values are very near hence the used model is accurate for the investigation of output properties. Based on the historical data approach, a regression equation has been obtained (Table 5.30) which was used to plot the 3D curve so that the effect of input parameters may be analyzed. Using equation 1 for peak strength, the 3D plot for input parameters infill density and infill angle has been obtained. The base shells of the 3D plot (Figure 5.40) signify that choosing a low value of infill angle and high value of infill density produces maximum peak strength while taking the third parameter (infill speed) constant as it contributed the least towards the output.

Table 5.25 Rank table for SN ratio for peak strength for 3D printed hybrid blend-based samples

Level	A	B	C
1	24.82	27.71	26.13
2	24.60	24.80	26.66
3	27.93	24.84	24.56
Delta	3.32	2.91	2.10
Rank	1	2	3

Table 5.26 Error in ANOVA model for all properties for 3D printed hybrid blend-based samples

Property	Peak Strength	Break Strength
Percentage error	11%	12%

Table 5.27 Confirmatory experiment results for 3D printed hybrid blend-based samples

Property	Peak Strength (MPa)	Break Strength (MPa)
Confirmatory experiment	30.29	25.58

Table 5.28 ANOVA for Quadratic model using the historical approach for 3D printed hybrid blend-based samples

Source	Sum of Squares	Degree of freedom	Mean Square	F-value	p-value	Significant/Not Significant
Model	722.97	8	90.37	59.73	< 0.0001	significant
A-A	2.47	1	2.47	1.63	0.2177	
B-B	193.76	1	193.76	128.07	< 0.0001	
C-C	1.57	1	1.57	1.04	0.3215	
AB	29.61	1	29.61	19.57	0.0003	
AC	71.32	1	71.32	47.14	< 0.0001	
BC	94.29	1	94.29	62.32	< 0.0001	
A^2	171.56	1	171.56	113.40	< 0.0001	
B^2	157.55	1	157.55	104.14	< 0.0001	
C^2	0.0000	0				
Pure Error	27.23	18	1.51			
Cor Total	750.20	26				

Table 5.29 Fit Statistics for peak strength for 3D printed hybrid blend-based samples

Std. Dev.	1.23		R^2	0.9637
Mean	20.16		Adjusted R^2	0.9476
C.V. %	6.10		Predicted R^2	0.9183
			Adeq Precision	25.1781

Table 5.30 Regression equation for peak strength, break strength, and modulus of elasticity for 3D printed hybrid blend-based samples

Peak Strength	$= +5.72+ +0.6142\times A-7.56\times B-0.3979\times C+3.33\times A\times B-8.27\times A\times C-7.87\times B\times C+8.87\times A^2+10.93\times B^2 +0.0000\times C^2$
Break strength	$= +5.08 + 0.8150\times A - 6.99\times B + -0.8037\times C + 2.74\times A\times B - 7.82\times A\times C - 7.00\times B\times C+8.35\times A^2+9.72\times B^2+0.0000\times C^2$
Modulus of Elasticity	$= +114.21 - 8.13\times A - 36.79\times B - 9.18\times C + 37.64\times A\times B - 37.50\times A\times C - 49.10\times B\times C + 37.28\times A^2 + 54.51\times B^2 + 0.0000\times C^2$

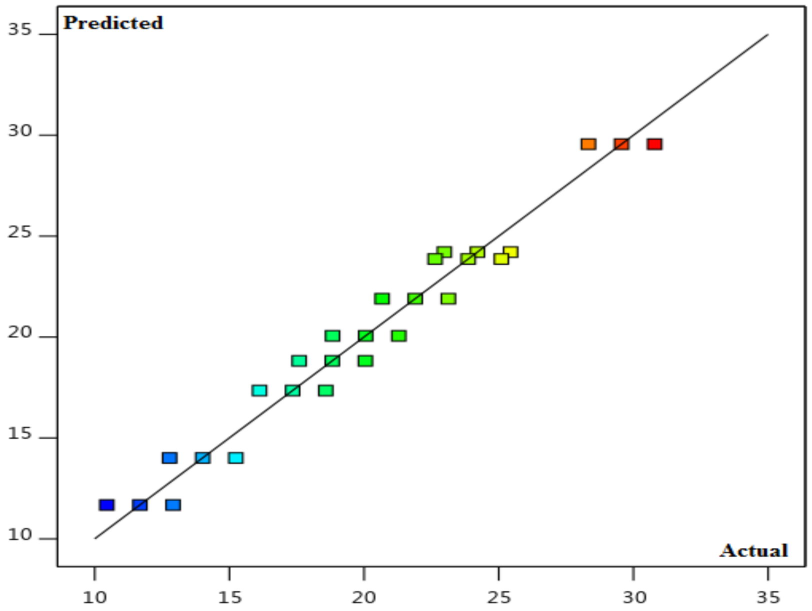

Figure 5.39 Predicted vs. Actual graph for peak strength of hybrid blend based 3D printed sample

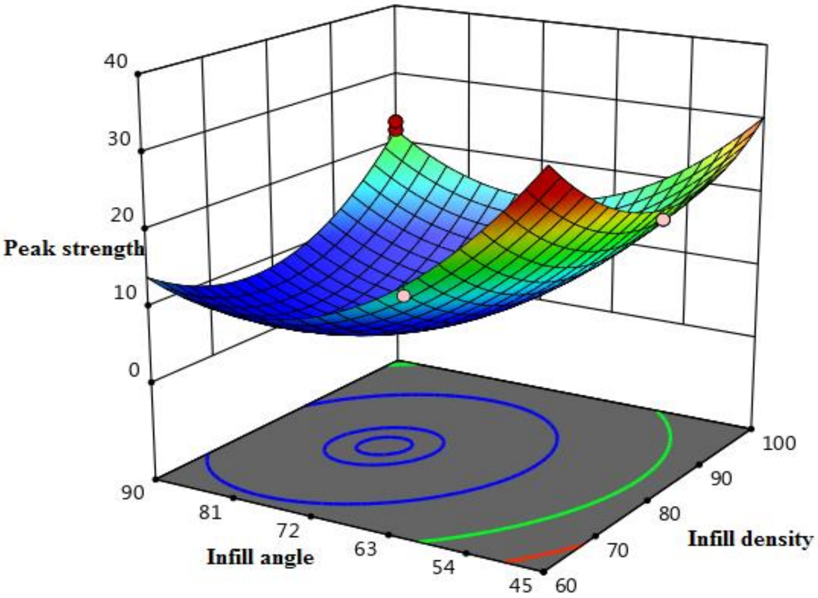

Figure 5.40 3D surface plot for peak strength of hybrid blend-based 3D printed sample

5.3.3 Shore D hardness of tensile samples

3D printed samples were subjected to shore D hardness testing and the hardness values for all 9 samples have been given in Figure 5.41 which indicates that the hardness of samples is related to mechanical properties. The samples which have shown better peak strength and break strength hardness have also shown a better trend. Moreover, the high hardness of samples reflected the low values of porosity.

5.3.4 Porosity results of tensile samples

All UTM tested parts were then subjected to porosity testing using photomicrographic analysis at ×100 magnification and it was observed that sample 7 has the least porosity value (Figure 5.42) of 6.02% and maximum value of porosity was possessed by sample 5 (16.12 %). This indicated that the porosity values of the samples have a direct correlation with the mechanical properties. It is a fact that in general, the high porosity of a structure leads to poor mechanical properties. Thus, the low structural porosity of 3D printed samples has shown better resistance towards fracture.

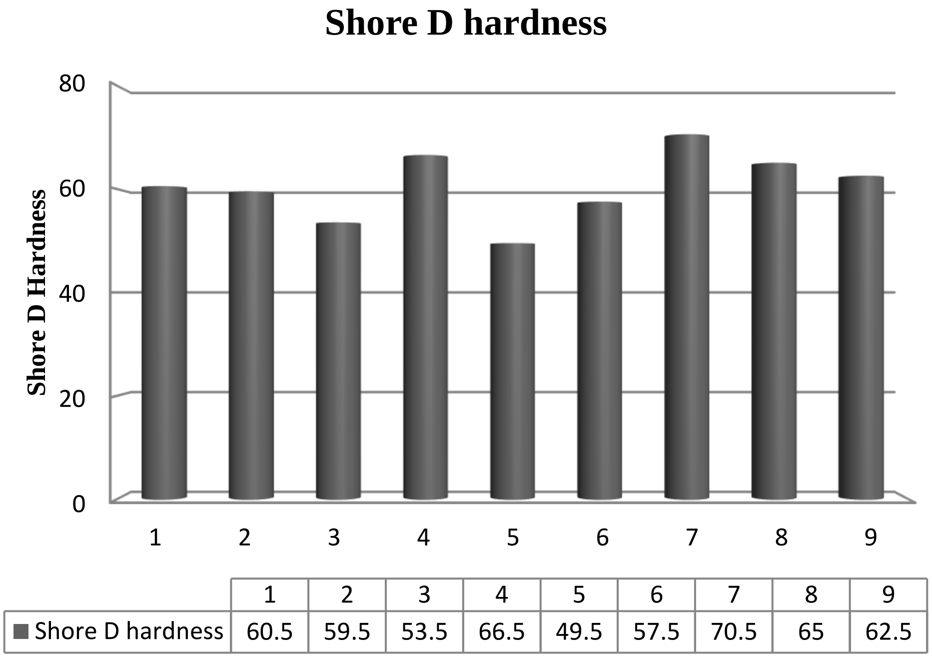

	1	2	3	4	5	6	7	8	9
■ Shore D hardness	60.5	59.5	53.5	66.5	49.5	57.5	70.5	65	62.5

Figure 5.41 Shore D hardness results of printed samples as per Table 4.5

Serial number	Metallurgical image analysis software (MIAS) image	Percentage Porosity
1	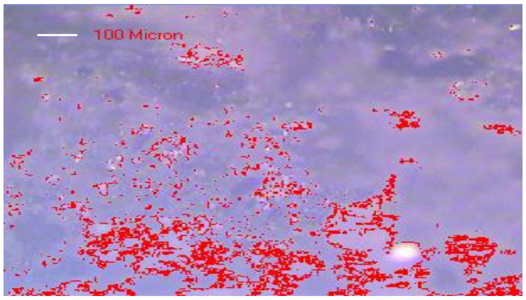	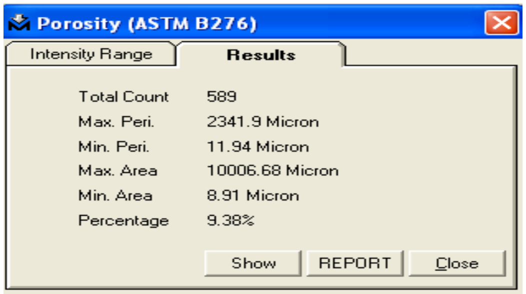 Total Count 589 Max. Peri. 2341.9 Micron Min. Peri. 11.94 Micron Max. Area 10006.68 Micron Min. Area 8.91 Micron Percentage 9.38%
2	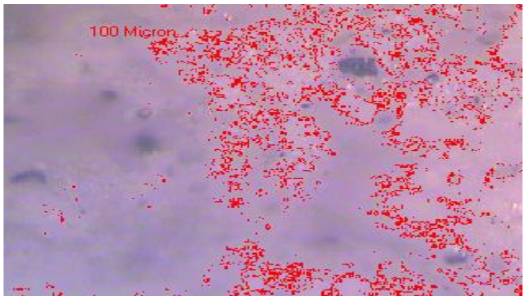	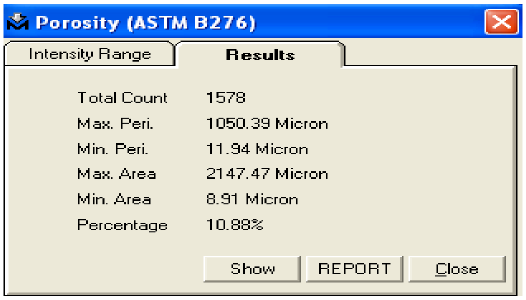 Total Count 1578 Max. Peri. 1050.39 Micron Min. Peri. 11.94 Micron Max. Area 2147.47 Micron Min. Area 8.91 Micron Percentage 10.88%
3	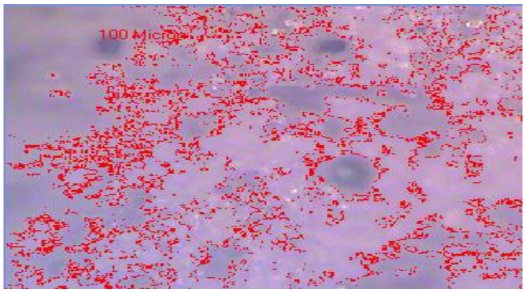	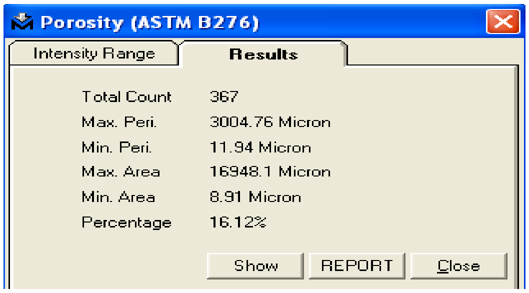 Total Count 367 Max. Peri. 3004.76 Micron Min. Peri. 11.94 Micron Max. Area 16948.1 Micron Min. Area 8.91 Micron Percentage 16.12%
4	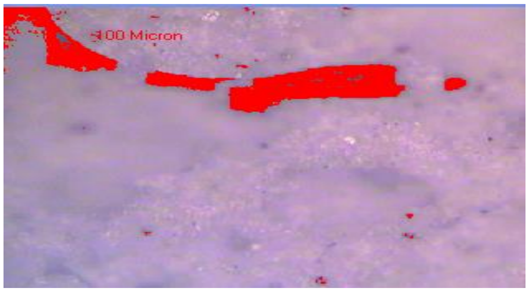	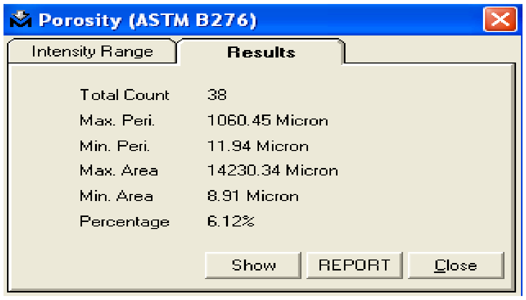 Total Count 38 Max. Peri. 1060.45 Micron Min. Peri. 11.94 Micron Max. Area 14230.34 Micron Min. Area 8.91 Micron Percentage 6.12%
5	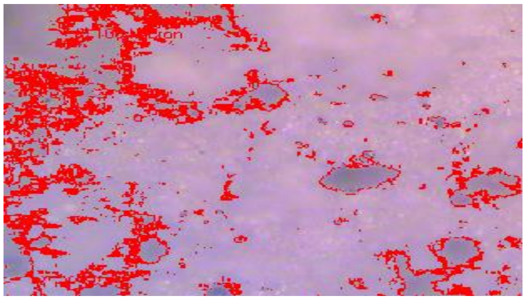	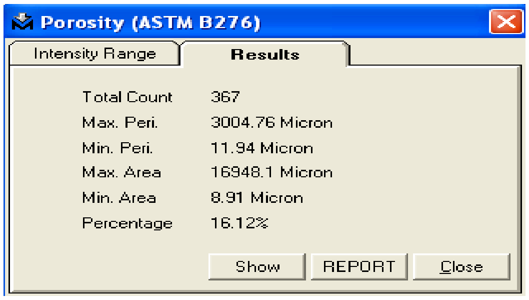 Total Count 367 Max. Peri. 3004.76 Micron Min. Peri. 11.94 Micron Max. Area 16948.1 Micron Min. Area 8.91 Micron Percentage 16.12%

6

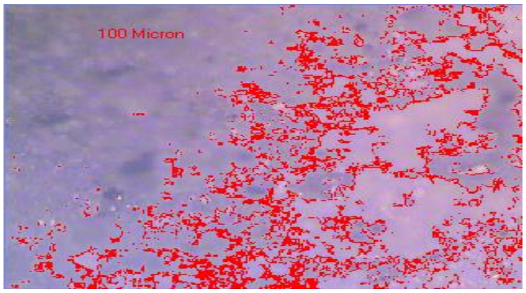

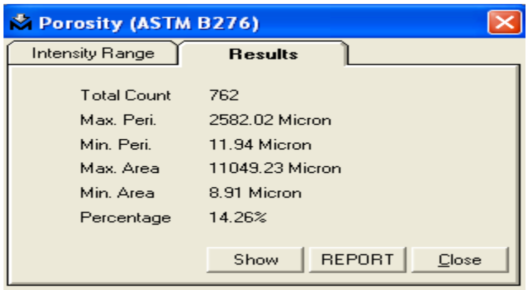

Porosity (ASTM B276)

Total Count	762
Max. Peri.	2582.02 Micron
Min. Peri.	11.94 Micron
Max. Area	11049.23 Micron
Min. Area	8.91 Micron
Percentage	14.26%

7

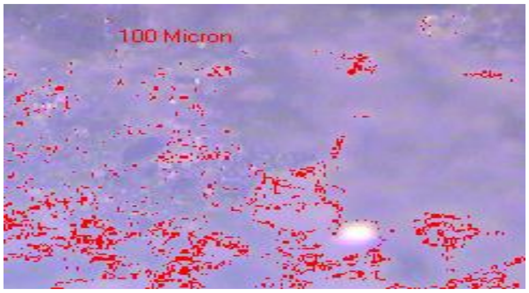

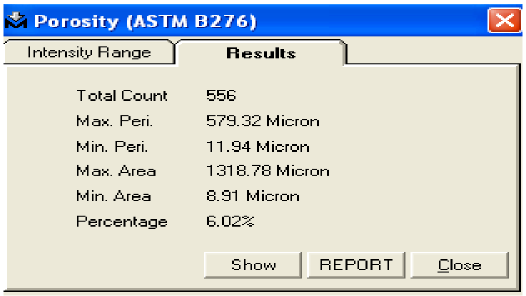

Porosity (ASTM B276)

Total Count	556
Max. Peri.	579.32 Micron
Min. Peri.	11.94 Micron
Max. Area	1318.78 Micron
Min. Area	8.91 Micron
Percentage	6.02%

8

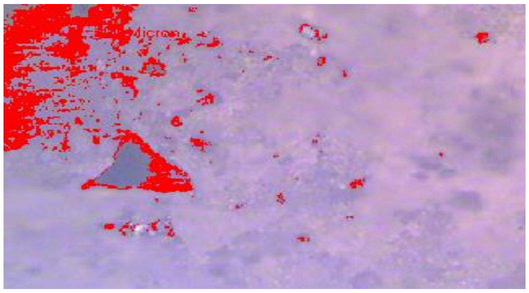

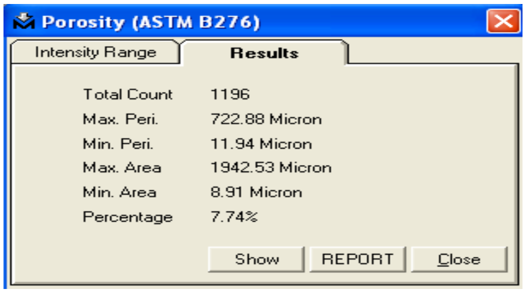

Porosity (ASTM B276)

Total Count	1196
Max. Peri.	722.88 Micron
Min. Peri.	11.94 Micron
Max. Area	1942.53 Micron
Min. Area	8.91 Micron
Percentage	7.74%

9

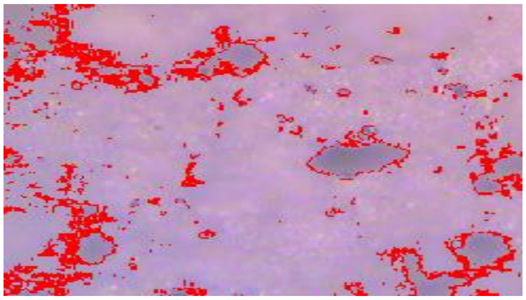

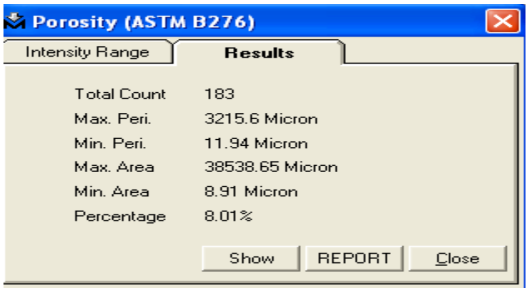

Porosity (ASTM B276)

Total Count	183
Max. Peri.	3215.6 Micron
Min. Peri.	11.94 Micron
Max. Area	38538.65 Micron
Min. Area	8.91 Micron
Percentage	8.01%

Figure 5.42 Porosity results of fractured samples (at ×100) as per Table 4.5

5.3.5 Micrographs of the fractured surface of tensile samples

The fractured samples (prepared as per Table 4.5) were tested on the tool maker’s microscope at ×30 magnification and photomicrographs were taken which indicate that the porosity holes are present on the surface as shown by Figure 5.43. For better clarity, photomicrographs observed in Figure 5.43 were re-processed for 3D rendering and surface roughness (Ra) analysis (Figure 5.44). As observed from Figure 5.44 (a –d) for samples with poor and best mechanical properties (i.e., samples prepared at serial numbers 5 and 7 as per Table 3), a more uniformly distributed structure with less Ra may be the key factor for controlling the mechanical properties.

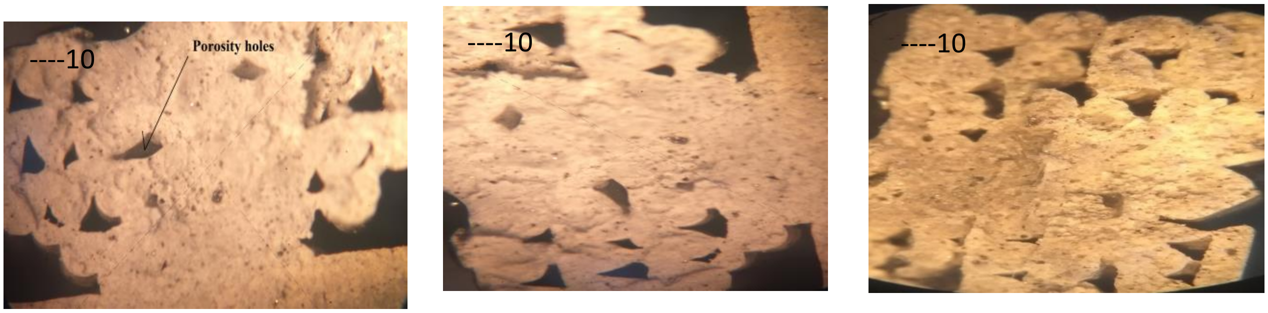

Experiment 1 Experiment 2 Experiment 3

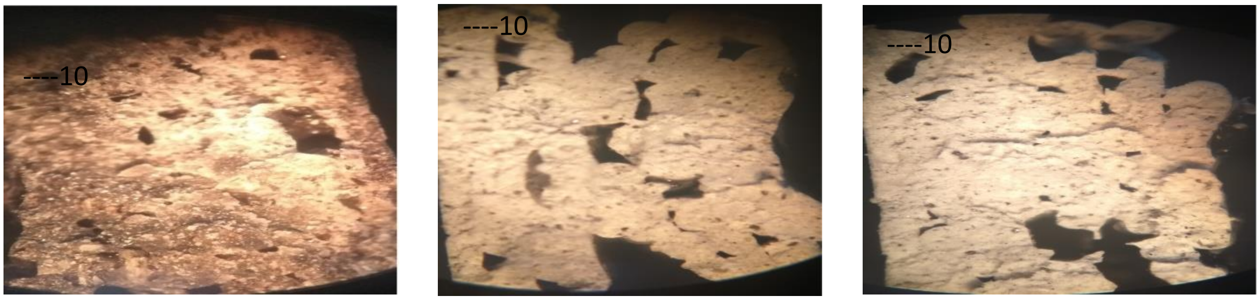

Experiment 4 Experiment 5 Experiment 6

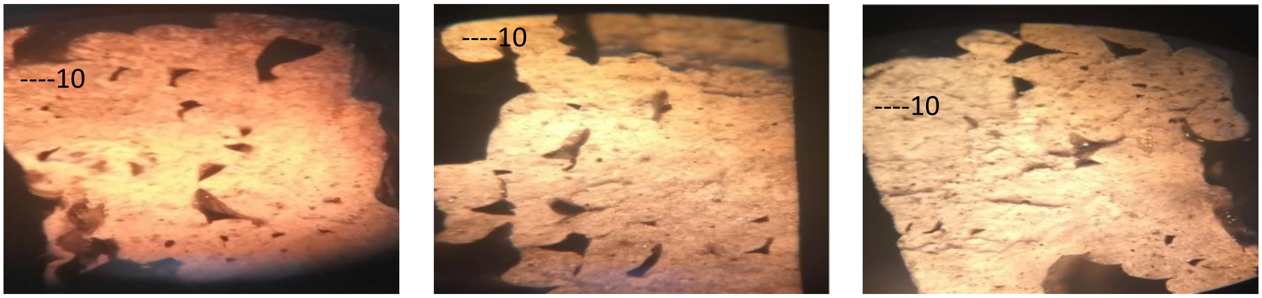

Experiment 7 Experiment 8 Experiment 9

Figure 5.43 Photomicrographs at x32 for fractured surface as per Table 4.5

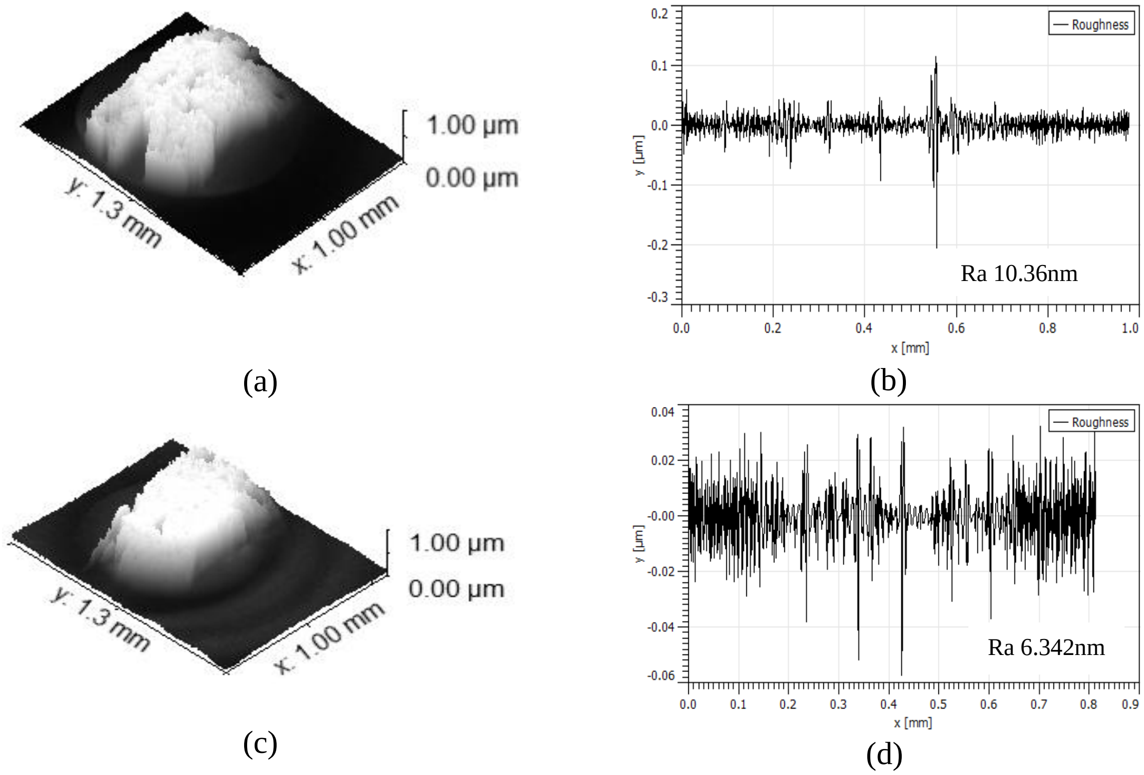

(a) (b)

(c) (d)

Fig. 5.44 (a) 3D Rendered photo-micrographic image for sample No. 5, (b) Ra profile for sample no. 5, (c) 3D Rendered photo-micrographic image for the sample prepared at Serial number 7, and (d) Ra profile for the sample prepared for sample no. 7 as per Table 4.5

5.3.6 SEM and EDAX characterization of the fractured surface of the hybrid blended matrix-based 3D printed prototype

The fractured samples on the UTM machine were subjected to SEM characterization so that the internal surface of 3D printed samples may be observed for correlation of mechanical properties with surface characteristics. Four different images were taken using different magnification varying from ×500 to ×3000 magnification scale for a 3D printed specimen/prototype made of the hybrid blended matrix. Figure 5.45 shows the SEM images of the prototype made of the hybrid blended matrix. It has been observed that several circular-shaped voids are present on the fractured surface which resulted in poor strength among the prepared composite particles using mechanical mixing, ultimately resulting in poor bonding of layers. Fig. 5.45 (e) shows the EDAX report of the hybrid blended matrix-based prototype (3 different spectrum (surface) were selected to observe the elemental composition present on the surface under observation) which specifies the presence of different atoms of carbon (due to PLA and PVC polymeric blend), chlorine (due to PVC) and

Fe (due to magnetite powder) throughout the surface of the observed fractured specimen which justifies the hybrid blending.

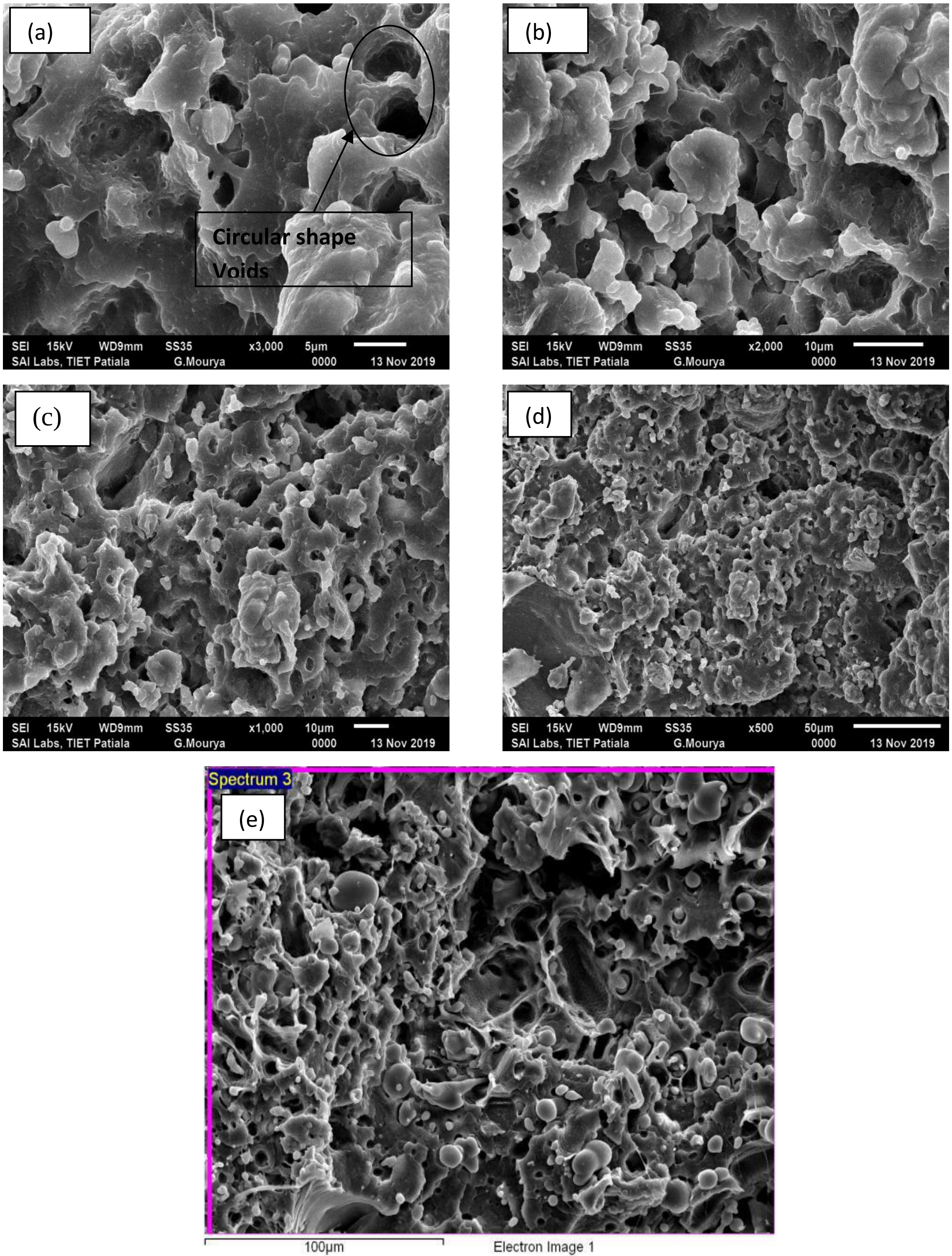

Spectrum	In Stats	C	O	Cl	Fe	Total
Spectrum 1	Yes	70.04	4.01	25.70	0.26	100.00

Spectrum 2	Yes	57.10	33.00	9.41	0.48	100.00
Spectrum 3	Yes	55.91	33.83	9.93	0.32	100.00

Figure 5.45 SEM image (a) at ×3000, (b) at ×2000, (c) at ×1000, (d) at ×500 magnification, and (e) EDS spectrum selected for elemental composition of fractured surface for hybrid blend based composite matrix

5.3.7 3D printing results for flexural specimens

Figure 5.46 shows the 3D printed flexural specimens as per ATSM D790 with in-house prepared composite feed-stock filament (as per stage 1).

Figure 5.46 3D printed flexural specimens as per Table 4.5

5.3.8 Flexural testing results for flexural specimen

For all the printed specimens, flexural test and pull-out test have been performed and properties recorded using the UTM interface on the machine as given by Table 5.31 and Table 5.32. For those values, the properties were analyzed using ANOVA to calculate the signal to noise (SN) ratios of properties (Table 5.33) for larger the better type case. As observed from Table 5.34, it was clear that the model was accurate as the percent residual error (2.13 %) was less than 5%, and the infill angle input parameter was also significant (P-value < 0.05). From rank Table 5.35, it was observed that the effect of infill angle was the most prominent as it was ranked 1st, infill density was ranked at 2nd and infill speed was the least significant for the process of printing. Stress Vs. strain relationship, as seen from Figure 5.47 (flexural tested samples), clearly demarcates the difference among printed samples (with different conditions). Sample at Serial number7 (Table 5.31) has shown maximum strain as well as stress. Similarly, from Figure 5.48 (pull-out tested samples) a similar trend was observed.

From the main effect plot (see Figure 5.49), it was ascertained that infill density of 100%, infill angle of 45°, and infill speed of 70 mm/s was the optimized condition for a peak load of the flexural property but a critical point was noticed that the required set of conditions were out of the design of experimentation. Therefore, it was necessary to perform a set of experimentation with the optimized condition. With optimized conditions, experimentation was performed and actual values of each property were obtained by flexural and it was found that the predicted and actual results were very close to each other as seen from Table 5.36.

Table 5.31 Flexural properties of FDM based 3D printed samples with standard deviation for hybrid blend-based sample

Flexural Properties						
Serial number	PL	PE	BL	BE	PS	BS
1	12.7±1.21	7.61±0.31	13.11±1.20	14.56±1.01	9.16±1.01	9.46 ±1.01
2	11.2±1.04	5.98±0.15	10.08±1.01	10.24±1.56	8.08±0.65	7.27 ±1.05
3	7.8±0.65	1.99±0.08	5.06±0.56	4.55±1.20	5.63±0.21	3.65±0.51
4	18.1±2.21	7.89±0.51	16.29±1.42	15.77±3.32	13.06±2.21	11.75 ±1.04
5	11.7±1.21	6.84±0.21	10.53±1.35	13.49±1.67	8.44 ±1.01	7.60 ±0.51
6	8.1±1.03	2.66±0.11	5.67±1.05	6.65±1.45	5.84 ±1.03	4.09 ±0.56
7	19.6±3.10	8.23±1.35	17.64±2.21	20.47±3.35	14.14±2.52	12.72±2.35
8	14.2±2.21	6.35±0.74	12.78±1.67	17.52±3.20	10.24 ±1.67	9.22 ±1.53
9	9.78±0.65	3.2±0.24	7.8±1.05	7.84±1.14	7.05 ±0.65	5.63±0.58

Note: PL: Peal Load; PE: Peak Elongation; BL: Break Load; BE: Break Elongation; PS: Peak Strength; BS: Break Strength. It should be noted that each sample was printed with 3 repetitions on the FDM setup so that deviation in properties may also be reported.

Table 5.32 Pull out properties FDM based 3D printed samples with standard deviation for hybrid blend-based sample

Pull Out Properties						
Serial number	PL	PE	BL	BE	PS	BS
1	50.21±4.52	32.45±3.54	48.21±4.20	30.4±3.54	36.22 ±4.52	34.78 ±2.65
2	45.21±3.54	29.13±4.52	40.12±3.14	28.56±4.52	32.61 ±3.54	28.94 ±3.54
3	42.23±3.12	26.12±4.01	38.54±3.54	25.87±3.61	30.46 ±2.65	27.80 ±4.52
4	55.05±5.54	32.15±4.52	52.14±4.52	34.18±3.54	39.71 ±3.54	37.61 ±2.65
5	50.23±4.52	28.12±3.54	46.24±3.61	30.61±4.52	36.23 ±4.52	33.35 ±3.54
6	40.63±3.12	24.13±2.36	38.62±3.54	28.51±3.54	29.31 ±3.54	27.86 ±4.52
7	63.41±4.85	40.12±4.52	59.91±4.52	40.12±3.61	45.74±3.42	43.21±3.67
8	59.54±3.12	35.26±2.81	55.63±3.54	36.54±4.52	42.95±2.65	40.13 ±3.54
9	56.23±4.52	33.85±3.54	50.84±4.52	32.12±3.61	40.56 ±4.52	36.67 ±4.52

Table 5.33 SN ratios for tested samples for flexural and pull-out properties for hybrid blend-based sample

SN ratios for Flexural properties (dB)						
Serial number	PL	PE	BL	BE	PS	BS
1	22.08	17.63	22.35	23.26	19.24	19.52
2	20.98	15.53	20.07	20.21	18.15	17.23
3	17.84	5.98	14.08	13.16	15.00	11.25
4	25.15	17.94	24.24	23.96	22.32	21.40
5	21.36	16.70	20.45	22.60	18.53	17.62
6	18.17	8.50	15.07	16.46	15.33	12.23
7	25.85	18.31	24.93	26.22	23.01	22.09
8	23.05	16.06	22.13	24.87	20.21	19.29
9	19.81	10.10	17.84	17.89	16.97	15.01
SN ratios for Pull out properties						

Serial number	PL	PE	BL	BE	PS	BS
1	34.02	30.22	33.66	29.66	31.18	30.83
2	33.10	29.29	32.07	29.12	30.27	29.23
3	32.51	28.34	31.72	28.26	29.68	28.88
4	34.82	30.14	34.34	30.68	31.98	31.51
5	34.02	28.98	33.30	29.72	31.19	30.46
6	32.18	27.65	31.74	29.10	29.34	28.90
7	36.04	32.07	35.55	32.07	33.21	32.71
8	35.50	30.95	34.91	31.26	32.66	32.07
9	35.00	30.59	34.12	30.14	32.16	31.29

Table 5.34 Analysis of Variance for SN ratios for peak load (Flexural property) for hybrid blend-based sample

Source	DF	Seq SS	Adj SS	Adj MS	F	P
Infill Density	2	10.131	10.131	5.0654	7.62	0.116
Infill Angle	2	49.830	49.830	24.9150	37.47	0.026
Infill Speed	2	1.215	1.215	0.6074	0.91	0.523
Residual Error	2	1.330	1.330	0.6649		
Total	8	62.505				

DF: Degree of freedom; Seq SS: sum of the square; Adj SS: adjusted sum of the square; F: Fisher value; P: Probability

Table 5.35 Response table for SN ratios for peak load (Flexural Property) for hybrid blend-based sample

Level	Infill density	Infill angle	Infill speed
1	20.30	24.36	21.10
2	21.56	21.80	21.98
3	22.90	18.61	21.68
Delta (Difference between maximum and minimum observed value)	2.60	5.75	0.88

Rank	2	1	3

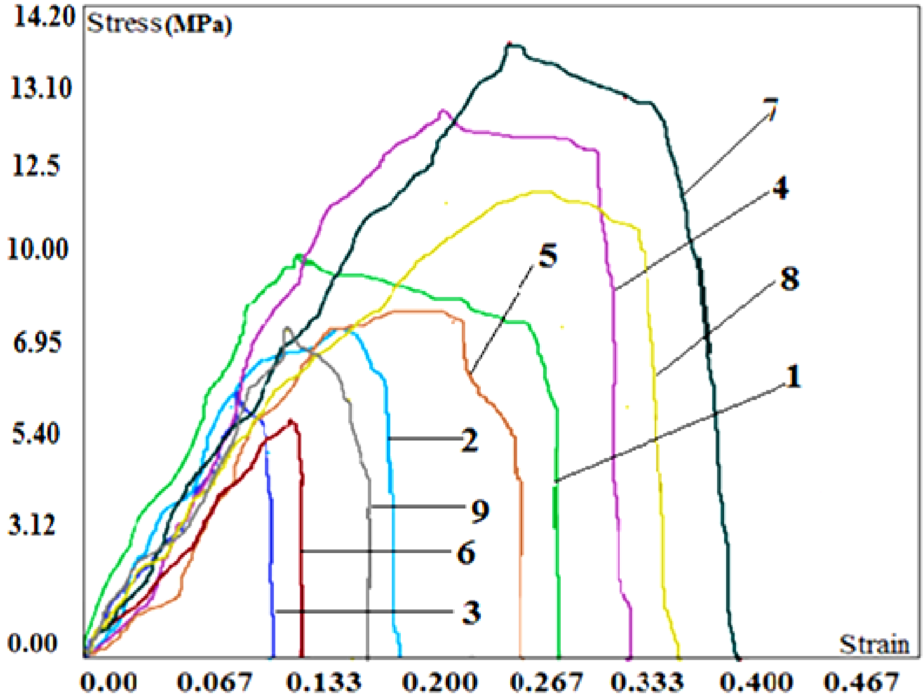

Figure 5.47 Stress Vs strain diagram for samples for flexural testing as per Table 4.5

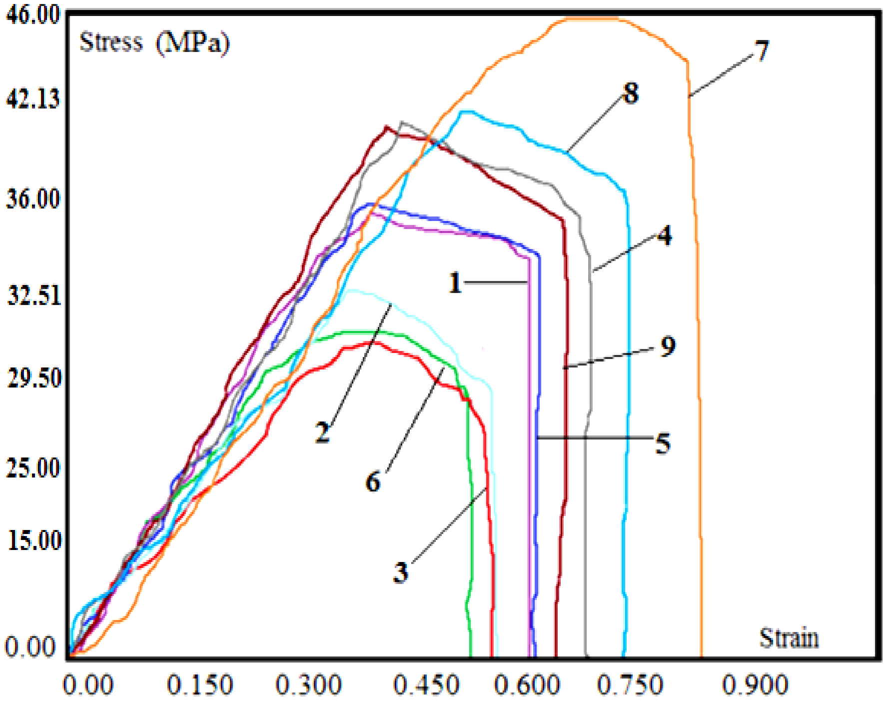

Figure 5.48 Stress Vs strain diagram of samples for pull out testing as per Table 4.5

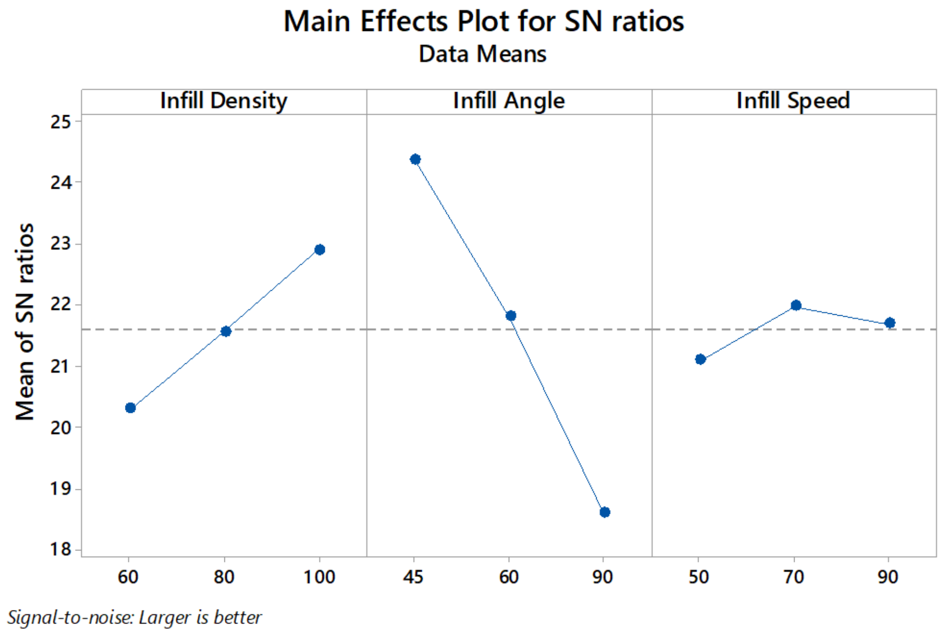

Figure 5.49 Main effect plot for SN ratio for peak load (for flexural specimen) for hybrid blend-based specimens

5.3.20 Optimization for the flexural and pull-out properties using ANOVA statistical tool

Note: m_A, m_B, and m_C are the maximum values of input processing parameters from Table 5.35.

K= mean of SN values for peak load analysis= 21.59

$$Ŋ\ (\mathrm{opt}) = \mathrm{m} + (\mathrm{ma} - \mathrm{m}) + (\mathrm{mb} - \mathrm{m}) + (\mathrm{mc} - \mathrm{m})$$

$$\mathrm{ma} = 22.90$$

$$mb = 24.36$$

$$mc = 21.98$$

Putting these values in the below equation

$$Ŋ\ \mathrm{opt} = 26.06$$

$$Y_{opt}^{2} = (10)^{Ŋ\frac{\mathrm{opt}}{10}} \ldots\ldots\ldots\ldots\ldots\ldots \text{for larger is the better case}$$

$$\mathrm{Y}_{\mathrm{opt}}^{2} = (10)^{26.06/10}$$

$$Y_{opt}^{2} = 403.65$$

$$Y_{opt} = 20.09\ dB$$

Similar studies have been performed for all other properties and predicted values have been found and compared with actual observed values for flexural and pull-out properties (see Table 5.36).

A multifactor optimization tool for all the SN values (Table 5.33) of flexural properties and pull-out properties were applied individually to know the best and the worst conditions of printing from which it was found that sample 7 was the best among all and sample 3 were the worst of all for flexural and pull-out properties (Table 5.37).

Table 5.36 Actual Vs predicted optimum values for each property of flexural specimen for hybrid blend-based sample

Flexural properties								
Serial number	Properties	K_a	K_b	K_c	K	Ŋ$_{opt}$	$Y_{(opt)}$ (predicted)	Y(actual)
1	Peak load	22.90	24.36	21.98	21.59	26.06	20.09	19.56
2	Peak elongation	14.82	17.96	14.53	14.08	19.15	9.07	10.24
3	Break load	21.63	23.84	20.72	20.13	25.93	19.79	19.65
4	Break elongation	22.99	24.48	21.53	20.96	27.08	22.59	20.93
5	Peak strength	20.06	21.52	19.14	18.75	23.22	14.49	15.54
6	Break strength	18.80	21.00	17.88	17.29	23.10	14.29	14.24
Pull out properties								
1	Peak load	35.51	34.96	34.31	34.13	36.52	66.99	68.54
2	Peak elongation	31.2	30.81	30.01	29.8	32.42	41.78	40.41
3	Break load	34.86	34.52	33.52	33.49	35.92	62.52	61.49
4	Break elongation	31.15	30.8	30.01	30	31.96	39.63	38.95
5	Peak strength	32.68	32.12	31.47	31.29	33.69	48.36	47.54
6	Break strength	32.02	31.68	30.69	30.65	33.09	45.13	44.59

Table 5.37 SN values for multifactor optimization of flexural and pull-out properties for hybrid blend-based sample

Multi-factor optimization	S. No 1	S. No 2	S. No 3	S. No 4	S. No 5	S. No 6	S. No 7	S. No 8	S. No 9

SN value (Flexural)	26.18	25.29	20.44	26.87	25.67	22.23	27.18	26.15	23.54
SN value (Pull out)	29.96	29.66	29.47	30.13	29.86	29.48	30.50	30.30	30.12

Experiment number 7 as shown by Table 5.37 has resulted in the best mechanical (flexural, pull-out properties). This sample was subjected to a Creo commercial structural analysis package for flexural testing (Figure 5.50). From rank Table 5.35, it was clear that the printed sample with an infill angle of 45° and infill density of 100% has given optimum result. This behavior may be attributed to the fact that the flexural testing instrument applies destruction force perpendicular to the surface (Figure 5.50) but the printed part had solid layers at 45° and high infill density provided low porosity due to which when destructing force is applied, the layers were strong enough to absorb the maximum load and thus provided the best results. In the case with printed part at 90° orientation, the layers were parallel to the destructing force and the strain was maximum at the lowest layer. Thus, the layer got separated easily due to which that sample was not capable of resisting applied load and get destroyed easily. It was noticed that with an increase in infill angle from 45-90°, the strength of printed samples decreased whereas with increasing infill density from (60-100 %) the strength of printed specimen increased. When the load was applied from UTM for the sample with 45° deposition, the layers resisted the maximum as strain lines are present at the bottom surface and the upper surface is in compression while the bottom surface is in tension, and the load gets distributed on several inclined layers. In contrast, when a sample with 90° deposition was tested with the same conditions, the material layers being parallel to the destructing force get easily separated. Due to this, poor properties were recorded for them. The cut-section ‘A-A’ clearly shows tensile loading in the lower layers and compressive loading in the upper layers of fractural test specimens. For more understanding, photomicrographs of fractured and un-fractured printed parts were taken at × 30 magnifications with tool maker’s microscope (Figure 5.51) and it has been observed that while flexural loading the inner zone was under compression and the outer was under tension.

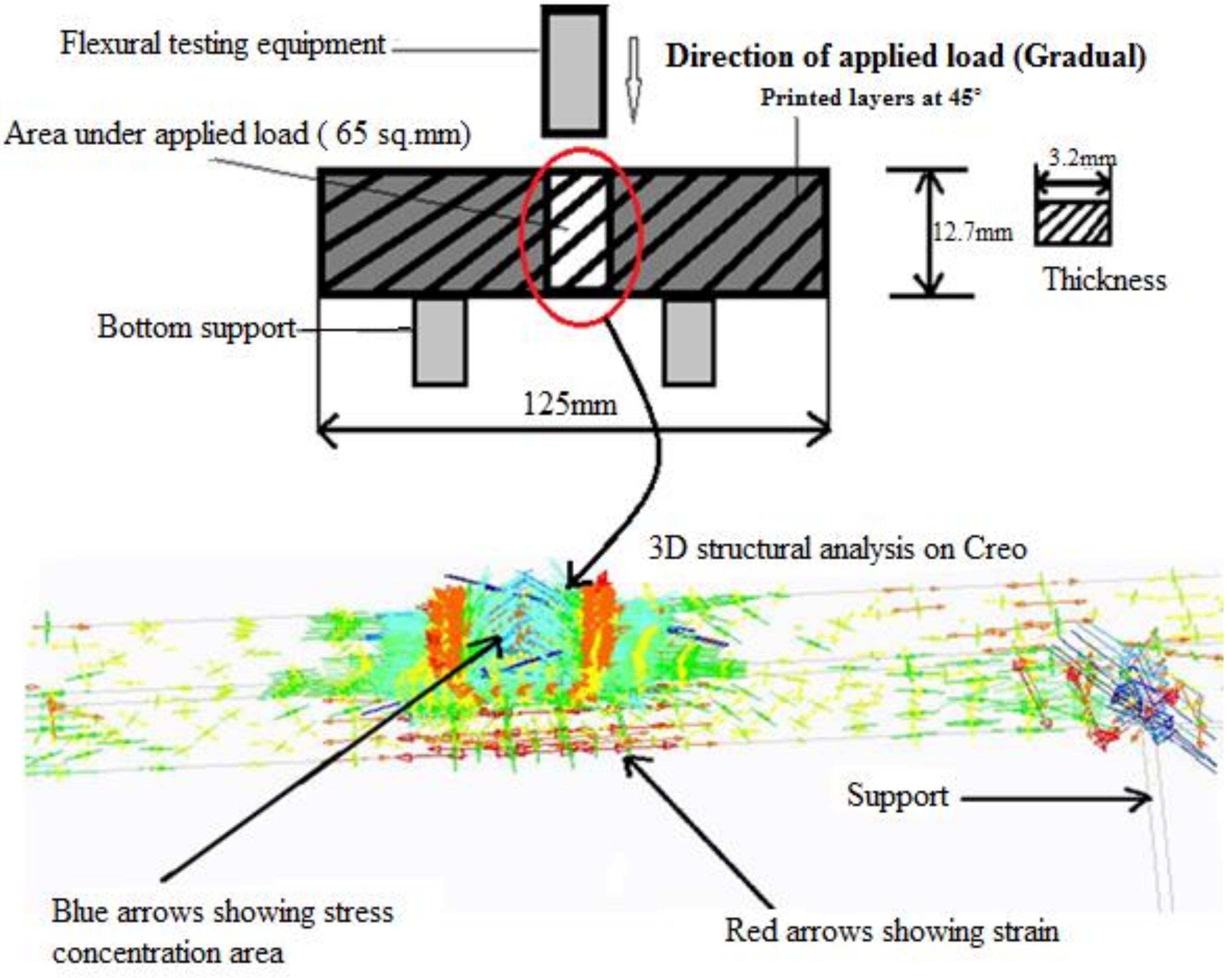

Figure 5.50 2D view of flexural testing with 3D simulation for stress and strain

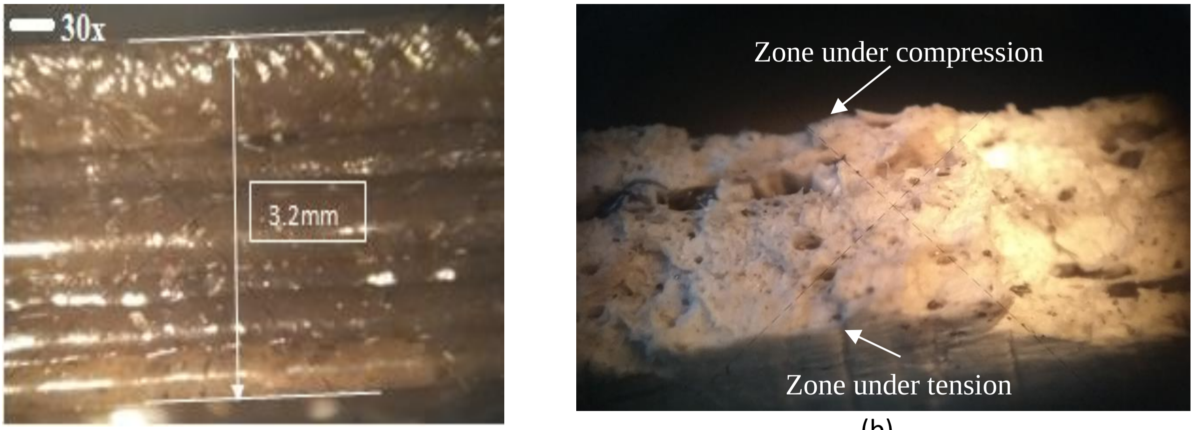

(a) (b)

Figure 5.51 Toolmaker microscopic image for (a) 3D printed part and (b) fractured part under flexural loading as per Table 4.5

5.3.21 Shore D hardness for 3D printed flexural specimens

3D printed samples were tested for their Shore D hardness characteristic as it was evident from past literature that hardness plays a crucial role in deciding the properties of the composite. From shore D testing, it was found that sample number 7 had maximum hardness whereas sample number 3 had the least hardness as depicted by Figure 5.52. Sample 7 was printed with the maximum density and the print angle was 45°. It, therefore, had the maximum hardness. The print density of sample 3 was the least (60%) and therefore interspacing was much prominent in sample 1. This caused the low hardness of the print sample. Photo-micrographic analysis (at 100× magnification) of samples (Figure 5.53) revealed that percentage porosity was also playing a role in the hardness and sample mechanical properties as is evident from Figure 5.53. The sample possessing the maximum hardness has the least porosity whereas the sample whose hardness was less possessed maximum porosity.

5.3.22 Surface roughness testing for 3D printed flexural specimens

From surface and mechanical performance, it was observed that sample 3 had the least mechanical performance (as per flexural and pull-out results) and sample 7the maximum mechanical performance. The photo-micrographic images were further processed with the image processing software package tool and Ra profile was observed (Figure 5.54). From the Ra profile, it was observed that sample 3 had a higher roughness value (Ra=51.48nm) than sample 7 (Ra=21.47nm) which may also be one of the reasons for its poor mechanical performance. The same was also visible from 3D rendered images of photomicrographs.

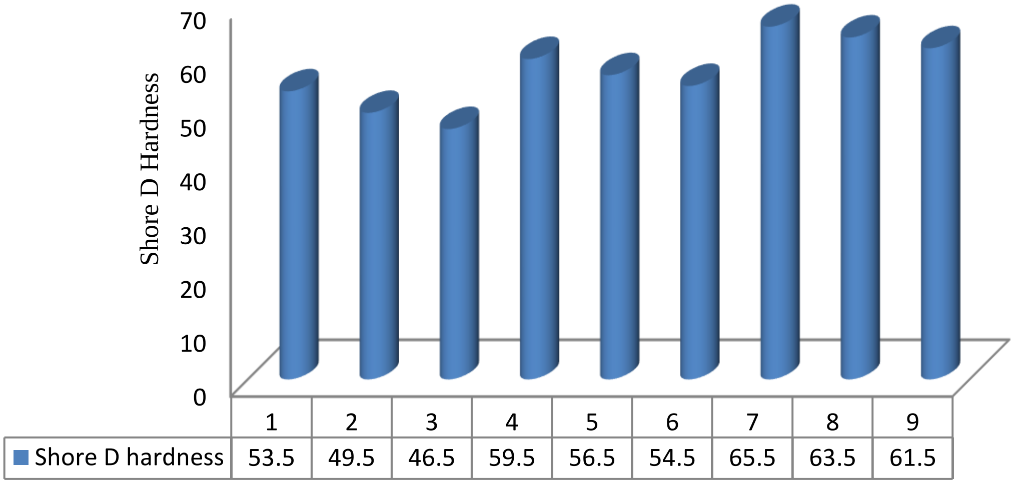

Figure 5.52 Shore D hardness of printed samples (as per Table 4.5)

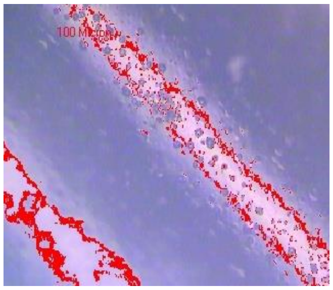

Sample at Serial number 1
(Porosity 10.24%)

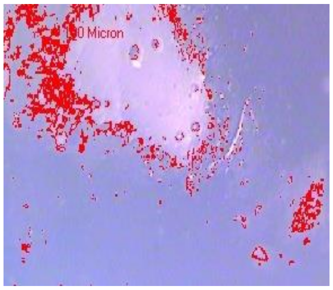

Sample at Serial number 2
(Porosity 12.41%)

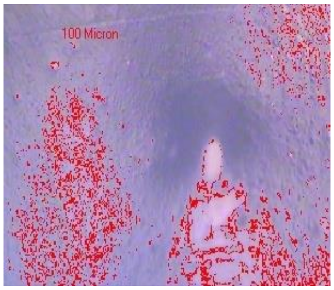

Sample at Serial number 3
(Porosity 13.65%)

Sample at Serial number4
(Porosity 8.74%)

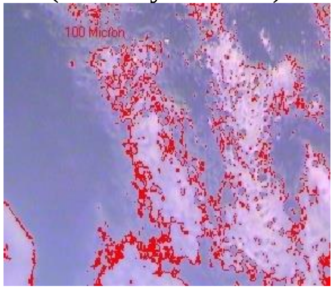

Sample at Serial number5
(Porosity 9.01%)

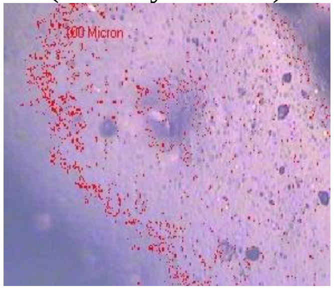

Sample at Serial number6
(Porosity 9.60%)

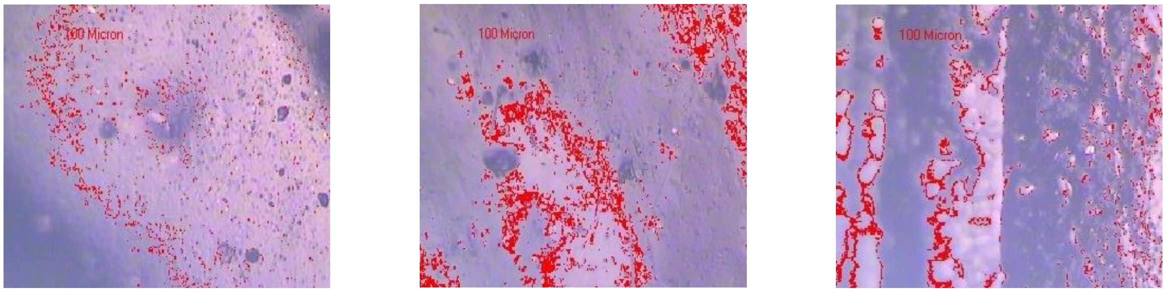

Sample at Serial number7 (Porosity 5.42%)
Sample at Serial number 8 (Porosity 6.41%)
Sample at Serial number 9 (Porosity 6.59%)

Figure 5.53 Photo-micrographic analysis for porosity (as per Table 4.5)

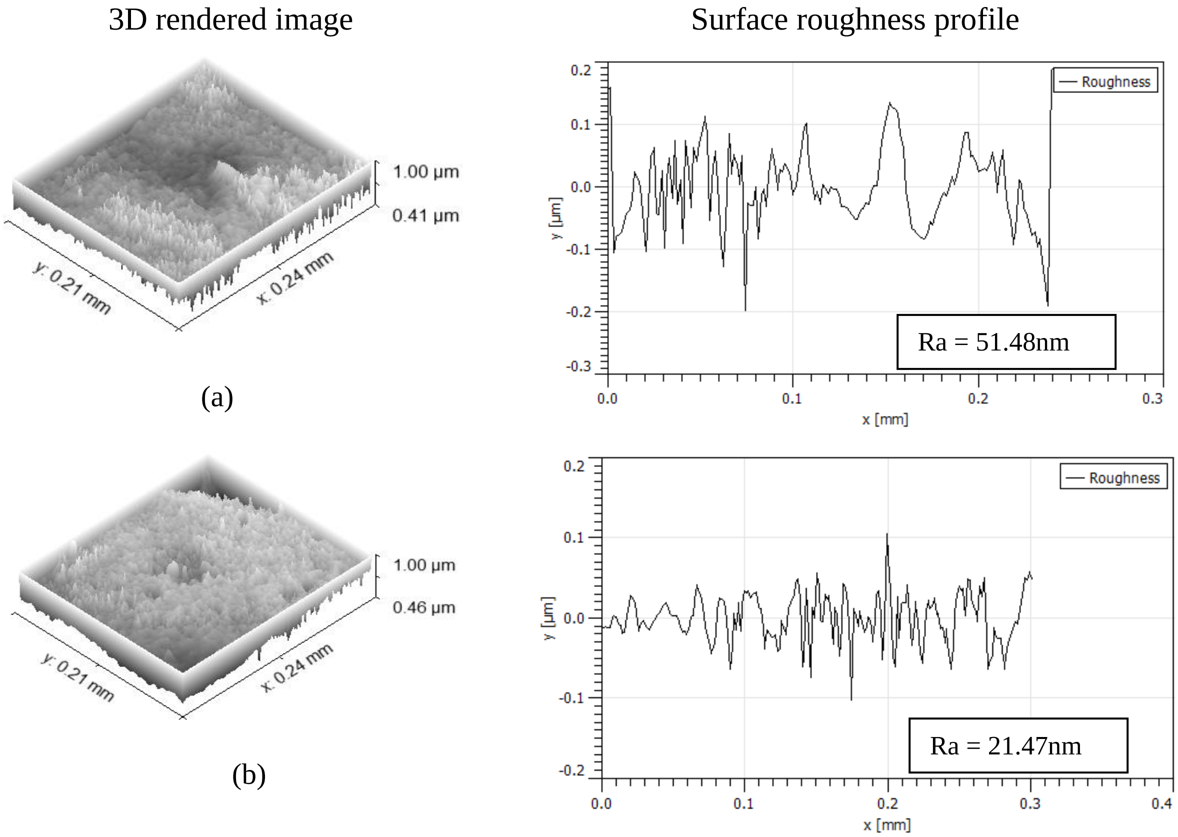

Figure 5.54 Surface roughness profile (at the cut-off length of 0.04mm), (a) for the sample at Serial number 3, (b) for the sample at Serial number7 (as per Table 4.5)

Based on the 3D rendered images, the amplitude distribution function (ADF) was noticed (Figure 5.55) which indicates that the sample at 7 (Table 5) was more uniformly distributed (normal distribution viewpoint) in comparison to the sample at 3 (which was more aligned towards left). ADF function gives a further explanation to surface roughness profile as sample 7 held a uniform spread of signature of the surface profiles.

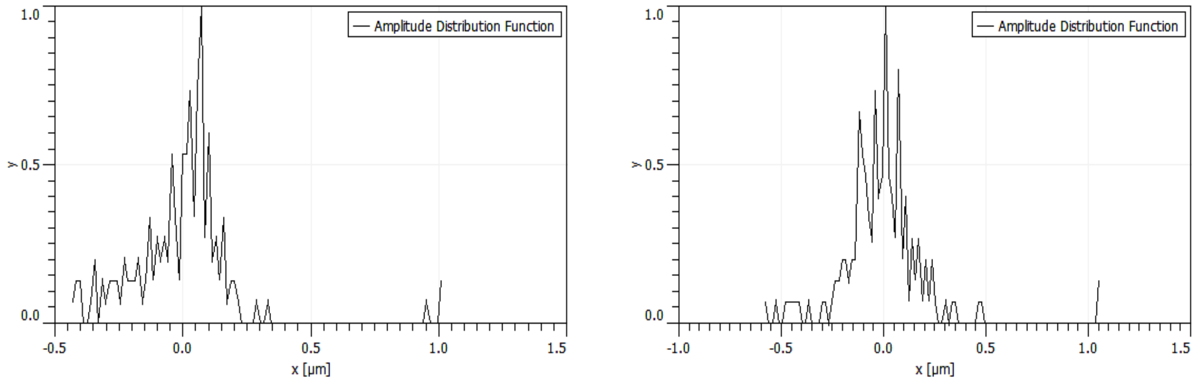

Figure 5.55 ADF (at the cut-off length of 0.04mm) for (a) sample at Serial number 3 and (b) sample at Serial number7 as per Table 4.5

5.3.23 Thermal conductivity results for 3D printed circular disc

The 3D printed discs on the FDM setup were subjected to thermal conductivity testing based on the "lee disc method". In the lee disc method, the 3D printed disc of Φ110mm (see Figure 4.7) was inserted between the steam chamber and lee disc (Figure 4.5), and a heater was used to generate steam by heating the setup. The steam-heated the steam chamber due to which the printed disc started conducting heat and the lee disc also started showing temperature reading using a connected sensor. After stabilization of temperature, the printed disc was taken out and the steam chamber and lee disc were made to touch each other so that the temperature may rise for measuring the dT/dt (temperature vs. time) plot. After calculation of dT/dt (Figure 5.56) the thermal conductivity was calculated.

$$\mathrm{k} = [\mathrm{m} \times \mathrm{c} \times (\mathrm{dT/dt}) \times \mathrm{thickness}] / \mathrm{A} \times (\mathrm{T1} - \mathrm{T2})$$

Value for mass, thickness, area and specific heat conductivity for lee disc are given below;

$$A = 3.14 \times 0.11 \times 0.11/4 = 0.0095\mathrm{m}^2$$

$$\mathrm{Thickness} = 1.74\ \mathrm{mm} = 0.00174\mathrm{m}$$

$$\mathrm{Mass\ of\ Lee\ disc\ (kg)} = 0.769\ \mathrm{kg}$$

$$\mathrm{C} = 377\ \mathrm{J/KgK}$$

$$\mathrm{Slope\ calculations\ for\ dT/dt\ plot\ (Fig. 7)} = (\mathrm{y2} - \mathrm{y1/x2} - \mathrm{x1})$$

$$y2 = 62$$

$$y1 = 51$$

$$x2 = 105$$

$$x1 = 5$$

$$dT/dt = (\mathrm{y2} - \mathrm{y1}/\mathrm{x2} - \mathrm{x1})$$

$$dT/dt = (62 - 51)/\,(105 - 5)$$

$$dT/dt = 0.11$$

Table 5.38 shows the measured thermal conductivity for the 9 sets of 3D printed discs. It was observed that the least thermal conductivity (0.139 W/mK) was obtained for sample 1 which was printed with 60% infill density, 45° of infill angle, and 50mm/s of infill speed. The maximum thermal conductivity of 0.2781 W/mK was obtained for sample 9 which was printed with a maximum infill density of 100%, infill angle of 90°, and infill speed of 70 mm/s. This may be because thermal conductivity is directly related to the uniform structure formation as with the least infill density the structure may have more voids/porosity which results in non-uniformity of links between the deposited materials and hence results in low percolation effect and thus ultimately resulted in poor thermal conductivity. Whereas for maximum infill density the printed sample may have fewer voids/porosity due to which links between the subsequent layers would be good enough to transfer heat without any resistance due to which the thermal conductivity has been improved as seen from Table 5.38. Also, the trend for thermal conductivity shows that as the infill density increases the thermal conductivity gets improved which again may be due to the reason that increase in infill density enhances the percolation effect due to fewer voids/ porosity between the deposited subsequent layers which ultimately helps to transfer heat from one side to the other.

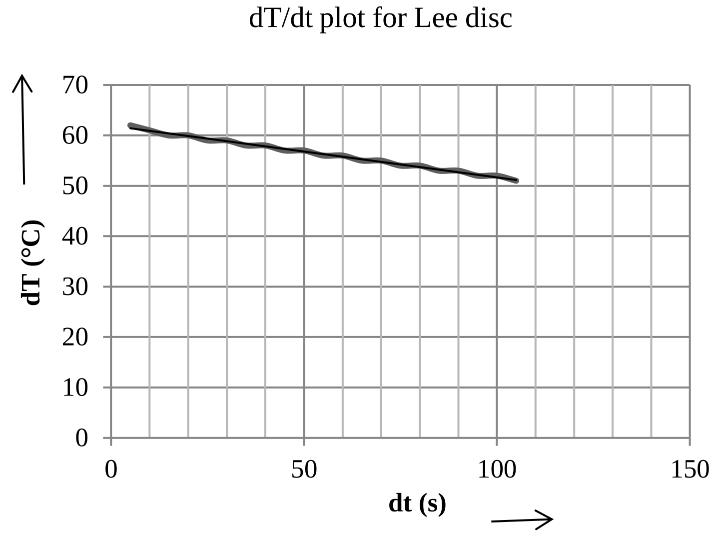

Figure 5.56 dT/dt plot from Lee disc apparatus

Table 5.38 Thermal conductivity for 3D printed discs for hybrid blend-based sample

Serial number	Temp 1(°C)	Temp 2(°C)	Thermal conductivity (W/mK)
1	99	57	0.139±0.009
2	99	58	0.142±0.014
3	99	59	0.146±0.021
4	99	66	0.177±0.016
5	99	68	0.188±0.024
6	99	68	0.188±0.013
7	99	75	0.243±0.017
8	99	76	0.253±0.011
9	99	78	0.278±0.022

For structural engineering applications, a low value of thermal conductivity is desirable. The lowest value was observed in the case of sample 1, whereas the highest value was observed in sample .9. The value for thermal conductivity for virgin PLA is around 0.23 W/mK. For processing conditions optimization, the thermal conductivity results were taken by using the

MiniTab software package tool and Taguchi L9 OA was used for optimization. Table 5.39 shows the ANOVA table for the SN ratio of thermal conductivity. It was observed that infill density played a significant role in the thermal conductivity of specimens of hybrid blended PLA matrix. The percentage contribution of infill density towards the output was maximum (97.60%) and it was the only parameter that was observed to be significant (P-value <0.05 and F value >10). Thus, it may be concluded that infill density is the only responsible input parameter for the thermal conductivity of the PLA hybrid blended matrix.

Table 5.39 ANOVA table for SN ratio of Thermal conductivity for hybrid blend-based sample

Source	DF	Seq SS	Adj SS	Adj MS	F	P	% Contribution
Infill Density	2	40.1574	40.1574	20.0787	208.68	0.005	97.60
Infill Angle	2	0.7546	0.7546	0.3773	3.92	0.203	1.8
Infill Speed	2	0.0414	0.0414	0.0207	0.22	0.823	0.1
Residual Error	2	0.1924	0.1924	0.0962			0.46
Total	8	41.1458					

DF: degree of freedom; Seq SS: sequential sum of the square; Adj SS: Adjusted sum of the square; F: Fisher’s value; P: Probability; %: percentage

5.3.24 Circumferential compressive testing results

The 3D printed discs based on DOE (Table 4.5) were subjected to UTM testing to ascertain the circumferential compressive properties for the printed disc. To avoid slippage of the disc while in compression, a specially designed holding fixture was printed on an FDM setup (which was made up of PLA material (Figure 4.6) and the disc was held tightly with the prepared holder (Figure 4.8). Table 5.40 shows the compressive properties (PL, BL, PS, and BS) for the 3D printed discs. Three samples for each experiment were printed and tested for compressive strength so that standard deviation may also be reported for the processing conditions. From Table 5.40, it is observed that compressive properties improved as the infill density increased and observed maximum for sample 9, printed with infill density 90%, infill angle of 90°, and infill speed of 70 mm/s which was in line with the observed thermal conductivity trends. It clearly showed that better diffusion of material in a layer fashion resulted in better mechanical properties as well as provided a proper linkage/bonding between extreme printed layers for better thermal conductivity. Figure

5.57 shows the stress vs. strain plot for the circular compressive testing which was further used to calculate the toughness of printed discs as shown by Table 5.41. From Figure 5.57, it was observed that the printed discs have shown some ductility as their strain curve suggests. This may be because the printed disc was of a low thickness (1.74mm) which may have given some flexibility towards distortion. Further, the stress vs. strain plot was used to evaluate the modulus of toughness. From Table 5.41, it was clear that sample 9 had a maximum modulus of toughness (0.7686 Pa) whereas sample 2 had the least value of modulus of toughness (0.2934). Infill density has played again a major role in modulus of toughness as the values of modulus of toughness have been observed to increase with increasing infill density. This shows that sample 9 may have better crash applications (where a larger modulus of toughness is required for circular sections).

Table 5.40 Circumferential compressive properties for 3D printed discs for hybrid blend-based sample

S. No	Peak load (KN)	Break load (KN)	Peak strength (Pa)	Break strength (Pa)
1	35.30±2.50	31.77±1.50	3.71±0.65	3.34±0.51
2	46.30±1.50	43.20±1.60	4.87±0.69	4.54±0.64
3	50.10±3.00	47.20±2.00	5.27±0.71	4.96±0.71
4	53.40±3.50	48.06±1.40	5.62±0.60	5.05±0.68
5	57.50±2.50	53.20±1.50	6.053±0.74	5.69±0.65
6	64.20±3.40	60.50±2.10	6.75±0.52	6.364±0.60
7	70.40±4.50	62.41±1.80	7.41±0.34	6.57±0.72
8	82.54±1.50	65.70±1.50	8.68±0.75	6.91±0.52
9	92.50±2.50	71.57±2.50	9.73±1.25	7.53±0.75

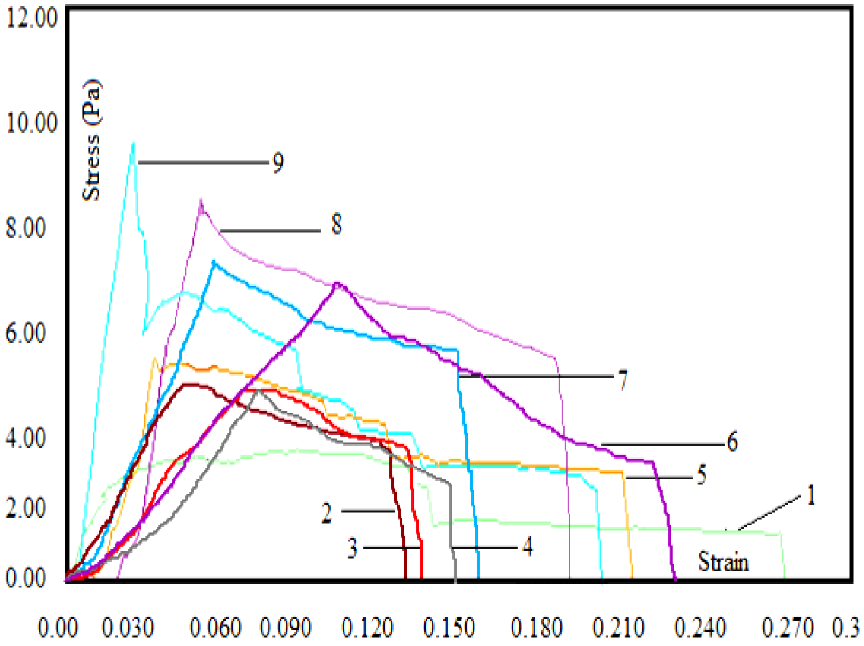

Figure 5.57 Stress vs. strain plot for compressive testing as per Table 4.5

Table 5.41 Modulus of toughness for 3D printed discs for hybrid blend-based sample

S. No	Break stress (Pa)	Strain	Modulus of toughness (Pa)
1	3.34	0.27	0.45
2	4.54	0.12	0.29
3	4.96	0.13	0.33
4	5.05	0.15	0.38
5	5.60	0.22	0.63
6	6.36	0.23	0.76
7	6.57	0.15	0.51
8	6.91	0.18	0.64
9	7.53	0.20	0.77

5.3.25 Optimization for compressive properties of the 3D printed circular disc

The properties observed from compression testing of the circular disc were further used for the optimization of printing conditions so that the processing conditions of 3D printing may be standardized for batch production. Table 5.42 shows analysis of variance (ANOVA) for the signal to noise (SN) ratios from which it was observed that maximum contribution (82.86%) was given by infill density and infill angle (15.54%) whereas infill speed has the least role to play towards the output. It was also observed that infill density and infill angle were the significant parameters for the 3D printing as their probability (p)-value was less than 0.05 and Fisher's (F) value greater than 10. Table 5.43 shows the rank table for a peak load of compressive tested samples from which it was observed that infill density was ranked 1st as its contribution was maximum towards the output. Infill angle was given 2nd rank and infill speed which was the least significant was given 3rd rank. Figure 5.58 shows the main effect plot for the SN ratios of peak load which highlights that infill density of 100%, infill angle of 90°, and infill speed of 70 mm/s were the optimized conditions for 3D printing of the disc on the FDM setup. It was observed that the optimized/suggested conditions were inside the selected DOE as experiment 9 (Table 4.5).

Table 5.42 ANOVA for SN ratios for peak load of compressive testing of 3D printed disc for hybrid blend-based sample

Source	DF	Seq SS	Adj SS	Adj MS	F	P	% Contribution
Infill Density	2	44.58	44.58	22.29	129.79	0.008	82.86
Infill Angle	2	8.36	8.36	4.18	24.35	0.039	15.54
Infill Speed	2	0.51	0.51	0.25	1.50	0.400	0.95
Residual Error	2	0.34	0.34	0.17			0.63
Total	8	53.80					

Table 5.43 Rank table for peak load of compressive testing of 3D printed disc for hybrid blend-based sample

Level	Infill Density	Infill Angle	Infill Speed
1	92.75	94.15	95.15
2	95.30	95.61	95.73
3	98.20	96.49	95.38
Delta	5.45	2.34	0.58

Rank	1	2	3

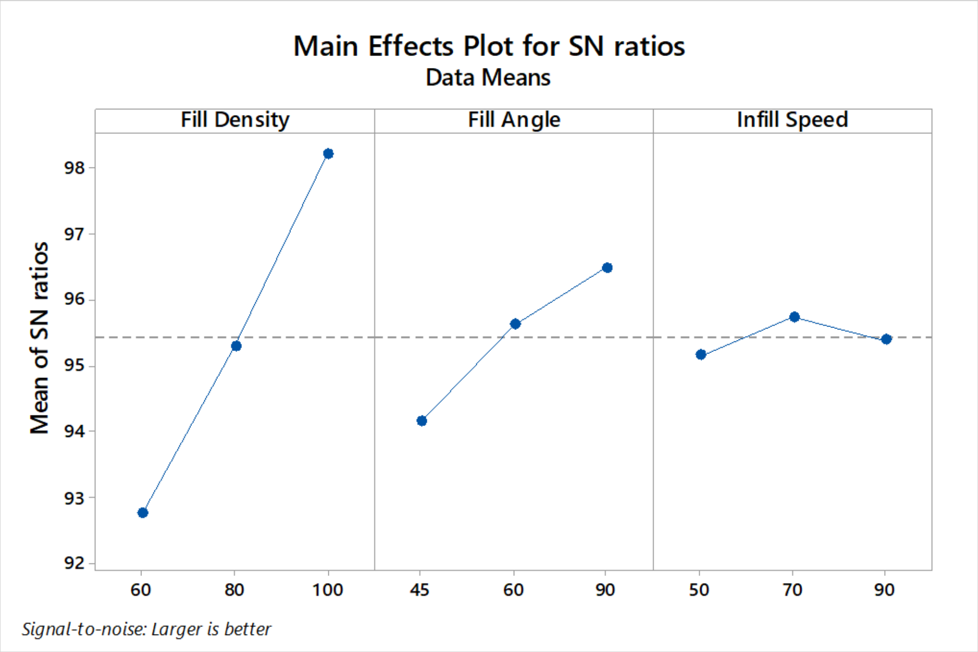

Figure 5.58 Main effect plot for SN ratios of peak load for compressive testing of 3D printed disc

$$\text{Ŋ opt} = m + (mA - m) + (mB - m) + (mC - m)$$

$$Y_{opt}^{2} = 10^{\text{Ŋ opt}/10}(\text{for properties, larger is the better case})$$

$$m = \text{SN mean of PL} = 95.42$$

$$mA = \text{max infill density from Table 9} = 98.2$$

$$mB = \text{max infill angle from Table 9} = 96.49$$

$$mC = \text{max infill speed from Table 9} = 95.73$$

$$\textit{putting all values in the equation}$$

$$\text{Ŋ opt} = 95.42 + (98.2 - 95.42) + (96.49 - 95.42) + (95.73 - 95.42)$$

$$\text{Ŋ opt} = 99.58\ \text{dB}$$

$$Y_{opt}^{2} = 10^{99.58/10}$$

$$Y_{opt} = 95.31\text{KN}$$

The actual peak load value for experiment number 9 (92.50 ± 2.50 KN) was very near the predicted value for the peak load (Table 5.40). All other properties were optimized on the same line as explained above and it was observed that similar trends have been obtained for all properties and predicted results were very close to the observed results of compressive testing.

5.3.26 Shore D hardness of the 3D printed circular disc

All the prepared samples were subjected to Shore D hardness testing. It was observed from the hardness values that the results are in line with the compressive properties. The sample which has maximum circumferential compressive strength also has shown maximum hardness. This may be because infill density has played a maximum role in output. In the case of samples 7,8 and 9, the samples were printed with maximum infill density. Due to this, better diffusion of the material may have occurred in subsequent layers which resulted in less void formation in the inter-space of the structure resulting in higher hardness values for the samples. Table 5.44 shows the Shore D hardness results for the samples printed on the FDM setup.

Table 5.44 Shore D hardness results for circular shape 3D printed samples for hybrid blend based sample

Serial number	Shore D hardness
1	58.5
2	57.5
3	55.5
4	59.5
5	58.5
6	59.5
7	63.5
8	64.5
9	65.5

5.3.27 Fractured surface analysis using tool maker microscope of the 3D printed circular disc

The fractured samples of compressive testing (Table 4.5) were subjected to the tool maker's microscope for fractured surface analysis using ×30magnification. It was observed from the fractured surface image that samples with lower infill density had maximum voids/porosity present in the composite matrix (Figure 5.59) which may be the reason for their poor mechanical and thermal performance. Samples 7, 8, and 9, printed with 100% infill density have shown fewer voids/porosity holes due to which their mechanical and thermal performance was better.

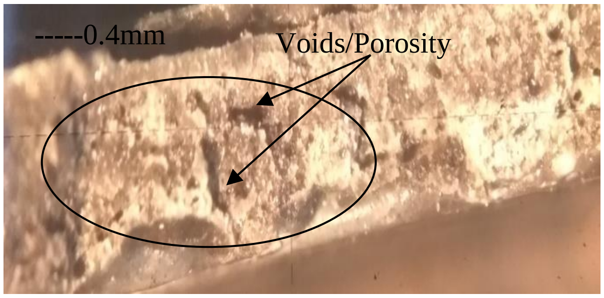

Sample as per serial number 1

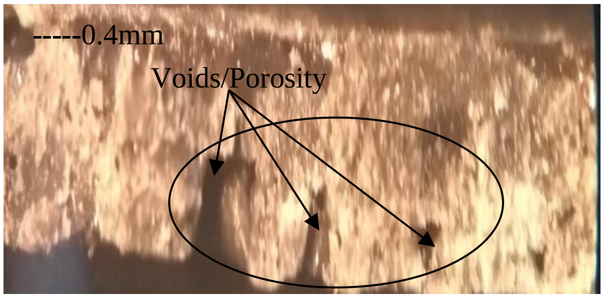

Sample as per serial number 2

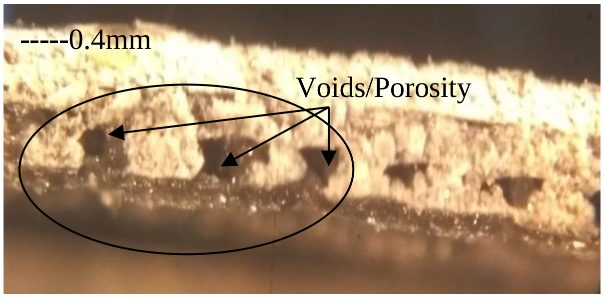

Sample as per serial number 3

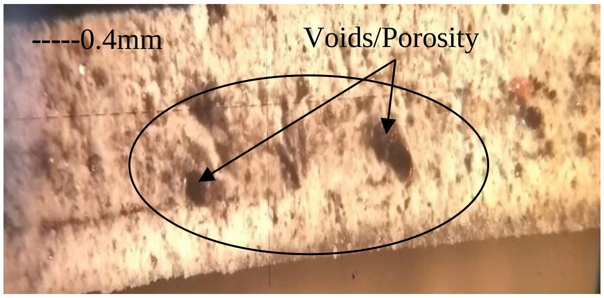

Sample as per serial number 4

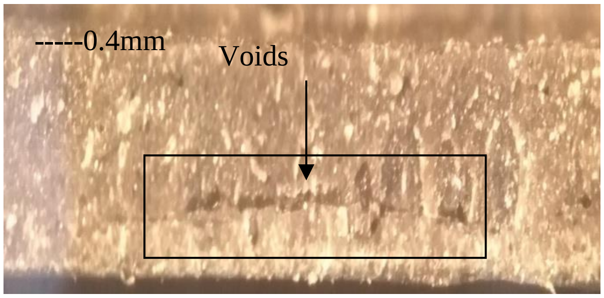

Sample as per serial number 5

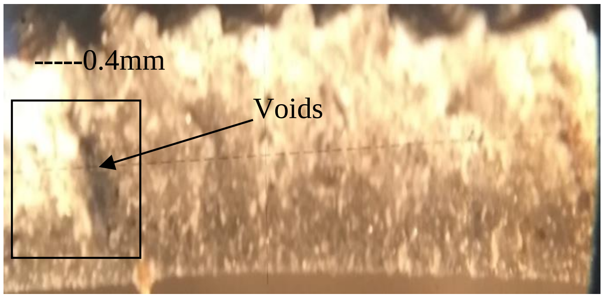

Sample as per serial number 6

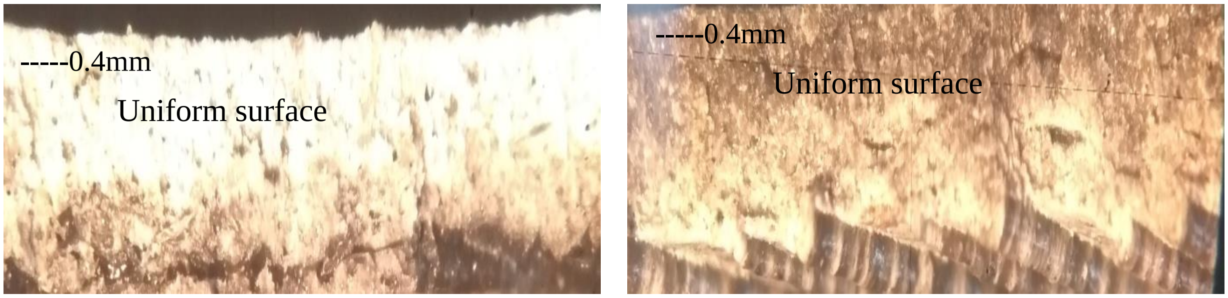

Sample as per serial number 7

Sample as per serial number 8

Sample as per serial number 9

Figure 5.59 Fractured surface observed under tool maker microscope as per Table 4.5

5.3.28 Surface roughness (based on image rendering) for best and worst samples

The photomicrographs of sample .9 (with best mechanical properties) and sample 1 (with poor mechanical properties) as per Table 5.40 were processed on image processing software to evaluate the Ra (Figure 5.60) using 3D rendered images. It has been observed that Ra for sample 1 (at the cut-off length of 0.04mm) was more than sample that of sample 9 (as per Table 4.5) which may also be one of the reasons for the poor mechanical and thermal properties of sample 1.

Serial number	3D rendered image	Roughness profile
1	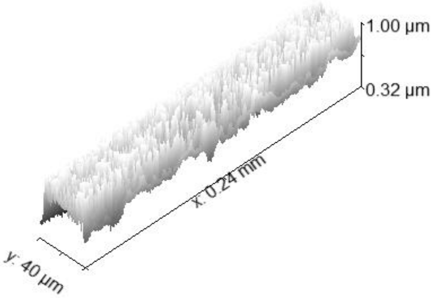	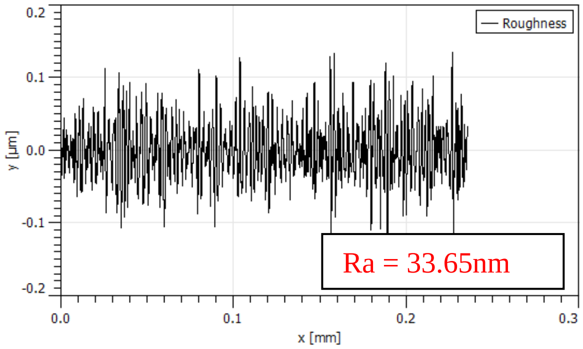

9

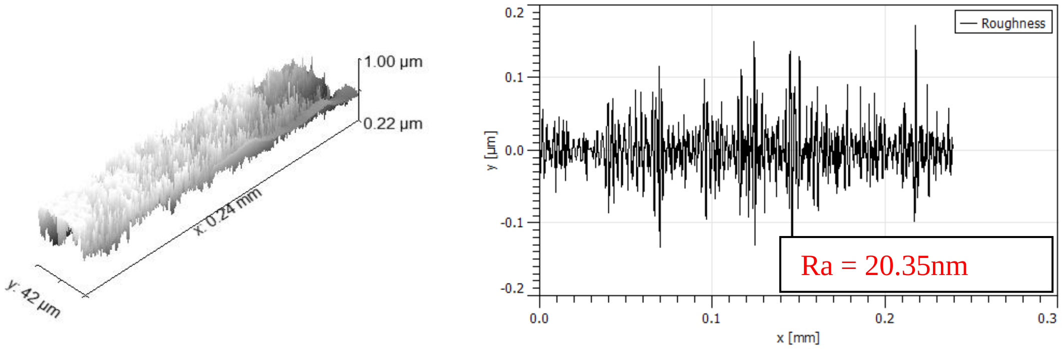

Figure 5.60 Surface roughness profile for 1st and 9th sample as per Table 4.5 for 3D printed disc

5.3.29 Electrical conductivity results

Four probe testing method of capacity 10^{-6} to 10^{6} S/cm was used for electrical conductivity measurement of 3D printed samples. It has been observed that the samples had very low electrical conductivity ($<10^{-6}$) due to which it was impossible to quantify the electrical conductivity. Hence, it was noted that the 20-weight percentage of magnetite powder in the PLA matrix has not shown improvement in the electrical conductivity of the composite matrix. This may be because the presence of PVC and wood dust which are insulators have dominated in electrical behavior of the composite. This also suggested that electrical properties were independent of FDM processing conditions as no improvement was observed in electrical conductance.

5.3.19 Dimensional deviation results

Table 5.45 shows the dimensional deviations in 3D printed parts on the FDM setup. From Table 5.45, it was made clear that for samples 1, 2, and 3, the deviation recorded in diameter and thickness was lower in comparison to other samples. It has been observed that as the infill density of samples was increased the deviation got enhanced. This may be because as the sample density increases the voids/porosity reduce resulting in better structure formation but due to low internal vacant space, the material after solidification has shown more deviation for thickness as well as for diameter. But for lower infill density, the vacant space as voids/porosity was more available due to which the expansion of material while solidifying filled the vacant space first. Due to this, low dimensional deviations have been observed. Further, the values of ΔD and ΔT were subjected to MiniTab 17 statistical software package tool for analysis of variance (ANOVA) optimization of dimensional deviations for the minimum is the better case (as less deviation is required for the production of prototypes to eradicate the extra post-processing of product). Figure 5.61 shows the main effect plot for the signal to noise (SN) ratio of ΔD which suggested that the least infill density (60%), low infill angle of 45°, and medium infill speed of 70mm/s were the optimized conditions for the least dimensional deviation for the 3D printed disc on FDM setup. Table 5.46 shows the ANOVA for SN ratios of ΔD, from which it was observed that infill density was the only significant parameter for the dimensional deviation feature for printed discs and has contributed maximum (91.83%) while the other two selected parameters of FDM processing were insignificant. It is noted that the optimized/suggested conditions were outside the design of experimentation (DOE) but from ANOVA table 5.46, it was clear that the infill angle and infill speed were the least significant as FDM processing condition. Also, as per Table 4.5 in sample 1; the suggested infill density and infill angle was present therefore in place of the suggested/optimized condition one may take sample 1as the standard conditions for the printing of discs for FDM printing. Table 5.47 shows the rank table for SN ratios of ΔD which suggests that the infill density was ranked 1st as per its contribution towards the output whereas infill speed was ranked 2nd and infill angle was ranked at 3rd position. From the ANOVA table, it was observed that the used statistical model was significant as the total residual error was 0.65% of the total error. Thus, the used model and observed values for the FDM setting were correct up to a 95% confidence interval. From the percentage contribution, it has been observed that infill density has contributed the most (91.83%), whereas the other two factors were not significant for the current investigation. It is known that surface properties such as hardness and electrical properties (electrical conductivity) are greatly dependent on the inner structure (porosity holes, bonding between polymer and reinforcements, proper adhesion between different molecules) of printed prototypes. Therefore, in the present case infill density has played a significant and maximum role towards the observed surface hardness and electrical properties. Moreover, the dimensional deviations are also the result of structural formation. Therefore, for the observed properties only infill density has the maximum role to play.

Table 5.45 Observed dimensional deviations for FDM printed discs for hybrid blend-based sample

Serial Number	Printed dia (mm)	Original dia (mm)	Printed thickness(mm)	Original thickness(mm)	ΔD(mm)	ΔT(mm)

1	110.86	110	1.67	1.74	0.86±0.21	-0.07±0.02
2	110.62	110	1.71	1.74	0.62±0.19	-0.03±0.01
3	110.9	110	1.73	1.74	0.9±031	-0.01±0.01
4	111.62	110	1.83	1.74	1.62±0.21	0.09±0.09
5	112.64	110	1.82	1.74	2.64±0.19	0.08±0.04
6	112.57	110	1.85	1.74	2.57±0.30	0.11±0.03
7	112.92	110	1.92	1.74	2.92±0.19	0.18±0.05
8	112.85	110	2.07	1.74	2.85±0.24	0.33±0.04
9	112.56	110	2.16	1.74	2.56±0.28	0.42±0.09

Table 5.46 ANOVA for SN ratios of ΔD for hybrid blend-based sample

Source	DF	Seq SS	Adj SS	Adj MS	F	P	Percentage contribution
Infill density	2	206.476	206.476	103.238	140.82	0.007	91.83
Infill angle	2	1.815	1.815	0.907	1.24	0.447	0.81
Infill Speed	2	15.067	15.067	7.534	10.28	0.089	6.71
Residual Error	2	1.466	1.466	0.733			
Total	8	224.824					

Table 5.47 Rank table for SN ratios of ΔD for hybrid blend-based sample

Level	Infill density	Infill angle	Infill Speed

1	2.126	-4.063	-5.329
2	-6.940	-4.459	-2.734
3	-8.856	-5.149	-5.608
Delta	10.982	1.087	2.874
Rank	1	2	3

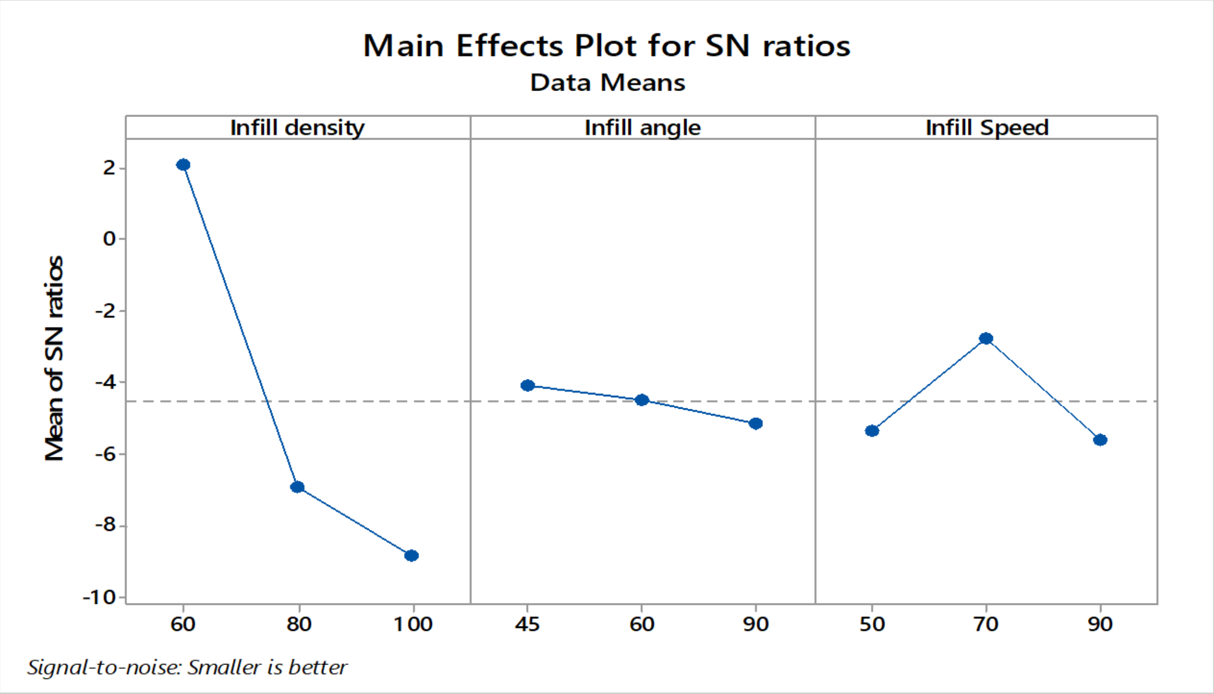

Figure 5.61 Main effect plot for SN ratio of ΔD for hybrid blend-based 3D printed sample

5.4 Results and discussion for stage 4

5.4.1 Multi-material printing results

First TSE of four PLA polymer-based different feedstock filaments of required diameter (1.75mm) have been performed and feedstock of sufficient length was obtained (Figure 5.62) and then 3D printing of different layers has been performed as per DOE (Table 4.8). Figure 5.63 shows different steps of multi-material printing. According to DOE (Table 4.8), the printing has been done and 9 different prototypes have been printed for mechanical and surface characterization.

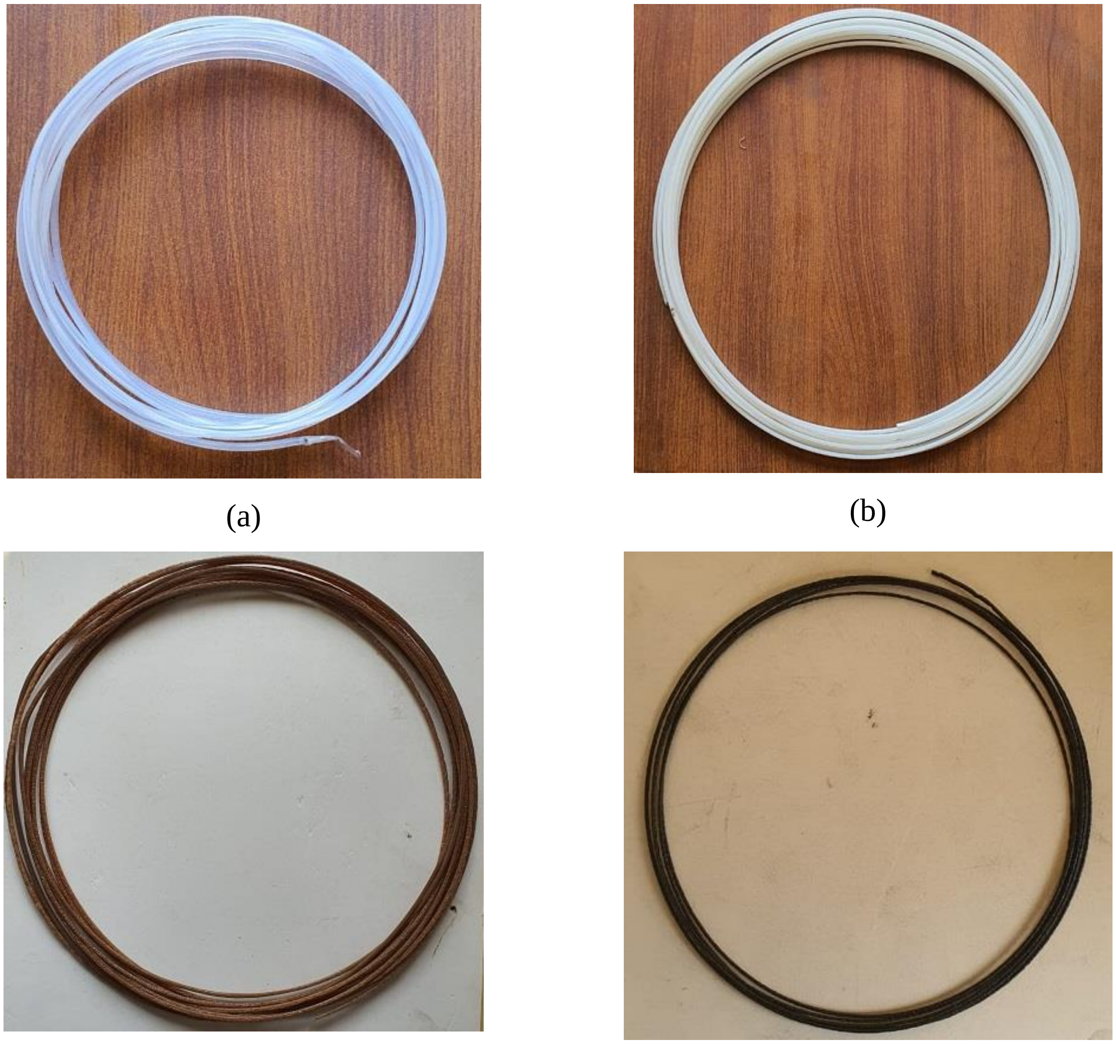

(a) (b)

(c) (d)

Figure 5.62 In-house developed feedstock filament of (a) PLA, (b) PLA/PVC, (c) PLA/wood powder, and (d) PLA/Fe_3O_4

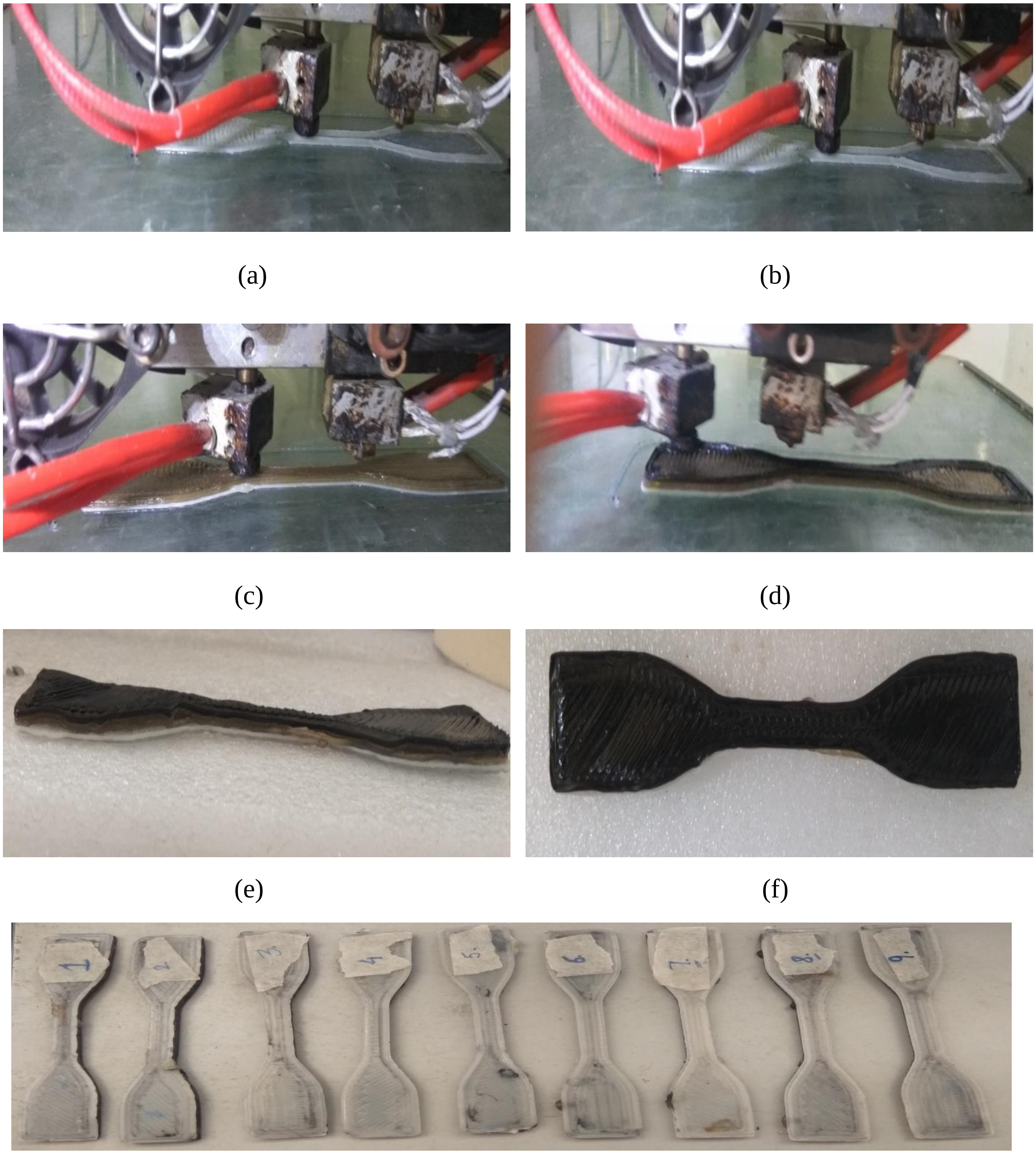

(a)

(b)

(c)

(d)

(e)

(f)

(g)

Figure 5.63 Printing for (a) Virgin PLA layer, (b) PVC reinforced PLA layer, (c) wood reinforced PLA layer, (d) Fe_3O_4 reinforced PLA layer, (e) multi-layer printed part (front view), (f) multi-layer printed part (top view) and (g) multi-layer printed parts (bottom view) as per Table 4.8

5.4.2 UTM testing results for multi-material 3D printed tensile specimen

The 3D printed parts as shown in Figure 5.63 were then subjected to UTM testing for mechanical properties analysis and various properties were identified for further optimization (table 5.48). It has been observed that maximum peak strength (46.28 MPa) and break strength (41.67 MPa) have been obtained for experiment number 7 whereas the least properties have been obtained for experimental condition 3 (peak strength 31.99 MPa and break strength: 28.79 MPa). The observed best values have been obtained for 45° infill angle, infill density of 100%, and infill speed of 90 mm/s. This may be due to the reason that in a 45° orientation angle, the supplanted layers are joined better with the subsequent layers and when tested for tensile property provide maximum resistance as destructing force and material deposition layer angle is different. Whereas in the case of the 3rd experiment, the infill angle is 90° due to which poor resistance to destruction has been seen as the layers are in the direction of applied force. Moreover, in the case of the 7th experiment, infill density is 100% which resulted in very low porosity holes and better joints between different layers have been formed which resulted in better tensile properties. In the case of the 3rd experiment infill density of 60% (lowest among DOE) may be the reason for poor mechanical properties. Figure 5.64 shows the stress vs. strain curve for UTM tested 3D printed parts. It has been observed that the multi-material printed parts were brittle as suggested by the stress vs. strain curve. Experiment 7 has shown maximum area under the curve which meant it has a maximum modulus of toughness (4.76 MPa) nearly double than any other sample whereas the least toughness has been observed for experiment 1 (1.752 MPa) (see Table 5.49).

Table 5.48 Tensile properties of multi material printed 3D parts

Serial number	PL (N)	BL (N)	PS(MPa)	BS(MPa)
1	730.100 ± 10	657.090 ± 12	34.767 ± 2.3	31.290 ± 0.95
2	714.400 ± 12	642.960 ± 10	34.019 ± 1.52	30.617 ± 2.3
3	671.700 ±9	604.530 ± 10	31.986 ± 0.95	28.787 ± 1.52
4	808.500 ± 12	727.650 ±9	38.500 ± 1.52	34.650 ± 0.95
5	745.800 ± 10	671.220 ± 12	35.514 ± 2.3	31.963 ± 2.3
6	707.500 ± 10	636.750 ± 8	33.690 ± 0.95	30.321 ± 1.52
7	971.800 ±9	874.620 ±9	46.276 ± 1.52	41.649 ± 2.3
8	896.300 ± 12	806.670 ± 12	42.681 ± 0.95	38.413± 1.52

9	788.000 ± 10	700.960 ± 10	37.524 ± 2.3	33.379 ± 0.95

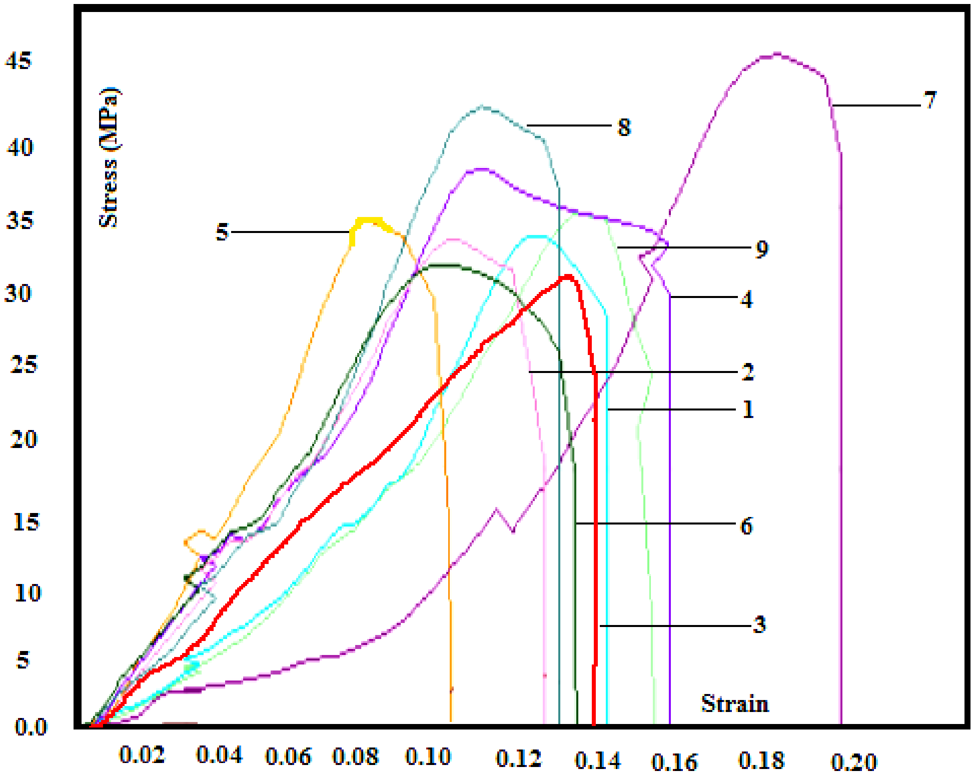

Figure 5.64 Stress vs. Strain curve for multi-material 3D printed parts as per Table 4.8

Table 5.49 Modulus of the toughness of printed parts of multi-material printed 3D parts

Experiment no.	PS (MPa)	Strain	Modulus of toughness (MPa) (1/2×stress×strain)
1	34.767	0.101	1.752
2	34.019	0.143	2.429
3	31.986	0.134	2.149
4	38.500	0.160	3.072
5	35.514	0.155	2.759
6	33.690	0.126	2.123
7	46.276	0.206	4.762

8	42.681	0.130	2.779
9	37.524	0.130	2.443

5.4.3 Optimization of mechanical properties for PL, BL, PS, BS

Table 5.48 has been further used for the optimization of printing conditions for mechanical properties using analysis of variance (ANOVA) statistical tool using Minitab 17 software package. Table 5.50 shows the ANOVA table for the signal to noise (SN) ratio of PL. It has been observed from the ANOVA table that the residual error (0.28726) is just 3.31% of the total error (8.66) which signifies that the model used for the optimization of printing conditions was significant. Infill density was found to be a significant parameter as its p-value (0.046) was less than 0.05. Table 5.51 shows the rank table of SN ratios for PL. It was observed from the rank table that infill density has been ranked 1st whereas infill angle and infill speed were ranked 2nd and 3rd, respectively as per their contribution toward output properties. Infill speed was the least significant as its contribution was least (0.71%) among selected input parameters for mechanical properties as shown in Table 5.50. From the main effect plot (Figure 5.65) of PL, it has been observed that infill density of 100%, infill angle of 45°, and infill speed of 90 mm/s were the optimized conditions for 3D printing of multi-material functionally graded parts. The optimized condition for 3D printing was present inside the DOE (Table 4.8) as experimental condition 7.

Table 5.50 ANOVA of SN ratios for PL of multi material printed 3D parts

Source	DF	Seq SS	Adj SS	Adj MS	F	P	% Contribution
Infill Density	2	6.01184	6.01184	3.00592	20.93	0.046	69.40
Infill Angle	2	2.30186	2.30186	1.15093	8.01	0.111	26.57
Infill Speed	2	0.06155	0.06155	0.03078	0.21	0.824	0.71
Residual Error	2	0.28726	0.28726	0.14363			3.31
Total	8	8.66253					

Table 5.51 Rank table for PL of multi material printed 3D parts

Level	Infill Density	Infill Angle	Infill Speed
1	56.96	58.39	57.77

2	57.53	57.86	57.72
3	58.91	57.16	57.92
Delta	1.95	1.23	0.19
Rank	1	2	3

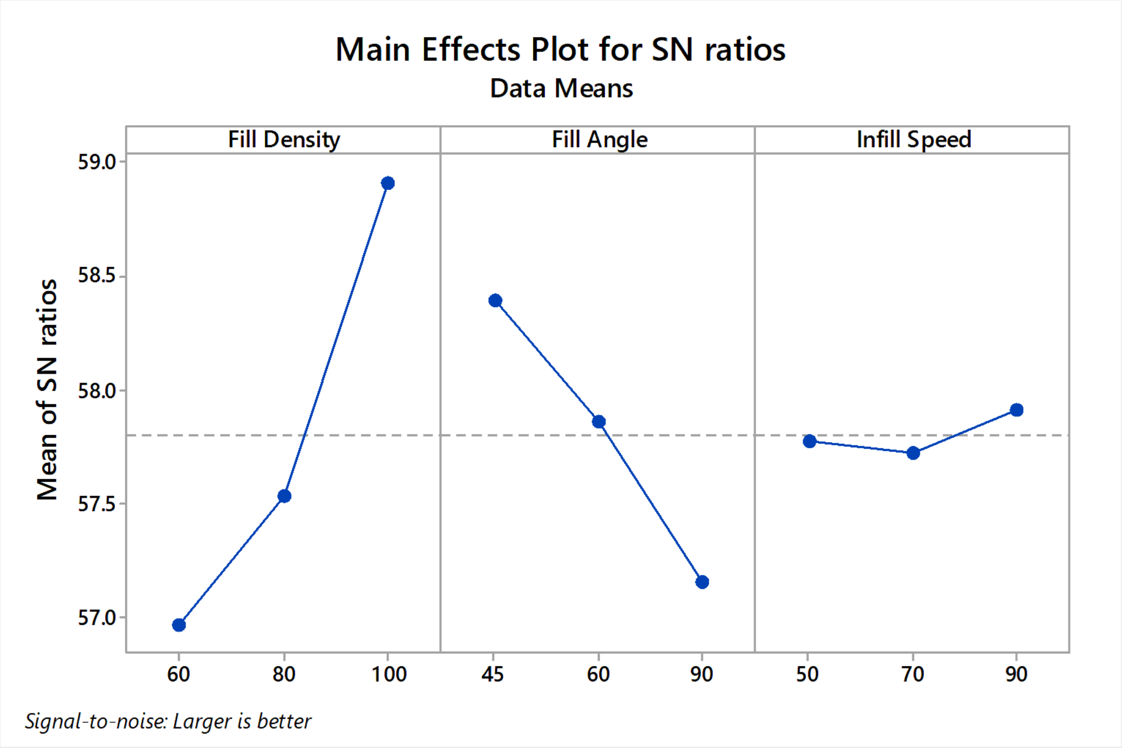

Figure 5.65 Main effect plot of SN ratios for PL for multi-material specimen

Further, the SN values of PL have been used for optimization and similar studies have been performed for BL, PS, and BS.

$$\text{Ŋ opt} = \text{m} + (\text{mA} - \text{m}) + (\text{mB} - \text{m}) + (\text{mC} - \text{m})$$

$$Y_{\text{opt}}^{2} = 10^{\text{Ŋ opt}/10} (\text{for properties, larger is the better case})$$

$$\text{m} = \text{SN mean of PL} = 57.80$$

$$\text{mA} = \text{max infill density from Table 5.51} = 58.91$$

$$\text{mB} = \text{max infill angle from Table 5.51} = 58.39$$

$$\mathrm{mC} = \text{ max infill speed from Table 5.51} = 57.92$$

$$\textit{putting all values in equation}$$

$$\text{Ŋ opt} = 57.80 + (58.91 - 57.80) + (58.39 - 57.80) + (57.92 - 57.80)$$

$$\text{Ŋ opt} = 59.62 \text{ dB}$$

$$\mathrm{Y}_{\mathrm{opt}}^{2} = 10^{59.62/10}$$

$$\mathrm{Y}_{\mathrm{opt}} = 956.66 \text{ N}$$

The optimized value was found to be near the observed actual PL (971.80 N) as provided in Table 5.48. Similar studies have been performed on all other properties and it has been found that the optimized values were near the actual observed values.

5.4.4 Regression and surface plot analysis for 3D printed multi-material component

Further, the values as observed from Table 5.48 were used for fitting regression model for 3 level interaction, and surface plots were formed for infill density and infill angle as input parameters while taking infill speed as constant; at 70 mm/s as it was the least significant and outputs on the third axis of the surface plot to show the behavior of output properties with input parameters on changing conditions. Table 5.52 shows the regression equations for PL, BL, PS, and BS. The obtained regression equations were used for surface plotting for behavior analysis. Figure 5.66 shows the surface plots for different properties. It has been observed from the surface plot of PL (Figure 5.66 (a)) that with the combination of low infill angle (Infill angle < 45°) and high infill density (> 100%), higher PL values have been observed. It has been validated by surface plots that higher infill angles lead to poor mechanical results (Table 5.48). Similarly, higher infill density leads to better tensile properties. Similar trends have been seen for BL, PS, and BS. From the surface plots, it has been observed that the optimized values for each property remain the same as higher infill density and low infill angle lead to better results in each case.

Table 5.52 Regression equations for PL, BL, PS, and BS

$\mathrm{PL} = 1186 - 12.08\ \text{Fill Density} - 2.480\ \text{Fill Angle} + 0.462\ \text{Infill Speed} + 0.1036\ \text{Fill Density} \times \text{Fill Density}$
$\mathrm{BL} = 1055 - 10.39\ \text{Fill Density} - 2.297\ \text{Fill Angle} + 0.415\ \text{Infill Speed} + 0.0898\ \text{Fill Density} \times \text{Fill Density}$

$$\mathrm{PS} = 56.5 - 0.57\ \mathrm{Fill\ Density} - 0.1181\ \mathrm{Fill\ Angle} + 0.0220\ \mathrm{Infill\ Speed} + 0.00493\ \mathrm{Fill\ Density} \times \mathrm{Fill\ Density}$$

$$\mathrm{BS} = 50.2 - 0.49\ \mathrm{Fill\ Density} - 0.1094\ \mathrm{Fill\ Angle} + 0.0198\ \mathrm{Infill\ Speed} + 0.00428\ \mathrm{Fill\ Density} \times \mathrm{Fill\ Density}$$

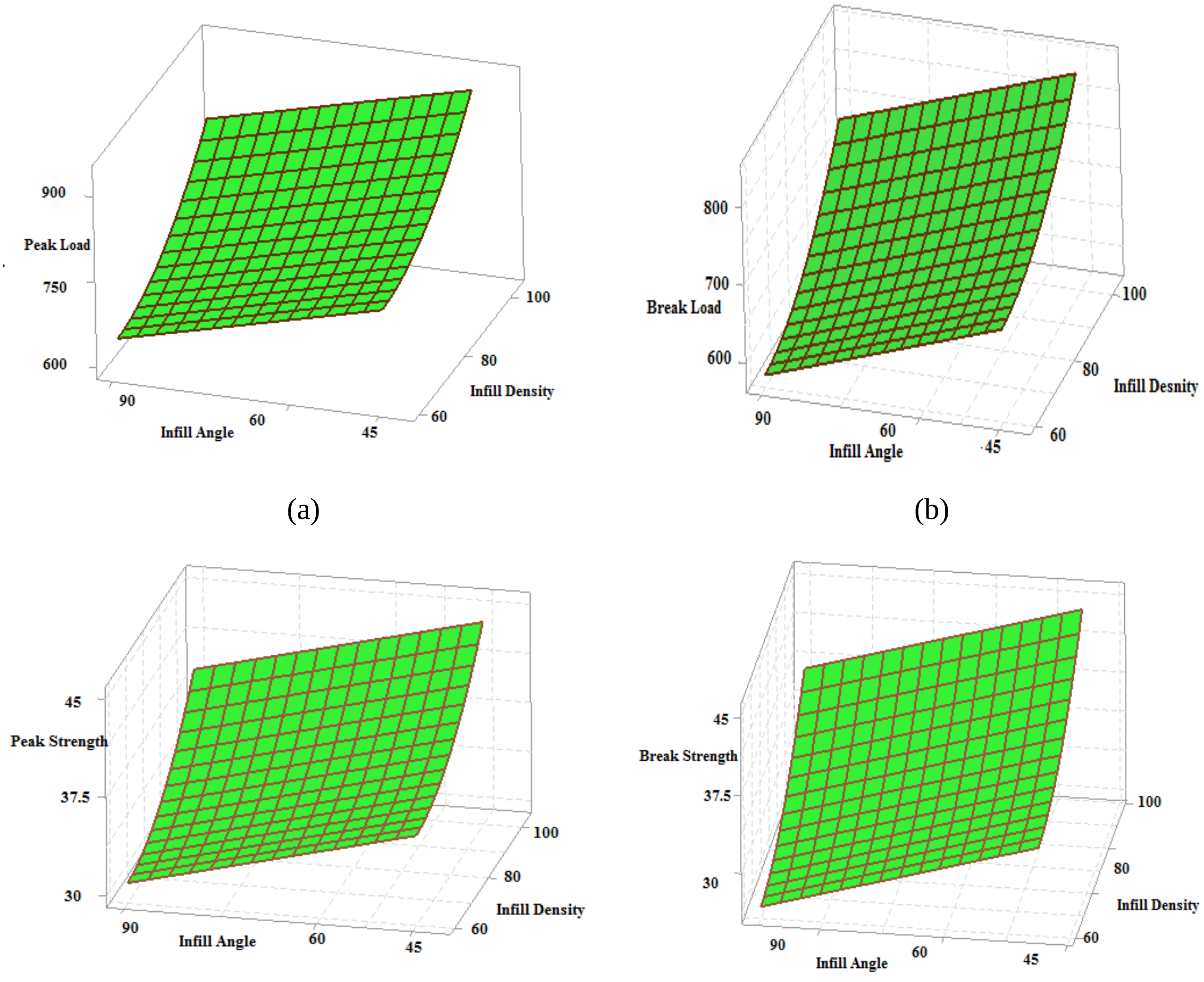

(a) (b)

(c) (d)

Figure 5.66 Surface plots for (a) PL, (b) BL, (c) PS, and (d) BS for multi-material specimen

5.4.5 Surface characterization

The 3D printed samples were tested for surface properties such as hardness using shore D tester on the bottom and top surfaces as the materials were different for each layer. Porosity was investigated at the cross-section of fractured samples and photomicrographs of fractured samples were taken to establish the relationship between surface and mechanical properties. Shore D hardness of 3D printed sample was investigated using shore D hardness tester. The top and bottom surfaces of printed samples were investigated to know the difference in hardness of different surfaces printed using different materials. After hardness measurement, it has been observed that the top surface (layer made of Fe_3O_4 reinforced PLA: $54 <$ Shore D hardness< 64) has low hardness than that of the bottom layer (layer made of virgin PLA: $77 <$ Shore D hardness < 80). It has also been observed that sample 7, printed with 100% infill density had maximum hardness (62.5 Shore D, Table 5.53) whereas sample 3 the lowest (54.5 Shore D) which meant that the hardness of samples was concerning mechanical properties as 7 samples had best tensile properties.

Table 5.53 Shore D hardness on the bottom and top surface of 3D printed samples for multi-material printed 3D parts

Experiment No.	Top surface hardness	Bottom surface hardness
1	55	78
2	56.5	78.5
3	54.5	79
4	58	79.5
5	57	78
6	57.5	79.5
7	62.5	79.5
8	60.5	77.5
9	62	78

5.4.6 Fractured surface image analysis

Photomicrographs of fractured samples have been taken on the tool maker’s microscope on a ×30 scale. It has been observed from the mechanical testing that by using the 3rd experimental condition, the printed sample had the least tensile property (Figure 5.67). The analysis of fractured surfaces from photo-micrographs has made it clear that the worst properties were due to large porosity holes present inside the printed specimen. Further, the 7th specimen with the best property, ha very low porosity holes which ultimately have given it more strength and better tensile and surface results. Similarly, the fractured cross-section of printed samples was subjected to surface rendering using the image analysis software package tool, through which surface roughness was investigated and similar trends have been observed as it was observed for fractured surface analysis by toolmakers microscope. It has been noted that for low density (Infill density: 60%) printed samples held maximum surface roughness (R_a>14 see Figure 5.68) whereas samples printed with high density (100% infill density) had low surface roughness (R_a<10) which ultimately resulted in better mechanical properties. For intermediate infill density (80%) the value of surface roughness varies in the range from 11<R_a<13 nm.

Serial number 1

Serial number 2

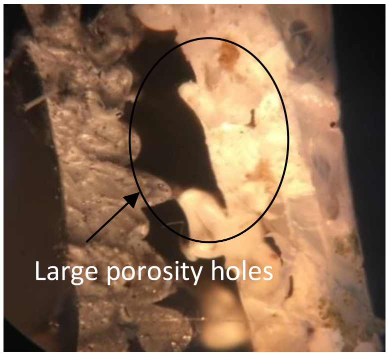

Serial number 3

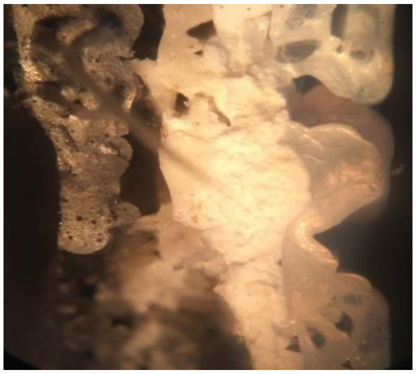

Serial number 4

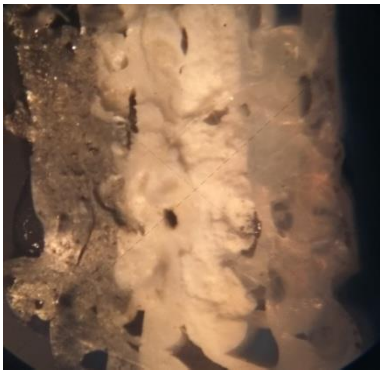

Serial number 5

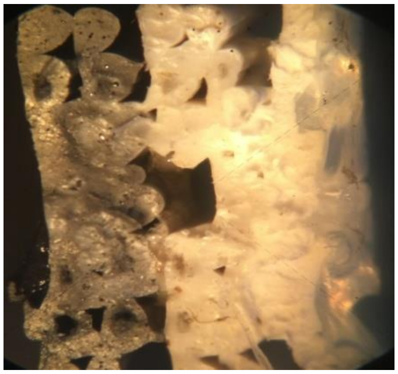

Serial number 6

Serial number 7

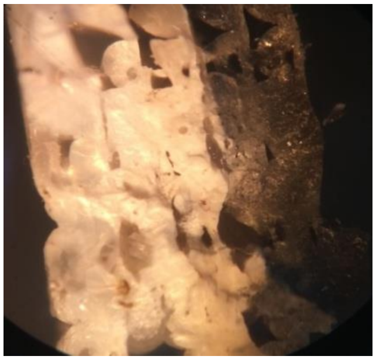

Serial number 8

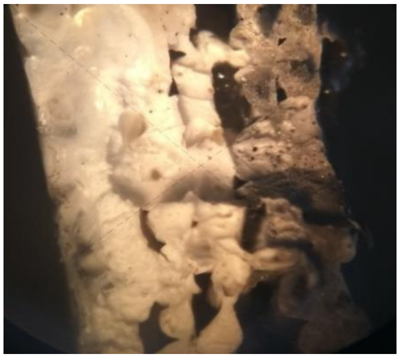

Serial number 9

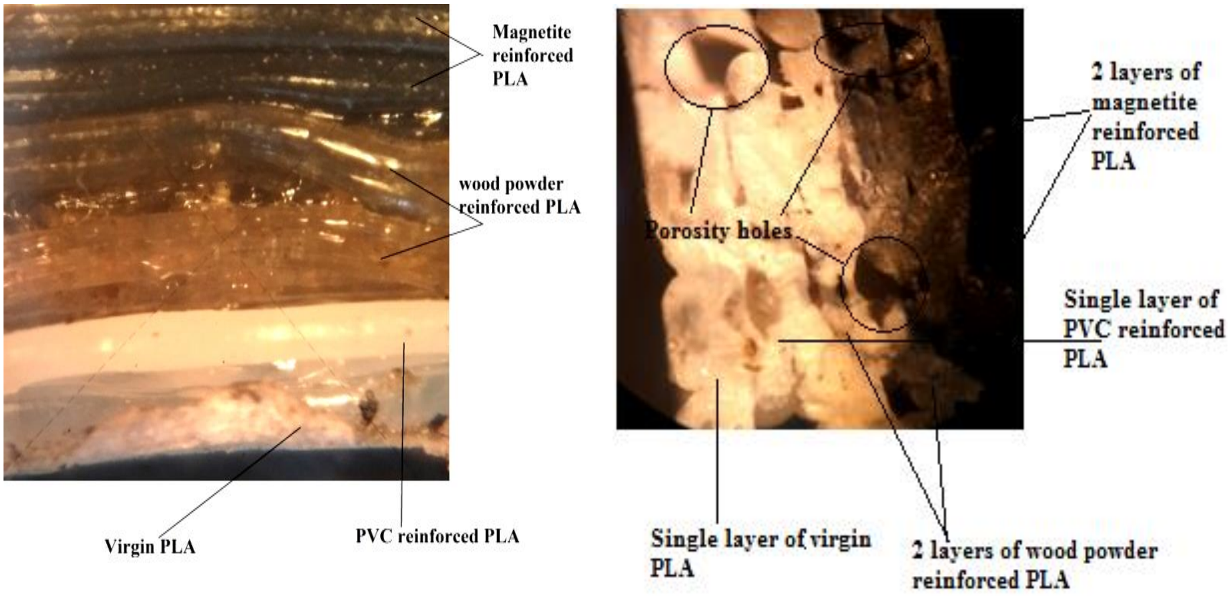

Figure 5.67 Tool maker's microscopic images at the cross-section of the fractured tensile specimen as per Table 4.8

Serial number	Rendered image	Roughness (R_a) value
1	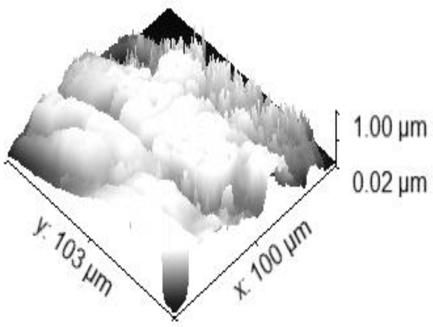	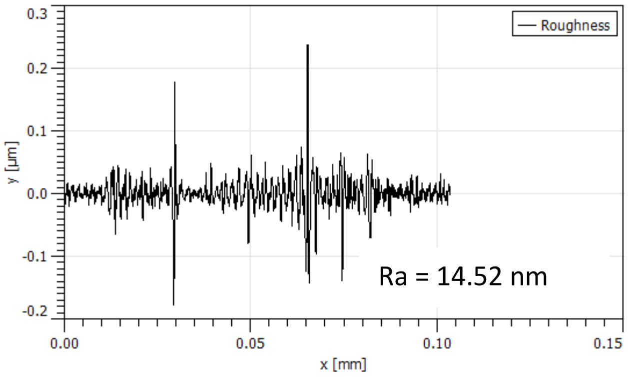
2	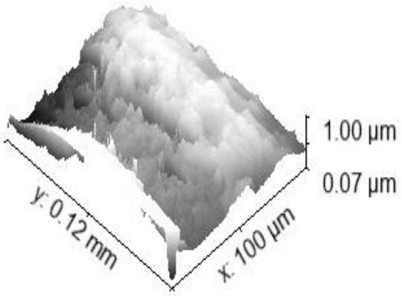	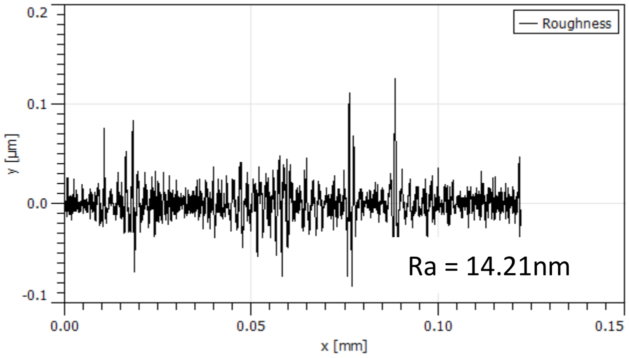

3

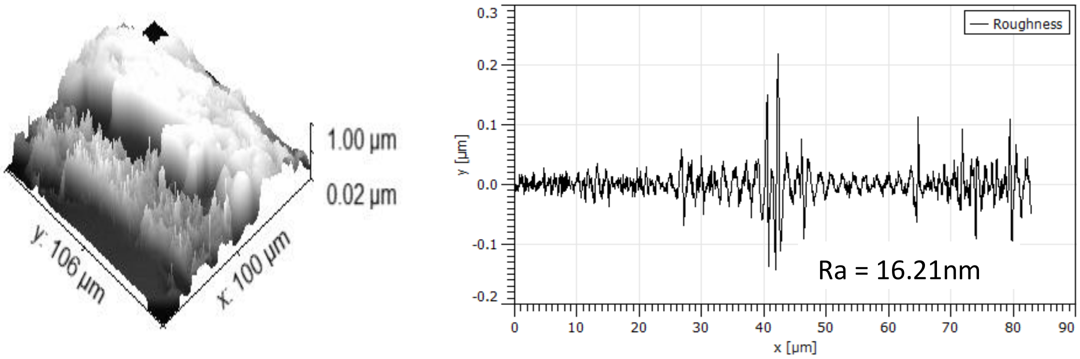
1.00 µm
0.02 µm
y: 106 µm
x: 100 µm
Roughness
y [µm]
0.3
0.2
0.1
0.0
-0.1
-0.2
0
10
20
30
40
50
60
70
80
90
x [µm]
Ra = 16.21nm

4

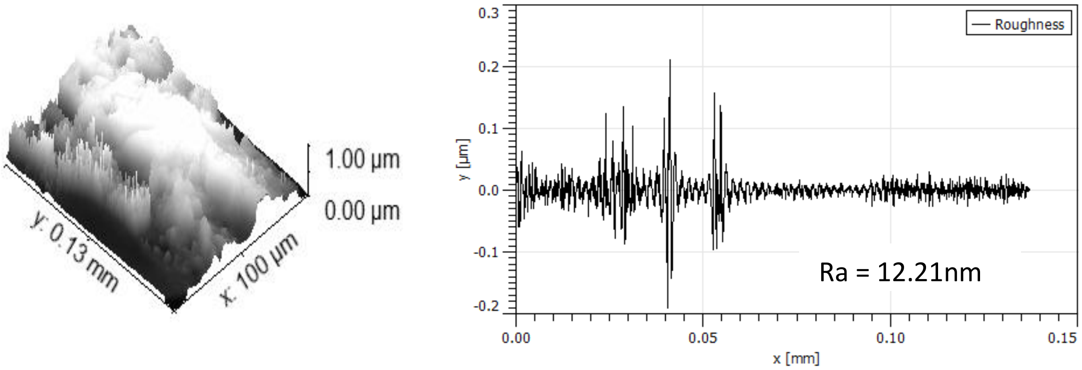
1.00 µm
0.00 µm
y: 0.13 mm
x: 100 µm
Roughness
y [µm]
0.3
0.2
0.1
0.0
-0.1
-0.2
0.00
0.05
0.10
0.15
x [mm]
Ra = 12.21nm

5

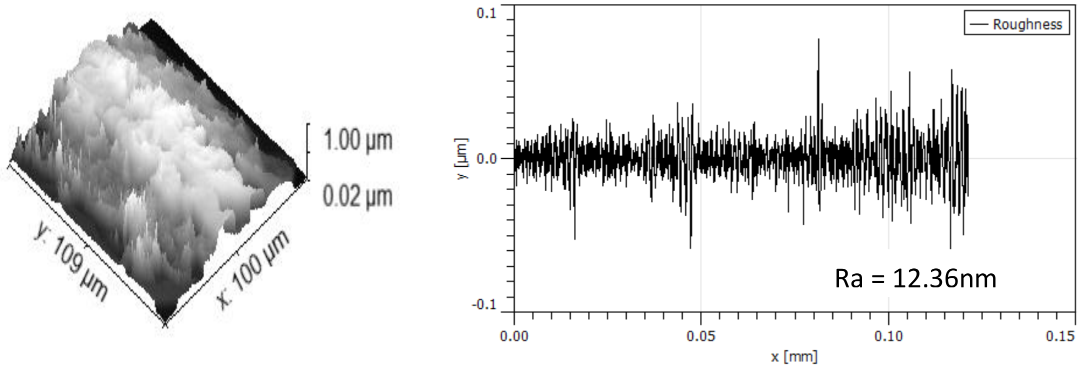
1.00 µm
0.02 µm
y: 109 µm
x: 100 µm
Roughness
y [µm]
0.1
0.0
-0.1
0.00
0.05
0.10
0.15
x [mm]
Ra = 12.36nm

6

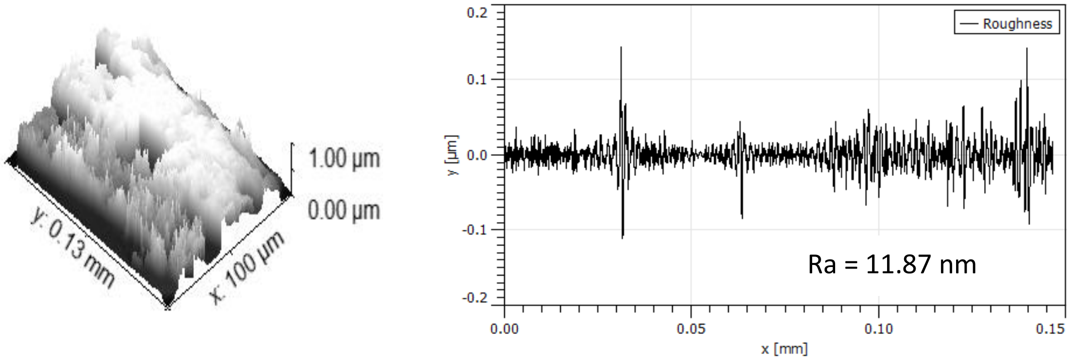
1.00 µm
0.00 µm
y: 0.13 mm
x: 100 µm
Roughness
y [µm]
0.2
0.1
0.0
-0.1
-0.2
0.00
0.05
0.10
0.15
x [mm]
Ra = 11.87 nm

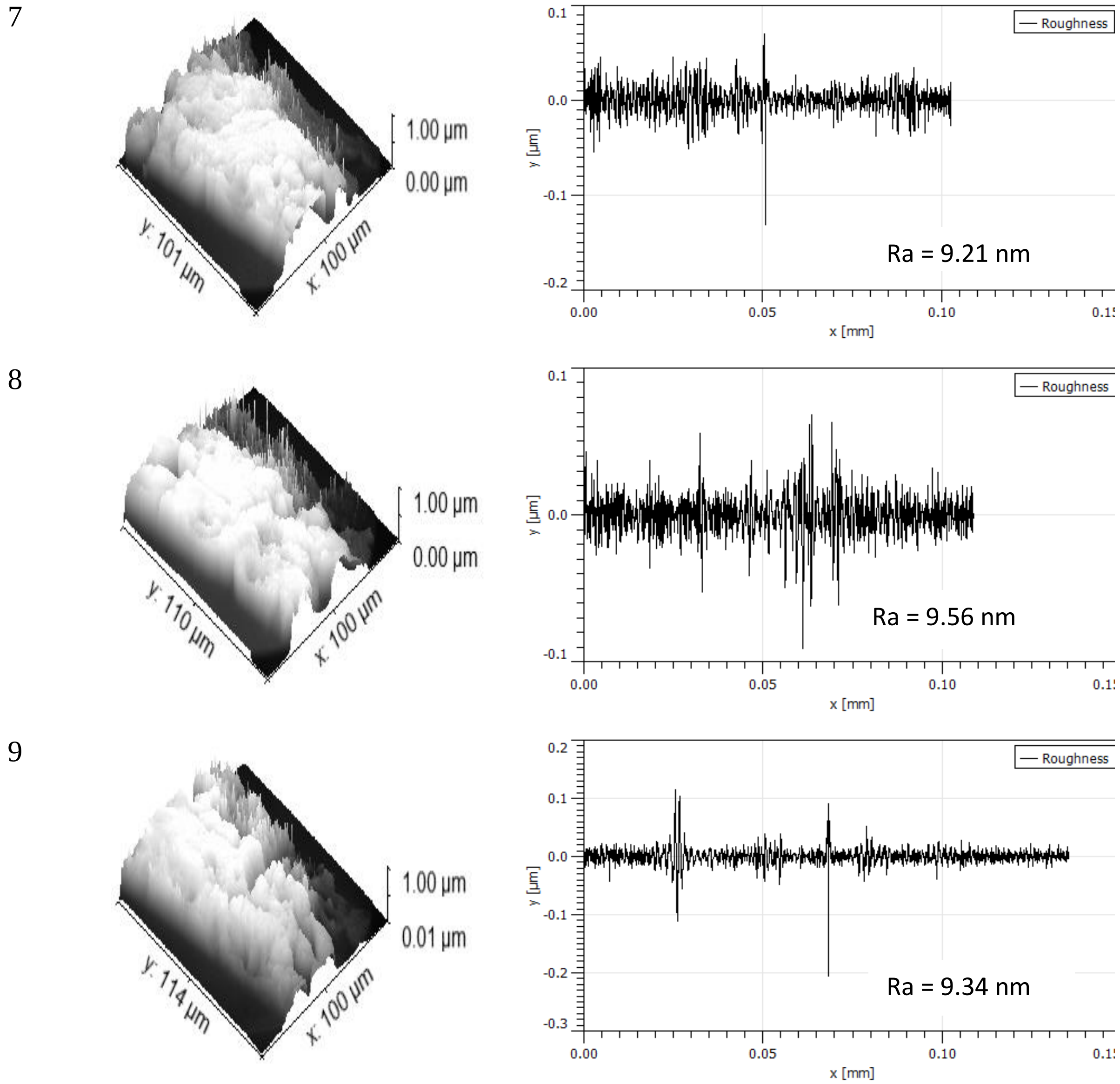

Figure 5.68 Surface roughness for multi-material printed part on the fractured cross-section as per Table 4.8

5.4.7 SEM and EDAX characterization of the fractured surface of multi-material matrix-based 3D printed tensile specimen

The fractured part of multi-material matrix-based 3D printed parts was also subjected to surface characterization using SEM image analysis. The 3D printed prototype held several interfaces at different locations therefore one SEM image at ×30 magnification was taken so that the whole surface may be captured to locate the different interfaces of different layers (Figure 5.69). Figure 5.70 shows the interface of PLA (100 weight percentage) and PLA/PVC (75/25 weight percentage) from which it was clear that the polymeric chain of PLA/PVC got embedded in the PLA (100 weight percentage) layer and has formed strong bonds due to which the mechanical properties improved in comparison with the single hybrid matrix. Figures 5.71 and 5.72 show the interfaces of PLA/PVC with PLA/wood powder (95/5 weight percentage) and PLA/wood powder with PLA/magnetite powder (80/20 wt.%) interfaces, respectively. Further, Figure 5.73 shows the EDAX characterization at 4 different locations for observing the elemental composition so that proper mapping of elements at different interfaces may be observed to know the molecular behavior while fusion at elevated temperature. As observed from the EDAX report (Table 5.54), spectrum location elements were different at different locations. Only in spectrum 1, the presence of Fe particles was observed which specifies that the layer contains PLA reinforced with magnetite powder at the extreme position. Thus, on the application of a magnetic field, the extreme layer may be magnetized (hence justifies the functionally graded layer formation). Similarly, spectrum 3 containing chlorine indicates that the layer is composed of PVC and PLA and provides ductility at the middle of the structure resulting in more stain capacity of the prototype. Spectrum 4 shows the presence of a 100% PLA layer as only carbon and oxygen are present as elements of that spectrum.

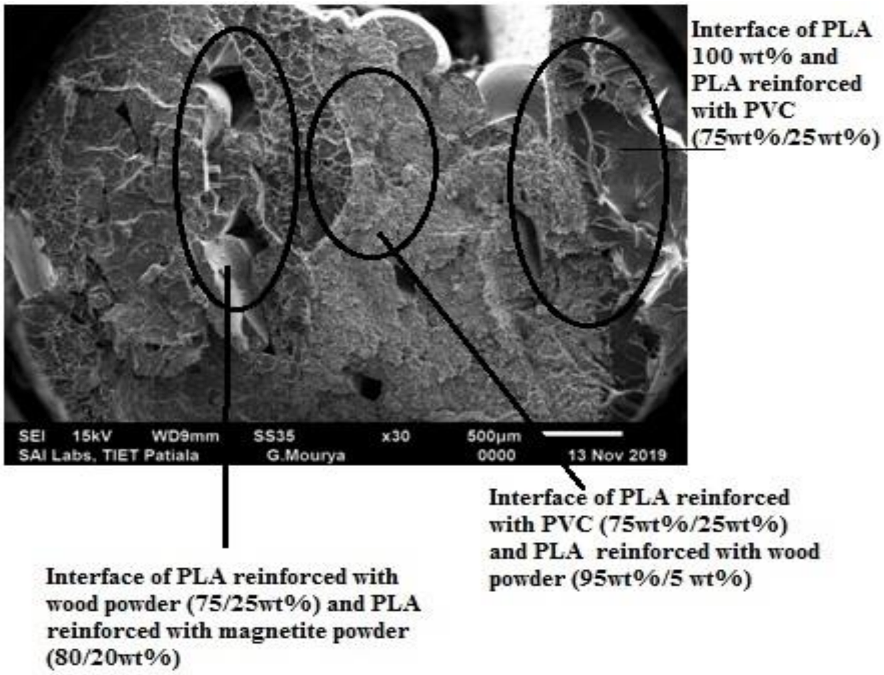

Figure 5.69 SEM image of fractured multi-material specimen at (a) ×30 magnification

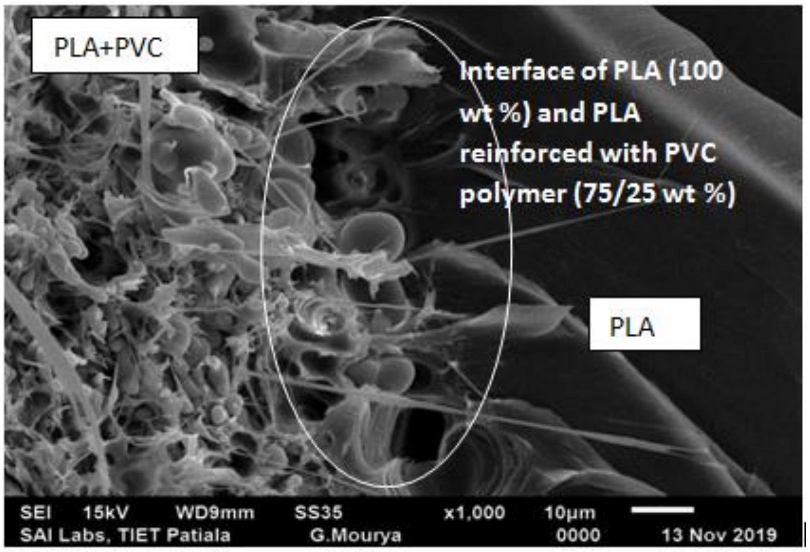

Figure 5.70 SEM image at ×1000 magnification for PLA and PLA/PVC interface

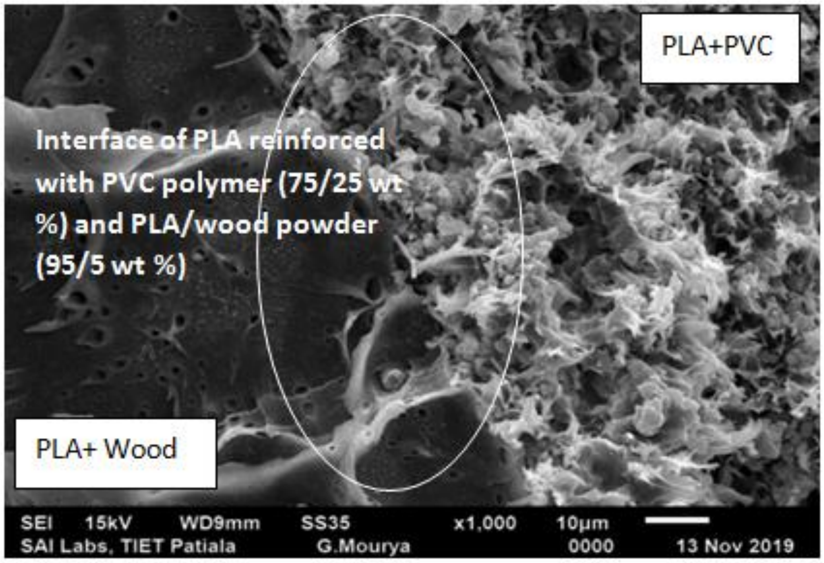

Figure 5.71 SEM image at ×1000 magnification for PLA/PVC and PLA/wood powder interface

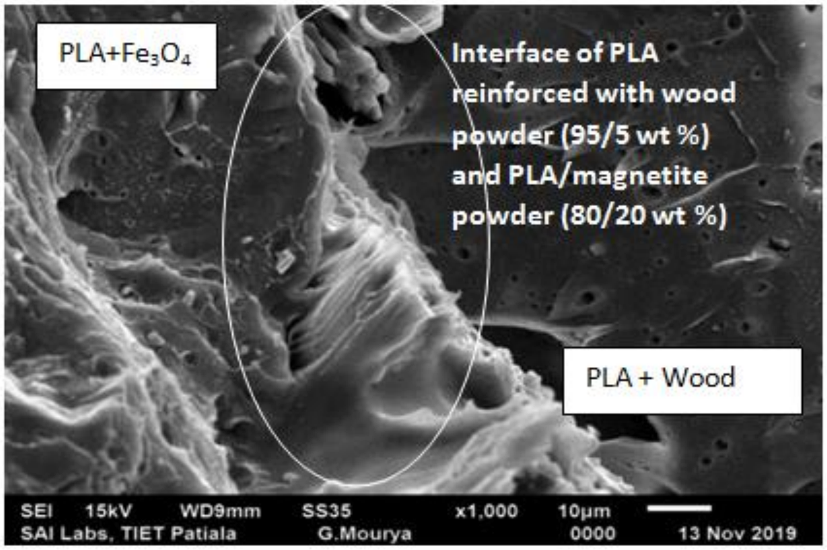

Figure 5.72 SEM image at ×1000 magnification for PLA/wood powder and PLA/magnetite powder interface

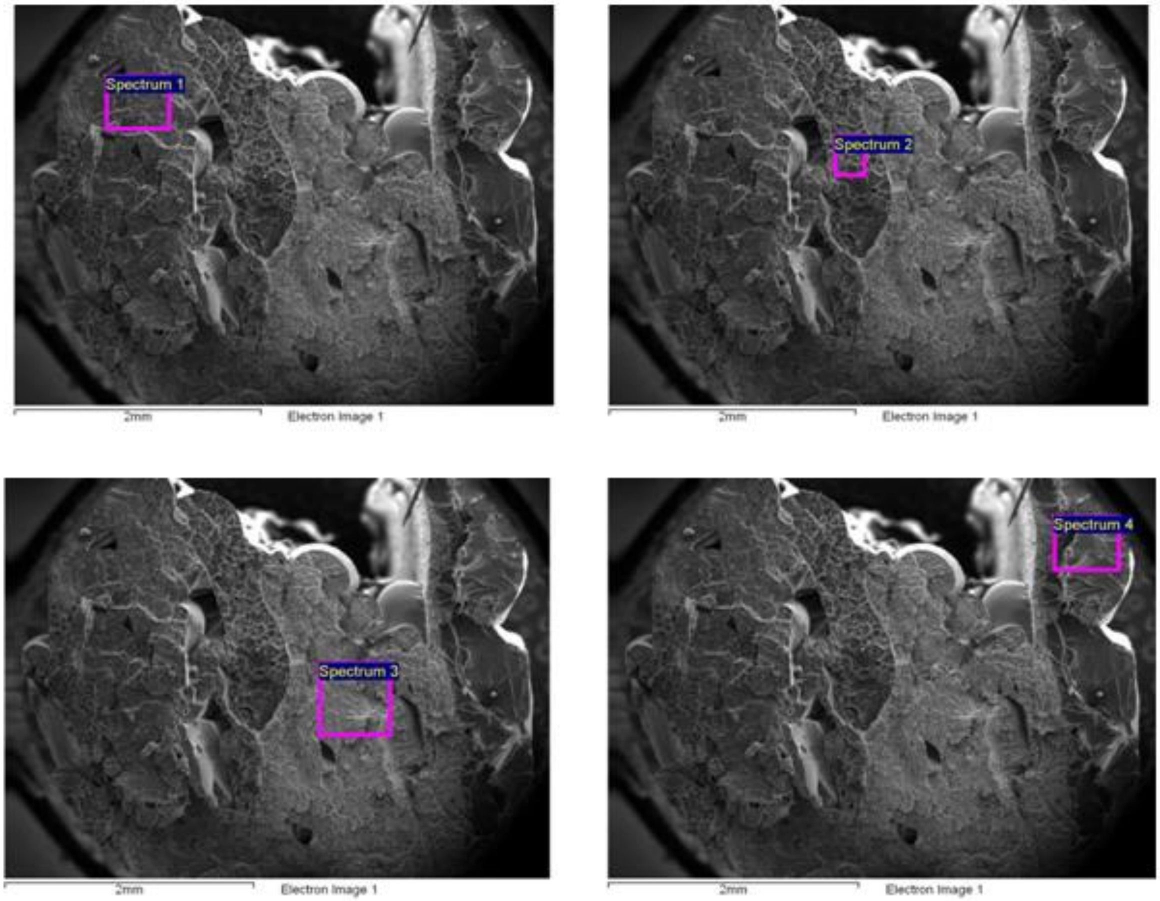

Figure 5.73Four selected spectrum at different location of the observed surface under EDS for multi-material matrix-based prototype

Table 5.54 Elemental composition present over the observed spectrum of multi-material matrix-based prototype under EDS testing

Spectrum	In stats.	C	O	Cl	Fe	Total
Spectrum 1	Yes	47.02	45.29	0.35	7.34	100.00
Spectrum 2	Yes	50.02	47.18	2.72	0.09	100.00
Spectrum 3	Yes	61.85	24.10	14.04	0.00	100.00
Spectrum 4	Yes	49.13	49.50	1.01	0.36	100.00

5.4.8 3D printing results for flexural specimens

For the preparation of functionally graded prototypes, four different feedstocks were used (Figure 5.62) at different layers of the printing. The bottom layer was printed with virgin PLA, the 2nd layer with PVC reinforced PLA. The 3rd and 4th layers were printed with wood powder reinforced PLA and the 5th and 6th (top) layers were printed with Fe_3O_4 reinforced PLA (with fixed layer height 0.53mm). Figure 5.74 (a) shows the top view of the printed sample, 5.74 (b) shows the bottom view of 3D printed flexural specimens using ASTM D790 standard and 5.74 (c) shows the UTM tested flexural specimens.

(a)

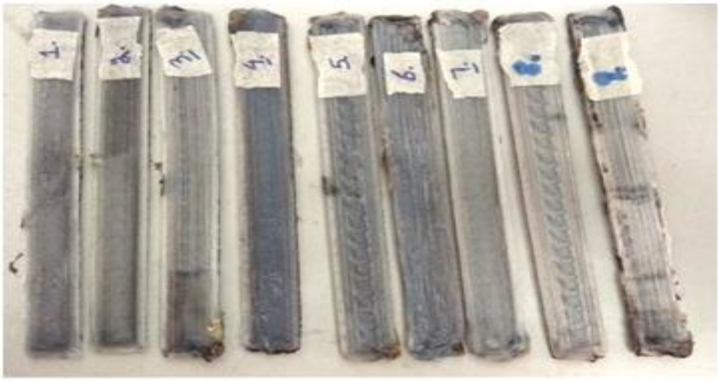

(b)

Figure 5.74 3D printed flexural specimens (a) Top view, (b) bottom view, and (c) UTM tested flexural specimens as per Table 4.8

5.4.9 Flexural and pull-out testing results of multi-material 3D printed specimens

The 3D printed samples were tested with UTM for flexural and pull-out properties. Table 5.55 shows the observed values of PL, BL, PS, and BS for flexural properties, and Figure 5.75 shows the stress vs. strain diagram for flexural tested specimens. From Table 5.55 it has been observed that experimental condition 7 provides the maximum values for all mechanical properties and sample 3 has shown poor results. This may be because sample 7 was printed with 100% infill density and 45° infill angle which resulted in the better joining of layers and least void formation due to which the specimen has shown excellent flexural properties in comparison to any other specimen. From the stress and strain curve, it was observed that sample 7 has maximum peak strength but the strain capacity was not maximum resulting in the brittle nature. Sample 8 has less peak strength than sample 7 but was found to be more ductile as its strain-absorbing capacity was higher. Based on Table 5.55 and Figure 5.75, modulus of toughness (Table 5.56) was calculated and it was observed that maximum modulus of toughness was found for sample 8. Therefore, sample 8 was considered a better candidate for crash applications than sample 7 which was found to be more brittle than sample 8. Similar studies were performed for pull-out tested specimens and properties PL, BL, PS, and BS (Table 5.57) were recorded for further analysis. From Table 5.57, it was observed that the trends seen for flexural properties were similar for pull-out properties (sample 7 was observed the best for pull properties and sample 3 was least effective). The poor properties for sample 3 may be due to reason that it was printed with the lowest infill density of 60% and infill angle of 90° which resulted in more void formation or poor joining of layers due to which it has given the least resistance to destruction. Figure 5.76 shows the stress vs. strain plot for pull-out tested specimen and it has been observed that sample 1 had a maximum modulus of toughness in case of pull-out testing (Table 5.58). But its peak strength was not the highest. Other than sample 1, test specimens printed with 100% infill density (samples 7, 8, and 9) have shown better results in the case of modulus of toughness.

Table 5.55 Observations of flexural testing of multi material specimen

Serial number	PL (KN)	BL (KN)	PS (MPa)	BS (MPa)
1	128.4 ± 6.67	115.56 ± 8.81	24.48 ± 3.20	22.03 ± 1.73
2	107.8 ± 8.81	97.02 ± 7.52	20.55 ± 2.21	18.5 ± 3.20
3	93.1 ± 7.52	83.79± 6.67	17.75 ± 1.73	15.98 ± 1.73
4	132.3 ± 8.81	119.07 ± 8.81	25.22 ± 3.12	22.7 ± 3.12
5	123.5 ± 6.67	111.15 ± 7.52	23.55 ± 1.73	21.19 ± 3.12
6	118.1 ± 7.52	106.29 ± 6.67	22.52 ± 3.20	20.27 ± 3.20
7	141.2 ± 7.52	127.08 ± 8.81	26.92 ± 3.12	24.23 ± 3.12
8	132.3 ± 8.81	119.07 ± 7.52	25.22 ± 1.73	22.7 ± 1.73
9	118.6 ± 6.67	106.74 ± 6.67	22.61 ± 3.20	20.35 ± 3.20

Table 5.56 Modulus of toughness for flexural specimens of multi material

Serial number	BS (MPa)	Strain	Modulus of toughness (1/2×BS×Strain) (MPA)
1	22.03	0.409	4.5051
2	18.5	0.51	4.7175
3	15.98	0.539	4.3066
4	22.7	0.46	5.2210
5	21.19	0.549	5.8166
6	20.27	0.58	5.8783
7	24.23	0.46	5.5729
8	22.7	0.631	7.1618
9	20.35	0.379	3.8563

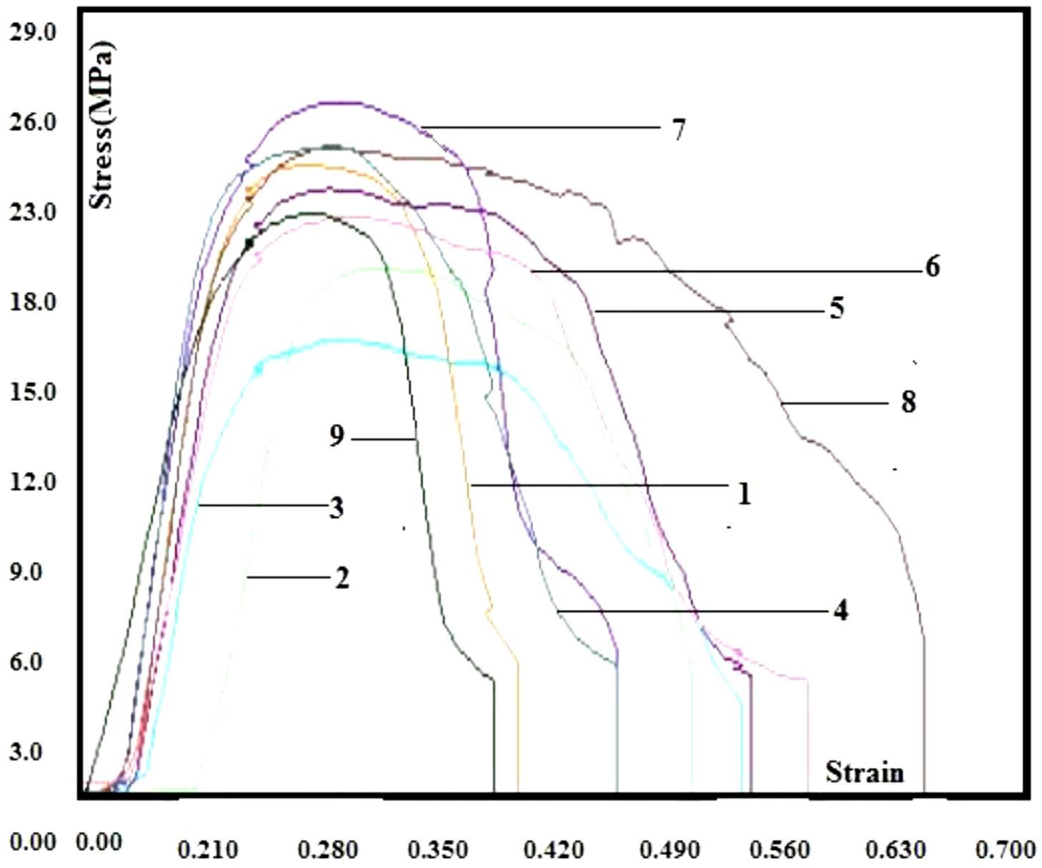

Figure 5.75 Stress vs. strain for flexural properties as per Table 4.8

Table 5.57 Pull out testing results of multi material specimen

Serial number	PL (KN)	BL (KN)	PS (MPa)	BS (MPa)
1	339.8 ± 6.67	305.82 ± 10.14	16.86 ± 3.67	15.17 ± 3.67
2	312.3 ± 10.14	281.07 ± 6.67	15.49 ± 2.14	13.94 ± 1.31
3	254 ± 9.31	228.6 ± 10.14	12.6 ± 1.31	11.34 ± 2.14
4	379.5 ± 10.14	341.55 ± 6.67	18.82 ± 3.67	16.94 ± 3.67
5	360.4 ± 9.31	324.36 ± 9.31	17.88 ± 2.14	16.09 ± 1.31
6	311.3 ± 6.67	280.17 ± 6.67	15.44 ± 3.67	13.9 ± 2.14
7	382.9 ± 9.31	344.61 ± 10.14	18.99 ± 1.31	17.09 ± 1.31
8	362.8 ± 10.14	326.52 ± 9.31	18 ± 2.14	16.2 ± 2.14
9	348.1 ± 6.67	313.29 ± 6.67	17.27 ± 3.67	15.54 ± 3.67

Table 5.58 Modulus of toughness for pull out properties of multi material specimen

Serial number	BS (MPa)	Strain	Modulus of toughness (1/2×BS×Strain) (MPA)
1	15.17	0.92	6.9782
2	13.94	0.11	0.7667
3	11.34	0.19	1.0773
4	16.94	0.38	3.2186
5	16.09	0.30	2.4135
6	13.90	0.26	1.8417
7	17.09	0.35	2.9907
8	16.20	0.30	2.4301
9	15.54	0.42	3.3022

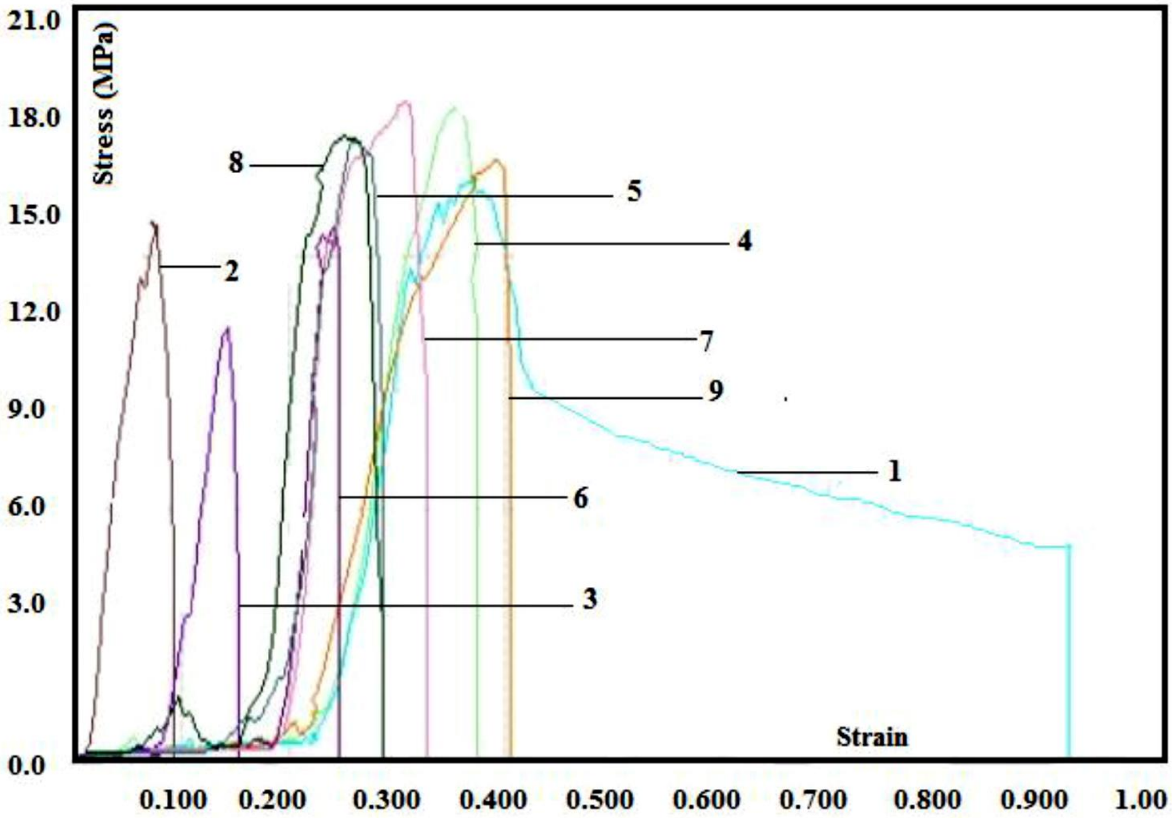

Figure 5.76 Stress vs. strain for pull out test as per Table 4.8

5.4.10 Optimization of flexural and pull-out properties

Optimization for a peak load of flexural property for a multi-material component

Based on the information in Tables 5.55 and 5.57, flexural and pull-out properties were further optimized so that a standard 3D printing condition may be obtained for statistical control of the output properties. The analysis of variance (ANOVA) method has been employed for optimization using MiniTab 17 statistical package tool. Table 5.59 shows the ANOVA table for the peak load property of the flexural tested specimen. It has been observed that infill angle has contributed maximum (48.85%) towards output whereas infill density has also significant contribution (41.70%) but infill speed has shown least contribution of only 6.66%. The residual error (0.2701) is just 2.89% of the total error which signifies that the model accuracy is within 95% confidence interval. Table 5.60 shows the rank table for the peak load property of the flexural specimen. From the rank table, it has been observed that infill angle has been ranked at 1st position and infill density at 2nd position whereas infill speed with the least contribution has been ranked 3rd or at the lowermost position. Figure 5.77 shows the main effect plot of peak load for the flexural tested sample and it has been observed that infill density of 100%, infill angle of 45°, and infill speed of 50 mm/s are the optimized condition for 3D printing. The optimized conditions were out of selected DOE (Table 4.8), therefore for peak load, flexural testing optimized values were again predicted. From ANOVA optimization, it has been found that the optimized value for the suggested condition was 150.48 N for peak load which was very near the actual value of peak load for sample 7. This may be because the infill density and infill angle are the same for sample 7 and the suggested/optimized condition of 3D printing. The difference was only in infill speed. As the infill speed has the least contribute towards the output, the difference in the value of peak load for suggested/optimized and actual condition (sample 7) was very less. Therefore, one may select the 7th experimental condition (Table 4.8) for 3D printing the flexural prototype of multi-material functionally graded material. Similar studies have been performed for all other mechanical properties and it has been ascertained that similar trends were present for all the properties of the flexural specimen. In the case of pull-out property, infill density of 100%, infill angle of 45° and infill speed of 70 mm/s were the optimized/suggested conditions for 3D printing. But from observations, it has been noted that infill speed has an insignificant role to play in the output. So it may be ignored and experimental condition 7 can be taken as the optimized condition for standardizing printing of prototypes.

Table 5.59 ANOVA for SN ratios of PL for flexural specimen

Source	DF	Seq SS	Adj SS	Adj MS	F	P	Percentage Contribution
Infill Density	2	3.9881	3.9881	1.9941	14.77	0.063	41.70
Infill Angle	2	4.6705	4.6705	2.3352	17.29	0.055	48.85
Infill Speed	2	0.6338	0.6338	0.3169	2.35	0.299	6.66
Residual Error	2	0.2701	0.2701	0.1350			22.89
Total	8	9.5625					

Table 5.60 Rank table for SN ratios of peak load for flexural specimen of multi material printed 3D parts

Level	Infill Density	Infill Angle	Infill Speed
1	40.73	42.53	42.02
2	41.90	41.64	41.52
3	42.30	40.77	41.40
Delta	1.57	1.76	0.61
Rank	2	1	3

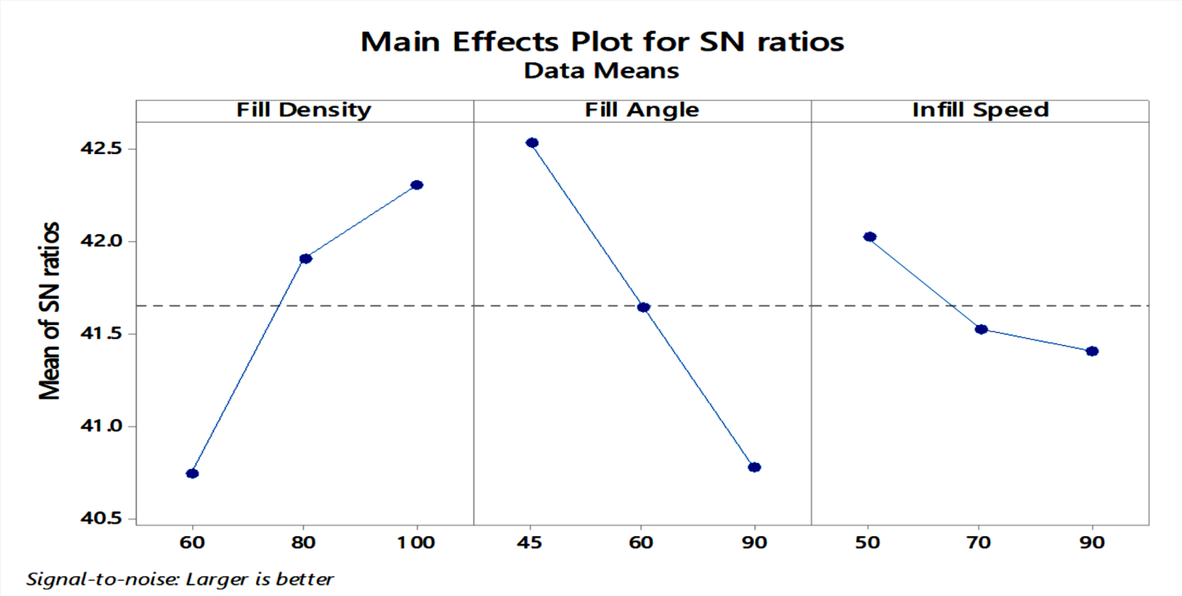

Figure 5.77 Main effect plot for SN ratio for the peak load of flexural specimens for multi-material specimens

$$\text{Ŋ opt} = m + (mA - m) + (mB - m) + (mC - m)$$

$$Y_{\text{opt}}^{2} = 10^{\text{Ŋ opt}/10}\text{(for properties, larger is the better case)}$$

$$m = \text{SN mean of PL} = 41.65$$

$$mA = \text{max infill density from Table 5.60} = 42.30$$

$$mB = \text{max infill angle from Table 5.60} = 42.53$$

$$mC = \text{max infill speed from Table 5.60} = 42.02$$

$$\textit{putting all values in equation}$$

$$\text{Ŋ opt} = 41.65 + (42.30 - 41.65) + (42.53 - 41.65) + (42.02 - 41.65)$$

$$\text{Ŋ opt} = 43.55\ \text{dB}$$

$$Y_{\text{opt}}^{2} = 10^{43.55/10}$$

$$Y_{\text{opt}} = 150.48\ \text{KN}$$

5.4.11 Shore D hardness results for flexural specimens of multi-material component

The surface hardness of 3D printed prototypes was measured on top and bottom surfaces as the two extreme surfaces were with different reinforcements. It has been observed from the hardness characterization that the top layer (PLA reinforced with 20 weight percentageFe_3O_4) was less hard than the bottom layer (virgin PLA). This may be because the virgin PLA layer has fewer voids and better-diffused material as compared to the reinforced PLA layer. Figure 5.78 shows the observed values of surface hardness on two extreme faces of flexural printed specimens. It should be noted that with higher infill density, surface hardness was improved for PLA reinforced with 20 weight percentage Fe_3O_4 powder, whereas for virgin PLA layer, no significant effect of infill density on hardness was recorded.

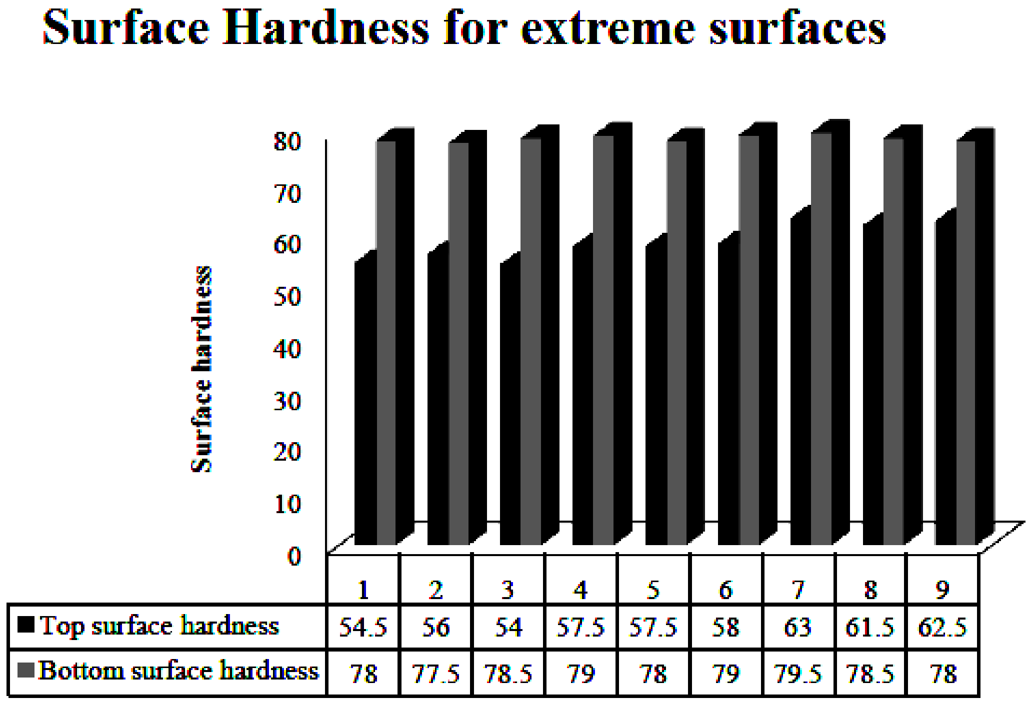

	1	2	3	4	5	6	7	8	9
■ Top surface hardness	54.5	56	54	57.5	57.5	58	63	61.5	62.5
■ Bottom surface hardness	78	77.5	78.5	79	78	79	79.5	78.5	78

Figure 5.78 Shore D surface hardness for extreme surfaces as per Table 4.8

5.4.12 Fractured surface analysis for flexural specimens of multi-material component

The tested samples were observed under tool maker's microscope on ×30 magnification and it has been observed over the cross-section of the fractured sample that specimens printed with infill density 100% had uniform diffusion of material which resulted in fewer voids (Figure 5.79) due to which the joint strength was more than that of lower infill density. Thus, it may be concluded from the fractured surface analysis that higher infill density (Infill density: 100%) and low infill angle (infill angle: 45°) result in uniform material deposition of diffused material on 3D platform resulting in better mechanical properties. The fractured surface photomicrographs were used for image analysis using an image analyzing software package tool for conversion of fractured surface image (which is in 2D) into the 3D rendered surface for further quantifying the surface roughness trends for the fractured specimens. It has been observed that a high Ra value was recorded for 3D printed flexural specimens with high infill angle and low infill density (Figure 5.80). This may be because with low infill density there may be some internal voids due to which the joining of diffused material was not proper which resulted in high roughness and ultimately in poor flexural and pull-out performance.

S.No. 1

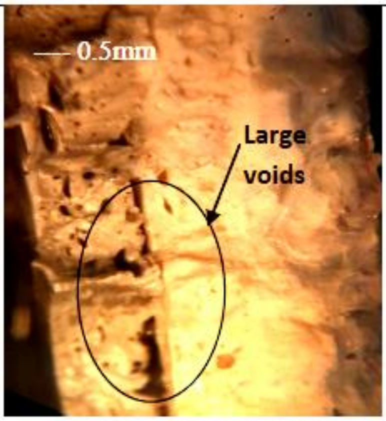

S.No. 2

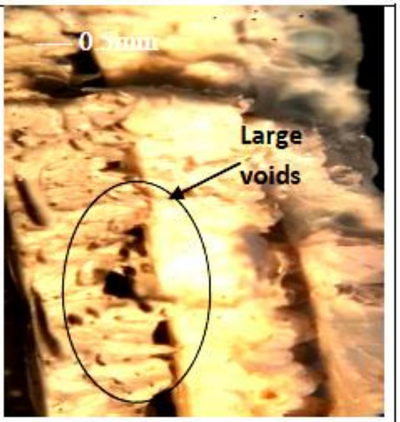

S.No. 3

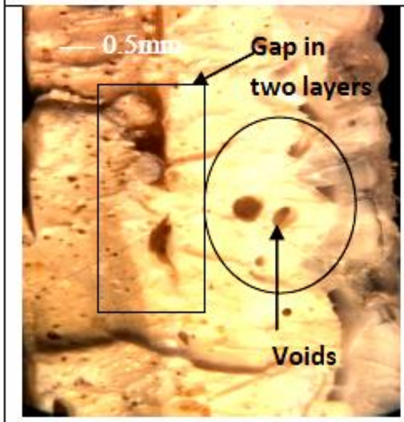

S.No. 4

S.No. 5

S.No. 6

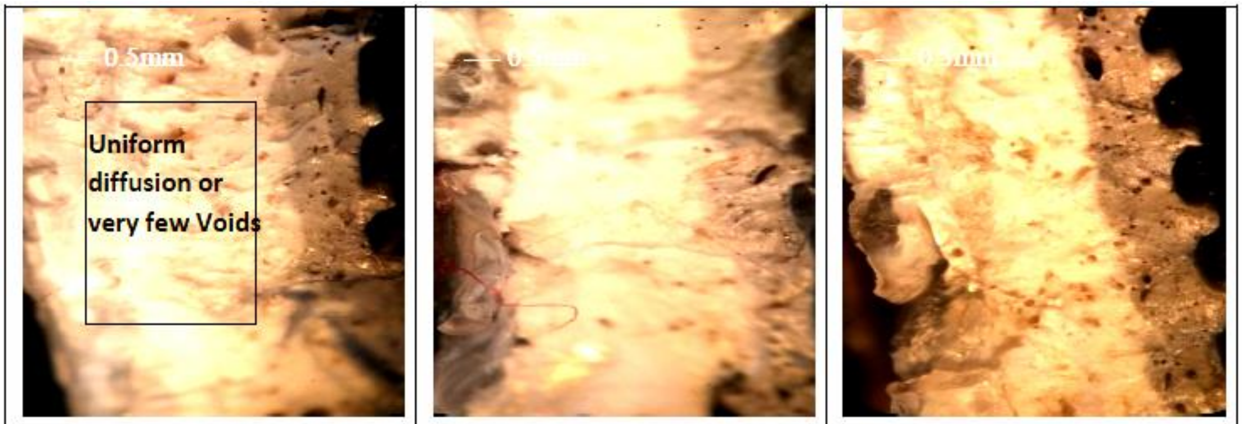

S.No. 7	S.No. 8	S.No. 9

Figure 5.79 Cross-section of fractured surface images for flexural specimens as per Table 4.8

Serial number	3D rendered photomicrograph	Roughness (Ra) value
1	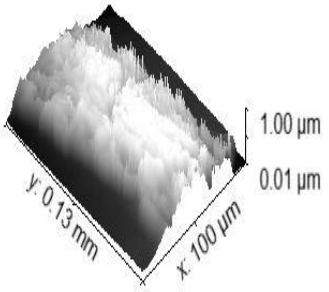	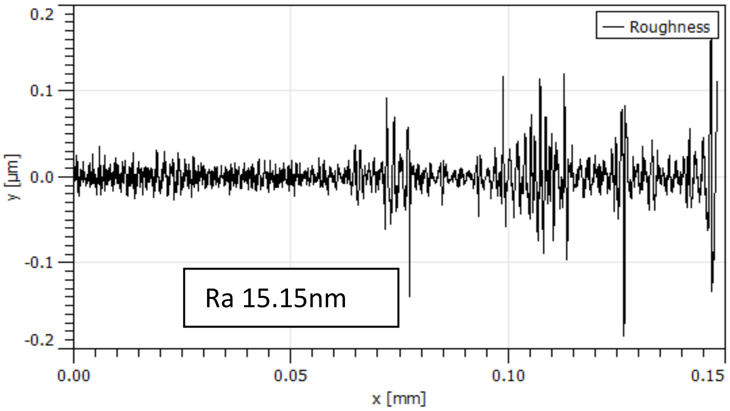
2	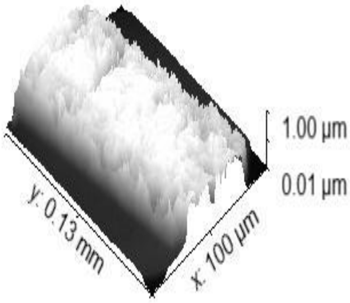	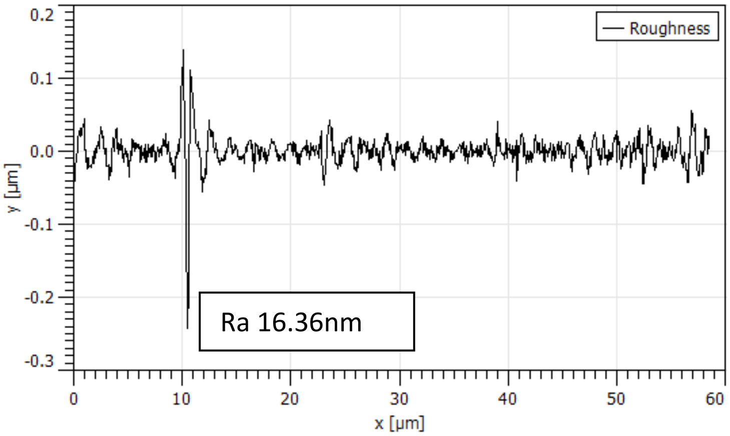

3

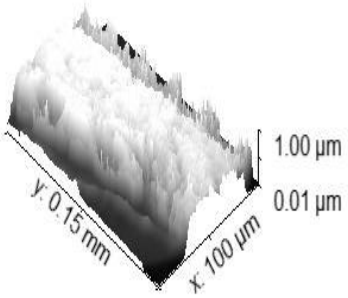
1.00 µm
0.01 µm
y: 0.15 mm
x: 100 µm

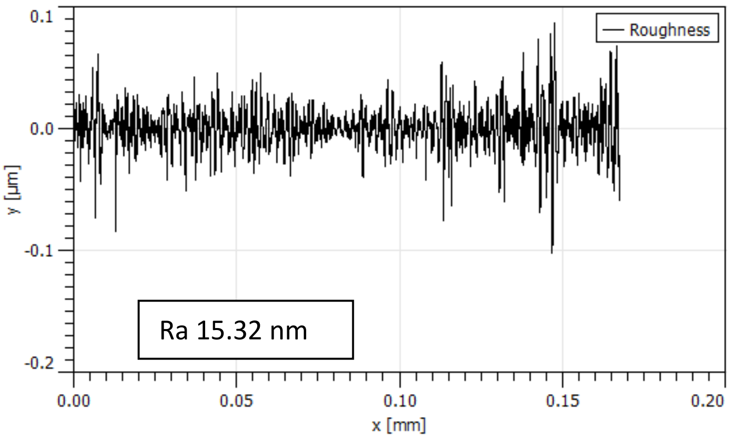
Roughness
Ra 15.32 nm
y [µm]
0.1
0.0
-0.1
-0.2
0.00
0.05
0.10
0.15
0.20
x [mm]

4

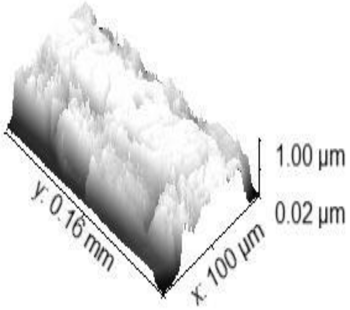
1.00 µm
0.02 µm
y: 0.16 mm
x: 100 µm

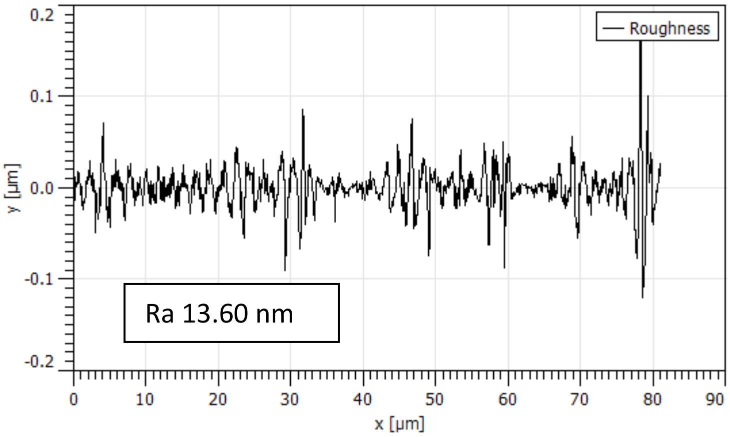
Roughness
Ra 13.60 nm
y [µm]
0.2
0.1
0.0
-0.1
-0.2
0
10
20
30
40
50
60
70
80
90
x [µm]

5

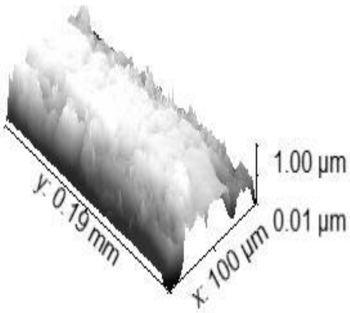
1.00 µm
0.01 µm
y: 0.19 mm
x: 100 µm

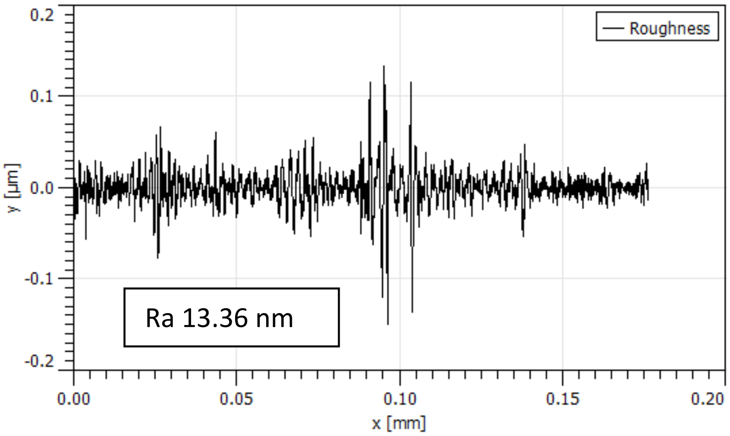
Roughness
Ra 13.36 nm
y [µm]
0.2
0.1
0.0
-0.1
-0.2
0.00
0.05
0.10
0.15
0.20
x [mm]

6

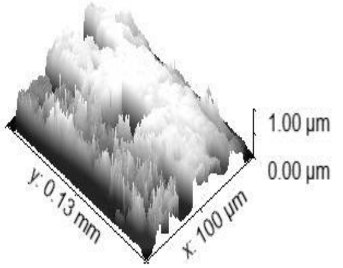
1.00 µm
0.00 µm
y: 0.13 mm
x: 100 µm

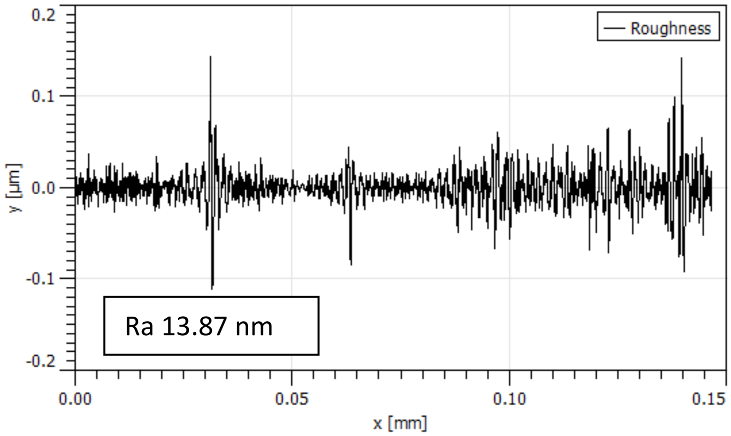
Roughness
Ra 13.87 nm
0.2
0.1
0.0
-0.1
-0.2
y [µm]
0.00
0.05
0.10
0.15
x [mm]

7

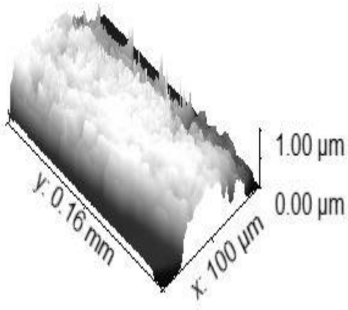
1.00 µm
0.00 µm
y: 0.16 mm
x: 100 µm

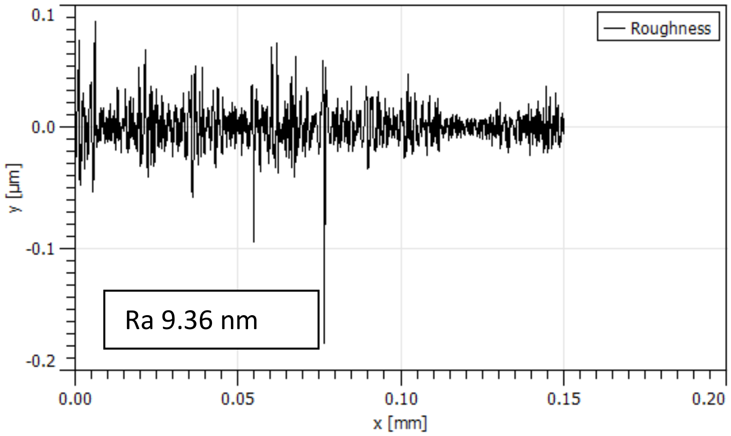
Roughness
Ra 9.36 nm
0.1
0.0
-0.1
-0.2
y [µm]
0.00
0.05
0.10
0.15
0.20
x [mm]

8

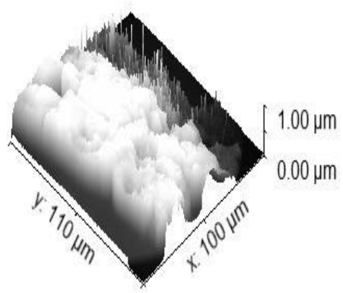
1.00 µm
0.00 µm
y: 110 µm
x: 100 µm

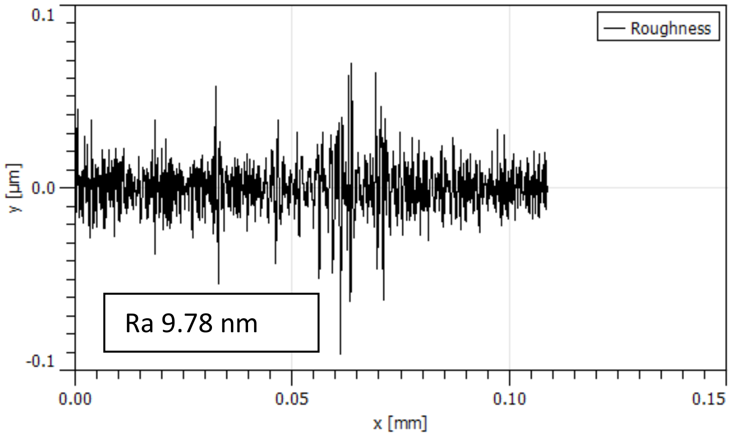
Roughness
Ra 9.78 nm
0.1
0.0
-0.1
y [µm]
0.00
0.05
0.10
0.15
x [mm]

9

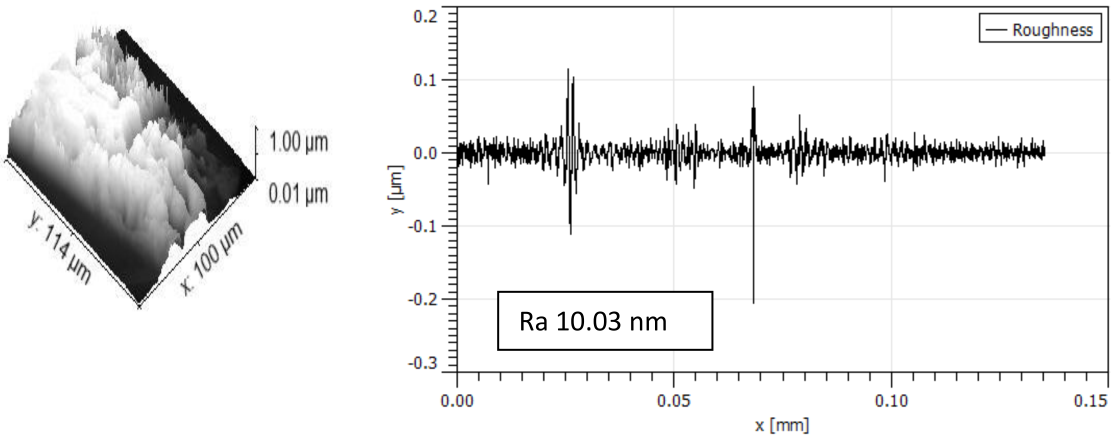

Figure 5.80 Processed image for the fractured surface of flexural tested samples as per Table 4.8

5.5 Results and discussion for stage 5

5.5.1 Extrusion and UTM results

The mechanical recycling of polymeric material of PLA composite was performed for three stags and feedstock was developed for each stage successfully. The images of recycled pellets were taken at each recycling step to differentiate between their conditions after each stage of recycling. Figure 5.81shows the actual images of virgin/polymeric blend and recycled pellets of PLA composites of different recycling stages. Table 5.61 shows the UTM results of different feedstock tested for their mechanical strength. From UTM results, it was observed that among the four different feedstocks of PLA composites, the first stage of feedstock developed with virgin polymeric blend was the best. As the material was processed again for different stages of recycling the material strength got reduced. This may be due to the reason that the first stage of feedstock was made of the virgin polymeric blend which holds an un-deformed chain of polymeric composition/ proportion.

The first stage of feedstock was unharmed in the manner that the polymeric blend has gone through the heating cycle for the first time in its life. But as the extruded material was again used as material in the second stage of recycling, the chain may have got disturbed due to passing through more heating cycles which affected the material strength by reducing the chain bonding capacity of the monomer. From Table 5.61, it may be observed that the properties for PLA (without reinforcement) in different recycled stages were not reduced significantly in comparison to the PLA composite matrix. This may be due to the reason that the PLA matrix was capable of passing through several heating cycles which may also be observed from Figure 5.81, where the change in material matrix color was very less compared to the first stage of recycling to the last stage. Similar results were observed for the PLA/Fe_3O_4 composite matrix that also resulted in less loss in mechanical properties for different stages of recycling. Figure 5.81 shows the minor changes in the color of the recycled material matrix of PLA/Fe_3O_4. Table 5.61 also shows the percentage mechanical property losses of materials for different stages of recycling using equation 1. From Table 5.61, it was observed that minimum mechanical property loss (-1.25%) was observed for the PLA/Fe_3O_4 material matrix which shows that the addition of Fe_3O_4 in the PLA matrix was beneficial as its mechanical strength and recycling life got improved. The recycling efficiency of PLA for stage 1 was at the second position in terms of minimal loss in mechanical strength.

The break elongation (BE) for PLA was seen to improve for two stages of recycling from 3.23mm to 6.65mm but for stage 3 the value decreased to 3.8mm which may be due to the reason that the PLA matrix has reported 36% of loss in its strength for stage 3. Also, the strain capacity of PLA recycled material was reduced to 0.063 (Figure 5.81). Similarly, other composites have reported a decrease in BE except for PLA/Fe_3O_4 for which it was observed that the matrix showed continuous improvement for the successive recycling stages. The reason for the improvement in the BE of PLA/Fe_3O_4 was observed to be the low losses in tensile strength of the matrix. For recycling stage 3, the matrix resulted in a 22% decrease in peak strength which means that the material is less hard and therefore the matrix exhibited improved BE under the loading condition. Moreover, the decrease in mechanical properties may be due to internal structural non-uniformity such as porosity, voids, etc.

Table 5.61 UTM testing results for different recycled material matrix of PLA composites

Composite	**PL(N)**	**PE (mm)**	**BL(N)**	**BE (mm)**	**PS(MPa)**	**BS(MPa)**	**% Loss (PS)**
PLA	84.3±2.12	1.52± 0.08	75.87± 3.21	3.23± 0.08	46.07± 1.42	41.56± 1.42	-
PLA R1	81.8±1.83	2.28± 0.10	73.62± 2.95	4.94± 0.14	44.03± 1.12	40.62± 1.12	-0.04
PLA R2	72±1.69	1.52± 0.08	64.8± 1.57	6.65± 0.17	37.95± 1.21	32.95± 1.25	-0.17
PLA R3	53.4±1.25	0.76± 0.02	48.06± 1.42	3.8± 0.12	29.21± 1.05	24.99± 1.12	-0.36
PLA/Wood	71.1±2.14	1.14± 0.04	63.99± 2.84	2.09± 0.08	40.25± 2.31	36.23± 1.86	-
PLA/Wood R1	72±2.04	0.95± 0.01	64.8± 2.36	2.66± 0.09	29.95± 0.98	26.95± 0.94	-0.25

PLA/Wood R2	36.2±0.78	0.76± 0.05	32.58± 1.42	0.95± 0.05	20.5± 1.42	18.45± 1.42	-0.49
PLA/Wood R3	44.6±1.21	0.95± 0.07	40.14± 1.76	0.95± 0.08	18.55± 0.86	16.7± 0.93	-0.53
PLA/PVC	19.6±0.85	0.76± 0.05	17.64± 0.83	0.76± 0.05	24.97± 1.05	22.47± 1.20	-
PLA/PVC R1	37.7±0.74	1.52± 0.08	33.93± 1.42	1.52± 0.08	21.34± 1.54	19.21± 1.34	-0.14
PLA/PVC R2	49± 0.63	0.76± 0.05	44.1± 2.14	0.95± 0.06	19.27± 1.24	17.34± 1.14	-0.22
PLA/PVC R3	20.5± 0.21	0.76± 0.04	18.45± 0.96	0.95± 0.05	11.61± 0.54	10.45± 0.86	-0.53
PLA/Fe_3O_4	79.4± 1.95	1.14± 0.05	71.46± 3.85	1.33± 0.08	44.95± 2.65	40.46± 1.53	-
PLA/ Fe_3O_4 R1	78.4± 2.31	1.52± 0.08	70.56± 2.94	1.52± 0.09	44.39± 1.63	39.95± 1.32	-0.01
PLA/ Fe_3O_4 R2	68.1± 1.83	1.9± 0.11	61.29± 1.85	2.09± 0.11	38.56± 1.40	34.7± 1.12	-0.14
PLA/ Fe_3O_4 R3	61.7± 1.76	1.14± 0.09	55.53± 1.04	5.13± 0.19	34.93± 1.63	31.44± 1.41	-0.22
PLA/Hybrid	60.40± 0.36	0.38± 0.01	13.68± 1.10	0.38± 0.01	19.36± 0.84	17.43± 0.76	-
PLA/Hybrid R1	56.45± 0.24	0.95± 0.04	12.78± 1.23	1.14± 0.04	18.09± 0.63	16.28± 0.64	-0.06
PLA/Hybrid R2	37.81± 0.29	1.14± 0.09	12.33± 1.42	1.33± 0.10	12.12± 0.45	10.91± 0.39	-0.37
PLA/Hybrid R3	26.15± 0.98	0.57± 0.03	36.99± 0.97	0.57± 0.03	8.38± 0.30	7.54± 0.28	-0.56

Note:

- → *Three samples were tested for each type of composite material and an average of those has been shown in Table 1.*
- → *R1: Recycling Stage 1; R2: Recycling stage 2; R3: Recycling stage 3*
- → *PL: Peak load; BL: Break Load; PE: Peak Elongation; BE: Break Elongation; PS: Peak Strength; BS: Break Strength; % Loss PS: Percentage loss in peak strength*
- → *% loss in PS = PS (virgin/blend)-PS (Recycled for different stages)/ PS (virgin/blend)*
- → $\% \; loss \; in \; PS = \frac{PS\;(virgin/blend) - PS\;(Recycled\;for\;different\;stages)}{PS(virgin/blend)}$

→ *The material matrix has been compared to their respective groups only as PLA recyclates were compared to PLA as the base, PLA/PVC recyclates were compared to PLA/PVC, etc.*

→ *A negative sign denotes the loss in strength*

→ *"Virgin" means the polymeric material extruded by the researcher in the lab after procuring the material in form of a granular structure to produce feedstock and recyclates.*

(e)

Figure 5.81 Images for virgin/blend and recycling pallets for (a) PLA, (b) PLA/wood powder, (c) PLA/PVC, (d) PLA/Fe_3O_4 powder and (e) hybrid blend of PLA/ PVC/ Fe_3O_4/ wood powder

From Table 5.61 it was observed that the maximum losses in mechanical properties were observed for the third stage of recycling for each material matrix was of PLA composite. The hybrid matrix of PLA/ PVC/ Fe3O4/ wood powder has shown maximum losses in mechanical properties 6.5% for stage 1, 37.40 % for the second stage, and 56.71% for the third stage which showed that the magnetostrictive polymeric matrix PLA/ PVC/ Fe3O4/ wood powder was recyclable only up to one stage and after that, it loses its mechanical strength significantly. This may be due to the reason that the wood powder and PVC present among the hybrid matrix has resulted in poor mechanical bonding between the chains of PLA polymer and ultimately resulted in significant property losses. The matrix of PLA/PVC has also shown 53.5% losses in mechanical strength at stage 3 but for the first two recycling stages, the matrix was stable and has incurred only up to 22% losses in mechanical strength whereas PLA/wood lost approximately 50% of mechanical strength for the second stage of recycling. This may be due to the reason that the wood powder present in the polymeric chain has degraded as it was passed through the second heating cycle and thus decreasing the chain strength of PLA significantly. Figure 5.81 (b) shows the changes in the colors of PLA/wood composite where it could be easily seen that in the first stage of recycling the material matrix is dark brown but as it passed through the second and the third heating cycles of extrusion, the color faded to light brown which was a clear signal of loss of wood particles from the composite material matrix.

Figure 5.82 shows the stress vs. strain curve for three stages of (a) PLA, (b) PLA/wood, (c) PLA/PVC, (d) PLA/Fe_3O_4 and (e) PLA/ PVC/ Fe_3O_4/ wood powder composite matrix. It was observed that as the material matrix was passing through heating cycles the matrix became brittle and thus showed sudden breakage while mechanical testing. This phenomenon of brittle failure was predominant in all other matrices of PLA composites whereas the matrix of PLA has shown some ductility (Figure 5.82 (a)).

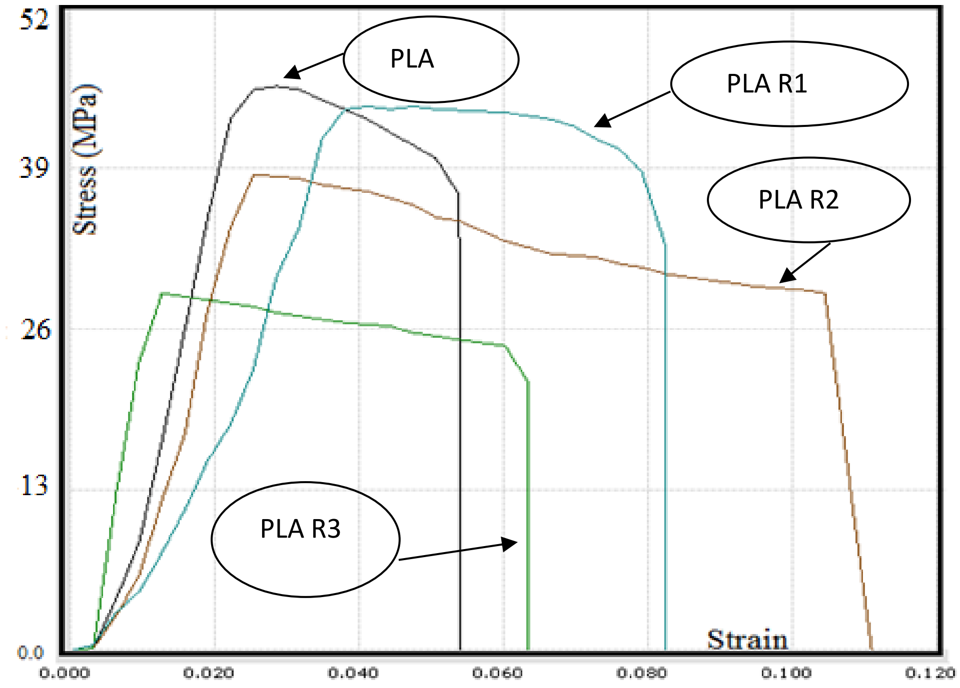

(a)

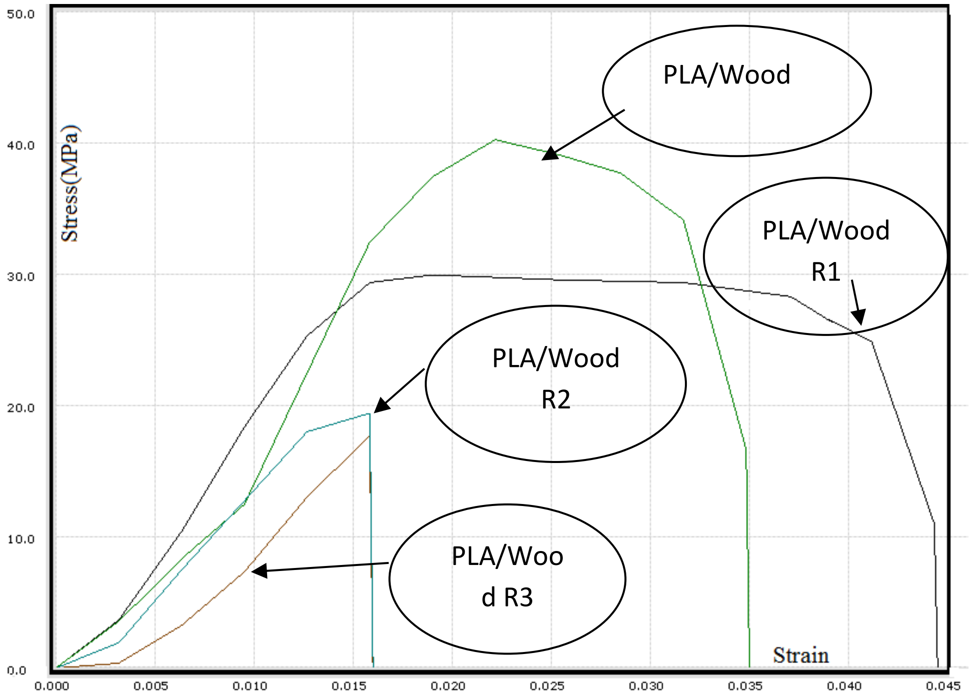

(b)

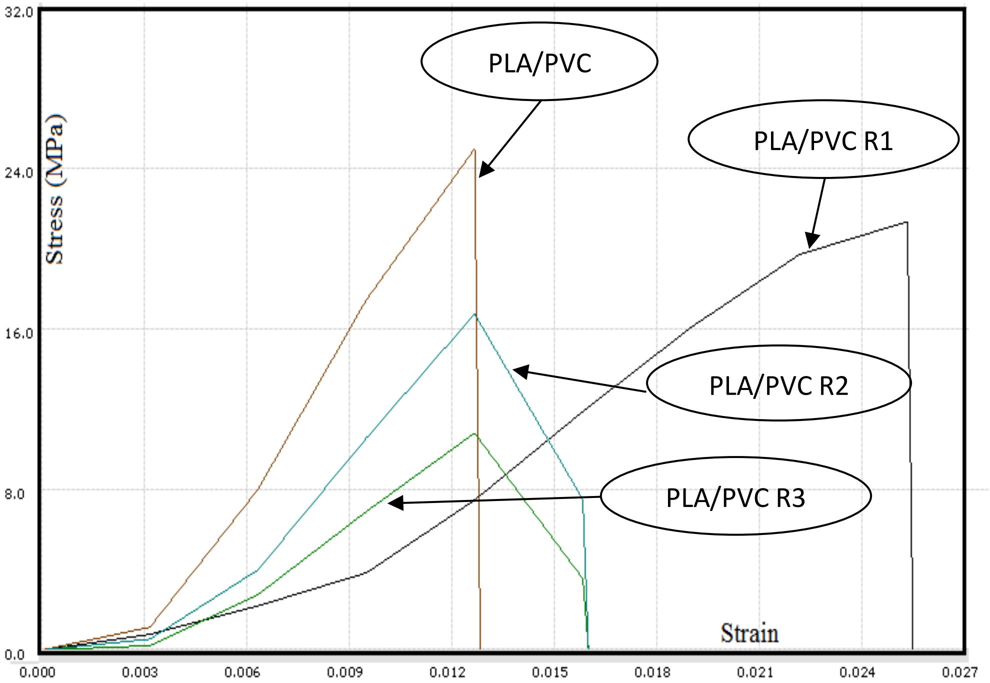
PLA/PVC
PLA/PVC R1
PLA/PVC R2
PLA/PVC R3
Stress (MPa)
Strain
32.0
24.0
16.0
8.0
0.0
0.000
0.003
0.006
0.009
0.012
0.015
0.018
0.021
0.024
0.027

(c)

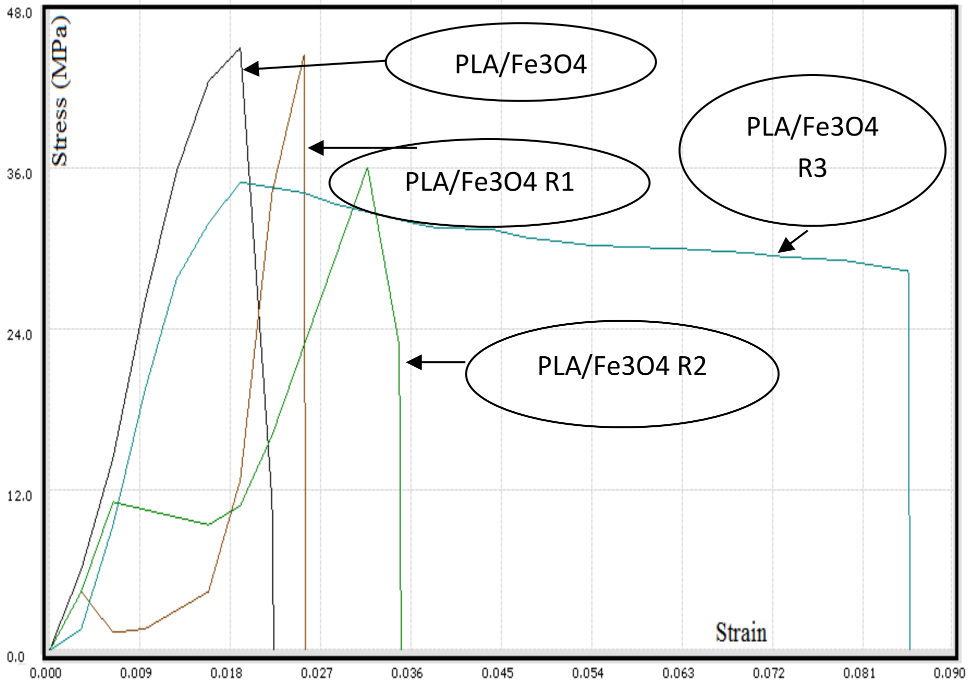
PLA/Fe3O4
PLA/Fe3O4 R1
PLA/Fe3O4 R3
PLA/Fe3O4 R2
Stress (MPa)
Strain
48.0
36.0
24.0
12.0
0.0
0.000
0.009
0.018
0.027
0.036
0.045
0.054
0.063
0.072
0.081
0.090

(d)

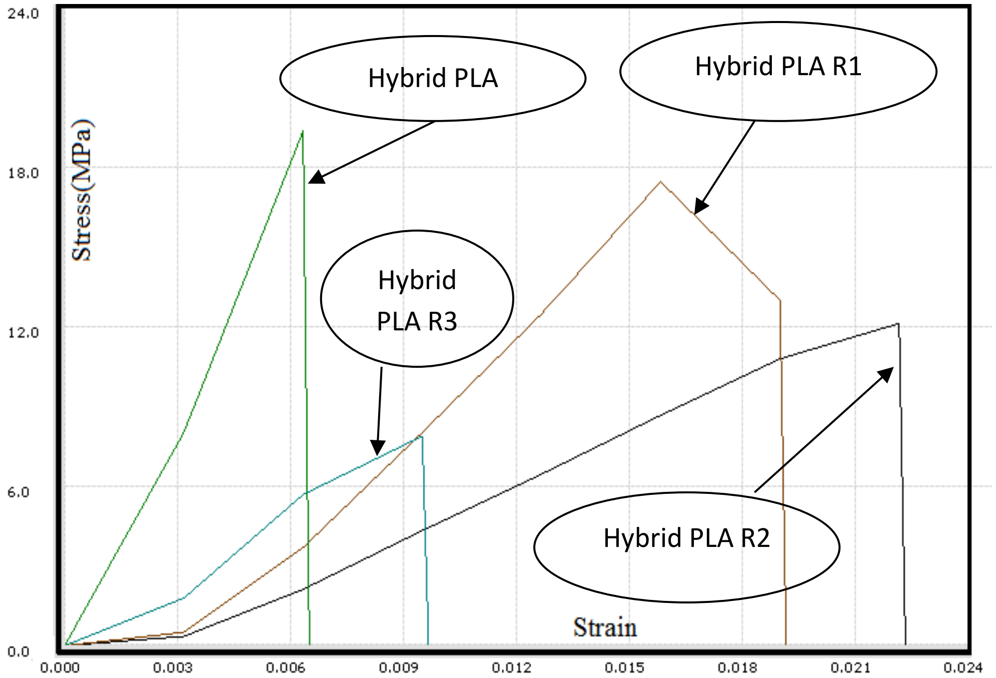

(e)

Figure 5.82 Stress vs. strain graph for virgin/blend and recycled pellets for 3 stages of (a) PLA (b) PLA/wood powder, (c) PLA/PVC, (d) PLA/Fe3O4 powder, and (e) Hybrid blend of PLA/PVC/wood/Fe3O4 powder

The stress vs. strain graph was further used for the calculation of modulus of toughness (MoT). Table 5.62 shows the MoT for different PLA composites and %age change in MoT with repeating heating and cooling through recycling stages. From Table 5.62 it was observed that for PLA material, the MoT improved for the first and second stage of recycling and maximum MoT (2.182 MPa) was observed for PLA R2 where it improved by more than 66.19%. But for the third stage, the material MoT decreased significantly which meant that the material matrix was degraded significantly and was no longer in a condition to holding its strength. This may be due to the reason that the percentage porosity and irregularities in the internal structure for PLA R2 may have increased which resulted in the poor matrix. Therefore, the internal structure testing through microscopic images became an important step to relate the material behavior. Similarly, PLA/Fe_3O_4 matrix has shown improvement in MoT for the increasing cycles of recycling, and maximum MoT was observed for PLA/Fe_3O_4 R3 (184.93% improvement over PLA/Fe_3O_4). For PLA/PVC matrix only the first stage of recycling has resulted in positive results, which may be due to the reason that as the recycling was performed for the second and the third recycling, the PVC degraded and thus formed incapable bonds among the PLA and PVC molecules.

Table 5.62 MoT values with standard deviation (SD) for different PLA composites of recycled material matrixes

Composite	PS(MPa)	Strain	MoT (MPa)	Relative change in MoT (percent)
PLA	46.07± 1.42	0.057± 0.02	1.31± 0.12	-
PLA R1	44.03± 1.12	0.081± 0.03	1.78± 0.16	0.36
PLA R2	37.95± 1.21	0.115± 0.06	2.18± 0.17	0.66
PLA R3	29.21± 1.05	0.063± 0.02	0.92± 0.09	-0.30
PLA/Wood	40.25± 2.31	0.035± 0.01	0.70± 0.08	-
PLA/Wood R1	29.95± 0.98	0.043± 0.02	0.64± 0.06	-0.08
PLA/Wood R2	20.5± 1.42	0.016± 0.01	0.16± 0.03	-0.77
PLA/Wood R3	18.55± 0.86	0.015± 0.02	0.14± 0.02	-0.79
PLA/PVC	24.97± 1.05	0.013± 0.009	0.16± 0.03	-
PLA/PVC R1	21.34± 1.54	0.0255± 0.02	0.27± 0.04	0.68
PLA/PVC R2	19.27± 1.24	0.0168± 0.01	0.16± 0.03	-0.002
PLA/PVC R3	11.61± 0.54	0.0165± 0.01	0.09± 0.01	-0.40
PLA/Fe3O4	44.95± 2.65	0.024± 0.01	0.53± 0.07	-
PLA/Fe3O4 R1	44.39± 1.63	0.026± 0.01	0.57± 0.09	0.07
PLA/Fe3O4 R2	38.56± 1.40	0.035± 0.02	0.67± 0.08	0.25
PLA/Fe3O4 R3	34.93± 1.63	0.088± 0.04	1.53± 0.15	1.84
PLA/Hybrid	19.36± 0.84	0.007± 0.01	0.07± 0.01	-
PLA/Hybrid R1	18.09± 0.63	0.019± 0.01	0.17± 0.04	1.53
PLA/Hybrid R2	12.12± 0.45	0.023± 0.01	0.14± 0.02	1.06
PLA/Hybrid R3	8.38± 0.30	0.01± 0.01	0.04± 0.01	-0.38

**Note:*

$$Percentage\ Variation\ in\ MoT = \frac{MoT\ (virgin/blend) - MoT\ (Recycled\ \ stages)}{MoT(virgin/blend)}$$

5.5.2 Fractured surface analysis results

The failure of recycled materials has shown an interesting trend that outlined the altered behavior of the composite material matrix (which is visible by the images of re-cycled matrixes Figure 5.81). Moreover, the stress vs. strain graph has identified the brittle nature of the recycled material matrix. But the reason for poor mechanical performance by recycled materials over the different stages may be its internal structure which could be harmed by the number of heating cycles. Therefore, fractured surface analysis was made using Tool Maker's microscope in which the fractured samples were examined under the microscope at ×30 magnification. The samples were tested at the internal cross-section of fractured surfaces from which it was observed that the PLA recyclates and PLA material matrix have shown neck formation (Figure 5.83 (a)) while all other samples held brittle failure as the fractured cross-section for all other composite matrix was flat and no neck formation has been observed. From the microscopic image of fractured the surface, it may be observed that the material matrix of PLA/Fe_3O_4 and hybrid matrix of PLA/PVC/Fe_3O_4/wood powder held several porosity holes/ voids at their surfaces. Also, it was observed that as the heating cycles increased or recycling stages increased the surface held more irregularities which was a clear sign of a relationship between mechanical properties and surface irregularities. It may be due to the reason that as the recycling stages increased, the polymeric chain of the composite got disturbed and the packing efficiency of the monomer got reduced due to elongated chain length of polymers which caused internal irregularities among molecular chain and resulted in more voids inside the structure (which ultimately reduced the mechanical strength of recycled composite matrix).

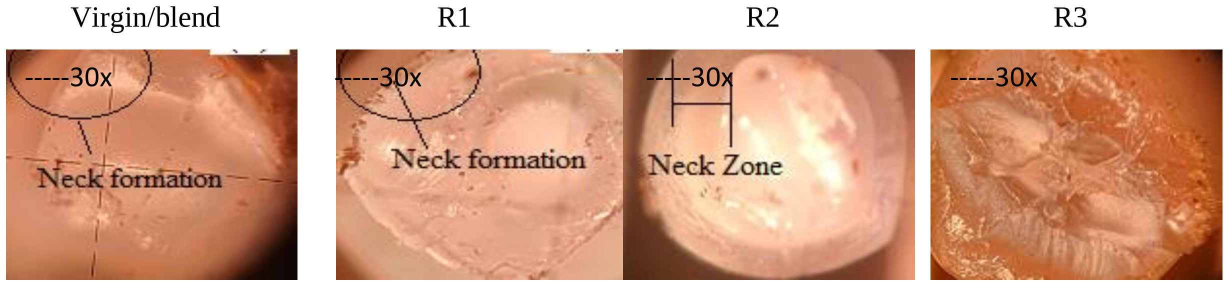

(a)

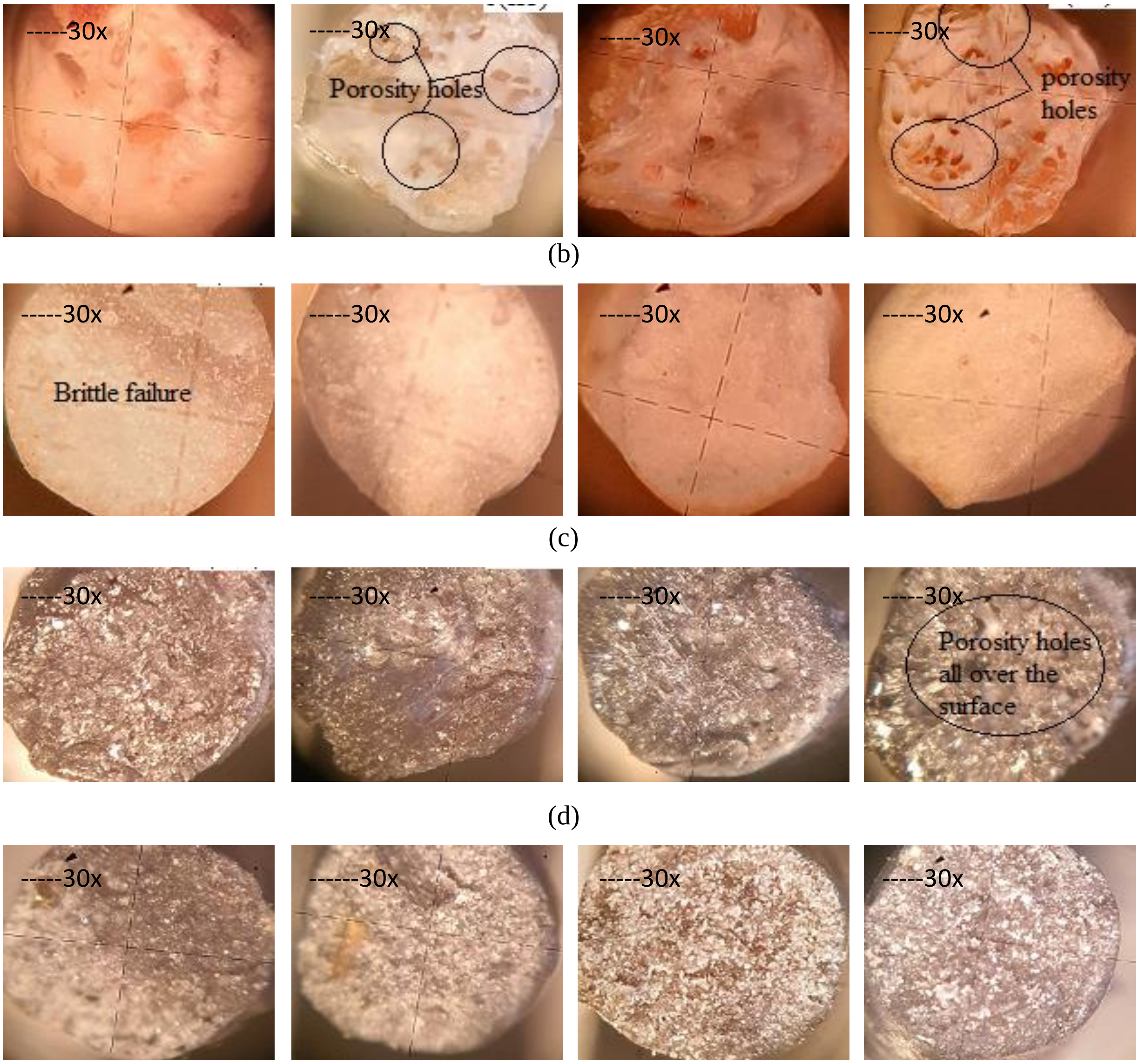

(b)

(c)

(d)

(e)

Figure 5.83 Tool maker's microscopic images of fractured specimens for (a) PLA pellets, (b) PLA/wood powder, (c) PLA/PVC, (d) PLA/Fe_3O_4 powder, and (e) Hybrid blend of PLA/Fe_3O_4 powder and recycled pellets

5.5.3 Porosity results

Figure 5.84 shows the porosity results of fractured samples of recycled composite matrix from which it was observed that the recycling strength was related to porosity holes directly. With the recycling stage, the relative percentage porosity observed to increase thus the internal structure of the composite after recycling was deteriorated further resulting in poor mechanical strength. A similar observation may be made by observing Figure 5.81 which highlights that the recyclates processed through TSE for stage 1 to stage 3 held a high amount of air inside the recycled matrix as the recyclates were thicker than their counterparts. Thus, when processed for feedstock these resulted in a larger number of porosity holes on the release of entrapped air. Similarly, when Figure 5.81 (b) was observed, it was found that the wood present in the matrix was burnt with the repeated recycling stages that resulted in fading of the dark brown color of the material matrix at recycling stage 1 to light brown at recycling stage 3. The increasing porosity holes with increasing recycling stages deteriorated the matrix of PLA composite for further recycling which ultimately resulted in 50-60 % of mechanical property losses at recycling stage 3. The maximum porosity was observed for the third stage of recycling in every group. The PLA/PVC/wood/ Fe3O4 powder composite for stage 3 held maximum porosity of 19.84 % and PLA/PVC for stage 3 held 19.58 % relative porosity and also their mechanical strength was the least among all. It gives clear evidence of a relationship between percentage porosity and mechanical performance of prepared feedstock of recycled material matrix of the PLA composite.

Virgin/Blend R1 R2 R3

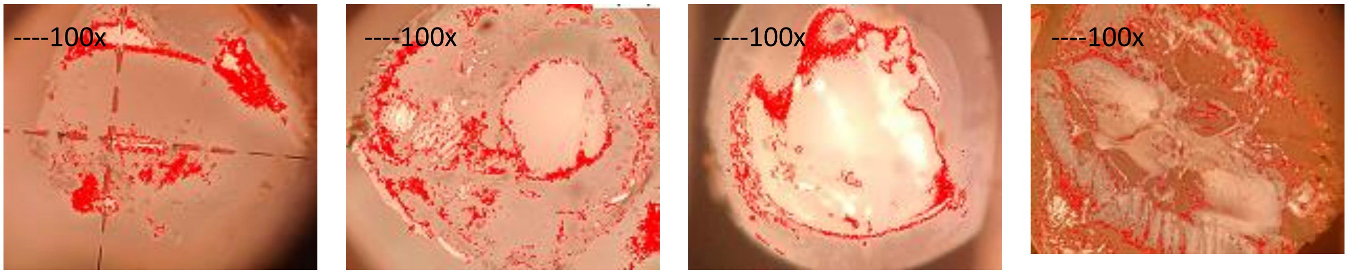

Porosity: 5.4% Porosity: 5.86% Porosity:8.26% Porosity: 9.7%

(a)

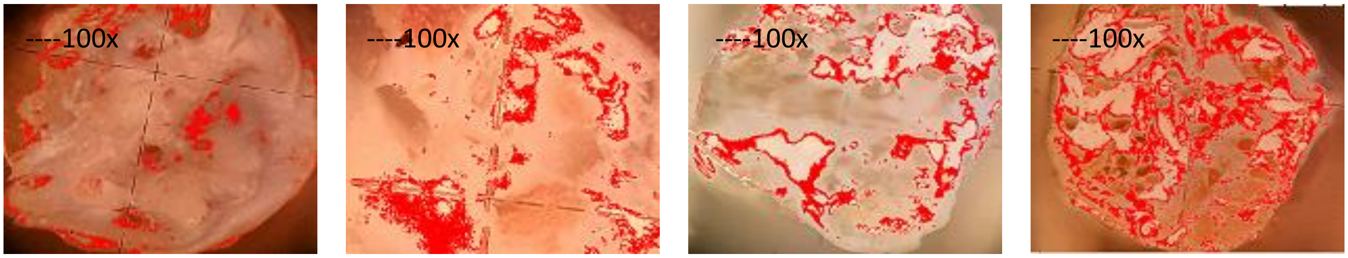

Porosity: 10.27% Porosity:15.75% Porosity: 17.23% Porosity: 19.58%

(b)

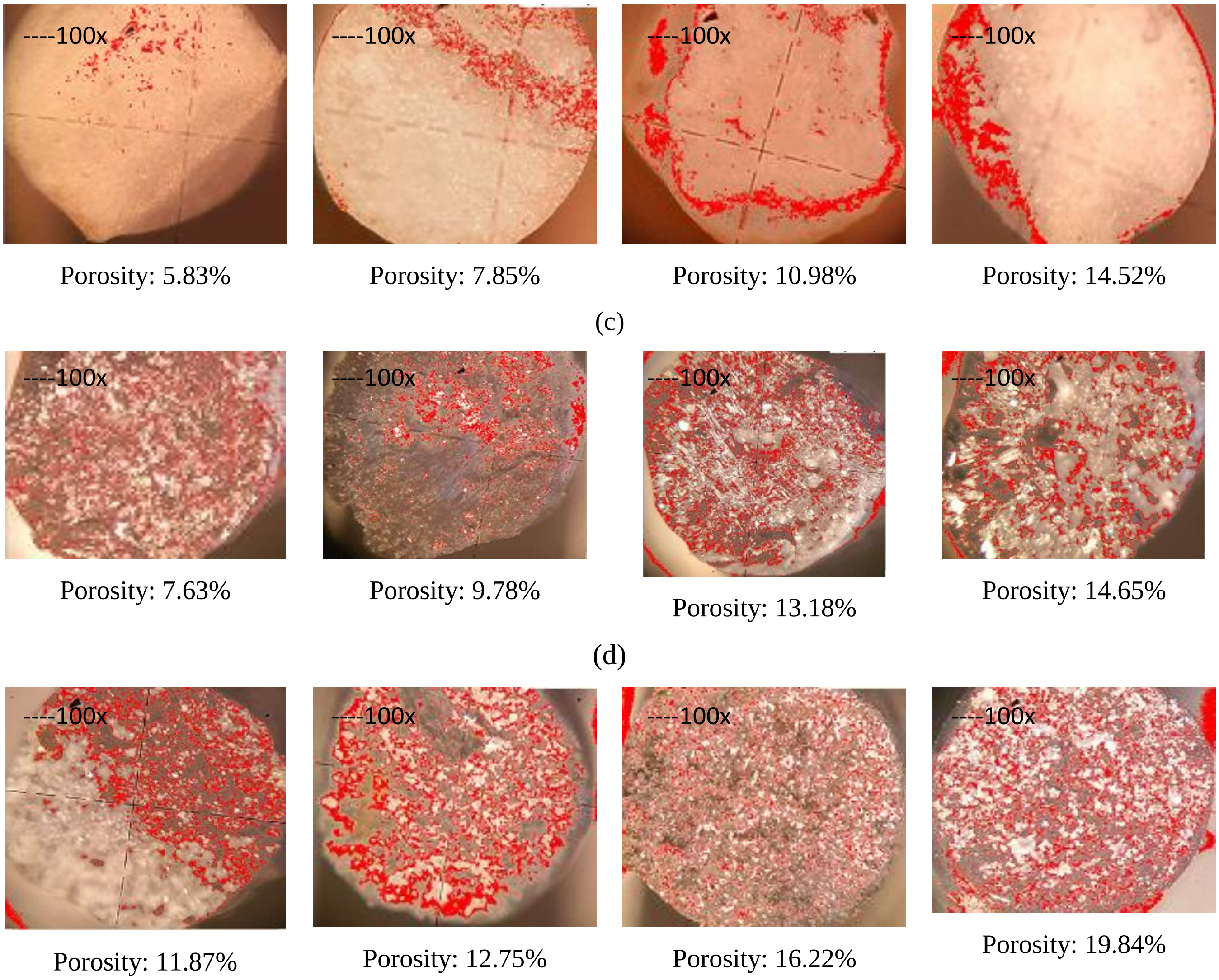

Porosity: 5.83% Porosity: 7.85% Porosity: 10.98% Porosity: 14.52%

(c)

Porosity: 7.63% Porosity: 9.78% Porosity: 13.18% Porosity: 14.65%

(d)

Porosity: 11.87% Porosity: 12.75% Porosity: 16.22% Porosity: 19.84%

(e)

Figure 5.84 Porosity results for (a) PLA, (b) PLA/wood powder, (c) PLA/PVC, (d) PLA/Fe3O4 powder and (e) hybrid blend of PLA/ PVC/ Fe3O4/ wood powder

5.5.4 DSC analysis

To prove that pure PLA remains pure PLA, the thermal testing using DSC was performed for two cycles of heating and cooling (heating cycle: 25°C to 200°C and cooling cycle 200°C to 25°C) cycles. Only 4 samples: PLA, PLA R1, PLA R2, and PLA R3 were tested for DC analysis. It was observed that for different cycles of recycling, there was a marginal change in the integral energy varying from 108mJ to 96mJ for the first heating cycle of DSC (Figure 5.85), whereas the onset temperature also varied from 144°C to 130°C, which meant that with the heating cycles of TSE the material matrix remains the same as the DSC graphs/trends were similar for each material matrix of PLA.

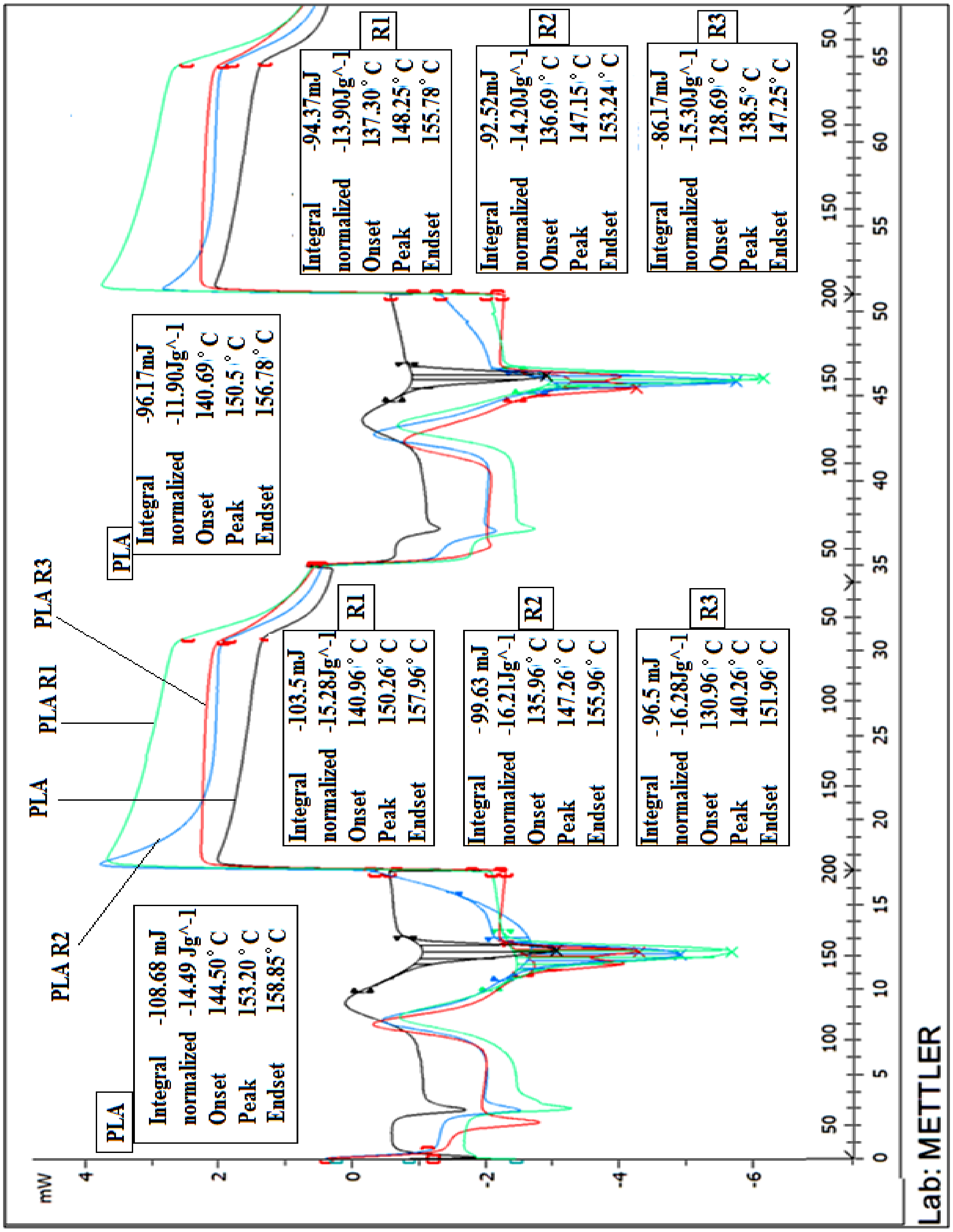

Figure 5.85 DSC analysis for samples of PLA, PLA R1, PLA R2, and PLA R3

It should be noted that for comparative purposes best samples of a hybrid composite of PLA prepared at stage 3 and a multi-material composite of PLA developed at stage 4 have been taken for calculation of standard deviation for experimental data sets. For calculating standard deviations (sigma σ) of the data set 10 samples have been prepared by using standard optimized conditions for both types of samples (condition no. 7 for hybrid as well as for multi-material prototype) and calculations were made using the following equation.

$$\sigma = \sqrt{\frac{1}{N}\sum_{i=1}^{N}(x_i - \mu)^2}.$$

It was found that the hybrid material component exhibited σ: 0.3375 for peak strength and σ: 0.4716 for surface hardness. Whereas in the case of multi-material prototypes σ was found to be 0.3214 and 0.4125 for peak strength and surface hardness respectively.

CHAPTER 6

CONCLUSIONS AND FUTURE SCOPE

This chapter highlights the conclusions of experimentation performed at various stages of the work.

6.1 Conclusions for stage 1

1. The results of the study suggest that for the combined optimization of mechanical properties, experiment number 10 (Table 4.3) with 170°C barrel temperature, torque 0.15Nm, composite mixture 1, and the load of 10kg are the optimized conditions for TSE. It has been noticed that only screw temperature is a significant parameter for TSE processing and other parameters contributed less than 2% collectively.
2. Optimized values of different mechanical properties; peak load, peak elongation, breaking load, break elongation, strength at peak, strength at break, percentage elongation at peak, percentage elongation at break, shore D hardness come as 41.97N, 4.43mm, 40.36N, 4.81mm, 18.03MPa, 16.43 MPa, 5.89, 7.32 and 66.60 shore D, respectively.
3. The high porosity (20.41%) of samples obtained from experiment no.17 resulted in poor surface hardness (58.5 Shore D) (which indicated the poor composite matrix) which ultimately resulted in poor mechanical properties. In contrast, experiment number10 has shown a low value of porosity (7.18%) and high hardness (65.8 Shore D) thus resulting in a better surface texture of the filament as observed from photomicrographs thus resulting in better mechanical performance.
4. DSC analysis shows that sample 10 is thermally stable in comparison to sample 17, contributing to better mechanical properties.
5. Further, VSM testing has indicated that all compositions held significant magnetic properties which may have usefulness for self-assembly and 4D applications.
6. Characterization for surface properties (surface hardness, surface roughness, porosity, and fractured surface analysis) have given conclusive evidence for the relationship between obtained mechanical performance and morphological properties of prepared feedstock filaments.
7. Extrusion condition 5 (as per Table 4.3) in which sample composition 2 (Fe_3O_4 25 weight percentage, PLA 52.5 weight percentage, PVC 15 weight percentage and wood particles

7.5 weight percentage), the torque of 0.12Nm, screw temperature of 165°C, and the load of 5Kg plays a crucial role and is the optimized condition for the magnetization whereas maximum magnetization has been obtained in experiment 2 which contained composition 1 in which 20% Fe_3O_4 is present.

8. Regression analysis of all the input parameters with output for different properties has shown that magnetization is the maximum when screw temperature is less than 165°C and composition lies between sample1 and 2. The lowest magnetization is found for the highest temperature and the sample having the lowest Fe_3O_4 content (sample 3; Fe_3O_4 = 17.5%).
9. From VSM analysis it has been found that all the samples having Fe_3O_4 in the matrix are of super-paramagnetic nature which is clear from their hysteresis loop and can be gainfully used for self-assembly applications.
10. Magnetic and mechanical properties are not in correlation with each other as verified from SEM and EDAX analysis and it is clear that few Fe_3O_4 particles are present on the surface of the filament which means that magnetite particles get mixed into the inner matrix of the surface. As magnetic properties are dependent solely on the presence of magnetite powder in the composite which is inside the composite matrix and thus therefore it is hard to find any correlation between magnetic and mechanical properties of a composite.
11. The magnetic and surface properties were statistical controlled and have shown Cp and Cpk values greater than 1 which signified that the processing condition of TSE (i.e. barrel temperature of 170°C, screw speed 45 rpm, and extrusion load of 5kg) is capable of producing feedstock filaments of required properties (magnetization, surface hardness, and surface porosity) for the number of times.

6.2 Conclusions for stage 2

1. The MFI of the composite increases with the loading of reinforcements in the PLA polymer matrix except for the wood powder which has shown a negative trend with increased loading. It is concluded that for successful multi-material printing, MFI is to be maintained to the nearest possible value so that proper fusion may occur among successive layers.
2. Mechanical properties were also reduced with the loading but with increasing Fe_3O_4 content in polymer composite matrix, mechanical properties have shown improvement. The Fe_3O_4 reinforcement in PLA has reduced the peak load, break load, strength at peak, and strength at the break but improved the break elongation, percentage elongation while peak elongation remained the same. For the reinforcement of PVC from 10 weight percent to 25 wt.%, peak elongation and break elongation have reduced by 47.61% and 50%, respectively. Shore D hardness and porosity results have supported the rheological and mechanical results. Hence, it is concluded that for possible multi-material printing the level of reinforcements may be selected as per desired mechanical properties in successive layers of the 3D printed parts.
3. DSC has been performed for samples which have suggested that all the samples were thermally stable as there was a marginal change in peak set and peak endpoints. Virgin PLA was the most thermally stable while for other reinforced samples, onset and peak temperature were stable but integral energy was found to decrease significantly for the successive cycles of DSC testing. Finally, the VSM of the sample suggested that magnetic properties were dependent on the content of Fe_3O_4 present in the composite while the presence of other foreign reinforcement does not affect the magnetic properties.

6.3 Conclusions for stage 3

1. The process optimization results have suggested that infill density of 100%, infill angle of 45°, and infill speed of 70 mm/s have given the best result for the peak strength and break strength.
2. ANOVA model suggested that there may be some missing terms in the model prepared based upon Taguchi L9 OA, which indicated poor predictability as the model was not significant due to error greater than 10%. Historical data approach has ascertained that interaction among input variables has played a greater role than that of single variable effect towards output which resulted in predictable model and the accuracy of the model was also higher.
3. Morphological analysis suggested that sample printed with maximum density and low infill angle has the minimum porosity and thus have shown better mechanical results.
4. From multifactor optimization of flexural and pull-out properties, it has been ascertained that experimental condition 7 (Infill density: 100; Infill angle: 45°; and Infill speed: 90mm/s) is the best printing condition and experimental condition 3 (Infill density: 60; Infill angle: 90°; and Infill speed: 90mm/s) is the worst among all.
5. From the stress and strain curve of the flexural specimen, it has been found that the sample with the best properties (sample 7) also holds maximum strain-absorbing capacity as its break elongation is 20.47mm and strain capacity is 0.4094 for flexural results whereas in the case of pull out, sample 7 holds break elongation of 40.12 and strain capacity of 0.8024. Hence, this may be considered as the best condition of 3D printing for crash applications.
6. From morphological testing of flexural and pull-out specimens, it has been found that mechanical properties are in a relationship with hardness, porosity, and surface roughness.
7. From Creo model analysis it may be concluded that strain increases downwards in the thickness and is maximum at the lowest layer due to which the failure starts from the base row in flexural testing. Therefore, it is recommended to use a small angle of printing. As the number of load-sharing layers increases, maximum strength is obtained.
8. From the thermal conductivity test, it has been ascertained that sample 9 printed with infill density 100%, infill angle 90°, and infill speed of 70 mm/sec, has shown maximum thermal conductivity (0.27817 W/mK). Also, it has been observed that with the increase in infill density, the thermal conductivity of the sample improved. Hence, from a thermal

conductivity viewpoint, the sample (Table 4.5) is a better candidate for structural engineering applications. However, the value of observed maximum thermal conductivity (for PLA matrix having self-assembly characteristics) is near the virgin PLA and can be used in structural engineering applications.

9. From circumferential compressive testing on UTM setup, it has been ascertained that infill density has maximum contribution towards the output and is a significant parameter along with infill angle, but infill speed has no significant role in output properties. Experimental condition 9 (Infill density 100%, infill angle 90°, and infill speed of 70 mm/sec) is the optimized condition for printing on an FDM setup. These results are at a 95% confidence level.
10. Further, morphological testing (surface hardness, fractured surface analysis, and surface roughness) has supported the observed behavior for compressive as well as thermal behavior of 3D printed samples.
11. From testing for electrical properties, it has been observed that the electrical properties were independent of FDM processing conditions as no improvement was observed in electrical conductance. The prepared composite has shown very low electrical conductivity ($<10^{-6}$ S/cm) which was favorable for non-structural engineering applications.
12. From dimensional deviation results for 3D printing of circular disc, it has been observed that infill density 60%, infill angle 45°and infill speed of 70mm/s are the optimized/suggested printing condition but sample number 1 as per DOE (Table 4.5) may also be taken as the optimized condition as only infill density was the significant parameter of the present investigation.

6.4 Conclusions for stage 4

1. From mechanical testing of the multi-material tensile specimen, it can be concluded that when the sample was printed with the highest density 100%, low infill angle of 45°, and infill speed of 90mm/s, then the properties obtained for multi-material printed sample are the maximum, such as peak strength of 46.28MPa and break strength of 41.65 MPa.
2. Modulus of the toughness of multi-material tensile specimen for sample 7 (4.762 MPa) was the highest among all whereas 1st sample held the lowest value for modulus of toughness. Thus, experimental condition 7 may also be used for printing prototypes of proposed material for high toughness applications.
3. The hardness of multi-material tensile specimen, measured on two surfaces (top and bottom) has revealed that the hardness value for the virgin PLA layer was greater than the hardness value for the top layer (magnetite reinforced PLA)
4. From the fractured surface analysis of multi-material tensile specimen using photomicrographs taken from tool maker's microscope, it has been observed that the printed samples with low density held maximum porosity holes due to which their performance was poor in comparison to the samples which were printed with high density.
5. Surface roughness of multi-material tensile specimen obtained from surface rendering revealed that the high roughness value of samples printed with low density was also one of the reasons for their poor performance.
6. The process optimization for the 3D printed flexural specimen of the multi-material component has suggested that infill density 100%, infill angle 45° and infill speed of 50 mm/s were the optimized conditions but from further optimization, it has been found that infill speed has insignificant contribution towards mechanical properties. Therefore, in place of suggested/optimized conditions, one may also use experimental condition 7 (Infill density: 100%, Infill angle: 45°, and infill speed: 90mm/s) as a standardized condition of printing.
7. The flexural testing for sample 7 has shown maximum flexural strength of 26.92 MPa whereas, in the case of pull-out testing, sample 7 has shown pull-out strength of 18.11 MPa.
8. Modulus of toughness for 3D printed flexural specimen of the multi-material component has revealed that 8th sample for flexural specimen and 1st sample for pull out tested

specimen held maximum modulus of toughness which meant that they came as suitable candidates for crash applications due to their ductile nature.

9. From fractured surface analysis and hardness result for the 3D printed flexural specimen of multi-material component, it may be concluded that higher density and low infill angle lead to better diffusion of material in the layer-by-layer fashion resulting in less void formation and better diffusion among different layers and thus results in better flexural and pull out performance.

6.4.1 Comparative result analysis for Hybrid and multi-material 3Dprinted components

Table 6.1 shows the summary of the investigation on comparison of properties of multi-material and hybrid blend PLA matrix-based 3D printed prototypes on FDM machine (with same standard printing conditions).

Table 6.1 Comparison of hybrid blended, and multi-material matrix-based 3D printed prototype

Properties	Hybrid blended PLA matrix-based prototype	Multi-material PLA matrix-based 3D printed prototype
Peak Strength	30 MPa (approx.)	47 MPa (157% greater than Hybrid Blended prototype)
Break Strength	26 MPa (approx.)	42 MPa (157% greater than Hybrid Blended prototype)
Functionally graded	Hybrid blend no alteration of properties in consecutive layers	Yes, functional gradation is possible by introducing different material matrix layers at different layer positions. (in the present investigation 4 different material matrix layers have been printed in a single prototype)
Aesthetic	Average as a rough aesthetic feature is visible	The good aesthetic is possible as different layer matrix gives a different look

Surface Roughness	Ra value of 759.8 nm	Only 40% roughness in comparison to hybrid material matrix-based prototype
4D nature	It may be less strongly attracted to the external magnetic field as the magnetite particles are present throughout the 3D printed prototype	It may be strongly attracted towards the external magnetic field as the last layer which is near to the external magnetic source consist of magnetite powder in a single layer rather than distributing magnetite in the whole component.

(a) The mechanical properties of multi-material blended PLA matrix-based 3D printed prototypes are superior to the hybrid blended PLA matrix-based functional prototypes. It has been ascertained that approximately 157% enhancement of mechanical properties was observed especially for break strength and peak strength values.

(b) From SEM analysis, it was observed that the multi-material blended PLA matrix-based 3D printed prototype had several interfaces where the PLA base polymer has shown a better affinity for different layers/interface due to which fusion of one layer into another composite layer was observed at interfaces which resulted in better mechanical properties.

(c) From 3D surface rendering it was observed that the multi-material blended PLA matrix-based 3D printed prototype has better Ra (approx. 60% less) than that of the hybrid blended PLA matrix-based prototype. Thus, a better Ra has resulted in better mechanical performance.

6.5 Conclusions for stage 5

1. The composite matrixes of PLA have lost 50-60% of their original peak strength for the third cycle of recycling except for the PLA/Fe_3O_4 and virgin matrix of PLA (which lost only 22% and 36% of mechanical strength, respectively). Hence, it may be concluded that after the third cycle, the PLA composite matrix will not be useful for 3D printing applications (mainly because of loss in strength).
2. As suggested by porosity testing and fracture surface analysis, the level of porosity and irregularities of the inner material matrix is found to be the key reasons for their significant loss in properties throughout recycling.
3. It was also observed that with the number of recycling stages the ductility of PLA was reduced, and brittle failure was observed for most of the recycled composite matrix.
4. From this study, it can be concluded that only the addition of Fe_3O_4 in the PLA matrix has improved the recycling life of PLA and also ductility was improved, and mechanical strength was significantly retained over the number of cycles.
5. There were also positive effects of recycling as the Modulus of toughness for PLA composite matrixes, in most of the cases, was improved (except for PLA/PVC composite) matrix which is an important property for polymeric matrix.
6. This study also suggests that the PLA composites retain 85-90 % of their mechanical strength (except PLA/PVC composite) for first recycling, 65-75 % of their strength up to the second stage of recycling, and 50% the third stage of recycling, whereas MoT of polymeric composite matrix improved (except for PLA/PVC).
7. From DSC analysis, it can be concluded that the thermal properties got reduced with recycling stages whereas the trends were found similar which meant that there was no change in the composition of the material matrix.

6.6 Limitations of work and future scope

The current work has been performed in 5 stages starting from the development of feedstock filament for hybrid and multi-material matrixes at stages 1 and 2 and then followed by 3D printing of functional prototypes using feedstock filaments developed at stage 3 and 4. At the last stage 5, recycling life for three stages of different polymeric matrixes has been ascertained. At each working stage, there was the certain limitation of the process which are mentioned as following.

6.6.1 Limitation and future scope for stage 1 and 2

In the first two stages mechanical-based blending was used as a processing technique for the polymer to reinforce different external reinforcements in the base matrix of PLA while the chemical assisted mechanical blending method using some suitable solvent was not explored thus in the future, researchers may use some suitable solvent to dissolve the base matrix and reinforcement for proper material matrix formation and similar studies may be performed for the chemically processed material matrix which may give better results.

6.6.2 Limitation and future scope for stage 3 and 4

At stages 3 and 4, 3D printing of functional prototypes were printed using a different set of processing parameters of the FDM machine while only infill density, infill angle, and infill speed were selected as the varying input process parameter while taking other parameters of the FDM machine as fixed. In the future researchers may take the number of the perimeter, raster width, infill pattern as varying input parameters and may find the effect of these on mechanical performance. In the present study for 3D printing of multi-material matrix the base polymeric matrix of PLA has been used whereas in the future one may take different polymeric materials in the single functional component in which glass transition temperature (Tg) of polymeric material may be taken as the base for selection of layer material at a specific location such as the material combined with high Tg must be 3D printed on base and the succeeding layers must have lower Tg otherwise the material may not have proper fusion.

6.6.3 Limitation and future scope for stage 5

In stage 5 the different polymeric composites were tested for their recycling compatibility from the sustainability viewpoint, but full life cycle assessment and techno-economic analysis were not performed thus in the future researchers may take the initiative of life cycle assessment and techno-economic analysis for different feedstock of polymeric composite developed on a lab scale.

REFERENCES

1. Khoo ZX, Teoh JE, Liu Y, Chua CK, Yang S, An J, Leong KF, Yeong WY. 3D printing of smart materials: A review on recent progresses in 4D printing. Virtual and Physical Prototyping. 2015 Jul 3; 10(3):103-22.
2. Kruth JP. Material incress manufacturing by rapid prototyping techniques. CIRP annals. 1991 Jan 1; 40(2):603-14.
3. Cullen AT, Price AD. Digital light processing for the fabrication of 3D intrinsically conductive polymer structures. Synthetic Metals. 2018 Jan 1; 235:34-41.
4. Qin, H., Cai, Y., Dong, J., & Lee, Y.-S. Direct Printing of Capacitive Touch Sensors on Flexible Substrates by Additive E-Jet Printing with Silver Nano inks. Journal of Manufacturing Science and Engineering. 2016; 139(3), 031011.
5. Sezer HK, Eren O. FDM 3D printing of MWCNT re-inforced ABS nano-composite parts with enhanced mechanical and electrical properties. Journal of Manufacturing Processes. 2019 Jan 1;37:339-47.
6. Ghita OR, Jamesb E, Trimble R, Evans KE. Physico-chemical behaviour of poly (ether ketone) (PEK) in high temperature laser sintering (HT-LS). J Mater Process Technol. 2014; 214: 969–78.
7. Shishkovsky IV, Volova LT, Kuznetsov MV, Morozov YG, Parkin IP. Porous biocompatible implants and tissue scaffolds synthesized by selective laser sintering from Ti and NiTi. J Mater Chem. 2008; 8:1309–17.
8. Dean, D.M., Napolitano, A.P., Youssef, J., Morgan, J.R. Rods, tori, and honeycombs: thedirected self-assembly of microtissues with prescribed microscale geometries. FASEB J. 2007; 21, 4005–4012.
9. Livoti, C.M., Morgan, J.R. Self-assembly and tissue fusion of toroid-shaped minimal building units. Tissue Eng. Part A. 2010; 16, 2051–61.
10. Mehesz, A.N., Brown, J., Hajdu, Z., Beaver, W., Silva, J.V.L. da, Visconti, R.P., Markwald, R.R., Mironov, V. Scalable robotic bio fabrication of tissue spheroids. Biofabrication. 2011; 3, 25002.
11. Wheeldon, I., Ahari, A.F., Khademhosseini, A. Microengineering hydrogels for stem cell bioengineering and tissue regeneration. JALA - J. Assoc. Lab. Autom. 2010; 15, 440–448.

12. Yamada, E., Yamada, M., Iwase, M., Sugaya, S., Seki, M. Replica Molding and Bonding of Micro structured Hydrogel Plates for Tissue Engineering Applications. Sci. Technol. 2011; 1834–1836.
13. Wu H, Liu W, He R, Wu Z, Jiang Q, Song X, Chen Y, Cheng L, Wu S. Fabrication of dense zirconia-toughened alumina ceramics through a stereolithography-based additive manufacturing. Ceramics International. 2017 Jan 1; 43(1):968-72.
14. Mao, Y., Ding, Z., Yuan, C., Ai, S., Isakov, M., Wu, J., Qi, H. J. 3D Printed Reversible Shape Changing Components with Stimuli Responsive Materials. Scientific Reports, 2016; 6(1).
15. Mao, Y., Yu, K., Isakov, M. S., Wu, J., Dunn, M. L., & Jerry Qi, H. Sequential Self-Folding Structures by 3D Printed Digital Shape Memory Polymers. Scientific Reports, 2015; 5(1).
16. Wu, J., Yuan, C., Ding, Z., Isakov, M., Mao, Y., Wang, T., Qi, H. J. Multi-shape active composites by 3D printing of digital shape memory polymers. Scientific Reports. 2016; 6(1).
17. Wei, H., Zhang, Q., Yao, Y., Liu, L., Liu, Y., & Leng, J. Direct-Write Fabrication of 4D Active Shape-Changing Structures Based on a Shape Memory Polymer and Its Nanocomposite. ACS Applied Materials & Interfaces. 2016; 9(1), 876–883.
18. Qin, H., Cai, Y., Dong, J., & Lee, Y.-S. Direct Printing of Capacitive Touch Sensors on Flexible Substrates by Additive E-Jet Printing With Silver Nano inks. Journal of Manufacturing Science and Engineering. 2016; 139(3), 031011.
19. Moore JP, Williams CB. Fatigue properties of parts printed by PolyJet material jetting. Rapid Prototyping Journal. 2015; 21(6), 675–685.
20. Philip R, Staffanson A. Improving the product development process with additive manufacturing [Internet] [Dissertation]. 2018. Available from: http://urn.kb.se/resolve?urn=urn:nbn:se:mdh:diva-40344.
21. Kim, K., Zhu, W., Qu, X., Aaronson, C., McCall, W.R., Chen, S. and Sirbuly, D.J., 2014. 3D optical printing of piezoelectric nanoparticle–polymer composite materials. ACS nano, 8(10), pp.9799-9806.
22. Meier, H., Haberland, C. and Frenzel, J., 2011. Structural and functional properties of NiTi shape memory alloys produced by selective laser melting. Innovative developments in design and manufacturing: advanced research in virtual and rapid prototyping, pp.291-296.

23. Meier, H., Haberland, C., Frenzel, J. and Zarnetta, R., 2009. Selective Laser Melting of NiTi shape memory components. In Innovative Developments in Design and Manufacturing (pp. 251-256). CRC Press.
24. Dadbakhsh, S., Speirs, M., Kruth, J.P., Schrooten, J., Luyten, J. and Van Humbeeck, J., 2014. Effect of SLM parameters on transformation temperatures of shape memory nickel titanium parts. Advanced Engineering Materials, 16(9), pp.1140-1146.
25. Rossiter, J., Walters, P. and Stoimenov, B., 2009, April. Printing 3D dielectric elastomer actuators for soft robotics. In Electroactive Polymer Actuators and Devices (EAPAD) 2009 (Vol. 7287, p. 72870H). International Society for Optics and Photonics.
26. Raviv, D., Zhao, W., McKnelly, C., Papadopoulou, A., Kadambi, A., Shi, B., Hirsch, S., Dikovsky, D., Zyracki, M., Olguin, C. and Raskar, R., 2014. Active printed materials for complex self-evolving deformations. Scientific reports, 4, p.7422.
27. Ge, Q., Qi, H.J. and Dunn, M.L., 2013. Active materials by four-dimension printing. Applied Physics Letters, 103(13), p.131901.
28. Yu, K., Ritchie, A., Mao, Y., Dunn, M.L. and Qi, H.J., 2015. Controlled sequential shape changing components by 3D printing of shape memory polymer multimaterials. Procedia Iutam, 12, pp.193-203.
29. Ge, Q., Dunn, C.K., Qi, H.J. and Dunn, M.L., 2014. Active origami by 4D printing. Smart Materials and Structures, 23(9), p.094007.
30. Bodaghi M, Damanpack AR, Liao WH. Adaptive metamaterials by functionally graded 4D printing. Materials & Design. 2017 Dec 5; 135:26-36.
31. Zhou, J., & Sheiko, S.S. Reversible shape shifting in polymeric materials, Journal of Polymer Science Part B: Polymer Physics. 2016; 54; 1365-1380.
32. Hager, M.D., Bode, S., Weber, C., Schubert, U.S. Shape memory polymers: Past, present and future developments, Progress in Polymer Science. 2015; 49; 3-33.
33. Ge Q, Dunn CK, Qi HJ, Dunn ML. Active origami by 4D printing. Smart Materials and Structures. 2014 Aug 11; 23(9):094007.
34. Liu F, Urban MW. Recent advances and challenges in designing stimuli-responsive polymers. Prog Polym Sci. 2010; 35; 3–23.
35. B. Qian, G.H. McKinley, A.E. Hosoi, Structure evolution in electro rheological fluids flowing through microchannels, Soft Matter. 2013; 9; 2889.

36. Kumar GS, Neckers DC. Photochemistry of azobenzene-containing polymers. Chem Rev. 1989; 89:1915–25.
37. Ishikawa M, Kitamura N, Masuhara H, Irie M. Size effect on photo inducedvolume change of polyacrylamide microgels containingtriphenylmethane leuco cyanide. Makromol Chem Rapid Commun. 2003;12:687–90
38. Mamada A, Tanaka T, Kungwatchakun D, Irie M. Photoinduced phase transition of gels. Macromolecules. 1990; 23:1517–9.
39. Sakai H, Ebana H, Sakai K, Tsuchiya K, Ohkubo T, Abe M. Photoisomerizationof spiropyran-modified cationic surfactants. J Colloid Interface Sci 2007; 316:1027–30.
40. Fissi A, Pieroni O, Angelini N, Lenci F. Photoresponsive polypeptides.Photochromic and conformational behaviour of spiropyran containingpoly (L-glutamate) under acid conditions. Macromolecules. 1999; 32:7116–21
41. Lukyanov BS, Ivanov NB, Nivorozhkin LE, Minkin VI, BorodkinGS. Photochromic and thermochromic spiranes. 2-Thioxo-3-phenyl-5, 5-diivietiiylspiro (1, 3-oxazolidine-4, 2-[2h]chromenes). Chem Heterocycl Compd. 1995; 31: 1096–102.
42. Sumaru K, Kameda M, Kanamori T, Shinbo T. Characteristic phasetransition of aqueous solution of poly(N-isopropylacrylamide)functionalized with spiro benzopyran. Macromolecules. 2004; 37: 4949–55.
43. Davim JP, Reis P. Drilling carbon fiber reinforced plastics manufactured by autoclave experimental and statistical study. Materials & design. 2003 Aug 1; 24(5):315-24.
44. Krishnaraj V, Prabukarthi A, Ramanathan A, Elanghovan N, Kumar MS, Zitoune R, Davim JP. Optimization of machining parameters at high speed drilling of carbon fiber reinforced plastic (CFRP) laminates. Composites Part B: Engineering. 2012 Jun 1; 43(4):1791-9.
45. Shirvanimoghaddam K, Hamim SU, Akbari MK, Fakhrhoseini SM, Khayyam H, Pakseresht AH, Ghasali E, Zabet M, Munir KS, Jia S, Davim JP. Carbon fiber reinforced metal matrix composites: Fabrication processes and properties. Composites Part A: Applied Science and Manufacturing. 2017 Jan 1; 92:70-96.
46. Davim JP, Reis P, Antonio CC. A study on milling of glass fiber reinforced plastics manufactured by hand-lay up using statistical analysis (ANOVA). Composite structures. 2004 Jun 1; 64(3-4):493-500.

47. Mujber TS, Szecsi T, Hashmi MS. Virtual reality applications in manufacturing process simulation. Journal of materials processing technology. 2004 Nov 30; 155:1834-8.
48. Begum S, Fawzia S, Hashmi MS. Polymer matrix composite with natural and synthetic fibres. Advances in Materials and Processing Technologies. 2020 Mar 6:1-8.
49. Kumar R, Singh R, Ahuja IP, Hashmi MS. Processing techniques of polymeric materials and their reinforced composites. Advances in Materials and Processing Technologies. 2020 Feb 20:1-7.
50. Singh N, Hui D, Singh R, Ahuja IP, Feo L, Fraternali F. Recycling of plastic solid waste: A state of art review and future applications. Composites Part B: Engineering. 2017 Apr 15; 115:409-22.
51. Fraternali F, Ciancia V, Chechile R, Rizzano G, Feo L, Incarnato L. Experimental study of the thermo-mechanical properties of recycled PET fiber-reinforced concrete. Composite Structures. 2011 Aug 1; 93(9):2368-74.
52. Amendola A, Smith CJ, Goodall R, Auricchio F, Feo L, Benzoni G, Fraternali F. Experimental response of additively manufactured metallic pentamode materials confined between stiffening plates. Composite Structures. 2016 May 10; 142:254-62.
53. Thrimurthulu KP, Pandey PM, Reddy NV. Optimum part deposition orientation in fused deposition modeling. International Journal of Machine Tools and Manufacture. 2004 May 1; 44(6):585-94.
54. Pandey PM, Thrimurthulu K, Reddy* NV. Optimal part deposition orientation in FDM by using a multicriteria genetic algorithm. International Journal of Production Research. 2004 Oct 1; 42(19):4069-89.
55. Pandey PM, Venkata Reddy N, Dhande SG. Virtual hybrid-FDM system to enhance surface finish. Virtual and Physical Prototyping. 2006 Jun 1; 1(2):101-16.
56. Pandey PM, Reddy NV, Dhande SG. Improvement of surface finish by staircase machining in fused deposition modeling. Journal of materials processing technology. 2003 Jan 10;132(1-3):323-31.
57. Campbell, T.A., Tibbits, S., and Garrett, B. The next wave: 4D printing, programming the material world. Washington, DC: The Atlantic Council, 2014; 1–15.
58. Campbell, T.A., Tibbits, S., and Garrett, B. The programmable world. Scientific American. 2014; 311 (5), 60–65.

59. Bajpai PK, Singh I, Madaan J. Development and characterization of PLA-based green composites: A review. Journal of Thermoplastic Composite Materials. 2014 Jan; 27(1):52-81.
60. Bajpai PK, Singh I, Madaan J. Comparative studies of mechanical and morphological properties of polylactic acid and polypropylene based natural fiber composites. Journal of Reinforced Plastics and Composites. 2012 Dec; 31(24):1712-24.
61. Chauhan SR, Kumar A, Singh I, Kumar P. Effect of fly ash content on friction and dry sliding wear behaviour of glass fiber reinforced polymer composites-A taguchi approach. Journal of Minerals and Materials Characterization and engineering. 2010 Apr 20; 9(04):365.
62. Lila MK, Singhal A, Banwait SS, Singh I. A recyclability study of bagasse fiber reinforced polypropylene composites. Polymer Degradation and Stability. 2018 Jun 1; 152:272-9.
63. Saroha V, Pabla BS, Bhogal SS. Characterization of ABS for Enhancement of Mechanical Properties. Vol no. 8, Issue no. 10, pp 2164-2167.
64. Singh R, Kumar S, Bedi P, Hashmi MS. On wear of 3D printed Al2O3 reinforced Nylon6 matrix based functional prototypes. Materials Today: Proceedings. 2020 Feb 25.
65. Yang Y, Boom R, Irion B, van Heerden DJ, Kuiper P, de Wit H. Recycling of composite materials. Chemical Engineering and Processing: Process Intensification. 2012 Jan 1; 51:53-68.
66. Lila MK, Singh B, Pabla BS, Singh I. Effect of environmental conditioning on natural fiber reinforced epoxy composites. Materials Today: Proceedings. 2018 Jan 1; 5(9):17006-11.
67. Luthra S, Kumar S, Garg D, Haleem A. Barriers to renewable/sustainable energy technologies adoption: Indian perspective. Renewable and sustainable energy reviews. 2015 Jan 1; 41:762-76.
68. Kumar S, Panda AK, Singh RK. A review on tertiary recycling of high-density polyethylene to fuel. Resources, Conservation and Recycling. 2011 Sep 1; 55(11):893-910.
69. Sadat-Shojai M, Bakhshandeh GR. Recycling of PVC wastes. Polymer degradation and stability. 2011 Apr 1; 96(4):404-15.
70. Frounchi, M. and Shamshiri, S. Magnetic nanoparticles-loaded PLA/PEG microspheres as drug carriers. *Journal of Biomedical Materials Research Part A*, 2015; *103*(5), pp.1893-1898.https://doi.org/10.1002/jbm.a.35317.
71. Zheng Y, Yanful EK, Bassi AS. A review of plastic waste biodegradation. Critical reviews in biotechnology. 2005 Jan 1; 25(4):243-50.

72. Tartakowski Z. Recycling of packaging multilayer films: New materials for technical products. Resources, conservation and recycling. 2010 Dec 1; 55(2):167-70.
73. Yousefpour A, Hojjati M, Immarigeon JP. Fusion bonding/welding of thermoplastic composites. Journal of Thermoplastic composite materials. 2004 Jul; 17(4):303-41.
74. Offringa AR. Thermoplastic composites—rapid processing applications. Composites Part A: Applied Science and Manufacturing. 1996 Jan 1; 27(4):329-36.
75. Biron M. Thermoplastics and thermoplastic composites. William Andrew; 2018 Jun 6.
76. Mantell SC, Springer GS. Manufacturing process models for thermoplastic composites. Journal of Composite Materials. 1992 Jan; 26(16):2348-77.
77. Glasser WG, Taib R, Jain RK, Kander R. Fiber-reinforced cellulosic thermoplastic composites. Journal of Applied Polymer Science. 1999 Aug 15; 73(7):1329-40.
78. Bledzki AK, Gassan J, Theis S. Wood-filled thermoplastic composites. Mechanics of composite materials. 1998 Nov 1; 34(6):563-8.
79. Schinner G, Brandt J, Richter H. Recycling carbon-fiber-reinforced thermoplastic composites. Journal of Thermoplastic Composite Materials. 1996 Jul; 9(3):239-45.
80. Denault J, Vu-Khanh T, Foster B. Tensile properties of injection molded long fiber thermoplastic composites. Polymer composites. 1989 Oct; 10(5):313-21.
81. Guo N, Leu MC. Additive manufacturing: technology, applications and research needs. Frontiers of Mechanical Engineering. 2013 Sep 1; 8(3):215-43.
82. Kruth JP, Leu MC, Nakagawa T. Progress in additive manufacturing and rapid prototyping. CIRP Annals-Manufacturing Technology. 1998; 47(2):525-40.
83. Wohlers TT, Caffrey T. Wohlers report 2014: 3D printing and additive manufacturing state of the industry annual worldwide progress report. Fort Collins, CO: Wohlers Associates; 2014.
84. Campbell I, Bourell D, Gibson I. Additive manufacturing: rapid prototyping comes of age. Rapid prototyping journal. 2012 Jun 8.
85. Zhou, S., Sun, J., Sun, L., Dai, Y., Liu, L., Li, X., Wang, J., Weng, J., Jia, W. and Zhang, Z. Preparation and characterization of interferon-loaded magnetic biodegradable microspheres. Journal of Biomedical Materials Research Part B: Applied Biomaterials: An Official Journal of The Society for Biomaterials, The Japanese Society for Biomaterials, and

The Australian Society for Biomaterials and the Korean Society for Biomaterials, 2008; 87(1), pp.189-196.

86. Asa'di, S., Frounchi, M. and Dadbin, S. Nanomagnetic poly (vinyl alcohol) hydrogels. In Advanced Materials Research Trans Tech Publications. 2014; Vol. 829, pp. 539-543.
87. Khatri A, Garg D, Dangayach GS. Critical Success Factors of Sustainable Manufacturing and Procurement: An Empirical Study. International Journal of Social Ecology and Sustainable Development (IJSESD). 2019 Jul 1; 10(3):17-27.
88. Gao B, Yang Q, Zhao X, Jin G, Ma Y, Xu F. 4D bioprinting for biomedical applications. Trends in biotechnology. 2016 Sep 1; 34(9):746-56.
89. N. Turner B, Strong R, A. Gold S. A review of melt extrusion additive manufacturing processes: I. Process design and modeling. Rapid Prototyping Journal. 2014 Apr 14; 20(3):192-204.
90. Kumar S, Singh R, Hashmi MS. Metal matrix composite: a methodological review. Advances in Materials and Processing Technologies. 2019 Oct 28:1-2.
91. Afrose MF, Masood SH, Nikzad M, Iovenitti P. Effects of build orientations on tensile properties of PLA material processed by FDM. In Advanced Materials Research 2014 (Vol. 1044, pp. 31-34). Trans Tech Publications.
92. Gong B, Cui S, Zhao Y, Sun Y, Ding Q. Strain-controlled fatigue behaviours of porous PLA-based scaffolds by 3D-printing technology. Journal of Biomaterials Science, Polymer Edition. 2017 Dec 12; 28(18):2196-204.
93. Luthra S, Garg D, Haleem A. An analysis of interactions among critical success factors to implement green supply chain management towards sustainability: An Indian perspective. Resources Policy. 2015 Dec 1;46:37-50.
94. Chowdhury RA, Rai A, Glynn E, Morgan P, Moore AL, Youngblood JP, Superior, processing-dependent thermal conductivity of cellulose Nanocrystal-Poly (vinyl alcohol) composite films, Polymer. 15(164); 2019:17-25.
95. Lewis JS, Barani Z, Magana AS, Kargar F, Balandin AA, Thermal and electrical conductivity control in hybrid composites with graphene and boron nitride fillers, Materials Research Express. 6(8): 2019: 085325.
96. Bodaghi, M., Damanpck, A.R., & Liao,W.H, Adaptive metamaterials by functionally graded 4D printing.Materials and Design. 2017; 135; 26-36.

97. Bastola, A.k, Paudel, M., & Li,L.. Development of hybrid magnetorheological elastomers by 3D printing.Polymer. 2018. DOI: 10.1016/j.polymer.2018.06.076.
98. Bristy,S.S., Rahman, M.A., Taur,K., Minami,H.& Ahmad,H. Preparation and characterization of magnetic γ-Al2O3 ceramic nanocomposite particles with variable Fe3O4 content and modification with epoxide functional polymer.Ceramics International. 2017. http://dx.doi.org/10.1016/j.ceramint.2017.11.187.
99. Abuzaid,W., Alkhader,M., & Omari,M.,. Experimental analysis of heterogeneous shape recovery in 4d printed honeycomb structures.Polymr Testing. 2018; 68; 100-109.
100. Caputo,M.P., Berowitz,A.E., Armstrong,A., Mullnr,P., & Solomon,C.V. 4D Printing of Net Shape Parts Made from Ni-Mn-Ga Magnetic Shape Memory Alloys.Additive Manufcturing. 2018..
101. Castro,N.J., Meinert,C, Levett,P., & Hutmacher,D.W. Current developments in multifunctional smart materials for 3D/4D bioprinting. Current Opinion in Biomedical Engineering. 2017; 2; 67-75.
102. Gao, B., Yang,Q., Zhao,X., Jin, G., Ma, Y., & Xu,F.,. 4D Bioprinting for Biomedical Applications. Trends in Biotechnology.2016; 34; 9.
103. Miao, S., Castro, N., Nowicki, M., Xia, L., Cui, H., Zhou, X., Zhu, V., Lee, S., Sarkar, K., Vozzi, G., Tabata, Y., Fisher, J., & Zhang, L.G, 4D printing of polymeric materials for tissue and organ regeneration, Materials Today. 2017. http://dx.doi.org/10.1016/j.mattod.2017.06.005.
104. Gharib, A., Karimi, M.S., Arani, A.G. Vibration analysis of the embedded piezoelectric polymeric nano-composite panels in the elastic substrate, Composites Part B. 2016; 101; 64-76.
105. Invernizzi, M., Turri, S., Levi, M., Suriano, R. 4D printed thermally activated self-healing and shape memory polycaprolactone based polymers, European Polymer Journal. 2018; 101; 169–176.
106. Jadhav, R.G., & Das, A.K. Four dimensional printing in healthcare**,** 3D printing in Medicine. 2017. http://dx.doi.org/10.1016/B978-0-08-100717-4.00010-7.
107. Lee, A.Y., An, J., &Chua, C.K. Two-Way 4D Printing: A Review on the Reversibility of3D-Printed Shape Memory Materials, Engineering 3. 2017; 663–674.

108. Liu, Y., Zhang, W., Zhang, F., Lan, X., Leng, J., Liu, S., Jia, X., Cotton, C., Sun, B., Gu, B., Chou, T.W. Shape memory behaviour and recovery force of 4D printed laminated Miura-origami structures subjected to compressive loading, Composites Part B. 2018.10.1016/j.compositesb.2018.07.053.

109. Ge, Q., Dunn, C.K., Qi, H.J., Dunn, M.L. Active origami by 4D printing, Smart Materials and Structures. 2014. Doi:10.1088/0964-1726/23/9/094007.

110. Irez, A.B., Bayraktar, E., & Miskioglu, I. Recycled and devulcanized rubber modified epoxy-based composites reinforced with nano-magnetic iron oxide, Fe3O4, Composites Part B. 2018; 148; 1–13.

111. Connal LA, Li Q, Quinn JF, Tjipto E, Caruso F, Qiao GG. pH-responsivepoly (acrylic acid) core cross-linked star polymers: morphologytransitions in solution and multilayer thin films. Macromolecules.2008; 41:2620–6.

112. Li G, Song S, Guo L, Ma S. Self-assembly of thermo- andpH-responsive poly(acrylic acid)-b-poly(N-isopropylacrylamide)micelles for drug delivery. J Polym Sci Part A: Polym Chem.2008; 46:5028–35.

113. Binks BP, Murakami R, Armes SP, Fujii S, Schmid A. pH-responsiveaqueous foams stabilized by ionizable latex particles. Langmuir.2007; 23:8691–4.

114. He E, Yue CY, Tam KC. Association behaviour of star-shapedpH-responsive block copolymer: four-arm poly (ethyleneoxide)-b-poly (methacrylic acid) in aqueous medium. Langmuir.2009; 25: 4892–9.

115. Munoz-Bonilla A, Fernandez-Garcia M, Haddleton DM. Synthesisand aqueous solution properties of stimuli-responsive triblock copolymers. Soft Matter. 2007; 3:725–31.

116. Munoz-Bonilla A, Fernandez-Garcia M, Haddleton DM. Synthesisand aqueous solution properties of stimuli-responsive triblock copolymers. Soft Matter. 2007; 3:725–31.

117. Ravi P, Dai S, Tan CH, Tam KC. Self-assembly of alkali-solublefullerene containing poly(methacrylic acid) in aqueous solution.Macromolecules. 2005; 38:933–9.

118. Hu L, Chu LY, Yang M, Wang HD, Hui NC. Preparation and characterizationof novel cationic pH-responsive poly (N, N-dimethylaminoethyl methacrylate) microgels. Langmuir. 2007; 311:110–7.

119. Snoswell DRE, Brill RK, Vincent B. pH-responsive microrods producedby electric-field-induced aggregation of colloidal particles. Adv Mater. 2007; 19: 1523–7.

120. Li D, He Q, Cui Y, Li J. Fabrication of pH-responsive nano compositesof gold nanoparticles/poly(4-vinylpyridine). Chem Mater.2007; 19:412–7.

121. Liu F, Urban MW. Dual temperature and pH responsiveness ofpoly (2-(N, N-dimethylamino) ethyl methacrylate-co-n-butyl acrylate)colloidal dispersions and their films. Macromolecules. 2008; 41:6531–9.

122. Butsele KV, Fustin CA, Gohy JF, Jerome R, Jerome C. Self-assemblyand pH-responsiveness of ABC miktoarm star terpolymers. Langmuir.2009; 25:107–11.

123. Wu XL, Huang WM, Ding Z, Tan HX, Yang WG, Sun KY. Characterization of the thermoresponsive shape-memory effect in poly (ether ether ketone) (PEEK). Appl Polym Sci. 2014;131,http://dx.doi.org/10.1002/APP.39844.

124. Shi Y, Yoonessi M, Weiss RA. High temperature shape memorypolymers. Macromolecules. 2013; 46:4160–7.

125. Koerner H, Strong RJ, Smith ML, Wang DH, Tan L-S, Lee KM, WhiteTJ, Vaia RA. Polymer design for high temperature shape memory:low crosslink density polyimides. Polymer. 2013; 54:391–402.

126. Xie F, Huang L, Liu Y, Leng J. Synthesis and characterization of hightemperature cyanate-based shape memory polymers with func-tional polybutadiene/acrylonitrile. Polymer. 2014; 55:5873–9.

127. Yakacki CM, Shandas R, Safranski D, Ortega AM, Sassaman K, Gall K.Strong, tailored, biocompatible shape-memory polymer networks.Adv Funct Mater. 2008;18:2428–35.

128. Song L, Hu W, Wang GJ, Niu GG, Zhang HB, Cao H, Wang KJ, Yang HA,Zhu SQ. Tailored (meth)acrylate shape-memory polymer networksfor ophthalmic applications. Macromol Biosci. 2010; 10:1194–202.

129. Hearon K, Nash LD, Volk BL, Ware T, Lewicki JP, Voit WE, Wilson TS,Maitland DJ. Electron beam crosslinked polyurethane shape mem-ory polymers with tunable mechanical properties. Macromol ChemPhys. 2013; 214:1258–72.

130. Hao J, Weiss RA. Mechanically tough, thermally activated shapememory hydrogels. ACS Macro Lett. 2013; 2:86–9.

131. Zeng C, Seino H, Ren J, Yoshie N. Polymers with multi shape memory controlled by local glass transition temperature. ACS Appl MaterInterfaces. 2014; 6:2753–8.

132. Bellin I, Kelch S, Langer R, Lendlein A. Polymeric triple-shape materials. Proc Natl Acad Sci USA. 2006; 103:18043–7.

133. Zotzmann J, Behl M, Feng YK, Lendlein A. Co-polymer networks based on poly(omega-pentadecalactone) and poly(epsiloncaprolactone) segments as a versatile triple-shapepolymer system. Adv Funct Mater. 2010; 20:3583–94.

134. Chatani S, Wang C, Podgoırski M, Bowman CN. Triple shape memory materials incorporating two distinct polymer networks formed by selective thiol Michael addition reactions. Macromolecules. 2014; 47:4949–54.

135. Yang X, Wang L, Wang W, Chen H, Yang G, Zhou S. Triple shape memory effect of star-shaped polyurethane. ACS Appl Mater Inter-faces. 2014; 6:6545–54.

136. Torbati AH, Nejad HB, Ponce M, Sutton JP, Mather PT. Properties of triple shape memory composites prepared via polymerization-induced phase separation. Soft Matter. 2014; 10:3112–21.

137. Luo Y, Guo Y, Gao X, Li B-G, Xie T. A general approach towards thermoplastic multishape memory polymers via sequence structure design. Adv Mater 2013; 25:743–8.

138. Xie T, Xiao X, Cheng Y-T. Revealing triple-shape memory effect by polymer bi-layers. Macromol Rapid Commun. 2009; 30:1823–7.

139. Zhao J, Chen M, Wang X, Zhao X, Wang Z, Dang Z-M, Ma L, HuG-H, Chen F. Triple shape memory effects of cross-linked polyethylene/polypropylene blends with co-continuous architecture. ACSAppl Mater Interfaces. 2013; 5:5550–6.

140. Hoeher R, Raidt T, Krumm C, Meuris M, Katzenberg F, Tiller JC. Tunable multiple-shape memory polyethylene blends. Macromol Chem Phys. 2013; 214:2725–32.

141. Xie T. Tunable polymer multi-shape memory effect. Nature2010; 464:267–70.

142. Li J, Liu T, Xia S, Pan Y, Zheng Z, Ding X, Peng Y. A versatile approach to achieve quintuple-shape memory effect by semi-interpenetrating polymer networks containing broadened glass transition and crystalline segments. J Mater Chem. 2011; 21:12213–7.

143. Kwon S, Kim KJ, Kim H, Kundu PP, Kim TJ, Lee YK and Choe S. Tensile property and interfacial dewetting in the calcite filled HDPE, LDPE, and LLDPE composites. Polymer, 2002; 43(25):6901–6909.

144. Valentino O, Sarno M, Rainone NG, Nobile MR, Ciambelli P, Neitzert HC and Simon GP. Influence of the polymer structure and nanotube concentration on the conductivity and

rheological properties of polyethylene/CNT composites. Physica E: Low-Dimensional Systems and Nanostructures, 2008; 40(7):2440–2445.

145. Lu JZ, Wu Q and Negulescu II. Wood-fiber/high-density-polyethylene composites: Coupling agent performance. Journal of Applied Polymer Science, 2005; 96(1):93–102.

146. Doh GH, Lee SY, Kang IA and Kong YT. Thermal behaviour of liquefied wood polymer composites (LWPC). Composite Structures, 2005; 68(1):103–108.

147. Deka BK, Maji TK and Mandal M. Study on properties of nanocomposites based on HDPE, LDPE, PP, PVC, wood and clay. Polymer Bulletin, 2011; 67(9):1875–1892.

148. Mead WT and Porter RS. The preparation and tensile properties of polyethylene composites. Journal of Applied Polymer Science, 1978; 22(11):3249–3265.

149. Tang H, Liu ZY, Piao JH, Chen XF, Lou YX and Li SH. Electrical behaviour of carbon black-filled polymer composites: Effect of interaction between filler and matrix. Journal of Applied Polymer Science, 1994; 51(7):1159–1164.

150. Jung J, Kim J, Uhm YR, Jeon JK, Lee S, Lee HM and Rhee CK. Preparations and thermal properties of micro- and nano-BN dispersed HDPE composites. Thermochimica Acta, 2010; 499(1-2): 8–14.

151. Minkova L, Peneva Y, Tashev E, Filippi S, Pracella M and Magagnini P. Thermal properties and micro hardness of HDPE/clay nanocomposites compatibilized by different functionalized polyethylenes. Polymer Testing, 2009; 28(5):528–533.

152. Kuang X, Kuang R, Zheng X and Wang Z. Mechanical properties and size stability of wheat straw and recycled LDPE composites coupled by waterborne coupling agents. Carbohydrate Polymers, 2010; 80(3): 927–933.

153. AlMaadeed MA, Ouederni M and Noorunnisa KP. Effect of chain structure on the properties of Glass fibre/polyethylene composites. Materials & Design, 2013; 47:725–730.

154. Sarkhel G and Choudhury A. Dynamic mechanical and thermal properties of PE-EPDM based jute fibre composites. Journal of Applied Polymer Science, 2008; 108(6):3442–3453.

155. Ogawa T, Mukai H and Osawa S. Mechanical properties of ultrahigh-molecular-weight polyethylene fiber-reinforced PE composites. Journal of Applied PolymerScience, 1998; 68(9):1431–1439.

156. Molefi JA, Luyt AS and Krupa I. Comparison of the influence of copper micro- and nano-particles on the mechanical properties of polyethylene/copper composites. Journal of Materials Science, 2009; 45(1):82–88.

157. Chacón JM, Caminero MA, García-Plaza E, Núñez PJ (2017) Additive manufacturing of PLA structures using fused deposition modeling: Effect of process parameters on mechanical properties and their optimal selection. Materials & Design 124:143–157.https://doi.org/10.1016/j.matdes.2017.03.065.

158. Lanzotti A, Grasso M, Staiano G, Martorelli M (2015) The impact of process parameters on mechanical properties of parts fabricated in PLA with an open-source 3-D printer. Rapid Prototyping Journal 21(5):604–617.https://doi.org/10.1108/RPJ-09-2014-0135

159. Zhou Y, Lei L, Yang B, Li J, Ren J (2018) Preparation and characterization of polylactic acid (PLA) carbon nano-tube nano-composites. Polymer Testing 68:34–38.https://doi.org/10.1016/j.polymertesting.2018.03.044.

160. Reinhardt M, Kaufmann J, Kausch M, Kroll L (2013) PLA-Viscose-Composites with Continuous Fibre Reinforcement for Structural Applications. Procedia Materials Science 2:137–143.https://doi.org/10.1016/j.mspro.2013.02.016.

161. Scaffaro R, Lopresti F, Botta L (2018) PLA based biocomposites reinforced with Posidonia oceanica leaves. Composites Part B: Engineering 139:1–11.https://doi.org/10.1016/j.compositesb.2017.11.048.

162. Nasrin R, Biswas S, Rashid TU, Afrin S, Jahan RA, Haque P, Rahman MM (2017) Preparation of Chitin-PLA laminated composite for implantable application. Bioactive Materials 2(4):199–207.https://doi.org/10.1016/j.bioactmat.2017.09.003.

163. Bouakaz BS, Habi A, Grohens Y, Pillin I (2017) Organomontmorillonite/graphene-PLA/PCL nanofilled blends: New strategy to enhance the functional properties of PLA/PCL blend. Applied Clay Science 139:81–91.https://doi.org/10.1016/j.clay.2017.01.014.

164. Gupta MK, Singh R (2018) Flexural and Dynamic Mechanical Analysis (DMA) of Polylactic Acid (PLA) Coated Sisal Fibre Reinforced Polyester Composite. Materials Today: Proceedings 5(2):6109–6114.https://doi.org/10.1016/j.matpr.2017.12.216.

165. Peponi L, Sessini V, Arrieta MP, and Navarro-Baena I, Sonseca A, Dominici F, Kenny J M (2018) Thermally-activated shape memory effect on biodegradable nano-composites based

on PLA/PCL blend reinforced with hydroxyapatite. Polymer Degradation and Stability 151:36–51.https://doi.org/10.1016/j.polymdegradstab.2018.02.019.

166. Singla RK, Zafar MT, Maiti SN, Ghosh AK (2017) Physical blends of PLA with high vinyl acetate containing EVA and their rheological, thermo-mechanical and morphological responses. Polymer Testing 63:398–406.https://doi.org/10.1016/j.polymertesting.2017.08.042.

167. Chen PY, Lian HY, Shih YF, Chen-Wei SM, Jeng RJ (2017) Preparation, characterization and crystallization kinetics of Kenaf fiber/multi-walled carbon nanotube/polylactic acid (PLA) green composites. Materials Chemistry and Physics 196:249–255.https://doi.org/10.1016/j.matchemphys.2017.05.006.

168. Wang Z, Xu Z, Lu Y, Hu L, Fan Y, Ma J, Zhou X (2017) Preparation of 3D printable micro/nanocellulose-polylactic acid (MNC/PLA) composite wire rods with high MNC constitution. Industrial Crops and Products 109:889–896.https://doi.org/10.1016/j.indcrop.2017.09.061.

169. Varsavas SD, Kaynak C (2018) Effects of glass fiber reinforcement and thermoplastic elastomer blending on the mechanical performance of polylactide. Composites Communications 8:24–30.https://doi.org/10.1016/j.coco.2018.03.003.

170. Rahman MM, Islam MS, Li GS (2018) Development of PLA/CS/ZnO nano-composites and optimization it’s mechanical, thermal and water absorption properties. Polymer Testing 68:302–308.https://doi.org/10.1016/j.polymertesting.2018.04.026.

171. Oksman K, Skrifvars M, Selin JF (2003) Natural fibres as reinforcement in polylactic acid (PLA) composites. Composites Science and Technology 63(9):1317–1324.https://doi.org/10.1016/S0266-3538 (03)00103-9.

172. Kelnar I, Kratochvíl J, Kaprálková L, Zhigunov A, Nevoralová M (2017) Graphite nano-platelets-modified PLA/PCL: Effect of blend ratio and nano-filler localization on structure and properties. Journal of the Mechanical Behaviour of Biomedical Materials 71:271–278. doi:10.1016/j.jmbbm.2017.03.028.

173. Leist SK, Gao D, Chiou R, Zhou J (2017) Investigating the shape memory properties of 4D printed polylactic acid (PLA) and the concept of 4D printing onto nylon fabrics for the creation of smart textiles. Virtual and Physical Prototyping 12(4):290–300.https://doi.org/10.1080/17452759.2017.1341815.

174. Ferreira RTL, Amatte IC, Dutra TA, Burger D. Experimental characterization and micrography of 3D printed PLA and PLA reinforced with short carbon fibers. Composites Part B: Engineering. 2017; 124:88-100.

175. Leist SK, Gao D, Chiou R, Zhou J. Investigating the shape memory properties of 4D printed polylactic acid (PLA) and the concept of 4D printing onto nylon fabrics for the creation of smart textiles. Virtual and Physical Prototyping. 2017;12(4): 290–300.

176. Lind JU, Busbee TA, Valentine AD, Pasqualini FS, Yuan H, Yadid M, Parker KK. Instrumented cardiac microphysiological devices via multimaterial three-dimensional printing. Nature Materials. 2016; 16(3):303–308.

177. Melnikova R, Ehrmann A, Finsterbusch K. 3D printing of textile-based structures by Fused Deposition Modelling (FDM) with different polymer materials. IOP Conference Series: Materials Science and Engineering 2014; 62:012018. doi:10.1088/1757-899x/62/1/012018.

178. Sabantina L, Kinzel F, Ehrmann A, Finsterbusch K. Combining 3D printed forms with textile structures - mechanical and geometrical properties of multi-material systems. IOP Conference Series: Materials Science and Engineering. 2015; 87:012005. doi:10.1088/1757-899x/87/1/012005.

179. Smith ML, Jones JFX. Dual-extrusion 3D printing of anatomical models for education. Anatomical Sciences Education. 2017; 11(1):65–72.

180. Gnanasekaran K, Heijmans T, Van Bennekom S, Woldhuis H, Wijnia S, De with G, Friedrich H. 3D printing of CNT- and graphene-based conductive polymer nanocomposites by fused deposition modeling. Applied Materials Today. 2017; 9: 21–28.

181. Yang C, Wang B, Li D, Tian X. Modelling and characterisation for the responsive performance of CF/PLA and CF/PEEK smart materials fabricated by 4D printing. Virtual and Physical Prototyping. 2017; 12(1): 69–76.

182. Luo Y, Wang G, Zhang B, Zhang Z. The influence of crystalline and aggregate structure on PTC characteristic of conductive polyethylene/carbon black composite. European Polymer Journal. 1998; 34(8):1221–1227.

183. Liu J, Li W, Guo Y, Zhang H, Zhang Z. Improved Thermal Conductivity of Thermoplastic Polyurethane via Aligned Boron Nitride Platelets Assisted by 3D Printing. Composites Part A: Applied Science and Manufacturing. 2019; 120:140-146.

184. Lin W, Shen H, Xu G, Zhang L, Fu J, Deng X. Single-layer temperature-adjusting transition method to improve the bond strength of 3D-printed PCL/PLA parts. Composites Part A: Applied Science and Manufacturing. 2018; 115:22-30.

185. Zhao, H., Saatchi, K., & Häfeli, U. O. Preparation of biodegradable magnetic microspheres with poly (lactic acid)-coated magnetite. Journal of Magnetism and Magnetic Materials, 2009; 321(10): 1356–1363.https://doi.org/10.1016/j.jmmm.2009.02.038.

186. Häfeli, U. O., & Pauer, G. J. In vitro and in vivo toxicity of magnetic microspheres. Journal of Magnetism and Magnetic Materials, 1999; 194(1-3): 76–82. https://doi.org/10.1016/S0304-8853(98)00560-5

187. Gómez-Lopera, S. ., Plaza, R. ., & Delgado, A. Synthesis and Characterization of Spherical Magnetite/Biodegradable Polymer Composite Particles. Journal of Colloid and Interface Science, 2001; 240(1): 40–47. https://doi.org/10.1006/jcis.2001.7579.

188. Zheng, W., Gao, F., & Gu, H. Magnetic polymer nano-spheres with high and uniform magnetite content. Journal of Magnetism and Magnetic Materials, 2005; 288: 403–410.https://doi.org/10.1016/j.jmmm.2004.09.125

189. Razzaq, M. Y., Anhalt, M., Frormann, L., & Weidenfeller, B. Thermal, electrical and magnetic studies of magnetite filled polyurethane shape memory polymers. Materials Science and Engineering: A, 2007; 444 (1-2): 227–235.https://doi.org/10.1016/j.msea.2006.08.083.

190. Ramesan, M. T. Fabrication, characterization, and properties of poly (ethylene-co-vinyl acetate)/magnetite nanocomposites. Journal of Applied Polymer Science, 2013; 131(7): DOI: 10.1002/APP.40116.

191. Tural, B., Ozkan, N., & Volkan, M. Preparation and characterization of polymer coated super paramagnetic magnetite nanoparticle agglomerates. Journal of Physics and Chemistry of Solids, 2009; 70(5): 860–866.https://doi.org/10.1016/j.jpcs.2009.04.007

192. Trifol Guzman, J., Plackett, D., Sillard, C., Szabo, P., Bras, J., & Daugaard, A. E. (2016). Hybrid poly (lacticacid)/nanocellulose/nanoclay composites with synergistically enhanced barrier properties and improved thermomechanical resistance. Polymer International, 65(8), 988-995. DOI: 10.1002/pi.5154

193. Nasrin, R., Biswas, S., Rashid, T. U., Afrin, S., Jahan, R. A., Haque, P., & Rahman, M. M. Preparation of Chitin-PLA laminated composite for implantable application. Bioactive Materials, 2017; 2(4), 199–207. doi:10.1016/j.bioactmat.2017.09.003.

194. Frounchi, M. and Shamshiri, S. Magnetic nanoparticles-loaded PLA/PEG microspheres as drug carriers. *Journal of Biomedical Materials Research Part A*, 2015; *103*(5), pp.1893-1898.https://doi.org/10.1002/jbm.a.35317

195. Zhou, S., Sun, J., Sun, L., Dai, Y., Liu, L., Li, X., Wang, J., Weng, J., Jia, W. and Zhang, Z. Preparation and characterization of interferon-loaded magnetic biodegradable microspheres. Journal of Biomedical Materials Research Part B: Applied Biomaterials: An Official Journal of The Society for Biomaterials, The Japanese Society for Biomaterials, and The Australian Society for Biomaterials and the Korean Society for Biomaterials, 2008; 87(1), pp.189-196.

196. Asa'di, S., Frounchi, M. and Dadbin, S. Nanomagnetic poly (vinyl alcohol) hydrogels. In Advanced Materials Research Trans Tech Publications. 2014; Vol. 829, pp. 539-543.

197. Frounchi, M. and Hadi, M. Effect of synthesis method on magnetic and thermal properties of polyvinylidene fluoride/Fe3O4 nanocomposites. Journal of Reinforced Plastics and Composites, 2013; 32(14), pp.1044-1051.

198. Ranjan, N., Singh, R., & Ahuja, I. S. Biocompatible Thermoplastic Composite Blended With HAp and CS for 3D Printing. Reference Module in Materials Science and Materials Engineering. 2018; doi:10.1016/b978-0-12-803581-8.11237-8.

199. Ranjan, N., Singh, R., & Ahuja, I. (). Preparation of Partial Denture with Nano HAp-PLA Composite under Cryogenic Grinding Environment Using 3D Printing. Reference Module in Materials Science and Materials Engineering. 2018; doi:10.1016/b978-0-12-803581-8.11240-8.

200. Singh, R., Kumar, R., Ranjan, N., Penna, R., & Fraternali, F. (). On the recyclability of polyamide for sustainable composite structures in civil engineering. Composite Structures, 2018; 184, 704–713.

201. N. Turner B, Strong R, A. Gold S. A review of melt extrusion additive manufacturing processes: I. Process design and modeling. Rapid Prototyping Journal. 2014 Apr 14; 20(3):192-204.

202. Singh R, Kumar R, Ahuja IP. Mechanical, thermal and melt flow of aluminum-reinforced PA6/ABS blend feedstock filament for fused deposition modeling. Rapid Prototyping Journal. 2018 Nov 12; 24(9):1455-68.

203. Afrose MF, Masood SH, Nikzad M, Iovenitti P. Effects of build orientations on tensile properties of PLA material processed by FDM. In Advanced Materials Research 2014 (Vol. 1044, pp. 31-34). Trans Tech Publications.

204. Afrose MF, Masood SH, Iovenitti P, Nikzad M, Sbarski I. Effects of part build orientations on fatigue behaviour of FDM-processed PLA material. Progress in Additive Manufacturing. 2016 Jun 1; 1(1-2):21-8.

205. Gong B, Cui S, Zhao Y, Sun Y, Ding Q. Strain-controlled fatigue behaviours of porous PLA-based scaffolds by 3D-printing technology. Journal of Biomaterials Science, Polymer Edition. 2017 Dec 12; 28(18):2196-204.

206. Kariz M, Sernek M, Obućina M, Kuzman MK. Effect of wood content in FDM filament on properties of 3D printed parts. Materials Today Communications. 2018 Mar 1; 14:135-40.

207. Lanzotti A, Grasso M, Staiano G, Martorelli M. The impact of process parameters on mechanical properties of parts fabricated in PLA with an open-source 3-D printer. Rapid Prototyping Journal. 2015 Aug 17; 21(5):604-17.

208. Ibrahim M, Badrishah NS, Sa'ude N, Ibrahim MH. Sustainable natural bio composite for FDM feedstocks. InApplied Mechanics and Materials 2014 (Vol. 607, pp. 65-69). Trans Tech Publications.

209. Song Y, Li Y, Song W, Yee K, Lee KY, Tagarielli VL. Measurements of the mechanical response of unidirectional 3D-printed PLA. Materials & Design. 2017 Jun 5; 123:154-64.

210. Q. Xue, J. Sun, Electrical conductivity and percolation behaviour of polymer nanocomposites, Polymer Nanocomposites, Springer2016, pp. 281-322.

211. Chowdhury RA, Rai A, Glynn E, Morgan P, Moore AL, Youngblood JP, Superior, processing-dependent thermal conductivity of cellulose Nanocrystal-Poly (vinyl alcohol) composite films, Polymer. 15(164); 2019:17-25.

212. Xu Y, Kraemer D, Song B, Jiang Z, Zhou J, Loomis J, Wang J, Li M, Ghasemi H, Huang X, Li X, Nanostructured polymer films with metal-like thermal conductivity. Nature communications. 10(1); (2019):1771.

213. Huang Y, Ellingford C, Bowen C, McNally T, Wu D, Wan C, Tailoring the electrical and thermal conductivity of multi-component and multi-phase polymer composites, International Materials Reviews. 28; 2019:1-35.

214. Taherian R, A review of composite and metallic bipolar plates in proton exchange membrane fuel cell: materials, fabrication, and material selection, J Power Sources. 265; 2014:370–390.

215. Yeetsorn R, Fowler MW, Tzoganakis C, A review of thermoplastic composites for bipolar plate materials in PEM fuel cells, Nanocomposites with unique properties and applications in medicine and industry. 2011:16.

216. Lewis JS, Barani Z, Magana AS, Kargar F, Balandin AA, Thermal and electrical conductivity control in hybrid composites with graphene and boron nitride fillers, Materials Research Express. 6(8): 2019: 085325.

217. Liu C, Dong Y, Lin Y, Yan H, Zhang W, Bao Y, Ma J, Enhanced mechanical and tribological properties of graphene/bismaleimide composites by using reduced graphene oxide with non-covalent functionalization, Composites Part B: Engineering. 165; 2019:491-9.

218. Shtein M, Nadiv R, Buzaglo M, Regev O, Graphene-Based Hybrid Composites for Efficient Thermal Management of Electronic Devices, ACS Appl. Mater. Interfaces. 7 (42); 2015: 23725–23730.

219. Agari Y, Uno T, Thermal conductivity of polymer filled with carbon materials: effect of conductive particle chains on thermal conductivity, Journal of applied polymer science. 30(5); 1985:2225-35.

220. Agari Y, Uno T, Estimation on thermal conductivities of filled polymers, Journal of Applied Polymer Science. 32(7); 1986:5705-12.

221. Agari Y, Ueda A, Nagai S, Thermal conductivity of a polymer composite, Journal of Applied Polymer Science. 49(9); 1993:1625-34.

222. Balandin AA, Ghosh S, Bao W, Calizo I, Teweldebrhan D, Miao F, Lau CN, Superior thermal conductivity of single-layer graphene, Nano letters. 8(3); 2008:902-7.

223. Chen H, Ginzburg VV, Yang J, Yang Y, Liu W, Huang Y, Du L, Chen B, Thermal conductivity of polymer-based composites: Fundamentals and applications, Progress in Polymer Science. 59; 2016:41-85.

224. Han ZD, Fina A, Thermal conductivity of carbon nano tubes and their polymer nanocomposites: a review, Prog Polym Sci. 36; 2011:914–44.

225. Huang XY, Jiang PK, Tanaka T, A review of dielectric polymer composites with high thermal conductivity, IEEE Electr Insul Mag. 27; 2011:8–16.

226. Guo Y, Lyu Z, Yang X, Lu Y, Ruan K, Wu Y, Kong J, Gu J, Enhanced thermal conductivities and decreased thermal resistances of functionalized boron nitride/polyimide composites, Composites Part B: Engineering. 164; 2019:732-9.

227. Gu JW, Lv ZY, Wu YL, Zhao RX, Tian LD, Zhang QY, Enhanced thermal conductivity of SiCp/PS composites by electro spinning-hot press technique, Compos Part A- Appl S. 79; 2015:8-13

228. Hu M, Yu D, Wei J, Thermal conductivity determination of small polymer samples by differential scanning calorimetry, Polym Test. 26; 2007:333–7.

229. Zhong C, Yang Q, Wang W, Correlation and prediction of the thermal conductivity of amorphous polymers, Fluid Phase Equilib. 181; 2001:195–202

230. Dashora P, Gupta G, On the temperature dependence of the thermal conductivity of linear amorphous polymers, Polymer. 37; 1996:231–4.

231. Wong YW, Lo KL, Shin FG, Electrical and thermal properties of composite of liquid crystalline polymer filled with carbon black, J Appl Polym Sci. 82; 2001:1549–55

232. Shenogin S, Bodapati A, Xue L, Ozisik R, Keblinski P, Effect of chemical functionalization on thermal transport of carbon nanotube composites, Appl Phys Lett. 85; 2004:2229–31.

233. Ahn, S.H., Montero, M., Odell, D., Roundy, S. and Wright, P.K., 2002. Anisotropic material properties of fused deposition modeling ABS. Rapid prototyping journal, 8(4), pp.248-257.

234. Ahn, S.H., Lee, C.S. and Jeong, W., 2004. Development of translucent FDM parts by post-processing. Rapid prototyping journal, 10(4), pp.218-224.

235. Arivazhagan, A. and Masood, S.H., 2012. Dynamic mechanical properties of ABS material processed by fused deposition modelling. Int. J. Eng. Res. Appl, 2(3), pp.2009-2014.

236. Dawoud, M., Taha, I. and Ebeid, S.J., 2016. Mechanical behaviour of ABS: An experimental study using FDM and injection moulding techniques. Journal of Manufacturing Processes, 21, pp.39-45.

237. Equbal, A., Sood, A.K., Toppo, V., Ohdar, R.K. and Mahapatra, S.S., 2010. Prediction and analysis of sliding wear performance of fused deposition modelling-processed ABS plastic

parts. Proceedings of the Institution of Mechanical Engineers, Part J: Journal of Engineering Tribology, 224(12), pp.1261-1271.

238. Equbal, A. and Sood, A.K., 2015. Investigations on metallization in FDM build ABS part using electroless deposition method. Journal of Manufacturing Processes, 19, pp.22-31.

239. Jami, H., Masood, S.H. and Song, W.Q., 2013. Dynamic response of FDM made ABS parts in different part orientations. In Advanced Materials Research (Vol. 748, pp. 291-294). Trans Tech Publications.

240. Kantaros, A. and Karalekas, D., 2013. Fiber Bragg grating based investigation of residual strains in ABS parts fabricated by fused deposition modeling process. Materials & Design, 50, pp.44-50.

241. Lee, B.H., Abdullah, J. and Khan, Z.A., 2005. Optimization of rapid prototyping parameters for production of flexible ABS object. Journal of materials processing technology, 169(1), pp.54-61.

242. Idris, M.H., Sharif, S. and Harun, W.S.W., 2008, December. Evaluation of ABS patterns produced from FDM for investment casting process. In Proceedings of the 9th Asia Pasific Industrial Engineering & Management Systems Conference (pp. 1299-1304).

243. Montero, M., Roundy, S., Odell, D., Ahn, S.H. and Wright, P.K., 2001. Material characterization of fused deposition modeling (FDM) ABS by designed experiments. Society of Manufacturing Engineers, 10(13552540210441166).

244. Nuñez, P.J., Rivas, A., García-Plaza, E., Beamud, E. and Sanz-Lobera, A., 2015. Dimensional and surface texture characterization in fused deposition modelling (FDM) with ABS plus. Procedia Engineering, 132, pp.856-863.

245. Rankouhi, B., Javadpour, S., Delfanian, F. and Letcher, T., 2016. Failure analysis and mechanical characterization of 3D printed ABS with respect to layer thickness and orientation. Journal of Failure Analysis and Prevention, 16(3), pp.467-481.

246. Singh, R. and Singh, G., 2014. Investigations for statistically controlled investment casting solution of FDM-based ABS replicas. Rapid Prototyping Journal, 20(3), pp.215-220.

247. Drummer, D., Cifuentes-Cuéllar, S. and Rietzel, D., 2012. Suitability of PLA/TCP for fused deposition modeling. Rapid Prototyping Journal, 18(6), pp.500-507.

248. Afrose, M.F., Masood, S.H., Nikzad, M. and Iovenitti, P., 2014. Effects of build orientations on tensile properties of PLA material processed by FDM. In Advanced Materials Research, Vol. 1044, pp. 31-34.

249. Afrose, M.F., Masood, S.H., Iovenitti, P., Nikzad, M. and Sbarski, I., 2016. Effects of part build orientations on fatigue behaviour of FDM-processed PLA material. Progress in Additive Manufacturing, 1(1-2), pp.21-28.

250. Cuiffo, M.A., Snyder, J., Elliott, A.M., Romero, N., Kannan, S. and Halada, G.P., 2017. Impact of the fused deposition (FDM) printing process on polylactic acid (PLA) chemistry and structure. Applied Sciences, 7(6), p.579.

251. Knoop, F., Schoeppner, V., Knoop, F.C. and Schoeppner, V., 2015, August. Mechanical and thermal properties of FDM parts manufactured with polyamide 12. In Proceedings of the 26th Annual International Solid Freeform Fabrication Symposium-An Additive Manufacturing Conference, Austin, TX, USA (pp. 10-12).

252. Jia, Y., He, H., Peng, X., Meng, S., Chen, J. and Geng, Y., 2017. Preparation of a new filament based on polyamide-6 for three-dimensional printing. Polymer Engineering & Science, 57(12), pp.1322-1328.

253. Li, H., Zhang, S., Yi, Z., Li, J., Sun, A., Guo, J. and Xu, G., 2017. Bonding quality and fracture analysis of polyamide 12 parts fabricated by fused deposition modeling. Rapid Prototyping Journal, 23(6), pp.973-982.

254. Rahim, T.N.A.T., Abdullah, A.M., Akil, H.M., Mohamad, D. and Rajion, Z.A., 2017. The improvement of mechanical and thermal properties of polyamide 12 3D printed parts by fused deposition modelling. eXPRESS Polymer Letters, 11(12), pp.963-982.

255. Cruz, P., Shoemake, E.D., Adam, P. and Leachman, J., 2015. Tensile strengths of polyamide based 3D printed polymers in liquid nitrogen. In IOP Conference Series: Materials Science and Engineering, Vol. 102, No. 1, p. 012020.

256. Domingo-Espin, M., Borros, S., Agullo, N., Garcia-Granada, A.A. and Reyes, G., 2014. Influence of building parameters on the dynamic mechanical properties of polycarbonate fused deposition modeling parts. 3D Printing and Additive Manufacturing, 1(2), pp.70-77.

257. Domingo-Espin, M., Puigoriol-Forcada, J.M., Garcia-Granada, A.A., Llumà, J., Borros, S. and Reyes, G., 2015. Mechanical property characterization and simulation of fused deposition modeling Polycarbonate parts. Materials & Design, 83, pp.670-677.

258. Gajdoš, I., Kaščák, Ľ., Spišák, E. and Slota, J., 2015. Flexural properties of FDM prototypes made with honeycomb and sparse structure. In Key Engineering Materials, Vol. 635, pp. 169-173.

259. Hill, N. and Haghi, M., 2014. Deposition direction-dependent failure criteria for fused deposition modeling polycarbonate. Rapid Prototyping Journal, 20(3), pp.221-227.

260. Salazar-Martin, A.G., Perez, M.A., García-Granada, A.A., Reyes, G. and Puigoriol-Forcada, J.M., 2018. A study of creep in polycarbonate fused deposition modelling parts. Materials & Design, 141, pp.414-425.

261. Masood, S.H., Mau, K. and Song, W.Q., 2010. Tensile properties of processed FDM polycarbonate material. In Materials Science Forum, Vol. 654, pp. 2556-2559.

262. Puigoriol-Forcada, J.M., Alsina, A., Salazar-Martín, A.G., Gomez-Gras, G. and Pérez, M.A., 2018. Flexural fatigue properties of polycarbonate fused-deposition modelling specimens. Materials & Design, 155, pp.414-421.

263. Smith, W.C. and Dean, R.W., 2013. Structural characteristics of fused deposition modeling polycarbonate material. Polymer testing, 32(8), pp.1306-1312.

264. Carneiro, O.S., Silva, A.F. and Gomes, R., 2015. Fused deposition modeling with polypropylene. Materials & Design, 83, pp.768-776.

265. Scotti, G., Nilsson, S.M., Haapala, M., Pöhö, P., AF Gennäs, G.B., Yli-Kauhaluoma, J. and Kotiaho, T., 2017. A miniaturised 3D printed polypropylene reactor for online reaction analysis by mass spectrometry. Reaction Chemistry & Engineering, 2(3), pp.299-303.

266. Bedi, P., Singh, R. and Ahuja, I.P.S., 2018. Effect of SiC/Al2O3 particle size reinforcement in recycled LDPE matrix on mechanical properties of FDM feed stock filament. Virtual and Physical Prototyping, 13(4), pp.246-254.

267. Boparai, K.S., Singh, R. and Singh, H., 2016. Modeling and optimization of extrusion process parameters for the development of Nylon6–Al–Al 2 O 3 alternative FDM filament. Progress in additive manufacturing, 1(1-2), pp.115-128.

268. Sa'ude, N., Masood, S.H., Nikzad, M., Ibrahim, M. and Ibrahim, M.H.I., 2013. Dynamic mechanical properties of copper-ABS composites for FDM feedstock. Int. J. Eng. Res. Appl, 3(3), pp.257-1263.

269. Dickson, A.N., Barry, J.N., McDonnell, K.A. and Dowling, D.P., 2017. Fabrication of continuous carbon, glass and Kevlar fibre reinforced polymer composites using additive manufacturing. Additive Manufacturing, 16, pp.146-152.

270. Gray IV, R.W., Baird, D.G. and Helge Bøhn, J., 1998. Effects of processing conditions on short TLCP fiber reinforced FDM parts. Rapid Prototyping Journal, 4(1), pp.14-25.

271. Kalita, S., Finley, J., Bose, S., Hosick, H. and Bandyopadhyay, A., 2002. Development of porous polymer-ceramic composites as bone grafts. MRS Online Proceedings Library Archive, 726.

272. Kumar, R., Singh, R. and Ahuja, I.P.S., 2018. Investigations of mechanical, thermal and morphological properties of FDM fabricated parts for friction welding applications. Measurement, 120, pp.11-20.

273. Corney, J., Masood, S.H. and Song, W.Q., 2005. Thermal characteristics of a new metal/polymer material for FDM rapid prototyping process. Assembly Automation, Vol. 25 Iss 4 pp. 309 – 315.

274. Ramli, M.S., Wahab, M.S., Ahmad, M. and Bala, A.S., 2016. FDM preparation of bio-compatible UHMWPE polymer for artificial implant. The International Journal of Advanced Manufacturing Technology, 11(8), pp.5473-5480.

275. Singh, N., Singh, R. and Ahuja, I.P.S., 2018. Recycling of polymer waste with SiC/Al2O3 reinforcement for rapid tooling applications. Materials Today Communications, 15, pp.124-127.

276. Singh Boparai, K., Singh, R. and Singh, H., 2016. Wear behaviour of FDM parts fabricated by composite material feed stock filament. Rapid Prototyping Journal, 22(2), pp.350-357.

277. Singh Boparai, K., Singh, R. and Singh, H., 2016. Experimental investigations for development of Nylon6-Al-Al2O3 alternative FDM filament. Rapid Prototyping Journal, 22(2), pp.217-224.

278. Sodeifian, G., Ghaseminejad, S. and Yousefi, A.A., 2019. Preparation of polypropylene/short glass fiber composite as Fused Deposition Modeling (FDM) filament. Results in Physics, 12, pp.205-222.

279. Tekinalp, H.L., Kunc, V., Velez-Garcia, G.M., Duty, C.E., Love, L.J., Naskar, A.K., Blue, C.A. and Ozcan, S., 2014. Highly oriented carbon fiber–polymer composites via additive manufacturing. Composites Science and Technology, 105, pp.144-150.

280. Berretta, S., Davies, R., Shyng, Y.T., Wang, Y. and Ghita, O., 2017. Fused Deposition Modelling of high temperature polymers: Exploring CNT PEEK composites. Polymer Testing, 63, pp.251-262.

281. Chen, Q., Mangadlao, J.D., Wallat, J., De Leon, A., Pokorski, J.K. and Advincula, R.C., 2017. 3D printing biocompatible polyurethane/poly (lactic acid)/graphene oxide nanocomposites: anisotropic properties. ACS applied materials & interfaces, 9(4), pp.4015-4023.

282. Chizari, K., Daoud, M.A., Ravindran, A.R. and Therriault, D., 2016. 3D printing of highly conductive nanocomposites for the functional optimization of liquid sensors. Small, 12(44), pp.6076-6082.

283. Christ, J.F., Aliheidari, N., Ameli, A. and Pötschke, P., 2017. 3D printed highly elastic strain sensors of multiwalled carbon nanotube/thermoplastic polyurethane nanocomposites. Materials & Design, 131, pp.394-401.

284. Coppola, B., Cappetti, N., Di Maio, L., Scarfato, P. and Incarnato, L., 2017, September. Layered silicate reinforced polylactic acid filaments for 3D printing of polymer nanocomposites. In 2017 IEEE 3rd International Forum on Research and Technologies for Society and Industry (RTSI), pp. 1-4. IEEE.

285. Dorigato, A., Moretti, V., Dul, S., Unterberger, S.H. and Pegoretti, A., 2017. Electrically conductive nanocomposites for fused deposition modelling. Synthetic Metals, 226, pp.7-14.

286. Dul, S., Fambri, L. and Pegoretti, A., 2016. Fused deposition modelling with ABS–graphene nanocomposites. Composites Part A: Applied Science and Manufacturing, 85, pp.181-191.

287. Gnanasekaran, K., Heijmans, T., Van Bennekom, S., Woldhuis, H., Wijnia, S., de With, G. and Friedrich, H., 2017. 3D printing of CNT-and graphene-based conductive polymer nanocomposites by fused deposition modeling. Applied materials today, 9, pp.21-28.

288. Kim, H., Fernando, T., Li, M., Lin, Y. and Tseng, T.L.B., 2018. Fabrication and characterization of 3D printed BaTiO3/PVDF nanocomposites. Journal of Composite Materials, 52(2), pp.197-206.

289. Kim, H., Johnson, J., Chavez, L.A., Rosales, C.A.G., Tseng, T.L.B. and Lin, Y., 2018. Enhanced dielectric properties of three phase dielectric MWCNTs/BaTiO3/PVDF

nanocomposites for energy storage using fused deposition modeling 3D printing. Ceramics International, 44(8), pp.9037-9044.

290. Prashantha, K. and Roger, F., 2017. Multifunctional properties of 3D printed poly (lactic acid)/graphene nanocomposites by fused deposition modeling. Journal of Macromolecular Science, Part A, 54(1), pp.24-29.